SO_2-Sorption in Metall-organischen Gerüstverbindungen für die potenzielle Anwendung in der Rauchgasentschwefelung

Dissertation

zur Erlangung des Doktorgrades
der Mathematisch-Naturwissenschaftlichen Fakultät
der Heinrich-Heine-Universität Düsseldorf

vorgelegt von

Philipp Brandt
aus Dormagen

Düsseldorf, Juli 2021

aus dem Institut für Anorganische Chemie und Strukturchemie I

der Heinrich-Heine-Universität Düsseldorf

Gedruckt mit der Genehmigung der

Mathematisch-Naturwissenschaftlichen Fakultät der

Heinrich-Heine-Universität Düsseldorf

Berichterstatter:

1. Prof. Dr. Christoph Janiak

2. Prof. Dr. Christian Ganter

Tag der mündlichen Prüfung: 17.09.2021

Eidesstattliche Erklärung

Ich versichere an Eides statt, dass die Dissertation von mir selbstständig und ohne unzulässige fremde Hilfe unter Beachtung der „Grundsätze zur Sicherung guter wissenschaftlicher Praxis“ an der Heinrich-Heine-Universität Düsseldorf erstellt worden ist. Die aus fremden Quellen direkt oder indirekt übernommenen Gedanken sind als solche kenntlich gemacht. Die Arbeit wurde bisher weder im Inland noch im Ausland in gleicher oder ähnlicher Form einer anderen Prüfungsbehörde vorgelegt. Es wurden keine früheren erfolglosen Promotionsversuche unternommen.

Ort, Datum

Unterschrift

Danksagung

An dieser Stelle möchte ich mich bei den Personen bedanken, die mich während des Studiums und meiner Promotion unterstützt und zum Gelingen dieser Arbeit beigetragen haben.

Bei Herrn Prof. Dr. Christoph Janiak möchte ich mich für die Aufnahme in seinem Arbeitskreis und für das Ermöglichens meines Promotionsvorhabens bedanken. Weiter danke ich ihm für zahlreiche interessante und konstruktive Diskussionen sowie insbesondere für den wissenschaftlichen Freiraum, den er mir bei der Wahl des Themas und während der Anfertigung dieser Arbeit gewährt hat. Auch danke ich ihm für die Möglichkeit zur Teilnahme an Fortbildungsseminaren und Konferenzen.

Herrn Prof. Dr. Christian Ganter danke ich für die Übernahme des Koreferates dieser Arbeit und für die offenen beratenden Gespräche und Unterstützung während meines Studiums.

Herrn Dr. Oliver Weingart möchte ich für zahlreiche Diskussionen und Einblicke in theoretische Hintergründe sowie die Kooperation in gemeinsamen Veröffentlichungen danken. Auch danke ich ihm für seine Geduld und Beharrlichkeit, wenn es darum ging neue Programme und Methoden auszuprobieren und sich in diese „reinzufuchsen".

Ein besonderer Dank gilt allen Kollegen, die mich im Zuge dieser Arbeit unterstützt haben. Dabei möchte ich mich bei Dr. Sebastian Glomb für die interessante Einführung in die Welt der Metall-organischen Gerüstverbindungen und bei Dr. Simon Millan für die herzliche Aufnahme im AK Janiak, für seinen Rat und die zahlreichen Denkanstöße bedanken.

Ganz besonders möchte ich mich an dieser Stelle bei Dr. Carsten Schlüsener für seine nie endende Hilfsbereitschaft, das Korrekturlesen dieser Arbeit, seine offenen Ohren und Rücksicht bei Ausführung des Lüftungsprotokolls bedanken. Wir wurden in dieser Zeit zu guten Freunden.

Dr. Alexander Nuhnen danke ich für seine Hilfe und Zusammenarbeit an gemeinsamen Veröffentlichungen und insbesondere für seine Arbeit zur Bestimmung von Adsorptionsenthalpien, die mir das Leben bei der Berechnung eben solcher deutlich erleichtert hat.

Bei Dr. István Boldog möchte ich mich ganz herzlich für seine ausschweifenden, aber stets lehrreichen und anregenden Diskussionen zu Themen wie Chemie, über Politik bis hin zur Philosophie bedanken. Auch danke ich ihm für sein großes Engagement und die Zusammenarbeit in der Praktikumslehre.

Zuletzt danke ich ihm für seine ständige kritische Hinterfragung des *status quo* und seinem unermüdlichen Antrieb diesen zu verbessern.

Shang-Hua Xing, Jun Liang und Yangyang Sun danke ich für die kooperative Zusammenarbeit bei verschiedenen Arbeiten und darüber hinaus für interessante Gespräche und den kulturellen Austausch. Bei den festangestellten Mitarbeitern Claudia Schäfer, Jutta Bourgeois sowie Birgit Tommes, Annette Ricken und Marcell Demandt bedanke ich mich für ihre allgemeine Unterstützung während meiner Promotion.

Meinen Bürokollegen Dr. Carsten Schlüsener, Dr. Bastian Moll, Dr. Marvin Siebels, Dr. Tobie J. Matemb Ma Ntep, Tobias Heinen, Dennis Woschko und Robert Oestreich danke ich für eine angenehme und entspannte Arbeitsatmosphäre. Für unterhaltsame Gespräche im Rahmen der Kaffeerunde möchte ich mich insbesondere bei Dr. Dennis Dietrich und Simon-Patrick Höfert bedanken.

Meinen beiden Bachelorstudenten, Ruben Poschkamp und Gülin Kurt danke ich für die stets motivierte und angenehme Zusammenarbeit und für ihren Einsatz im Labor und die daraus resultierenden Beiträge zu dieser Arbeit.
Für ausgelassene, feucht fröhliche Abende auf dem Dach und das feierabendliche Darten danke ich allen hieran Beteiligten. Moritz Steinert danke ich für gemeinsame abenteuerliche Expeditionen innerhalb des Universitätsgeländes.

Bei Alexander Berger, George Oguto und Julius Piontkowitz möchte ich mich für die gegenseitige Unterstützung in gemeinsamen Modulen und Praktika während des Studiums sowie für die unternommenen, lustigen außeruniversitären Aktivitäten bedanken.

Ein besonderer Dank geht an meine Familie, die mich während meines gesamten Studiums bedingungslos unterstützt hat und mir Halt gab.

Abschließend gilt mein größter Dank dem für mich wichtigsten Menschen auf dieser Welt. Bianca, ich danke dir, dass du immer für mich da bist, ich dir alles erzählen kann, du geduldig bist und mich auffängst, wenn es gerade mal nicht so läuft.

Kurzzusammenfassung

In dieser Arbeit wurde eine Auswahl an literaturbekannten MOFs, ausgewählt aufgrund ihrer spezifischen Eigenschaften, bezüglich ihres Adsorptionsverhaltens gegenüber SO_2 und weiteren Aspekten, wie Selektivität und Stabilität untersucht. Das Hauptaugenmerk wurde dabei auf die zugängliche Oberfläche, das zugängliche Porenvolumen, Poren- sowie Poreneingangsdurchmesser und funktionelle Gruppen gesetzt. Auf Basis von entsprechend gemessenen Einzelgasisothermen konnten mit Hilfe von „*ideal adsorbed solution theory*" (IAST) Rechnungen SO_2/CO_2-Selektivitäten bestimmt werden und damit Aussagen über das potenzielle Gastrennverhalten der untersuchten Materialien getroffen werden. Die Ergebnisse dieser Untersuchungen ermöglichten es, systematische Einflussfaktoren für die SO_2-Sorption in entsprechenden Netzwerken zu identifizieren und damit die Effizienz bei der Suche nach potenziellen Adsorbentien für die Anwendung in adsorptionsbasierten Rauchgasentschwefelungsprozessen zu verbessern.

In den angefertigten SO_2-Sorptionsstudien wurden einerseits hoch stabile Zr- und Al-MOF untersucht, andererseits wurden prototypische MOFs im direkten Vergleich zu industriell etablierten porösen Materialien wie Zeolith, Silicagel oder Aktivkohle analysiert.

Entsprechend ihrer hohen Oberfläche zeigten die untersuchten MOFs im Vergleich zu anderen porösen Materialien hohe Aufnahmekapazitäten für SO_2. Eine wiederholte Materialcharakterisierung nach Exposition gegenüber SO_2 legte jedoch auch deutliche Schwächen vieler MOF-Materialien dar, welche teilweise degradierten bzw. nicht vollständig regeneriert werden konnten.

Allgemein zeigte sich eine gute Korrelation der SO_2-Aufnahmekapazität bei 293 K und 1 bar mit der zugänglichen Porenoberfläche, weitgehend unabhängig von anderen Strukturmerkmalen der Gerüstverbindungen. Da typische Rauchgasmischungen jedoch nur geringe Mengen SO_2 (500 – 3000 ppm) enthalten ist für die Rauchgasentschwefelung (engl. *flue gas desulfurization*, FGD) insbesondere die Niedrigdruckadsorption relevant. Eine Korrelation der SO_2-Aufnahmekapazität bei 293 K im Druckbereich ≤ 0,1 bar mit der Porenoberfläche wurde jedoch nicht beobachtet. Stattdessen konnte ein Zusammenhang zwischen dem porenlimitierenden Durchmesser eines porösen Materials, womit hier der kleinste Durchmesser einer Pore oder eines Porenzugangs gemeint ist, und der SO_2-Aufnahme im Bereich von 0,01 – 0,1 bar bei 293 K gezeigt werden. Hierbei erwiesen sich insbesondere mikroporöse Adsorbentien mit Porendurchmessern zwischen 4 und 8 Å als vielversprechend, welche

in der Größenordnung des kinetischen Durchmessers von SO_2 (4,1 Å) liegen.

Als eine weitere Möglichkeit zur Einflussnahme auf die Niedrigdruck-SO_2-Adsorption in MOFs wurden Porenfunktionalisierungen untersucht. Aminofunktionalisierte MOFs konnten einerseits zu einer erhöhten Affinität des Netzwerkes zu leicht polarisierbarem SO_2 führen, zeigten andererseits aber auch ein schlechteres Abschneiden in den Stabilitätstests verglichen mit ihren nicht-funktionalisierten Varianten.

Weiter wurden für ausgewählte MOFs die isosterische Adsorptionsenthalpie nahe einer Beladung von Null (ΔH_{ads}^{0}) für SO_2 berechnet, wodurch die stärkste Wechselwirkung zwischen Gastmolekül und Netzwerk bestimmt werden konnte. Die ΔH_{ads}^{0}-Werte waren in guter Übereinstimmung mit Dichtefunktionaltheorie (DFT) basierten Berechnungen für präferierte Bindungsstellen von SO_2 in entsprechenden MOFs. Dabei zeigte sich, dass insbesondere μ-OH Gruppen innerhalb der *secondary building unit* (SBU) attraktive Bindungsstellen für SO_2 darstellen können.

In einer weiteren Studie wurden MOFs, mit außergewöhnlich hoher Oberfläche bzw. besonderer Stabilität ausgewählt und bezüglich SO_2-Sorption und potenziellem Gastrennungsvermögen untersucht. MOF-177 mit einer BET-Oberfläche von 4100 $m^2\,g^{-1}$ zeigte einen Rekord-Gasaufnahme von 25,7 mmol g^{-1} für die SO_2-Sorption bei 293 K und einem Druck von 1 bar, erwies sich allerdings als instabil gegenüber der Exposition von SO_2.

Das Al-MOF MIL-160 hingegen zeigte mit 7,2 mmol g^{-1} zwar eine deutlich niedrigere Maximalkapazität konnte jedoch mit einer hohen SO_2-Aufnahme im Niederdruckbereich bei Temperaturen zwischen 293 und 373 K und seiner hohen Stabilität überzeugen. Weitere Untersuchungen zum Trennvermögen von MIL-160 ergaben IAST-Selektivitäten von 128 (SO_2/CO_2; v:v; 10/90) sowie eine erfolgreiche Retention von SO_2 in simulierten als auch experimentellen Durchbruchskurven mit einer anwendungsrelevanten Gasmischung ($N_2/CO_2/SO_2$; v:v:v; 84,9 : 15,0 : 0,1). Diese Ergebnisse zeichnen MIL-160 als vielversprechenden Kandidaten für adsorptionsbasierte, regenerative FGD-Prozesse aus.

Abstract

In this work, a selection of MOFs known in the literature, chosen for their specific properties, were investigated in terms of their adsorption behavior towards SO_2 and other aspects, such as selectivity and stability. Here, special attention was paid to the accessible surface, the accessible pore volume, pore and pore-entrance diameters, and functional groups of investigated MOFs. Based on the measured single gas isotherms, SO_2/CO_2 selectivities could be determined using "ideal adsorbed solution theory" (IAST) calculations and thus statements could be made about the potential gas separation behavior of the investigated materials. The results of these studies enabled the identification of systematic factors influencing SO_2 sorption in corresponding networks, thus improving efficiency in the search for potential adsorbents for use in adsorption-based flue gas desulfurization processes.

should enable the identification of systematical influencing factors on the SO_2 sorption in the corresponding frameworks and thus enhance the efficiency of the search after potential adsorbents for the application in adsorption-based flue gas desulphurization processes.

In the performed SO_2 sorption studies on the one hand highly stable Zr- and Al-MOFs were investigated, and on the other hand a series of prototype MOFs were analyzed in direct comparison to other established porous materials such as zeolites, silica gel, or activated carbon.

Following their high surface area, investigated MOFs showed comparatively high absorption capacities for SO_2, however, it was also shown that the accessible surface can be partially degraded or not completely regenerated after exposure to SO_2. In general, the SO_2 uptake capacity at 293 K and 1 bar was found to correlate well with the accessible pore surface area, largely independent of other structural features of the frameworks. However, since typical flue gas mixtures contain only small amounts of SO_2 (500 – 3000 ppm), low-pressure adsorption is particularly relevant for flue gas desulfurization (FGD). The fraction of SO_2 in flue gas is typically around 500 – 3000 ppm. However, a correlation of the SO_2 capacity at 293 K in the low-pressure region ($\leq$ 0.1 bar) and the pore surface area was not observed. Instead, a relationship between the pore-limiting diameter, which is the smallest diameter of a pore or pore access of a porous material, and the SO_2 uptake in the range of 0.01-0.1 bar at 293 K was observed. Microporous adsorbents with pore diameters between 4 and 8 Å, near the kinetic diameter of SO_2 (4.1 Å), have proven to be particularly promising. As a further possibility to influence the low-pressure SO_2 adsorption, pore functionalization was investigated. On the one hand, Amino functionalized

ligands showed an enhanced affinity of the framework to easily polarizable SO_2, but on the other hand, they also showed worse performance in the stability tests compared to their non-functionalized variants.

Further, for selected MOFs the isosteric adsorption enthalpy near zero loading (ΔH_{ads}^{0}) for SO_2 was calculated, allowing to determine the strongest interaction between the guest molecule and the network. The ΔH_{ads}^{0}-values were in good agreement with density functional theory (DFT) based calculations for preferred binding sites of SO_2 in corresponding MOFs. Herein, μ-OH groups within the networks´ secondary building units (SBU) tend to be attractive binding sites for SO_2.

In a further study selected MOFs with special properties, such as high surface area or exceptional stability, were investigated concerning SO_2 sorption and potential gas separation capability. MOF 177, with a BET surface area of 4100 $m^2 g^{-1}$, showed a record uptake value of 25.7 mmol g^{-1} for SO_2 at 293 K and a pressure of 1 bar but did not prove to be robust against corrosive SO_2. The Al-MOF MIL-160, on the other hand, showed a lower capacity with 7.2 mmol g^{-1} SO_2 uptake, but its high SO_2 adsorption in the low-pressure range at elevated temperatures between 293 – 373 K and high stability were convincing. Further investigations on the separation capability of MIL-160 resulted in IAST-selectivity values of 128 (SO_2/CO_2; v:v; 10/90) and successful retention of SO_2 in simulated as well as experimental breakthrough curves with an application-related gas mixture ($N_2/CO_2/SO_2$; v:v:v; 84.9 : 15.0 : 0.1). These results mark MIL-160 as a promising candidate for adsorption-based, regenerative FGD-processes.

Publikationsliste

Erstautorschaften

Philipp Brandt, Shang-Hua Xing, Jun Liang, Gülin Kurt, Alexander Nuhnen, Oliver Weingart, Christoph Janiak: "Zirconium and Aluminum MOFs for Low-Pressure SO_2 Adsorption and Potential Separation: Elucidating the Effect of Small Pores and NH_2-Groups"
ACS Appl. Mater. Interfaces, **2021**, *13*, 29137–29149. DOI: 10.1021/acsami.1c06003

Philipp Brandt, Alexander Nuhnen, Seçil Öztürk, Gülin Kurt, Jun Liang, Christoph Janiak: "Comparative Evaluation of Different MOF and Non-MOF Porous Materials for SO_2 Adsorption and Separation Showing the Importance of Small Pore Diameters for Low–Pressure Uptake"
Adv. Sustainable Syst. **2021**, *5*, 2000285. DOI: 10.1002/adsu.202000285

Philipp Brandt, Alexander Nuhnen, Marcus Lange, Jens Möllmer, Oliver Weingart, Christoph Janiak: "Metal–Organic Frameworks with Potential Application for SO_2 Separation and Flue Gas Desulfurization"
ACS Appl. Mater. Interfaces, **2019**, *11*, 17350–17358. DOI: 10.1021/acsami.9b00029

Co-Autorschaften

Shang-Hua Xing, Jun Liang, Philipp Brandt, Felix. Schäfer, Alexander Nuhnen, Tobias Heinen, István Boldog, Jens Möllmer, Marcus Lange, Oliver Weingart, Christoph Janiak: "Capture and Separation of SO_2 Traces in Metal-Organic Frameworks via Pre-synthetic Pore Environment Tailoring by Methyl Groups"
Angew. Chem. Int. Ed. **2021**, *60*, 2–10. DOI: 10.1002/anie.202105229

Jun Liang, Shang-Hua Xing, Philipp Brandt, Alexander Nuhnen, Carsten Schlüsener, Yangyang, Sun, Christoph Janiak: "A chemically stable cucurbit[6]uril-based hydrogen-bonded organic framework for potential SO_2/CO_2 separation
J. Mater. Chem. A, **2020**, *8*, 19799–19804. DOI: 10.1039/d0ta07457h

Bastian Moll, Tim Müller. Carsten Schlüsener, Alexa Schmitz, Philipp Brandt, Seçil Öztürk, Christoph Janiak: "Modulated synthesis of thiol-functionalized fcu and hcp UiO-66(Zr) for the removal of silver(I) ions from water"

Mater. Adv. **2021**, *2*, 804-812. DOI: 10.1039/D0MA00555J

Tim-Oliver Knedel, Stefan Buss, Iván Maisuls, Constantin G. Daniliuc, Carsten Schlüsener, Philipp Brandt, Oliver Weingart, Annette Vollrath, Christoph Janiak, Cristian A. Strassert: "Encapsulation of Phosphorescent Pt(II) Complexes in Zn-Based Metal-Organic Frameworks toward Oxygen-Sensing Porous Materials"

Inorg. Chem. **2020**, *59*, 7252–7264. DOI: 10.1021/acs.inorgchem.0c00678

Anas Alrefai, Suvendu Sekhar Mondal, Alexander Wruck, Alexandra Kelling, Uwe Schilde, Philipp Brandt, Christoph Janiak, Sophie Schönfeld, Birgit Weber, Lawrence Rybakowski, Carmen Herrman, Katlen Brennenstuhl, Sascha Eidner, Michael U. Kumke, Karsten Behrens, Christina Günter, Holger Müller, Hans-Jürgen Holdt: "Hydrogen-bonded supramolecular metal-imidazolate frameworks: gas sorption, magnetic and UV/Vis spectroscopic properties"

Inclusion Phenom. Macrocyclic Chem. **2019**, *94*, 155-165. DOI: 10.1007/s10847-019-00926-6

Abkürzungsverzeichnis

Å	Ångström (1 Å = 10^{-10} m)
ads.	Adsorption
as	*as-synthesized* (wie synthetisiert)
atm	Physikalische Atmosphäre (1 atm = 101325 kg ms^{-2})
BET	Brunauer-Emmett-Teller
CAU	Christian-Albrecht-Universität
CTF	*covalent triazine framework* (kovalente triazinbasierte Gerüstverbindung)
CUS	*coordinatively unsaturated site* (Koordinativ ungesättigte Stelle)
H_2BDC	Terephthalsäure, Benzol-1,4-dicarbonsäure
H_2BTC	Trimesinsäure, Benzol-1,3,5-tricarbonsäure
des.	Desorption
DFT	Dichtefunktionaltheorie
DMF	*N,N*-Dimethylformamid
DUT	Technische Universität Dresden
eq.	Äquivalente
exp.	experimentell
FGD	*flue gas desulfurization* (Rauchgasentschwefelung)
fum	Fumarat
H_2FDC	2,5-Furandicarbonsäure
GCMC	*Grand canonical Monte Carlo*
H_{ads}	Adsorptionsenthalpie
HKUST	*Hong Kong University of Science and Technology*
HSAB	*Hard and Soft Acids and Bases*
IAST	*ideal adsorbed solution theory*
IUPAC	*International Union of Pure and Applied Chemistry* (Internationale Union für reine und angewandte Chemie)
J	Joule
K	Kelvin

µm	Mikrometer
mbar	Millibar
MeIm	2-Methylimidazol
MFM	*Manchester Framework Material*
MIL	*Matériaux´de l´Institut Lavoisier* (Materialien des Instituts Lavoisier)
min	Minute
mL	Milliliter
n. a.	*not available* (nicht verfügbar)
n. d.	*not determined* (nicht bestimmt)
NOTT	*University of Nottingham*
NU	*Northwestern University*
MOF	*Metal-organic framework* (Metall-organische Gerüstverbindung)
OMS	*open metal site* (offene Metallstelle)
Pa	Pascal
p. a.	*pro analysi* (zur Analyse)
PLD	*pore limiting diameter* (porenlimitierender Durchmesser)
PM	*particulate matter* (Feinstaub)
ppb	*parts per billion* (Teile von einer Milliarde)
ppm	*parts per million* (Teile von einer Millionen)
Q_{st}	Adsorptionswärme
PXRD	*powder x-ray diffraction* (Pulverröntgendiffraktometrie)
SAPO	Siliziumaluminophosphat
S_{BET}	BET-Oberfläche
SBU	*secondary building unit* (sekundäre Baueinheit)
STP	standard temperature and pressure
TGA	Thermogravimetrische Analyse
UiO	*Universitet i Oslo* (Universität Oslo)
wt%	Gewichtsprozent
ZIF	*Zeolitic imidazolate framework* (Zeolitische Imidazolat Gerüstverbindung)

Inhaltsverzeichnis

1 Einleitung

1.1 Metall-organische Gerüstverbindungen

Als eine junge Klasse der anorganisch-organischen Hybridmaterialien konnten Metall-organische Gerüstverbindungen (engl. *metal-organic frameworks*, MOFs) in den wissenschaftlichen Untersuchungen der letzten Jahrzehnte eindrucksvoll unter Beweis stellen welche Vorteile einzigartige, gleichmäßige und poröse Netzwerke mit sich bringen.[1,2] Dabei werden ihre physikalischen und chemischen Materialeigenschaften insbesondere von synergistische Effekte ihrer Struktur und Zusammensetzung bestimmt.[3]

Arbeiten zu Koordinationspolymeren von Hoskins und Robson stellten dabei die Grundlage für die später von Yaghi geprägte „retikuläre Chemie" in Bezug auf MOFs dar.[4,5,6,7]

MOFs werden durch die IUPAC als Koordinationsnetzwerke mit organischen Liganden und potenziellen Holräumen definiert.[8] MOFs werden aus einer Kombination von anorganischen und organischen Baueinheiten gebildet.

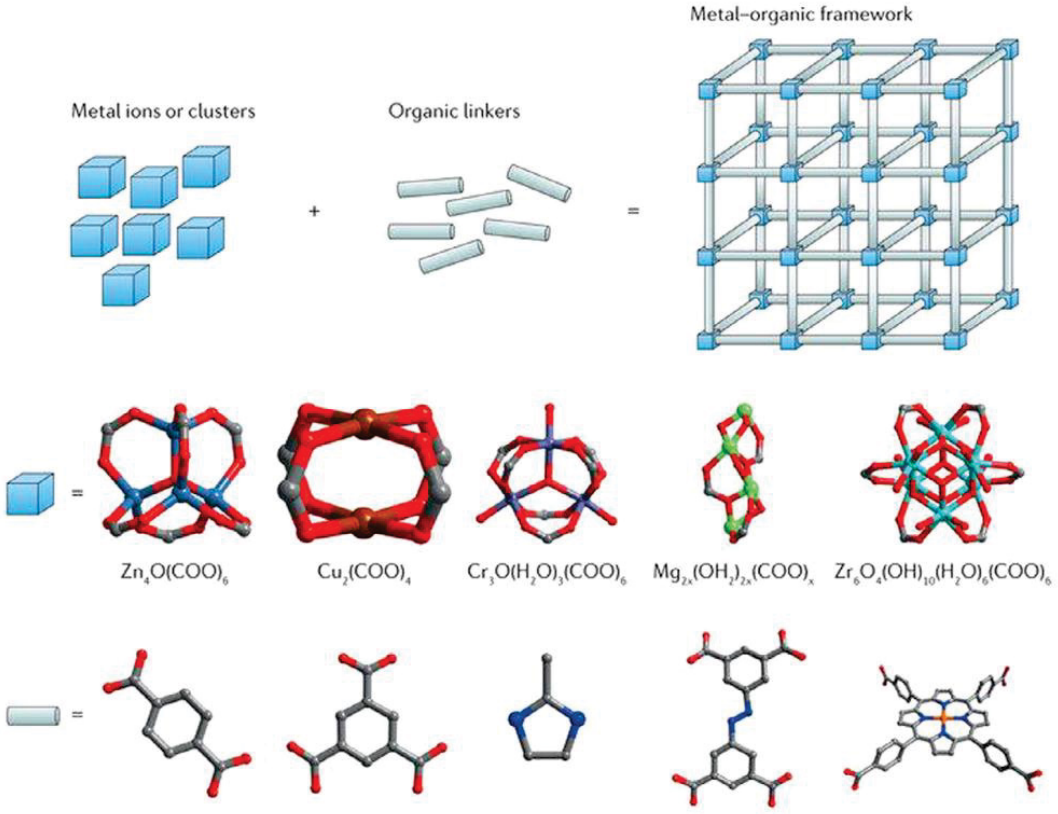

Abb. 1: Strukturelles Model von MOFs (obere Reihe), repräsentativen SBUs (mittlere Reihe) sowie Liganden (untere Reihe). Nachdruck mit Genehmigung von Referenz 9. Copyright 2016 Springer Nature.

Multidentale Liganden (Lewis-Base) verbrücken dabei über funktionelle Gruppen benachbarte Metallcluster (Lewis-Säure) durch koordinative Bindungen, wodurch zwei bis dreidimensionale Strukturen entstehen (Vgl. Abb. 1). Unter den bisher untersuchten Koordinationsgruppen der Liganden sind beispielsweise Carboxylate, Azolate, Sulfonate und Phosphonate zu finden. Liganden mit Carboxylat- oder Azolat-Funktionen und einem starren Kohlenstoffrückgrat als Korpus bilden besonders stabile MOFs aus (Vgl. Abb. 2).[10,11]

Die *secondary building unit* (SBU) besteht aus einem molekularen Komplex bzw. Cluster sowie den koordinierenden Atomen (O, N, etc.) des Liganden und beschreibt damit die Koordinationsgeometrie des Knotenpunkts zwischen einzelnen Liganden. Die SBU ist somit entscheidend für die Topologie eines Netzwerkes.[6] Obwohl MOFs häufig Merkmale von Kristallinität und Porosität aufweisen, sind diese Kriterien nicht bzw. nur eingeschränkt in der Definition eines MOFs eingebunden. Dies ist dadurch begründet, dass manche MOFs dynamische Strukturänderungen induziert durch äußere Einflüsse durchlaufen. Solche Einflüsse können Druck-, Temperaturänderungen oder die Einlagerung von Gastmolekülen sein. Aufgrund dieser potenziellen Dynamik kann sich sowohl die Kristallinität als auch die Porosität eines Netzwerkes verändern.[8]

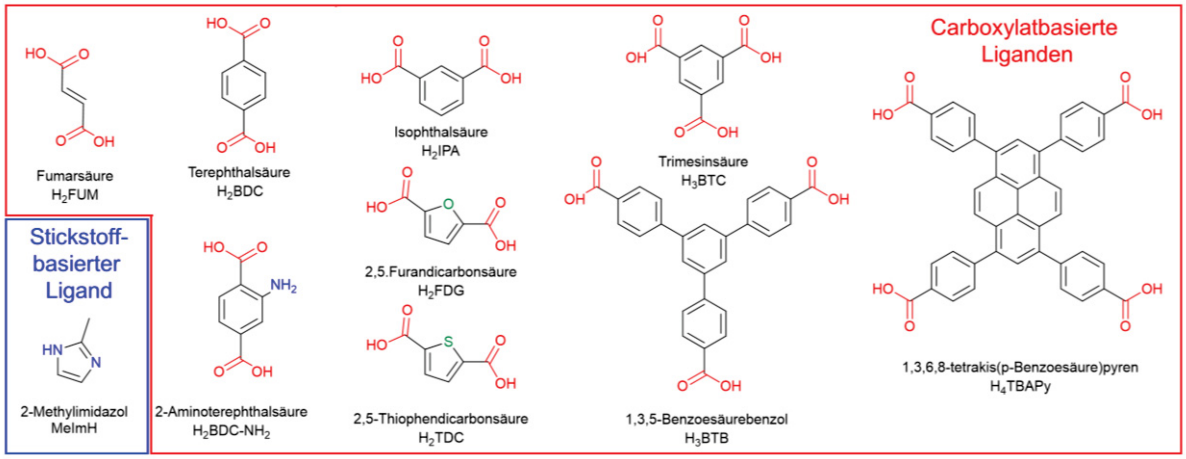

Abb. 2: Die für diese Arbeit relevanten carboxylat- und stickstoffbasierte Liganden.

Mikroporöse Zeolithe oder Alumophosphate sowie mesoporöse Silicate zählen zu den wichtigsten geordneten porösen Materialien und finden Anwendung in zahlreichen Gebieten. Allerdings sind sie im Unterschied zu MOFs stark eingeschränkt in der Modifikation von Struktur oder Oberflächeneigenschaften.[12,13,14]

Durch den modulartigen Aufbau von MOFs aus organischen Liganden mit Metallclustern bzw.

Metallionen, sind viele verschiedene Kombinationen mit unterschiedlichen Koordinationszahlen und -geometrien möglich. Bislang wurden über 70000 verschiedene MOF-Strukturen in der Literatur beschrieben.[15,16] Die dabei gebildeten Netzwerke verfügen in der Regel über eine gleichmäßige Topologie und Porenstruktur.[3]

Daraus ergibt sich die Möglichkeit zu einer gewissen „Designbarkeit", durch die MOFs in ihrer chemischen Natur (Metallkation und organischer Ligand), der Porengröße (mikro- bis mesoporös) sowie der geometrischen Form ihrer Poren (kubische oder sphärische Käfige, dreieckige, quadratische oder hexagonale Tunnel) angepasst werden können.[2,17] Da „Designbarkeit" aber eine Vorhersage über bisher unbekannte Strukturen impliziert, soll dieser Punkt im Folgenden näher erläutert werden.

Hierbei hilft das Konzept der SBUs, bei dem Bausteine eines Netzwerkes zu geometrischen Körpern oder Formen simplifiziert werden. Diese Bausteine können unter Beachtung ihrer Konnektivität miteinander kombiniert werden, um auf der Basis von bekannten Topologien Vorhersagen zu hypothetischen Strukturen machen zu können.[6,18]

Ein einfaches Beispiel stellt hierbei die Verlängerung von starren, linearen Carboxylatliganden dar. Die Erweiterung eines Liganden wie Terephthalat um zusätzliche Benzoleinheiten zu Biphenyl-4,4´-dicarboxylat bzw. Terphenyl-4,4´-dicarboxyylat führt bei erfolgreicher MOF-Synthese mit gleichem Metallzentrum auch zu einer gleichen Topologie, welche jedoch durch die veränderten Zellparameter oft zu erhöhten Oberflächen und Porenvolumina führt (Vgl. Abb. 3 links).[19] Dieser Ansatz wurde in der Literatur unter dem Begriff der „isoretikulären" Erweiterung bekannt und insbesondere von Yaghi *et al.* geprägt.[2,20]

Des Weiteren kann eine Veränderung der Koordinationsgeometrie, beispielsweise durch Austausch des Metallkations innerhalb der SBU, in Kombination mit dem gleichen Liganden zu einer andersartigen Topologie führen. Dies wird am Beispiel der Kombination von Terephthalat mit den unterschiedlichen Metallkationen Zn^{2+}, Cr^{3+} und Zr^{4+} zu den jeweiligen MOF-Strukturen MOF-5 (kubisch), MIL-101 (MTN Topologie) und UiO-66 (fcu Topologie) in Abb. 3 (rechts) verdeutlicht.[21,22]

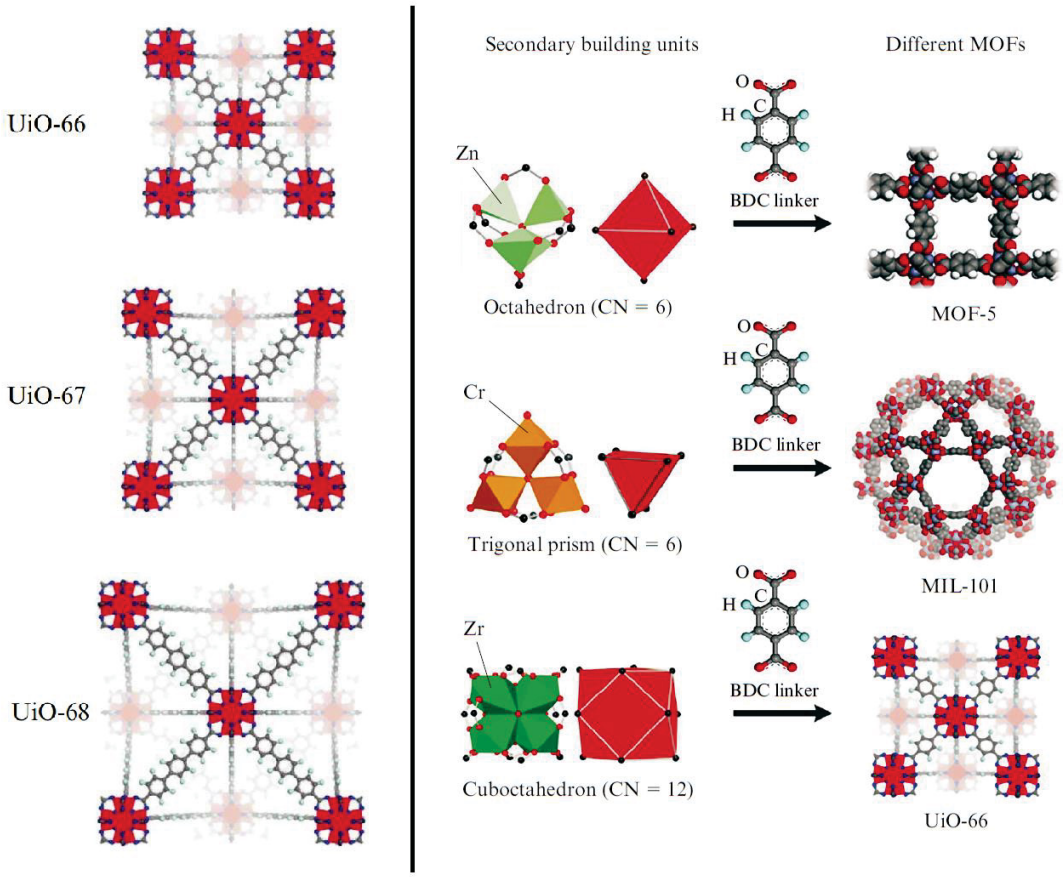

Abb. 3: Linke Seite: Isoretikuläre Erweiterung durch Verlängerung des Liganden. Terephthalat in UiO-66 (oben), Biphenyl-4,4´-dicarboxylat in UiO-67 (mittig) und Terphenyl-4,4´-dicarboxyylat in UiO-68 (unten). Nachdruck mit Genehmigung von Referenz 21. Copyright 2008 American Chemical Society. Rechte Seite: Strukturen von verschiedenen MOFs mit Terephthaltat als Ligand. SBU und Koordinationspolyeder (links) schematische Überstruktur des MOFs (rechts). Nachdruck mit Genehmigung von Referenz 22. Copyright 2010 Springer.

Die letztliche Struktur des MOFs kann durch die Auswahl des Metallsalzes und des Liganden gesteuert werden. Zusätzlich können auch noch weitere Synthesebedingungen maßgeblich Einfluss auf die Topologie, Morphologie, Partikelgröße, Kristallinität, Porosität und Defektstellen einer MOF-Struktur nehmen.[23,24] Besonders wichtige Faktoren bei der MOF-Synthese sind die Wahl der Synthesemethode, des Lösungsmittels, der Temperatur und die Reaktionszeit sowie die etwaige Zugabe eines Modulators (Abb. 4).[25]

Als etablierte Synthesemethoden sind die Solvothermal-, Rückfluss- und Mikrowellensynthese zu nennen, bei denen die Reaktanden unter thermischer Energiezufuhr in gelöster Form und unter Selbstassemblierungsprozessen zunächst die SBUs bilden, welche weiter zur komplexen Struktur vernetzt werden.

Die Solvothermalsynthese, welche in einem geschlossenen Gefäß bei autogenem Druck und oberhalb der Siedetemperatur des Lösungsmittels durchgeführt wird, stellt häufig eine ideale Methode zur Synthese von MOF-Einkristallen dar.[26] Die Rückflusssynthese kann eine geeignete Methode für ein *Upscaling* einer Synthesevorschrift sein, allerdings wird das Produkt hier durch kontinuierliches Rühren in der Regel als Pulver erhalten.[25,27] Mikrowellensynthesen können bereits nach kurzen Reaktionszeiten von wenigen Minuten zu einer erfolgreichen MOF-Bildung führen. Zudem sorgt das schnelle und gleichmäßige Erhitzen durch die Mikrowellenbestrahlung für besonders kleine MOF-Partikel mit enger Größenverteilung.[28]

Die bisher seltene mechanochemische Synthese hat den Vorteil, dass hier kein bzw. nur sehr geringe Mengen an Lösungsmittel erforderlich sind und die benötigte thermische Energie vollständig durch Reibung zugeführt wird.[29] Die sonochemische Synthese nutzt Hochleistungs-Ultraschall, bei dem durch Implosion von Kavitationsblasen hochenergetische Schockimpulse entstehen, welche zu lokalen Hotspots mit Temperaturen von 5000 °C und Drücken von 2000 atm führen, wodurch die Bildung von MOF-Kristallisationskeimen unterstützt wird. Gleichzeitig wird das Kristallwachstum durch extreme Abkühlraten begrenzt.[30,31]

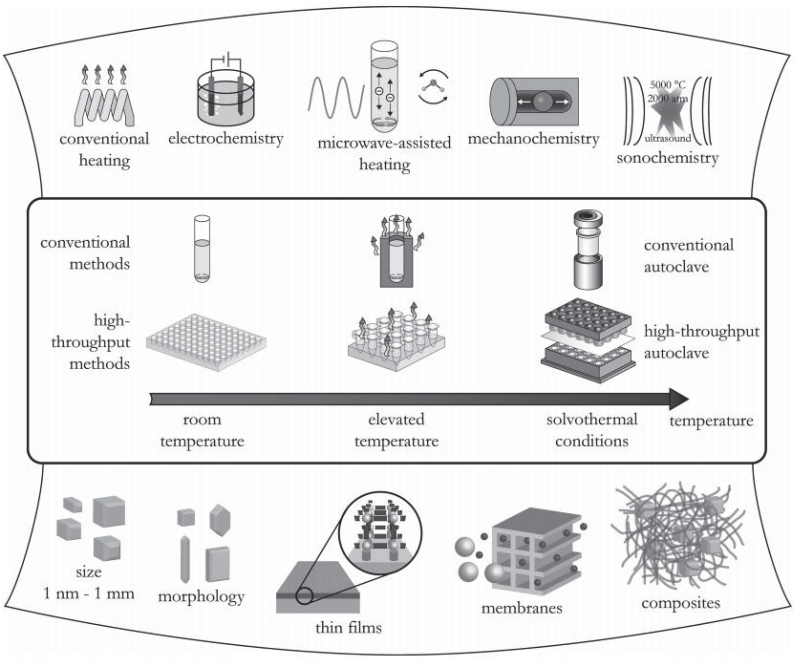

Abb. 4: Überblick zu verschiedenen Synthesemethoden (oben), Durchsatzverfahren bei entsprechenden Temperaturen (mittig) und die Reaktionsprodukte mit verschiedenen Eigenschaften (unten). Nachdruck mit Genehmigung von Referenz 25. Copyright 2012 American Chemical Society.

Während der Kristallisation werden Lösungsmittelmoleküle als „Platzhalter“ in die potenziell poröse Struktur eingebaut. Dies bewirkt eine Stabilisierung des Gerüsts und wird auch als „Templat-Effekt“ bezeichnet.[32] Da die Wahl des Lösungsmittels Einfluss auf die Bildung der SBU hat, kann dessen Austausch, bei ansonsten gleichen Präkursoren, zu unterschiedlichen MOF-Strukturen führen.[33] Ein weiteres Phänomen, welches durch das Lösungsmittel beeinflusst wird, ist die Interpenetration.[34] Hierbei werden zwei oder mehrere gleichartige Netzwerke parallel gebildet und wachsen dabei durch die Porenöffnungen des jeweils anderen Netzwerkes, jedoch ohne dabei kovalent mit diesem verbunden zu sein.[35]

Eine weitere Möglichkeit die Kinetik der MOF-Kristallisation zu beeinflussen, besteht in der Zugabe von Modulatoren als Additive, was einerseits zu hochkristallinen oder aber defektreichen Strukturen führen kann.[24,36] Eines der am besten untersuchten MOFs im Forschungsfeld des „defect engeneering“ ist UiO-66, dessen SBU idealerweise über 12 Liganden mit benachbarten Zirkoniumoxidoclustern verbrückt ist. Durch die hohe Konnektivität in UiO-66 ist die Struktur auch noch bei einer hohen Anzahl an Defektstellen stabil, wobei hier zwischen fehlenden Linkern und fehlenden Clustern unterschieden werden kann.[37,38]

Syntheserouten bei Raumtemperatur oder geringen Heiz- bzw. Abkühlungsraten und entsprechend langen Reaktionszeiten können ein langsames Kristallwachstum mit geringer Anzahl an Kristallisationskeimen bewirken, was entsprechend zu vergleichsweise großen, qualitativ hochwertigen MOF-Kristalliten führen kann, wie sie zur Strukturbestimmung für die Einkristallstrukturanalyse benötigt werden.[39]

Neben der Topologie lassen sich auch Oberflächeneigenschaften von MOFs beeinflussen. Dies kann unter anderem durch Funktionalisierung der SBU bzw. des Liganden erfolgen. Man unterscheidet zwischen den verschiedenen Strategien der *pre- bzw. post*-synthetischen und der *in situ* Funktionalisierung.[40,41] Hierdurch können Poreneigenschaften wie beispielsweise Polarität, Hydrophilie, Flexibilität oder Porenvolumen beeinflusst werden.[42,43,44]

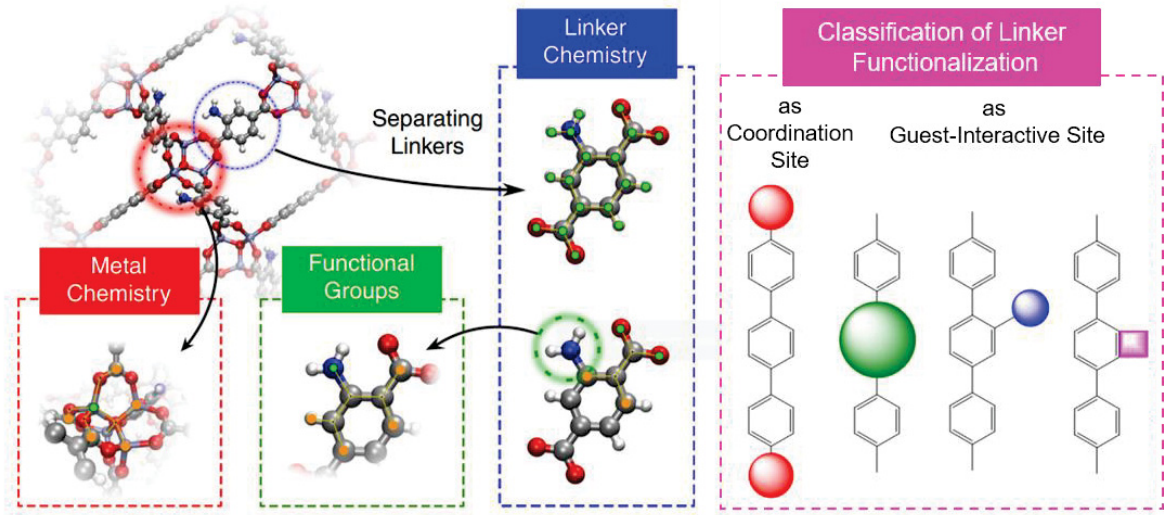

Abb. 5: Bereiche in MOFs: Metallcluster, Linker und funktionelle Gruppen. Nachdruck mit Genehmigung von Referenz 15. Copyright 2020 Springer Nature. Nachdruck mit Genehmigung von Referenz 42. Copyright 2019 Elsevier.

Obwohl MOFs ein reges wissenschaftliches Interesse erfahren und durch ihre Porosität zahlreiche potenzielle Applikationen denkbar sind, konnte der Einsatz von MOFs bisher noch keine breite industrielle Anwendung finden.[45] Dabei scheitert der Einsatz oft an mangelnder Langzeitstabilität unter normalen bzw. anwendungsspezifischen Bedingungen.[46,47] Aus diesem Grund ist die „Stabilität" im Bereich der MOFs auch nicht als absolute Charaktereigenschaft zu beurteilen, sondern muss differenziert, entsprechend der Bedingungen, denen das Material ausgesetzt wurde, bewertet werden. Parameter zur Überprüfung der Stabilität eines MOFs sind beispielsweise die Beständigkeit in organischen Lösungsmitteln bzw. in wässrigen Lösungen (pH-Abhängigkeit), die Temperatur oder der Druck. Trotz der Vielzahl an bekannten MOF-Strukturen gibt es bisher nur eine begrenzte Anzahl an MOFs, die sich unter nicht-inerten Bedingungen, außerhalb ihrer Mutterlauge, über längere Zeit handhaben lassen, ohne dabei eine Degradierung innerhalb der Netzwerkstruktur beobachten zu können.[48]

Diese Instabilität kann dadurch begründet werden, dass ein poröses Netzwerk bei enthalpisch getriebener Kristallisation in der Regel eine höhere Energie, verglichen zu seiner entropisch bevorzugten dichten Phase, innehat und damit nur metastabil ist.[49]

Eine geläufige Methode zur Überprüfung der Stabilität ist die wiederholte Charakterisierung derselben Probe mittels Pulverdiffraktometrie (engl. *powder X-ray diffraction*, PXRD) und Stickstoffsorption.

Dadurch kann ein Vergleich der Kristallinität bzw. Porosität dieser Probe, vor und nach Exposition zu spezifischen Substanzen oder Bedingungen, aufgestellt werden.[50] Stabilitäten können allgemein in die drei Hauptkategorien, **chemische** Stabilität, **thermische** Stabilität und **mechanische** Stabilität unterteilt werden.

Die **chemische** Stabilität bezieht sich auf die Beständigkeit eines Stoffes gegenüber Auswirkungen der Exposition zu verschiedenen Chemikalien, wie beispielsweise Feuchtigkeit, Säuren, Basen oder Lösungsmitteln in ihrer Umgebung.[51]

Es gibt verschiedene Strategien, um die chemische Stabilität, also die Beständigkeit gegenüber Hydrolyse oder anderen chemischen Reaktionen, eines MOFs zu verbessern.[52] Thermodynamisch kann zum einen die Stärkung der koordinativen Bindung zwischen Liganden (Lewis-Base) und Metallkation (Lewis-Säure), nach Pearsons Konzept der „*Hard and Soft Acids and Bases*" (HSAB), durch die Wahl von sauren Metallionen mit hoher Ladungsdichte (Al^{3+}, Zr^{4+}) oder dem Einsatz von Liganden mit stark komplexierenden funktionellen Gruppen mit hohen pK_a-Werten (z.B. Azol-Derivate) erfolgen.[47] Allerdings ist es denkbar, dass hier die gegenüberstehende dichte Phase mit derselben Metall-Ligand-Bindung gleichermaßen stabilisiert wird und damit nur die Energiebarriere für einen Phasenübergang erhöht wird. Zum anderen kann die Wahl von kinetisch inerten Metallionen dazu führen, dass die Energie eines potenziellen Übergangszustandes erhöht und dadurch die Metall-Ligand-Bindung stabilisiert wird. Die Raten des Ligandenaustauschs werden dabei am Beispiel des homoleptischen Austauschs von Metall-Aqua-Komplexen quantifiziert und können für oktaedrische Aquakomplexe bis zu 19 Größenordnungen auseinanderliegen (Vgl. Abb. 6).[53,54,55] Des Weiteren kann eine Strategie der Abschirmung dazu führen, dass die Metallkation-Ligand-Wechselwirkung vor Angriffen konkurrierender Spezies, durch Einführung sterisch anspruchsvoller Gruppen oder durch Erhöhung des hydrophoben Charakters eines Materials geschützt wird.[48]

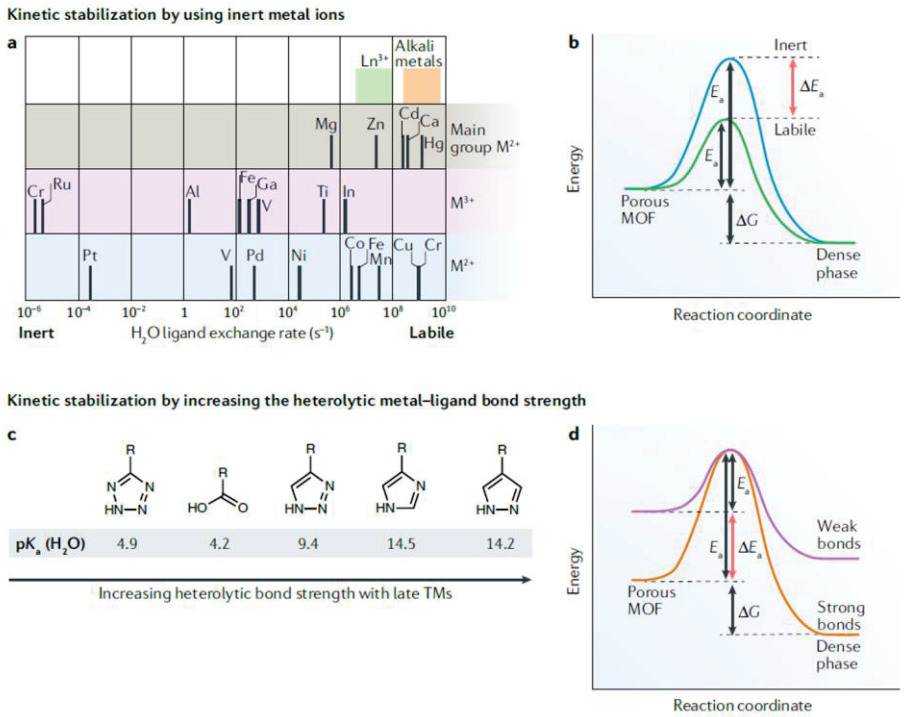

Abb. 6: Auswahlkriterien für kinetisch stabilisierte MOFs. a) Austauschraten von H_2O Liganden in Metallaquakomplexen. b) Energiediagramm für kinetisch inertere oder labile Metallionen. c) Trends zur Stärkung der heterolytischen Bindung d) Energiediagramm für eine starke oder schwache Metall-Ligand-Bindung. Nachdruck mit Genehmigung von Referenz 46. Copyright 2019 Springer Nature.

Die **thermische** Stabilität eines MOFs wird typischerweise mittels thermogravimetrischer Analyse (TGA) untersucht und ist aufgrund von verschiedenen Einflussfaktoren, wie den anorganischen und organischen Bestandteilen sowie der Topologie einer Struktur, nur schwer vorhersagbar. Es zeigte sich jedoch, dass Metallionen in ihrer jeweils stabilsten Oxidationsstufe mit zunehmender Oxidationszahl thermisch stabiler werden (Fe(III), Cr(III), Al(III), Zr(IV)).[48] Auch der Wechsel zu interpenetrierten MOFs führt durch eine verringerte Porengrößen oft zu einer erhöhten thermischen Stabilität, verglichen zu den entsprechenden nicht-interpenetrierten Netzwerken.[52] Des Weiteren konnte bei MOFs mit unendlichen (Ketten) anstelle von diskreten SBUs bei ansonsten gleichen Metallionen und Liganden, häufig eine erhöhte thermische Stabilität nachgewiesen werden. Kurze aromatische Liganden sowie eine defektfreie und dichte Packung des Netzwerkes können die thermische Stabilität in MOFs weiter positiv beeinflussen.[48]

Mechanische Stabilität, in Bezug auf MOFs, bezeichnet deren Belastbarkeit unter erhöhtem Druck oder Vakuum. Diese wird insbesondere bei der „Aktivierung", dem Entfernen des nach der Synthese in den Poren vorliegenden Lösungsmittels auf die Probe gestellt.[48] Hierbei werden im MOF

eingeschlossene Lösungsmittelmoleküle durch thermische Behandlung und bzw. oder das Anlegen eines Vakuums evaporiert und somit aus den Poren entfernt. Das Austreten von Lösungsmittelmolekülen kann jedoch, durch Zunahme der Oberflächenspannung während des Verdampfens, mit stark wirkenden Kapillarkräften verbunden sein, die zu einer Beschädigung bis hin zu einem Kollaps der porösen Struktur führen kann.[55] Um diesem Effekt entgegenzuwirken, werden häufig Methoden des Lösungsmittelaustausches hin zu Lösungsmitteln mit einem niedrigeren Siedepunkt vorgenommen.[56]

Zwei weitere Methoden für die Aktivierung von porösen Materialien, stellen die überkritsche Trocknung sowie die Gefriertrocknung dar. In beiden Methoden wird die Oberflächenspannung und die damit verbundenen Kapillarkräfte durch einen veränderten Phasenübergang verringert, wodurch eine schonendere Aktivierung erreicht werden kann.[56,57] Da die mechanische Stabilität typischerweise quadratisch mit der Dichte einhergeht, kann auch hier Interpenetration, eine hohe Konnektivität und kurze Liganden zu einer erhöhten mechanischen Stabilität führen.[58,59]

Aufgrund ihrer Porosität werden MOFs hinsichtlich zahlreicher potenzieller Anwendungen untersucht (Abb. 7).[51] Dazu zählen beispielsweise die heterogene Katalyse, bei der MOFs durch ihre hohen Oberflächen aktiven Metallzentren und potenziellen Ligandenfunktionalitäten, einerseits selbst als Katalysatoren eingesetzt werden oder andererseits als Trägermaterialien für andere katalytisch aktive Spezies dienen können.[60,61,62] Auch der Einsatz von MOFs als Sensoren für Gase und flüchtige organische Verbindungen (engl. *volatile organic compounds*, VOC) wird zunehmend erforscht und beruht auf Änderungen der chemischen oder physikalischen Eigenschaften eines MOFs bei Exposition zu einem spezifischen Gastmolekül.[63] Typische Arbeitsprinzipien von MOF-Sensoren basieren auf Magnetismus, elektrischer Leitfähigkeit, Lumineszenz oder Farbgebung.[64,65]

Weitere mögliche Anwendungsgebiete von MOFs stellen beispielsweise Wirkstofftransport, Protonenleitung oder nicht-lineare Optiken dar.[66,67,68]

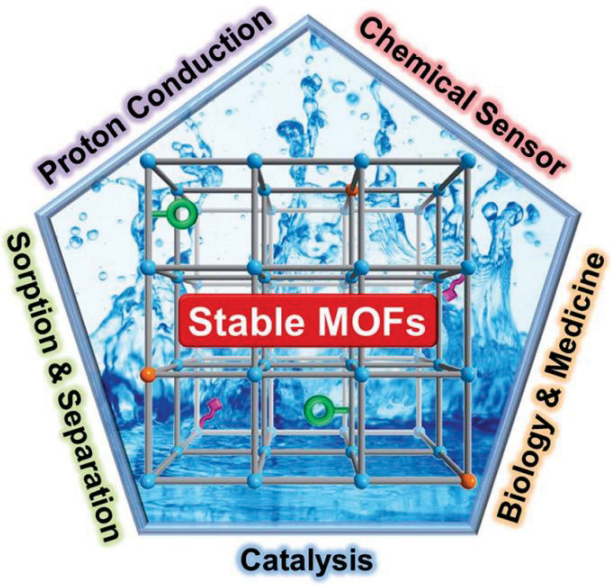

Abb. 7: Schematische Darstellung von stabilen MOFs, bestehend aus Metallclustern (blau oder orangene Kugeln), organischer Ligand (graue Stäbe) und funktionelle Gruppen (grüne und pinke Segmente) für verschiedene potenzielle Anwendungen. Nachdruck mit Genehmigung von Referenz 51. Copyright 2019 Royal Chemical Society.

Eines der wohl am besten untersuchten potenziellen Anwendungsgebiete von MOFs stellt die reversible Gasadsorption dar.[69,70] Als Materialien für die Gasspeicherung bieten MOFs eine hohe volumenspezifische Aufnahme, was vor allem für die Lagerung von Wasserstoff und Methan interessant ist.[71,72,73] Des Weiteren können MOFs für die selektive Trennung von Gasgemischen eingesetzt werden.[74,75] Hierbei können Prozesse der Bio- oder Erdgasaufbereitung unterstützt oder aber unkontrollierte Schadstoffemissionen von Rauchgasen reduziert werden.[76] Auf das Verfahren der Rauchgasentschwefelung, bei der selektiv SO_2 aus Rauchgasen entfernt wird, wird aufgrund der Relevanz für diese Arbeit noch einmal detailliert in Abschnitt 1.4 eingegangen.

1.2 Theorie Gassorption

Da die Porosität eine der zentralen Eigenschaften von MOFs darstellt, kommt der Untersuchung der Oberfläche und des Porenvolumens besondere Bedeutung bei der Charakterisierung von MOFs zu. Die Untersuchung der Porosität erfolgt mittels Gassorptionsanalyse, bei der ein Analysegas (Adsorptiv) an der Oberfläche eines zu untersuchenden Stoffes (Adsorbens) adsorbiert. Das adsorbierte Molekül (Adsorpt) wird Teil der Grenzfläche zwischen Adsorbens und Adsorptiv (Adsorbat) (Abb. 8).

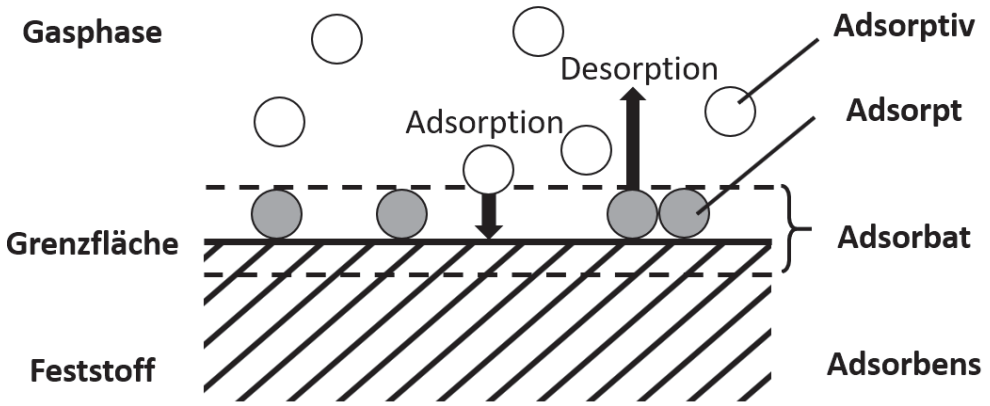

Abb. 8: Schematische Darstellung und Terminologie der Adsorption.

Es kann dabei zwischen den zwei Arten, Physisorption und Chemisorption unterschieden werden. Physisorption zeichnet sich durch schwache van-der-Waals-Wechselwirkungen ($\approx 20 - 40\,kJ \cdot mol^{-1}$) aus und ist typischerweise reversibel.[77] Weiter kann bei der Physisorption Adsorpt als Adsorptionsstelle für weiteres Adsorptiv dienen, wodurch die Ausbildung von Multischichten ermöglicht wird. Bei der deutlich stärkeren Chemiesorption ($\approx 200\,kJ \cdot mol^{-1}$) kann es zu kovalenten Bindungen in der Adsorbatphase, welche als Monolage vorliegt, kommen und ist in der Regel irreversibel.[78] Für die Darstellung des Adsorptionsgleichgewichts konnten sich Adsorptionsisothermen in der wissenschaftlichen Praxis durchsetzen und werden als Auftragung der Beladung n in Abhängigkeit des Partialdrucks p/p_0 des Adsorptivs bei konstanter Temperatur dargestellt.

Der Charakterisierung poröser Materialien mittels Gassorptionsmessungen liegt der Physisorption zugrunde, während weitere Wechselwirkungen, induziert durch Dipol- oder Quadrupolmoment des Adsorptivs, unterdrückt werden sollen. Als Adsorptive für die Gassorptionsanalyse werden typischerweise Inertgase wie Stickstoff oder Argon eingesetzt. Stickstoff kann durch seine Hantelform zwar verschiedene Orientierungen an einer Oberfläche einnehmen, hat aber den Vorteil der einfachen und kostengünstigen Handhabung. Argon weist als einatomiges Molekül hingegen kein Quadrupolmoment auf und kann durch einen geringeren kinetischen Durchmesser ($Ø_{kin}(Ar)$ = 340 pm; $Ø_{kin}(N_2)$ = 364 pm) auch noch in sehr kleinen Mikroporen Zugang finden.[79] Adsorptionsprozesse sind stark abhängig von Temperatur und Druck und werden deshalb unter isothermen Bedingungen am Siedepunkt des Adsorptivs durchgeführt (N_2: 77 K; Ar: 87 K). Dies hat den Vorteil, dass bei Normaldruck unterhalb des Sättigungsdampfdruck des Adsorptivs gemessen

werden kann. Eine Einteilung der Isothermen in verschiedene Typen erfolgt dabei auf Grundlage der Empfehlungen der IUPAC, welche 1985 veröffentlicht und 2015 aktualisiert wurde.[80,81]

Es wird insgesamt zwischen sechs Isothermentypen unterschieden, wobei insbesondere strukturelle Eigenschaften wie die Porengröße Einfluss auf die Isothermenform nehmen (Abb. 9). Für Porengrößen wurden deshalb die Begriffe Mikroporen (<2 nm), Mesoporen (2 – 50 nm) und Makroporen (>50 nm) eingeführt.[81]

Reversible Typ I-Isothermen sind insbesondere bei mikroporösen Materialen zu beobachten. Kennzeichnend für Typ I-Isothermen ist ein steiler Anstieg der Adsorption, welcher bereits bei sehr geringen Partialdrücken (p/p_0) erfolgt und durch starke Wechselwirkung zwischen Adsorbens und Adsorptiv aufgrund der kleineren Porendurchmesser zu erklären ist. Dabei wird die Gasaufnahme von dem zugänglichen Porenvolumen und nicht von der zugänglichen inneren Oberfläche beschränkt. Typ I(a)-Isothermen sind in der Regel Materialien mit Porendurchmessern < 1 nm zuzuordnen, während Typ I(b)-Isothermen Materialien mit Porendurchmessern zwischen 1 – 2,5 nm zu beobachtet sind.[81]

Typ II- und Typ III-Isothermen hingegen sind charakteristisch für nicht-poröse oder makroporöse Feststoffe. In Typ II-Isothermen lagert sich zunächst das Adsorptiv in einer Monolage an der Oberfläche des Adsorbens an, welche bei weiterer Erhöhung des Partialdrucks zu Multischichten erweitert wird, was anschließend bei hohen Partialdrücken zur Kondensation innerhalb der Poren führt. Typ III-Isothermen weisen im Gegensatz zu Typ II-Isothermen keine Monoschichtenadsorption, sondern deutlich schwächere Adsorbens-Adsorbat-Wechselwirkungen auf, was sich in einer Multilagenadsorption mit endlicher Gasaufnahme bei Sättigungsdruck $p/p_0 = 1$ zeigt.

Typ IV-Isothermen lassen sich mesoporösen Adsorbentien zuordnen und zeichnen sich durch einen zweistufigen Adsorptionsprozess aus, bei dem die Gasaufnahme zunächst über Mono- und Multischichtenadsorption geschieht und weiter über Kapillarkondensation bei höheren Partialdrücken erfolgt. Im Gegensatz zu Typ II-Isothermen erreicht die Gasaufnahme in Typ IV-Isothermen jedoch bei vollständiger Porenfüllung ein Plateau. Bei den zuvor behandelten Isothermentypen (I-III) lagen Adsorptions- und Desorptionsisotherme genau übereinander, was bedeutet, dass der Adsorptionsprozess ungehindert reversibel ist. Sollte die Desorptionsisotherme

oberhalb der Adsorptionsisotherme verlaufen, so spricht man von einer Hysterese. Das Auftreten einer Hysterese bei Typ IV(a)-Isothermen ist das Unterscheidungsmerkmal zu reversiblen Typ IV(b)-Isothermen. Diese Hysterese kann in Abhängigkeit des Adsorptivs und der Temperatur, bei Materialien mit Porendurchmessern > 4 nm beobachtet werden.

Typ V-Isothermen zeigen, wie auch Typ III-Isothermen, vergleichsweise schwache Adsorbens-Adsorbat-Wechselwirkungen, gefolgt von einem steilen Anstieg der Gasaufnahme bei höheren Partialdrücken, was durch Clusterbildung zu erklären ist. Die anschließende Porenfüllung wird durch ein Plateau bei hohem Partialdruck aufgezeigt.

Abschließend zeigen Typ VI-Isothermen charakteristische Adsorptionsstufen, die Schicht für Schicht aufeinander folgen und bei nicht-porösen Materialien zu beobachten sind.[81]

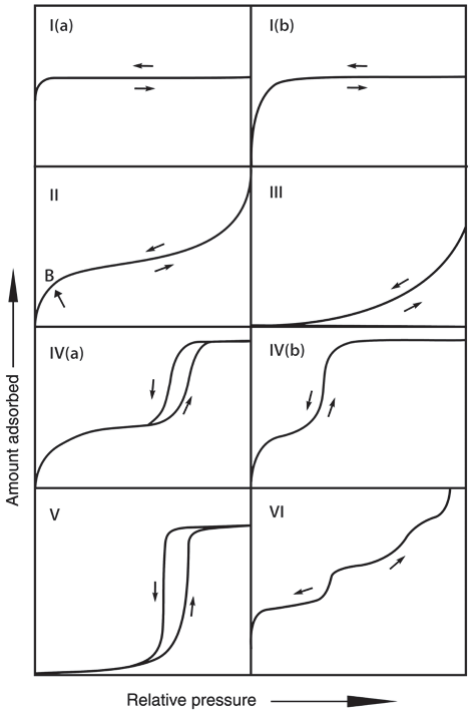

Abb. 9. Die verschiedenen Isothermentypen nach IUPAC Klassifizierung. Nachdruck mit Genehmigung von Referenz 81. Copyright 2015 De Gruyter, IUPAC.

Die Bestimmung der spezifischen inneren Oberfläche eines porösen Materials ist für dessen Charakterisierung von zentraler Bedeutung. Hierbei konnte sich die nach den Erfindern Brunauer, Emmett und Teller benannte BET-Methode bei der Bestimmung von Oberflächen in nicht-porösen, mikro- oder mesoporösen Feststoffen, mithilfe entsprechender Gassorptionsisothermen, etablieren. Die BET-Methode kann als eine Weiterentwicklung des Langmuir-Modells angesehen werden, da hier im Gegensatz zum Vorgängermodell nicht nur Monolagenadsorption, sondern auch

Multilagenadsorption berücksichtigt wird (Abb. 10).[82,83] Ein weiterer wichtiger Unterschied der beiden Modelle ist die Stärke der angenommenen Wechselwirkungen. Während das Langmuir-Modell von starken Adsorbens-Adsorbat-Wechselwirkungen im Bereich von Chemisorption ausgeht, basiert das BET-Modell auf den deutlich schwächeren Van-der-Waals-Wechselwirkungen und ist damit der Physisorption zuzuordnen. Zudem basiert die BET-Theorie auf folgenden Annahmen:

1. Es liegt eine homogene Oberfläche vor bei der alle Adsorptionsplätze energetisch gleichwertig sind.
2. Die Adsorptionsenthalpie (ΔH_{ads}) zwischen Adsorbens und Adsorbat kann nur aus den Wechselwirkungen der ersten Adsorptionsschicht bestimmt werden.
3. Jedes einzelne Adsorbatmolekül der ersten Schicht kann als weitere Adsorptionsstelle für Gasmoleküle weiterer Schichten dienen, was zur Ausbildung von Multilagen führt.
4. Wechselwirkungen treten nur bei Adsorbatmolekülen benachbarter Schichten auf, wobei die Adsorptionsenthalpie der zweiten und allen höheren Schichten der Kondensationsenthalpie (ΔH_{kond}) des Adsorptivs entspricht und die oberste Schicht im Gleichgewicht mit der Gasphase steht.

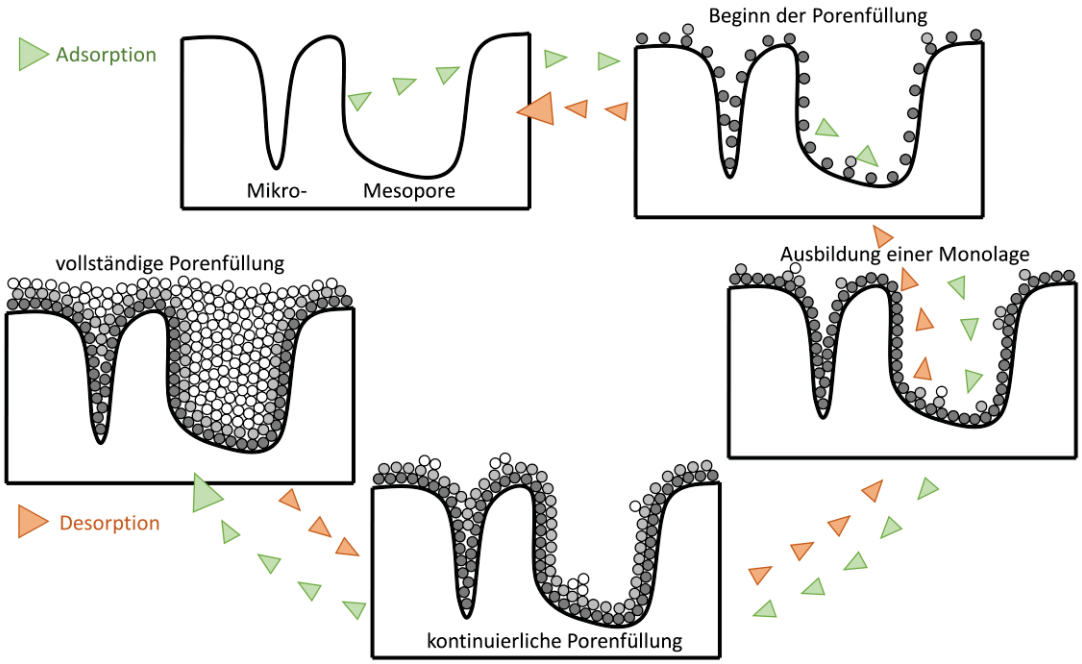

Abb. 10: Schematische Darstellung der Porenfüllung eines mikro- und mesoporösen Adsorbens mit Adsorptivmolekülen. Erste Schicht (dunkelgrau), zweite Schicht (hellgrau) und höherlagige Schichten (weiß).

Bei der Darstellung der Sorptionsisotherm wird typischerweise die adsorbierte Stoffmenge gegen den Relativdruck aufgetragen. Die Berechnung der spezifischen Oberflächen eines Feststoffs unter Anwendung der BET-Methode erfolgt dann durch die Linearisierung der BET-Gleichung. Dabei wird die spezifischen Monolagenkapazität n_m mit der spezifischen Aufnahmekapazität n in Zusammenhang gebracht, welche vom Relativdruck p/p_0 abhängig ist. Die BET-Konstante C ist dabei ein exponentiell von der Energie der Monolagenadsorption abhängiger Parameter und damit ein Maß für die Adsorbens-Adsorbat-Wechselwirkung. C liegt typischerweise bei Werten zwischen 2 und 150.

$$n = \frac{n_m C \left(\frac{p}{p_0}\right)}{\left(1 - \left(\frac{p}{p_0}\right)\right)\left(1 - \frac{p}{p_0} + C\left(\frac{p}{p_0}\right)\right)}$$

Nach Umformung der BET-Gleichung zu f(x) = mx + b:

$$\frac{1}{n\left(\left(\frac{p_0}{p}\right) - 1\right)} = \frac{C-1}{n_m C}\left(\frac{p}{p_0}\right) + \frac{1}{n_m C}$$

Aus der Steigung ($m = C\text{-}1/(n_m C)$) und dem Ordinatenabschnitt ($b = 1/(n_m C)$) lässt sich nach weiterer Umformung n_m wie folgt berechnen:

$$n_m = \frac{1}{m + b}$$

In der Auftragung von $1/[n(p_0/p)\text{-}1]$ gegen p/p_0, welche auch als BET-Plot bezeichnet wird, können für Typ II und Typ IV-Isothermen mit N_2 als Adsorptiv, Adsorptionspunkte mit linearer Steigung, typischerweise im Bereich von 0,05 – 0,30 p/p_0 ausgewählt werden und weiter die spezifische Monolagenkapazität n_m bestimmt werden. Für mikroporöse Materialien ist der lineare Bereich hin zu niedrigeren Partialdrücken verschoben.[81]

Um abschließend die spezifische BET-Oberfläche S_{BET} eines Adsorbens bestimmen zu können, müssen neben der Monolagenkapazität n_m weitere Konstanten wie die Querschnittsfläche σ_m des Adsorbats, die Avogadro-Konstante N_A und das Gewicht des Adsorbens m_a berücksichtigt werden.

$$S_{BET} = \frac{n_m N_A \sigma_m}{m_a}$$

Bei Anwendung der BET-Theorie auf mikroporöse Materialien mit Typ I-Isothermen bzw. Isothermen, die sowohl Merkmale von Typ I und Typ II oder Typ I und Typ IV aufweisen, ist besondere Achtsamkeit geboten, da hier Mono- und Multilagenadsorption und Mikroporenfüllung

nicht eindeutig voneinander abgegrenzt werden können und es mehrere lineare Bereiche im BET-Plot geben kann.[84] Aufgrund dieser Schwierigkeit führte Rouquerol drei objektive Auswahlkriterien für die BET-Methode ein, die bei der Bestimmung der auf die Monolagenkapazität zurückzuführenden Adsorptionspunkte angewendet werden sollten. Die Auftragung von $n(1-p_0/p)$ gegen p/p_0, dem sogenannten Rouquerol-Plot, dient dabei zur Überprüfung der folgenden Kriterien:[81]

1. Die BET-Konstante C muss positiv sein.
2. Der Auswahlbereich sollte so gewählt werden, dass der Term $n(1-p/p_0)$ mit zunehmendem p/p_0 kontinuierlich steigt.
3. Der Wert für p/p_0, welcher der Monolagenkapazität n_m zugeordnet wurde, sollte im BET-Bereich liegen.

Da mikroporöse Materialien einige der einleitend genannten Annahmen zur BET-Theorie nicht erfüllen, ist der absolute Wert der BET-Oberfläche vielmehr von qualitativer als quantitativer Natur. Deshalb lautet die Empfehlung der IUPAC, BET-Oberflächenangaben für mikroporöse Materialien als „Fingerabdruck" dieser Adsorbentien zu betrachten, welcher nur für den Vergleich mit anderen mikroporösen Materialien genutzten werden sollte. Dennoch zeigte sich durch den Vergleich mit theoretischen Berechnungen von Oberflächen mikroporöser MOFs eine gute Anwendbarkeit dieser Methodik.[81]

Weiter kann mittels Gassorption das totale Porenvolumen V_p von Adsorbentien, deren Porengrößenverteilung im Bereich von Mikro- oder Mesoporen liegt und deren Adsorptionsisotherme in einem Plateau endet (Typ I, IV und V), ermittelt werden (Abb. 11).[85,86] Unter der grundlegenden Annahme, dass das Adsorpt kurz vor der Sättigung ($p/p_0 = 0{,}98$) als flüssiges Kondensat ρ_{fl} entsprechend der Gurvich-Regel vorliegt, kann V_p über das molare Volumen V_m, das adsorbierte Gasvolumen V_{ads} und der Molaren Masse wie folgt berechnet werden:[87,88]

$$V_{p,Gurvich} = \frac{V_{ads}}{V_m} \times \frac{M}{\rho_{fl}}$$

Jedoch sind die Isothermenplateaus, insbesondere von Typ I-Isothermen, nicht vollkommen horizontal, was eine Anwendung der Gurvich-Regel zur Bestimmung des Mikroporenvolumens erschwert. Deshalb wird häufig ein makroskopisches Verfahren durchgeführt, bei dem ein Vergleich zu einem nicht-porösen Referenzmaterial mit chemisch ähnlicher Oberflächenstruktur

vorgenommen wird und auf den die BET-Methode anwendbar ist. Als „t-Plot“ bezeichnet man die Auftragung des adsorbierten Stickstoffs gegen die statistische Dicke *t* einer adsorbierten Schicht auf einem nicht-porösen Referenzmaterial bei entsprechendem Druck. Der Schnittpunkt der Geraden mit der Ordinate gibt dabei das zugängliche Mikroporenvolumen des Adsorbens an.[89] Allerdings konnte Galarneau *et al.* in einer Vergleichsstudie zeigen, dass die Schichtdicke *t* in mikroporösen Materialien mit Porendurchmessern < 10 σ (wobei σ dem Durchmesser des Adsorbats entspricht) nicht nur vom Relativdruck p/p_0, sondern auch durch die stärkere Krümmung der Oberfläche und somit auch von dem Porendurchmesser abhängig ist. Dieser intrinsische Fehler innerhalb der t-Plot Methode führt dazu, dass Werte für Mikroporenvolumina bei Adsorbentien mit entsprechend kleinen Porengrößen systematisch zu niedrig bestimmt werden.[90]

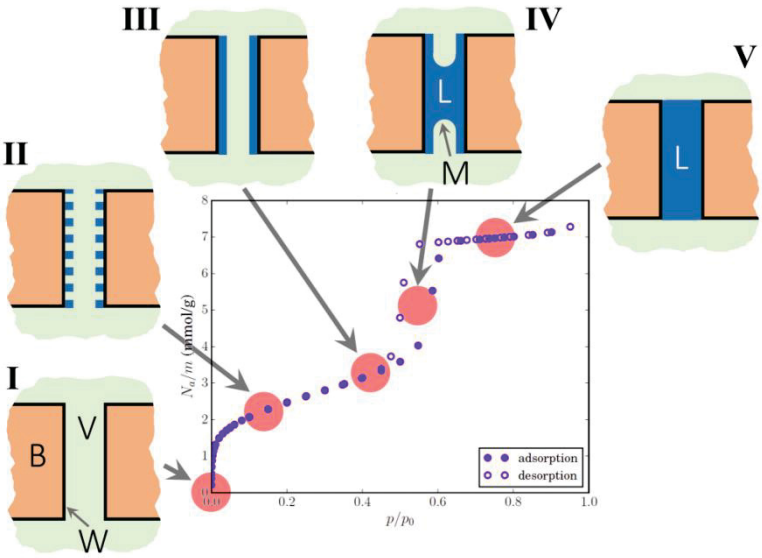

Abb. 11: Schematische Darstellung der unterschiedlichen Phasen bei der Porenfüllung: unbesetzte Oberfläche (I), vereinzelte Adsorption (II), Bildung einer Monolage (III), Kapillarkondensation (IV) und vollständige Porenfüllung (V). Pfeile und rote Punkte ordnen die Phasen dem jeweils entsprechenden Bereich der Sorptionsisotherme zu. B, feste Masse; V, Dampf; L, Flüssigkeit; W, Porenwand; M, Miniskus. Datenpunkte der Isotherme stammen von einem mesoporösen Silicagel. Nachdruck mit Genehmigung von Referenz 85. Copyright 2018 American Physical Society.

Alternativ ist es auch möglich das Mikroporenvolumen mittels Molekularsimulationen zu berechnen. Hierzu werden Modelle, basierend auf nicht-lokaler Dichte-Funktional-Theorie (NLDFT) oder *Grand canonical Monte Carlo* (GCMC) Simulationen eingesetzt, um Aussagen über das Verhalten von Adsorbat-Kondensat innerhalb der Poren treffen zu können. Für Standardadsorbentien wie Zeolithe,

Silicagele oder Aktivkohlen wurden deshalb entsprechende Modelle für beispielsweise zylinderförmige, schlitzförmige oder sphärische Poren entwickelt, um unterschiedliche Oberflächen und Porenstrukturen berücksichtigen zu können. Da MOFs jedoch in ihren spezifischen Strukturen und Oberflächeneigenschaften zum Teil stark von den zuvor genannten Standardmaterialien abweichen, ist eine Übertragung der vorhandenen Modelle nur begrenzt anwendbar.[86]

1.3 Adsorptionsbasierte Gastrennung

Die Trennung von Mischungen ist eine der bedeutendsten Prozesse in der chemischen Industrie, welche mit schätzungsweise 10 – 15 % des weltweiten Energieverbrauchs in Zusammenhang steht.[91] Darunter sind als relevante industrielle Gastrennprozesse das Erfassen von CO_2-Emissionen (CO_2/Luft oder CO_2/H_2), die Erdgasaufbereitung (CO_2/CH_4, N_2/CH_4, H_2S/CH_4), die Sauerstoffaufreinigung (O_2/N_2) oder die Auftrennung von Edelgasen und die Trennung von leichten Kohlenwasserstoffen (Olefine/Paraffine oder lineare Isomere/verzweigte Isomere) zu nennen. Die soeben genannten Trennprozesse sind aufgrund von ähnlichen Molekülgrößen oder physikalischen Eigenschaften oft schwierig und bedürfen energieintensiver Verfahren.[92] In Abb. 12 sind Fortschritte der adsorptionsbasierten Gastrennung der letzten Jahrzehnte in Bezug auf MOFs dargestellt.

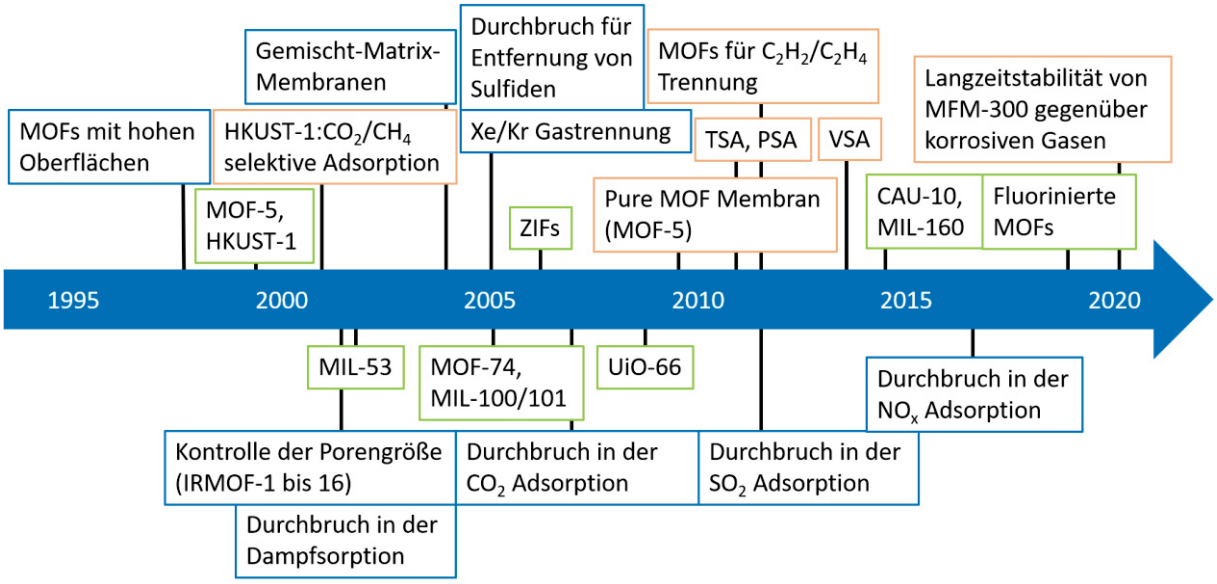

Abb. 12: Meilensteine der MOF-Forschung in Bezug auf Anwendungen für die adsorptionsbasierte Gastrennung.

Nachfolgend werden zunächst einige grundlegende Begrifflichkeiten in Bezug auf adsorptionsbasierte Trennverfahren erläutert.

Die **Adsorptionskapazität** oder auch Beladung, bezeichnet die quantitative Angabe der gewichts- bzw. volumenspezifischen Gasaufnahme eines Adsorbens und ist stark abhängig von Parametern wie Temperatur und Druck. Es kann zwischen verschiedenen Adsorptionskapazitäten differenziert werden. Die *statische Gleichgewichtskapazität* entspricht der Gasaufnahme eines unverbrauchten Adsorbens im equilibrierten Zustand mit der Gasphase bei konstanten Bedingungen (Temperatur und Druck). Die *dynamische Gleichgewichtskapazität* beschreibt die Adsorptionskapazität eines Adsorbat-Bettes, welches von einem Adsorptiv mit konstanter Geschwindigkeit durchströmt wird und liegt typischerweise bei Werten zwischen 50 – 70 % der statischen Beladung. Die für die Anwendung relevante *nutzbare Kapazität* berücksichtigt weiter, dass das Adsorbat-Bett niemals bis zur vollständigen Sättigung beladen wird und kann nach Bedarf angepasst werden.[93]

Die **Adsorptionsenthalpie** ist ein Parameter zur Bestimmung der Affinität, also der Stärke der Wechselwirkungen zwischen Adsorbens und Adsorptiv. Demzufolge ist die Adsorptionsenthalpie eine wichtige Größe bei der Bestimmung der Adsorptionsselektivität und dem Energieaufwand, der für die Desorption des Gasmoleküls benötigt wird. Die Adsorptionsenthalpie ΔH_{ads} entspricht der negativen Adsorptionswärme (Q_{st}) und ist abhängig von der adsorbierten Menge n eines Adsorptivs. Auf Basis von mindestens zwei Adsorptionsisothermen des gleichen Adsorptivs, gemessen bei unterschiedlichen Temperaturen ($\Delta T \leq 20$ K), kann ΔH_{ads} mittels der Clausius-Clapeyron Gleichung bestimmt werden. Hierzu werden aus den Isothermen Datenpaare des Drucks p und der Beladung n evaluiert, welche bei den jeweiligen Temperaturen die gleiche Beladung aufweisen. Dieser Ansatz wird deshalb auch als „isosterische“ Methode bezeichnet.[94]

$$\Delta H_{ads}(n) = -R \cdot ln\left(\frac{p_2}{p_1}\right)\frac{T_1 \cdot T_2}{(T_2 - T_1)}$$

R entspricht dabei der idealen Gaskonstante.

Eine ebenfalls weit verbreitete Methode für die Bestimmung von Adsorptionsenthalpien ist die Virial-Analyse, welche sich insbesondere für stark polarisierbare Moleküle wie CO_2 und SO_2 eignet.[95,96] Für die Berechnung der isosterischen Enthalpien werden die Aufnahmewerte zweier Adsorptionsisothermen mit einem Polynom global gefittet

$$ln\,p = ln\,n + \frac{1}{T}\sum_{i=0}^{m} a_i n^i + \sum_{i=0}^{m} b_i n^i$$

und die zugehörigen differentiellen isosterischen Enthalpien berechnet:[97]

$$\Delta H_{ads}(n) = R \cdot \sum_{i=0}^{m} a_i\, n^i$$

Da adsorbierte Teilchen untereinander wechselwirken können, verändert sich die Adsorptionsenthalpie mit dem Bedeckungsgrad der Oberfläche. Deshalb wird die Adsorptionsenthalpie in der Literatur oft als einzelner Wert bei niedriger Beladung ΔH^0_{ads} (mit n gegen 0) angegeben. Dabei muss jedoch darauf geachtet werden, dass genügend Adsorptionspunkte bei entsprechend niedrigem Druck gemessen wurden, um Aussagen zu den Adsorptionsenergien, der ersten Moleküle an bevorzugten Bindungsstellen, treffen zu können.[94]

Die **Adsorptionsselektivität** beschreibt das Adsorptionsverhalten eines Adsorbens in Mehrkomponenten-systemen. Hierbei konkurrieren die vorliegenden Komponenten um die begrenzte Anzahl an Adsorptionsstellen an der Adsorbat-Oberfläche, weshalb es bei Trennprozessen von Vorteil ist, wenn eine Komponente bevorzugt adsorbiert wird. Die Selektivität S einer Komponente 1 über eine Komponente 2 ist nach der folgenden Gleichung definiert:

$$S_{12} = \frac{x_1 y_2}{x_2 y_1}$$

Wobei y_i der Molfraktion der Komponente i in der gesamten Gasmischung und x_i der Molfraktion der Komponente i in der adsorbierten Gasmischung entspricht. Dabei sind y_1 und y_2 bekannt, während x_1 und x_2 durch Multigas-Adsorptionsexperimente bestimmt werden können.[98] Als Alternative zu aufwendigen Multigas-Adsorptionsexperimenten werden jedoch häufig auch Einzelgas-Adsorptionsisothermen der zu trennenden Komponenten verwendet, um die Selektivität eines Adsorbens zu bestimmen. Nach Durchführung von Einzelgasadsorptionsexperimenten ist die partialdruckabhängige Beladung beider Komponenten bekannt, wodurch im Folgenden eine Vorhersage über das Adsorptionsverhalten einer Gasmischung dieser Komponenten getroffen werden kann. Die von Myers und Prausnitz begründete *ideal adsorbed solution theory* (IAST) ist, auch über 50 Jahre nach ihrer Einführung, die weitverbreitetste Methode zur Abschätzung von Selektivitäten in Studien zu Multikomponentengasadsorption.[99]

Dabei wurde die Theorie hauptsächlich auf Basis der drei folgenden Annahmen entwickelt:

1. Adsorbatmoleküle einer Mischung haben den gleichen Zugang zur Oberfläche des Adsorbens.
2. Das Adsorbens ist homogen.
3. Die adsorbierte Phase ist eine ideale Lösung, in der Interaktionen zwischen Molekülen gleich stark sind.

Schwächen von IAST zeigen sich jedoch bei der Anwendung mit polaren Adsorptiven oder wenn eine Komponente bedeutend stärker als die andere Komponente adsorbiert wird.[100] IAST-Selektivitäten eignen sich deshalb vorwiegend für den qualitativen Vergleich und bieten damit bei der Erforschung der Selektivität erste Indizien für das Trennvermögen von Adsorbentien, denen jedoch experimentelle Messungen wie die der statisches Multigas-Adsorption, dynamischer Durchbruchskurven oder Molekularsimulationen von Multikomponenten-Gasmischungen folgen sollten.[92]

1.4 Rauchgasentschwefelung

Im nachfolgenden Kapitel wird zunächst der Kontext der Atmosphärenchemie von SO_2 und der damit verbundenen Relevanz der Rauchgasentschwefelung (engl. *flue gas desulfurization*, FGD) erörtert. Anschließend werden die derzeitig eingesetzten Techniken und Methoden zu FGD-Prozessen dem Verfahren der adsorptionsbasierten Rauchgasentschwefelung gegenübergestellt. Weiter wird der aktuelle Stand der wissenschaftlichen Forschung in Bezug auf selektive Gassorption von SO_2 in MOFs wiedergegeben.

Die Verbrennung von fossilen Rohstoffen wie Kohle, Erdöl oder Erdgas steht trotz des Ausbaus erneuerbarer Energien auch noch in naher Zukunft im Mittelpunkt der Energieerzeugung und wird von einem stetig steigenden globalen Energieverbrauch gestützt. Die dabei entstehenden Abgase wie beispielsweise CO_2, SO_x und NO_x können schwerwiegende Folgen für Klima, Umwelt und die Gesundheit des Menschen auslösen.[101,102] Typische Brennstoffe zur Energiegewinnung wie Kohle oder Erdöl enthalten zwischen 0,5-5 wt% Schwefel, welches während des Verbrennungsprozesses oxidiert wird.[103]

$$S_8 + 8\,O_2 \rightarrow 8\,SO_2$$

$$8\,SO_2 + 4\,O_2 \rightleftharpoons 8\,SO_3$$

Vor allem in urbanen Regionen werden durch die ständige Smogbelastung insbesondere Menschen mit Herz- oder Lungenkrankheiten gefährdet, was sich in einer erhöhten Wahrscheinlichkeit auf vorzeitige Todesfälle widerspiegelt.[104] Smog verschlechtert allerdings nicht nur die Luftqualität, sondern kann in der Atmosphäre auch zu troposphärischem Ozon (O_3) oder saurem Regen[105] reagieren. Darüber hinaus tragen SO_2-Emissionen durch Umwandlung in Sulfat-Ionen (SO_4^{2-}) auch zur Bildung von Feinstaub (Partikel mit einem Durchmesser ≤ 2,5 µm) bei (Abb. 13).[106]

$$SO_2 + OH^{\cdot} \rightarrow HSO_3^-$$
$$HSO_3 + O_2 \rightarrow SO_3 + HO_2$$
$$SO_3 + H_2O \rightarrow H_2SO_4$$
$$H_2SO_4 + 2NH_3 \rightarrow (NH_4)_2SO_4$$

Die bei der Verbrennung von Kohle entstehenden Rauchgase weisen neben den Hauptbestandteilen N_2 und CO_2, abhängig von der Art des Verbrennungsprozesses, typische zwischen 500 – 3000 ppm SO_2.[107] Trotz effizienter Reinigungsmethoden summierten sich die anthropogenen SO_2-Emissionen im Jahr 2018 auf 63 Mt, wovon 27 Mt auf die Verbrennung von Kohle zurückgeführt werden können.[108]

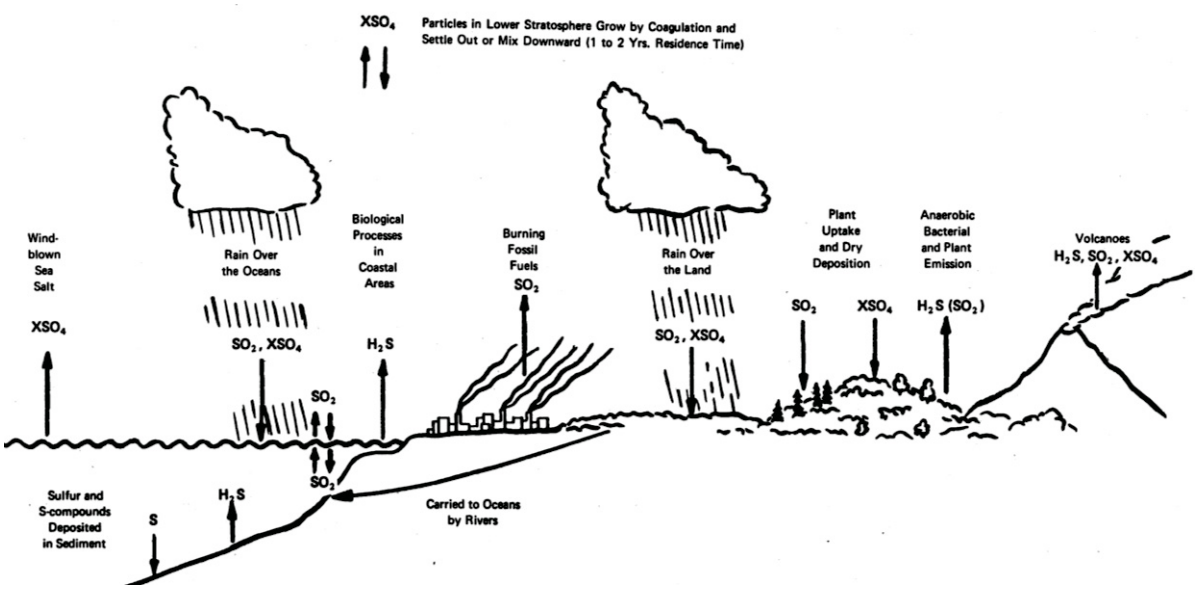

Abb. 13: Quellen und Senken von atmosphärischen Schwefelverbindungen. Nachdruck mit Genehmigung von Referenz 109. Copyright 1972 American Association for the Advancement of Science.

Während der letzten Jahrzehnte konnte das Bewusstsein für die schädliche Wirkung der Luftverschmutzung innerhalb der Politik und der Gesellschaft signifikant gesteigert werden.[110] Daraus folgend wurden Überwachungsmechanismen und Regulatoren für die Emission von Abgasen, die

insbesondere für den Energie-, Industrie- und Transportsektor eingeführt, welche mit der Zeit stufenweise weiter verschärft wurden. Die internationale Seeschifffahrtsorganisation beschloss beispielsweise mit dem MARPOL-Übereinkommen (Kurzform engl. „*International Convention for the Prevention of Pollution from Ships*“) neue Regelungen für Verschmutzungsgrenzwerte für den Schiffverkehr. Dabei regelt die Anlage VI die Anforderungen an Abgaswerte, worunter auch SO_2-Emissionen fallen. Zulässige SO_2-Emissionen sind dadurch ab dem Jahr 2020 weltweit, auf 0,5 % begrenzt wobei es den Schiffsbetreibern überlassen bleibt, ob sie zum Erreichen der Vorgaben Treibstoff mit entsprechend niedrigerem Schwefelgehalt oder Rauchgas-Reinigungssysteme verwenden.[111]

Die Forschung an neuen Methoden zur Emissionskontrolle mit flexiblen, effizienten und kostengünstigen Einsatzmöglichkeiten, wird mit hohem Interesse verfolgt und durch zahlreiche Investitionen unterstützt.[112] Denn neben den primären Auswirkungen von SO_2 Emissionen gibt es sekundäre Auswirkungen, die keinesfalls vernachlässigt werden sollten. So können bereits Spuren von SO_2 in Abgasen Adsorbentien für CO_2 oder Katalysatoren zur selektiven Reduktion von NO_x inaktivieren und damit die Effizienz essenzieller Schritte innerhalb der Rauchgasreinigung verringern.[113,114,115]

Es gibt vielfältige Methoden, die zu einer Verringerung von SO_2 Emissionen führen und dabei unterschiedliche Vor- und Nachteile mit sich bringen, so dass die Wahl der Methode oft von äußeren Faktoren wie z.B. Platzbedarf, Zugang zu Ressourcen etc. abhängig ist.[103] Eine Möglichkeit SO_2-Emissionen zu reduzieren besteht darin, fossile Rohstoffe vor Ihrer Verbrennung von schwefelhaltigen Bestandteilen zu befreien.[116] Dies ist jedoch mit erheblichen Kosten innerhalb des Raffinerieprozesses verbunden oder kann beispielsweise bei der Kohlenwäsche die Brenneigenschaften verändern.

Bei den Techniken der Abgasreinigung ist die Rauchgasentschwefelung durch ihre Vielfältigkeit, hohe Effizienz und vergleichsweise geringen Kosten die am weitesten verbreitete Methode (Abb. 14). Die breite Auswahlmöglichkeit an zugänglichen Sorbenzien ermöglicht die Anpassung an spezifisch vorherrschende Bedingungen, wodurch die Effizienz der Rauchgasreinigung weiter gesteigert werden kann.[117] Zwei weitere Unterteilungen, auf die im folgenden Text noch weiter eingegangen wird, sind die Unterscheidung zwischen der „feuchten“ und der „trockenen“ Rauchgasentschwefelung sowie zwischen einmalig nutzbaren- und regenerierbaren Adsorbentien.

Bei der „feuchten“ Rauchgasentschwefelung werden wässrige Lösungen von Löschkalk ($Ca(OH)_2$) oder Kalkstein ($CaCO_3$) als typische Absorbenzien eingesetzt. Bei diesen einmalig nutzbaren Adsorbentien wird SO_2 irreversibel gebunden und reagiert entsprechend der nachfolgenden Reaktionsgleichungen. Das dadurch gewonnene Calciumsulfit kann zu Gips umgesetzt werden, welches Einsatz in der Bauindustrie findet.[118,119]

Löschkalk: $Ca(OH)_2 + SO_2 \rightarrow CaSO_3 + H_2O$

Kalkstein: $CaCO_3 + SO_2 \rightarrow CaSO_3 + CO_2$

Calciumsulfit: $CaSO_3 + \frac{1}{2}O_2 + 2H_2O \rightarrow CaSO_4 \cdot 2(H_2O)$

Die „feuchte“ Rauchgasentschwefelung erreicht, im Vergleich zur „trockenen“ Variante, eine höhere Effizienz von bis zu 99 %. Allerdings ist diese Methode auch mit höheren Kapital-, Operations- und Handhabungskosten verbunden, da sie mit einem aufwendigeren Aufbau, einem hohen Wasserverbrauch und der Entsorgung von Abwässern verbunden ist.[103,120]

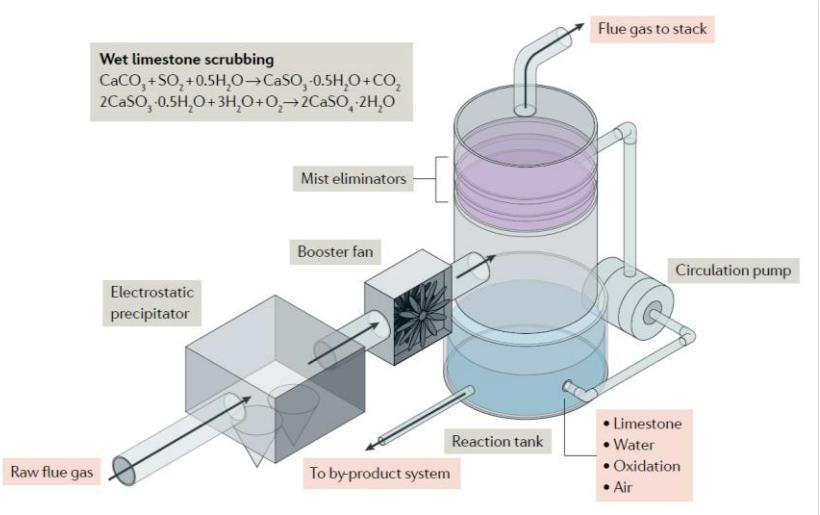

Abb. 14: Schematische Darstellung der Rauchgasentschwefelung mittels feuchter Kalksteinwäsche. Nachdruck mit Genehmigung von Referenz 121. Copyright 2019 Springer Nature.

Alternativ können regenerierbare Adsorbentien eingesetzt werden, um SO_2 aus Rauchgasen einzufangen. Das Einbinden einer Regenerationseinheit ist zwar, unabhängig von der FGD-Methode, mit höheren Kapitalkosten verbunden, bietet aber dennoch einige Vorzüge.[103] Zum einen kann das so gewonnene SO_2 im Nachgang konzentriert desorbiert und zu hochwertigeren Produkten wie elementarem Schwefel (Claus-Prozess)[122] oder Schwefelsäure (Doppel-Kontaktverfahren)[123] umgesetzt werden. Zum anderen kann die Menge an Abfallprodukten reduziert werden. Gleichzeitig

führt die Wiederverwendbarkeit der Adsorbentien zu geringeren Operations- und Handhabungskosten, was diese Methode im Blick auf Nachhaltigkeit und Zukunftsaussichten besonders attraktiv macht.[103,117]

Eine der weitverbreitetsten Methoden der feuchten, regenerativen FGD ist der Wellman-Lord Prozess. Hierbei reagiert SO_2 mit einer wässrigen Lösung Natriumsulfit zu Natriumhydrogensulfit, welches durch Erhitzen zu einem Großteil wieder in Natriumsulfit umgewandelt werden kann.[124]

Im Linde-Solinox-Prozess wird SO_2 aus Rauchgasen, nach dem Prinzip der physikalischen Gaswäsche, in einem organischen Lösungsmittel mit geringem Wassergehalt gelöst.[125] Dies bietet den Vorteil, dass SO_2 in der Lösung schwach gebunden ist und damit leicht regeneriert werden kann. Außerdem können bei diesem Prozess auch bei schwankenden Eingangskonzentrationen stabile Ausgangskonzentrationen erreicht werden.[126]

Als weitere Verfahren der gipsfreien Rauchgasentschwefelung sind die feuchte Magnesiumoxid-Methode oder der wässrige Ammoniak-Prozess zu nennen, welche jeweils nach den folgenden Reaktionsgleichungen ablaufen:[117,127]

Magnesiumoxid-Methode: $Mg(OH)_2 + SO_2 + 5H_2O \rightarrow MgSO_3 \cdot 6H_2O$

$2MgSO_3 + O_2 \rightarrow 2MgSO_4$

Ammoniak-Prozess: $2(NH_4)OH + SO_2 \rightarrow (NH_4)_2SO_3 + H_2O$

$2(NH_4)_2SO_3 + O_2 \rightarrow 2(NH_4)_2SO_4$

Die „trockene“ Rauchgasentschwefelung verbindet hingegen Vorteile wie eine leichtere Handhabbarkeit der festen Produkte sowie einen niedrigeren Energie- und Wasserverbrauch.[103]

Bei der Rauchgasentschwefelung mittels Sprühtrocknung wird eine wässrige Suspension eines Absorbers wie beispielsweise Löschkalk in einer Kolonne mittels Rotationszerstäubers zu einem feinen Nebel versprüht. Dieser Adsorbat-Nebel reagiert unter Kontakt mit heißem Rauchgas nach dem Prinzip der Löschkalk-Wäsche, wobei Wasser verdampft und das Nebenprodukt direkt als festes Pulver erhalten werden kann.[103,117]

Als Alternative zu den bereits vorgestellten Methoden der Rauchgasentschwefelung konzentriert sich diese Arbeit auf die adsorptionsbasierte regenerative SO_2-Sorption. Geläufige Methoden zur Validierung von Adsorbentien im Labormaßstab beruhen dabei in der Regel auf dynamischen

(Durchbruchsexperimente) oder statischen (volumetrische oder gravimetrische) Gassorptionsmessungen.

Durchbruchsexperimente erfassen die dynamische Adsorption einer Gasmischung bei Durchströmung eines Adsorberbettes. Die charakteristische Adsorptionsdynamik eines Adsorbers lässt sich anhand von zeitlich aufgelösten Beladungsprofilen festhalten, wobei die Austrittskonzentration hinter der Schüttung in der Regel mittels Massenspektrometrie detektiert wird. Unter idealen Strömungsverhältnissen mit einer homologen Schüttung und konstantem Gasstrom lässt sich zudem der Massentransferkoeffizient bestimmen.[128] Durchbruchsexperimente bieten damit den Vorteil, neben thermodynamischen auch kinetische Informationen zu liefern. Mit bereits zuvor eingängig beschriebenen statischen Adsorptionsmessungen wird hingegen primär die Thermodynamik von Adsorptionsgleichgewichten untersucht.

Ideale Adsorbentien verfügen deshalb über eine hohe Gasaufnahmekapazität, wodurch die Anwendungsintervalle verlängert werden können bevor eine Sättigung erreicht wird und in die Regenerationsphase gewechselt werden muss. Gleichzeitig muss ein effektives Adsorbens eine hohe Affinität gegenüber SO_2 aufweisen, um selektiv gegenüber konkurrierenden Gasen wie N_2 und CO_2 zu sein, da diese Gase in typischen Rauchgasmischungen einen vielfach höheren Anteil darstellen ($N_2 \sim 84{,}9\,\%$; $CO_2 \sim 15\,\%$; $SO_2 \leq 0{,}1\,\%$).[129] Übertragen auf die Einzelgassorption sollten SO_2-Isothermen bevorzugt dem Typ-I entsprechen. Die damit verbundene Niedrigdruckadsorption ist dabei oft gut vereinbar mit dem Prinzip der Druckwechsel-Adsorption (engl. *pressure swing adsorption*, PSA) bei dem das Adsorbens innerhalb eines schmalen Druckbereichs energieeffizient regeneriert werden kann.[130] Adsorbentien sollten unter milden Bedingungen, ideal bei Raumtemperatur und unter Vakuum oder mittels Stickstoffstrom, regenerierbar sein und müssen harschen Anwendungsbedingungen wie Korrosivität (SO_2, NO_x), Feuchtigkeit und erhöhten Temperaturen $\geq 100\,°C$ über mehrere Hundert Arbeitszyklen widerstehen können. Die Synthese dieser Adsorbentien sollte leicht skalierbar und mit kostengünstigen und ökologisch unbedenklichen Edukten realisierbar sein.

Gut etablierte poröse Materialien wie Aktivkohlen, Silicagele oder Zeolithe verbinden Vorteile wie simple und kostengünstige Synthesewege mit einer enormen chemischen und thermischen Stabilität. Allerdings verfügen diese Materialien in der Regel über eine geringe Adsorptionskapazität und zeigen

entweder eine besonders schwache (AC oder Silicagel) oder eine besonders starke Affinität (Zeolithe) zu SO_2. Dies führt im ersten Fall zu einer geringen Selektivität oder im zweiten Fall zu einer energieintensiven Regeneration.

Der Einsatz von MOFs als Adsorbentien für die Rauchgasentschwefelung könnte durch ihre Variabilität passgenaue Lösungen für eine effiziente, selektive und regenerative SO_2-Sorption bieten. In diesem Zusammenhang kann ein wachsendes Interesse an Untersuchungen der Adsorptionseigenschaften von MOFs gegenüber chemischen Kampfstoffen oder giftigen Gasen wie SO_2, NO_x beobachten werden.[131,132,133,134,135] Eine besondere Herausforderung liegt darin, Materialien zu finden, die bereits bei niedrigem Druck eine gute Adsorptionskapazität und -selektivität sowie eine hohe Robustheit vereinen. Ein optimales Adsorbens zeichnet sich durch eine hohe Adsorptionskapazität bei niedrigen Partialdrücken, einer guten Adsorptionsselektivität und einer hohen Robustheit gegenüber den bei der Rauchgasentschwefelung vorherrschenden Bedingungen aus.

Insbesondere die Stabilität gegenüber sauren und oxidativen Gasen (SO_2 und NO_x) ist ein wichtiger Faktor, da die Oxidation des Metallions einen großen Einfluss auf die Kinetik einer potenziellen Ligandensubstitution haben kann.[46] Auch die Kombination aus Exposition gegenüber korrosiven Gasen unter feuchten Bedingungen stellt für die Stabilität vieler MOF-Materialien eine Hürde dar.[136] Typischerweise enthalten Rauchgase zwischen 5 und 7 % Wasser, welches in Kombination mit SO_2 zur Bildung von schwefliger Säure (H_2SO_3) oder Schwefelsäure (H_2SO_4) führen kann.[137,138] Diese Säuren könnten zu einer Protonierung der koordinierenden funktionellen Gruppe des Liganden führen, wodurch die koordinative Metall-Ligand-Bindung gespalten und das Netzwerk zersetzt bzw. destabilisiert werden würde.[139]

Erste Arbeiten bezüglich der SO_2 Sorption in MOFs wurden im Jahr 2010 von Liu *et al.* zu FMOF-2 und von Behrooz *et al.* zu verschiedenen Berliner-Blau-Analoga veröffentlicht und gaben damit den Anstoß für weitere Untersuchungen von MOFs als Adsorbens für SO_2.[140,141] Schröder *et al.* konnten in umfangreichen Studien zu der von ihnen eingeführten MOF-Reihe, der Manchester-Framework-Materials (MFM), durchführen ,in denen diese hinsichtlich der potenziellen Entfernung von CO_2, SO_2 und NO_x aus Rauchgasen untersucht wurden.[142,143] Dabei konnten neue Erkenntnisse bezüglich der Gerüst-Gast-Wechselwirkungen mit Bezug auf präferierte Bindungsstellen von SO_2 in MFM-300

mittels Methoden der *in situ*-Synchrotron-Pulverdiffraktometrie und *in situ*-inelastischen-Neutronenstreuung gewonnen werden.[95] Weiterhin konnte die Indium-Variante MFM-300(In) erfolgreich als Sensor für SO_2 eingesetzt werden und zeigte hierbei ein herausragendes Detektionslimit von 75 ppb.[135] Das Cu-basierte MOF MFM-170 wies eine außergewöhnlich hohe SO_2-Aufnahme (17,5 mmol g^{-1} bei 25 °C und 1 bar) auf und konnte unter Vakuum bei Raumtemperatur regeneriert werden. Gleichzeitig war es robust gegenüber feuchter SO_2-Exposition. Die unerwartet hohe Stabilität ist durch die strukturellen Eigenschaften von MFM-170 zu erklären. Das $Cu_2(O_2CR)_4$-Schaufelrad wird zum einen über den gewinkelten Liganden 4′4′′′-(Pyridin-3,5-diyl)bis([1,1′-biphenyl]-3,5-dicarboxylsäure)) mit den benachbarten SBUs verbrückt. Gleichzeitig koordiniert das Stickstoffatom des Pyridylrings an eine der beiden freien Koordinationsstellen des Cu-Schaufelrades, wodurch ein untypisches (3,36)-verknüpftes *txt*-Netzwerk entsteht. Die zweite offene Metallstelle (OMS) kann hingegen als Adsorptionsstelle für SO_2 fungieren.[144]

Im Jahr 2014 publizierte Studien von Sun *et al.* und Song *et al.* konnten Vorhersagen zu SO_2-Adsorptionseigenschaften für insgesamt 18 verschiedene MOFs und Zeolithe treffen. Die Grundlage dieser Arbeiten waren Molekularsimulationen, basierend auf der DFT-Methode, welche zur Bestimmung von simulierten Gas-Adsorptionsisothermen eingesetzt wurden. Aus diesen Isothermen ließen sich die potenzielle Selektivitäten der Materialien in Bezug auf die Adsorption von Rauchgasmischungen abschätzen und Aussagen zur Korrelation des Adsorptionsverhaltens mit verschiedenen Materialeigenschaften treffen.[145,146]

Xing *et al.* untersuchten eine Gruppe von Netzwerken bei denen Metallionen (Cu^{2+}, Zn^{2+} oder Ni^{2+}) mittels Stickstoffdonor-Liganden zweidimensionale Gitter ausbilden und weiter über Säulen von Hexafluorosilikat-Anionen (SiF_6^{2-}) zu dreidimensionalen Quadratgittern verknüpft werden. Hierbei zeigten insbesondere die MOFs SIFSIX-1-Cu und SIFSIX-2-Cu-i herausragende Eigenschaften in der Niedrigdruck-SO_2-Sorption.[147]

Ein ähnliches Prinzip machten sich auch Eddaoudi *et al.* bei der Entwicklung von KAUST-7 und KAUST-8 zu Nutze. Hierbei wurden Ni^{2+}-Ionen zunächst mit Pyrazinliganden und anschließend mittels $(AlF_5H_2O)^{2-}$ oder $(NbOF_5)^{2-}$-Oktaedern zu porösen Netzwerken verbunden. Für beide Materialien konnte in Durchbruchsexperimenten eine hohe Selektivität bei der Adsorption von SO_2 aus Rauchgasmischungen ermittelt werden. Ferner zeichneten sich sowohl KAUST-7 als auch

KAUST-8 durch eine enorme Robustheit, auch unter feuchten Bedingungen, aus.[148] Ibarra *et al.* untersuchten den Einfluss von vorher-adsorbiertem Ethanol auf die Adsorptionseigenschaften von MFM-300(Sc). Hierbei zeigte sich, dass geringe Mengen Ethanol (2,6 wt%) die SO_2-Adsorptionskapazität von MFM-300(Sc) um bis zu 40 % erhöhen konnten. Allerdings wurde nach mehreren aufeinander folgenden SO_2-Ad- und -Desorptionszyklen ersichtlich, dass das Ethanol innerhalb des Netzwerkes mit zunehmender Anzahl an Zyklen aus dem Netzwerk verdrängt wird.[149] Vor kurzem konnte in weiteren Studien die exzellente chemische Stabilität der beiden MOFs NOTT-401 und des partiell fluorinerten MIL-101(Cr)-F4(1 %) nach bis zu 50 SO_2-Sorptionszyklen dargelegt werden.[150,151]

Diese Zusammenstellung zeitgenössischer Literatur zeigt, dass MOFs ein hohes Potenzial für den Einsatz als Adsorbens für Anwendungen der Rauchgasentschwefelung innehaben. Es bedarf jedoch weitere Forschung, um benannte Hürden zu überwinden, wobei diese Arbeit einen Beitrag zu diesem Unterfangen geben soll.

2 Motivation und Aufgabenstellung

SO_2 ist ein giftiges Gas, dessen Emissionen nicht nur Umwelt und Klima schaden, sondern auch die menschliche Gesundheit gefährden. Deshalb werden weltweit große Anstrengungen unternommen, um anthropogene SO_2-Emissionen zu minimieren. Die Methode der trockenen und regenerativen Rauchgasentschwefelung könnte nach weiterer Forschung und Entwicklung eine zukunftsweisende Alternative für die weitverbreitetsten klassischen, feuchten, absorptionsbasierte Methoden der Abgasreinigung sein.

Ziel dieser Arbeit war es, ausgewählte MOFs auf Ihre SO_2-Sorptionseigenschaften, mit dem Hintergrund der potenziellen Anwendung in der regenerativen Rauchgasentschwefelung, zu untersuchen.

Die Untersuchung der Materialien sollte grundlegend auf Basis von SO_2-Einzelgassorptionsisothermen, gemessen bei 293 K im Druckbereich zwischen 0,001 – 1 bar, erfolgen. Der Vergleich von literaturbekannten, gut untersuchten Materialien sollte es ermöglichen, spezifische Einflussfaktoren für die SO_2-Sorption, insbesondere im Niedrigdruckbereich, zu identifizieren, um die Effizienz bei der Suche nach vielversprechenden Adsorbentien für die SO_2-Sorption zu steigern. Der Vergleich sollte auf grundlegenden Materialeigenschaften wie der zugänglichen Oberfläche und dem Porenvolumen sowie der Porengröße, aber auch auf dem Einfluss des Metallkations sowie funktioneller Gruppen basieren.

Des Weiteren sollte die Stabilität der porösen Materialien in Bezug auf Exposition gegenüber SO_2 sowohl unter trockenen als auch feuchten Bedingungen untersucht werden. Dies sollte durch wiederholte Charakterisierung der zuvor exponierten Proben erfolgen, wodurch etwaige Veränderungen der Kristallinität und der Oberfläche bestimmt werden können. Ferner sollten für die untersuchten Materialien „*ideal adsorbed solution theory*“ Selektivitäten auf der Grundlage von Einzelgasisothermen von SO_2 und CO_2 bestimmt werden, um eine erste Einschätzung für deren potenzielles Trennvermögen in der Rauchgasentschwefelung geben zu können. Abschließend sollte die Adsorptionsenthalpie ΔH_{ads} für ausgewählte MOFs bestimmt werden, um die Bindungsenergie der SO_2···Adsorbens-Wechselwirkungen abschätzen zu können.

Die relevanten Ergebnisse dieser Arbeit sollten aufgearbeitet und in internationalen, wissenschaftlichen Journalen veröffentlicht werden.

3 Kumulativer Teil

In den nachfolgenden Kapiteln 3.1 bis 0 werden die Ergebnisse dieser Dissertation, welche in Form von Publikationen in internationalen Journalen veröffentlicht wurden, in kumulativer Form dargestellt. Die Publikationen werden entsprechend dem Design der Originalveröffentlichung des jeweiligen Journals in antichronologischer Reihenfolge präsentiert und verfügen über ein jeweils eigenes Abbildungs-, Tabellen- und Literaturverzeichnis. Vorgestellt zu jeder Publikation ist eine kurze Einordnung des Kontextes für die hier vorliegende Dissertation, sowie die Beiträge der beteiligten Autoren zu finden.

Anschließend folgt in den Kapiteln 3.4 bis 3.5 eine Zusammenstellung weiterer Veröffentlichungen mit Eigenanteilen und Bezug zu SO_2-Sorption in MOFs. Hierzu werden jeweils eine kurze Zusammenfassung und die Beiträge der Autoren zu der entsprechenden Publikation aufgezeigt.

3.1 Zirconium and Aluminum MOFs for Low-Pressure SO_2 Adsorption and Potential Separation: Elucidating the Effect of Small Pores and NH_2-Groups

Philipp Brandt, Shang-Hua Xing, Jun Liang, Gülin Kurt, Alexander Nuhnen, Oliver Weingart, Christoph Janiak

ACS Appl. Mater. Interfaces, **2021**, *24*, 29137–29149

DOI: 10.1021/acsami.1c06003, Referenz [152]

Die Entwicklung von MOF-Materialien mit hoher Robustheit gegenüber harschen Bedingungen, wie sie bei der Anwendung der industriellen Rauchgasentschwefelung vorherrschen, stellt noch immer eine große Herausforderung dar.

In dieser Arbeit wurden stabile zirkonium- und aluminiumbasierte MOFs hinsichtlich ihrer Sorptionseigenschaften für die selektive Gastrennung von Schwefeldioxid (SO_2) gegenüber Kohlendioxid (CO_2) untersucht. Die bestimmten SO_2/CO_2-IAST-Selektivitäten bei einer SO_2-Molfraktion von 0,01 und einem Druck von 1 bar lagen bei Werten zwischen 22 und 53. MOFs mit Porengrößen im Bereich des kinetischen Durchmessers von SO_2 (4,1 Å) oder mit aminofunktionalisierten Liganden zeigten eine erhöhte Affinität zu SO_2. Zusätzlich wurde die Beständigkeit der Materialien gegenüber trockenem und feuchtem SO_2 getestet, um eine erste Bewertung der Stabilität der Materialien unter praxisorientierten Bedingungen treffen zu können.

Ferner wurden Dichtefunktionaltheorie Rechnungen für die drei repräsentativen MOFs Zr-Fum, Al-Fum und NH_2-MIL-53(Al) durchgeführt, um die präferierten Adsorptionsstellen zu ermitteln. Dabei stellte sich heraus, dass bei allen drei MOFs μ-OH···O=S=O Wechselwirkungen (jeweils –51.5, –51.1 und –49.1 kJ mol^{-1}) zu beobachten sind. Dieses Ergebnis spiegelt die Bedeutung der μ-OH-Funktionalitäten, innerhalb der SBUs dieser MOFs, bei der Adsorption von SO_2 wider. Dabei waren die Energien der stärksten Bindungspositionen in guter Übereinstimmung mit den Ergebnissen aus experimentell bestimmten isosterischen Asdsorptionsenthalpie bei einer Beladung nahe Null (ΔH_{ads}^{0}).

Anteile an der Veröffentlichung:

- Idee, Konzept experimenteller Arbeiten, Analytik und Manuskript (bis auf gelistete Ausnahmen).
- Aufarbeitung der Ergebnisse, Verfassung des Manuskripts und das Erstellen der Tabellen und der Abbildungen mit Ausnahme der MOF-Strukturen (von Herrn Dr. Jun Liang) und der Abbildungen in Zusammenhang mit theoretischen Rechnungen (von Frau Dr. Shang-Hua Xing und Herrn Dr. Oliver Weingart). Korrektur durch Herrn Prof. Dr. Christoph Janiak.
- Synthese und Charakterisierung der Materialien mit Unterstützung von Frau Gülin Kurt und Herrn Dr. Alexander Nuhnen.
- Rechnungen zu Dichtefunktionaltheorie wurden von Frau Dr. Shang-Hua Xing und Herrn Dr. Oliver Weingart durchgeführt.
- Rechnungen zu Grand Canonical Monte Carlo Simulationen wurden von Herrn Dr. Oliver Weingart durchgeführt.

ACS APPLIED MATERIALS & INTERFACES

www.acsami.org Research Article

Zirconium and Aluminum MOFs for Low-Pressure SO_2 Adsorption and Potential Separation: Elucidating the Effect of Small Pores and NH_2 Groups

Philipp Brandt, Shang-Hua Xing, Jun Liang, Gülin Kurt, Alexander Nuhnen, Oliver Weingart,* and Christoph Janiak*

Cite This: *ACS Appl. Mater. Interfaces* 2021, 13, 29137−29149 Read Online

ABSTRACT: Finding new adsorbents for the desulfurization of flue gases is a challenging task but is of current interest, as even low SO_2 emissions impair the environment and health. Four Zr- and eight Al-MOFs (Zr-Fum, DUT-67(Zr), NU-1000, MOF-808, Al-Fum, MIL-53(Al), NH_2-MIL-53(Al), MIL-53(tdc)(Al), CAU-10-H, MIL-96(Al), MIL-100(Al), NH_2-MIL-101(Al)) were examined toward their SO_2 sorption capability. Pore sizes in the range of about 4−8 Å are optimal for SO_2 uptake in the low-pressure range (up to 0.1 bar). Pore widths that are only slightly larger than the kinetic diameter of 4.1 Å of the SO_2 molecules allow for multi-side-dispersive interactions, which translate into high affinity at low pressure. Frameworks NH_2-MIL-53(Al) and NH_2-MIL-101(Al) with an NH_2-group at the linker tend to show enhanced SO_2 affinity. Moreover, from single-gas adsorption isotherms, ideal adsorbed solution theory (IAST) selectivities toward binary SO_2/CO_2 gas mixtures were determined with selectivity values between 35 and 53 at a molar fraction of 0.01 SO_2 (10.000 ppm) and 1 bar for the frameworks Zr-Fum, MOF-808, NH_2-MIL-53(Al), and Al-Fum. Stability tests with exposure to dry SO_2 during ≤10 h and humid SO_2 during 5 h showed full retention of crystallinity and porosity for Zr-Fum and DUT-67(Zr). However, NU-1000, MOF-808, Al-Fum, MIL-53(tdc), CAU-10-H, and MIL-100(Al) exhibited ≥50−90% retained Brunauer−Emmett−Teller (BET)-surface area and pore volume; while NH_2-MIL-100(Al) and MIL-96(Al) demonstrated a major loss of porosity under dry SO_2 and MIL-53(Al) and NH_2-MIL-53(Al) under humid SO_2. SO_2 binding sites were revealed by density functional theory (DFT) simulation calculations with adsorption energies of −40 to −50 kJ·mol^{-1} for Zr-Fum and Al-Fum and even above −50 kJ·mol^{-1} for NH_2-MIL-53(Al), in agreement with the isosteric heat of adsorption near zero coverage (ΔH^0_{ads}). The predominant, highest binding energy noncovalent binding modes in both Zr-Fum and Al-Fum feature μ-OH$^{\delta+}$...$^{\delta-}$OSO hydrogen bonding interactions. The small pores of Al-Fum allow the interaction of two μ-OH bridges from opposite pore walls with the same SO_2 molecule via OH$^{\delta+}$...$^{\delta-}$OSO$^{\delta-}$...$^{\delta+}$HO hydrogen bonds. For NH_2-MIL-53(Al), the DFT high-energy binding sites involve NH$^{\delta+}$...$^{\delta-}$OS together with the also present Al-μ-OH$^{\delta+}$...$^{\delta-}$OS hydrogen bonding interactions and C_6-$\pi^{\delta-}$...$^{\delta+}SO_2$, N$^{\delta-}$...$^{\delta+}SO_2$ interactions.

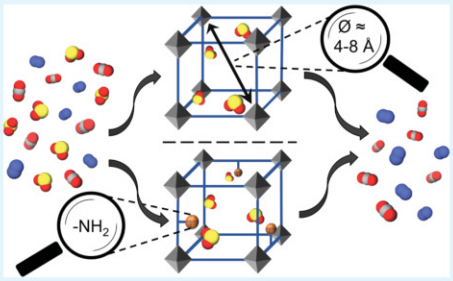

KEYWORDS: *sulfur dioxide, pore size, adsorption, metal−organic framework, flue gas desulfurization*

■ INTRODUCTION

A large fraction of the toxic gas sulfur dioxide (SO_2) is emitted into the atmosphere from industrial processes and fossil fuel combustion.[1] In 2018, energy-related coal combustion was accountable for 43% of SO_2 emissions worldwide.[2] SO_2 emissions are damaging to the biosphere both through the formation of acid rain and by contributing to air pollution issues, such as particulate matter (PM) with a diameter of ≤2.5 μm.[3−5]

Typically, wet limestone scrubbing or treatment by amine-based absorbents are used to remove SO_2 from flue gases. In both cases, the absorption is usually irreversible or accompanied by energy-intensive processes.[6] Calcium sulfite is the product of limestone scrubbing and is oxidized to produce flue-gas-desulfurization (FGD) gypsum, which is mainly utilized in the construction industry. Yet, lime-stone scrubbing leaves up to 150−450 ppm of SO_2, which can significantly reduce other flue gas purification processes by inactivating sorbents for CO_2 removal or catalysts for selective reduction of NO_x.[7−9] On the other hand, reversible SO_2 adsorption could be utilized in a much fruitful way by aiming at producing the industrially crucial sulfuric acid, without other by-products.[10] Dry FGD technol-

Received: April 1, 2021
Accepted: May 27, 2021
Published: June 11, 2021

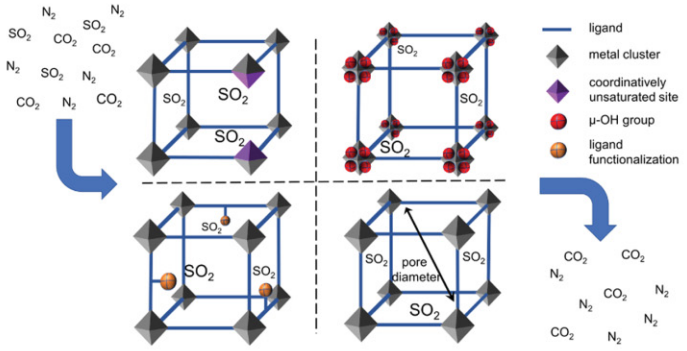

Figure 1. Schematic visualization of potential influencing factors for the low-pressure adsorption of SO_2 in porous materials.

Scheme 1. Zr- and Al-MOFs Investigated for SO_2 Adsorption[a]

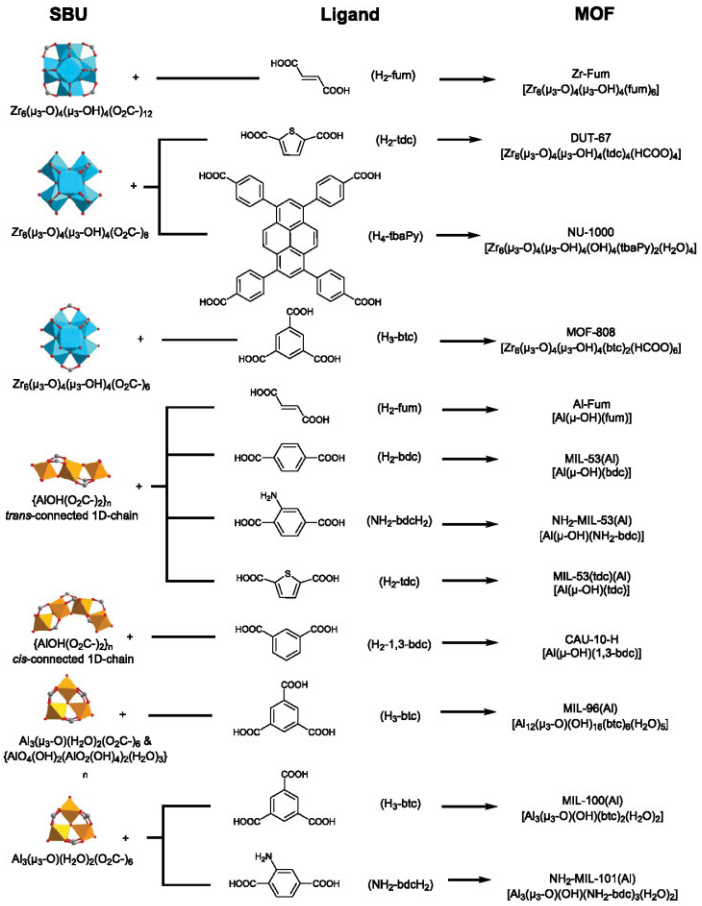

[a]Secondary building units (SBUs) depict the metal, carbon (gray), oxygen (red), and metal coordination polyhedra of Zr (cyan) and Al (orange) (left column), which are connected via the organic carboxylate ligands (acid form in the middle column) to form respective MOFs (right column).

ogies are expected to become competitive if cycling-efficient adsorbents with quantitative SO_2 removal would be available to balance the higher capital costs for a regeneration unit.[11]

Metal−organic frameworks (MOFs) represent a promising adsorbent class due to record-holding surface areas (>7000 m^2 g^{-1}) and uniform and designable porosity, typically in the microporous domain.[12] A combination of both inorganic and

https://doi.org/10.1021/acsami.1c06003
ACS Appl. Mater. Interfaces 2021, 13, 29137−29149

organic building units is the reason for the high variety and tunability of MOF materials. Owing to their high porosity, MOFs outperform competing adsorbents, like zeolites and activated carbons, leading to a considerable number of studies related to various gas storage and gas separation applications,[13−15] including the capture of toxic and polluting gases.[16−22]

Until about 8 years ago, research on SO_2 adsorption of MOFs was of specialized interest,[23−26] but recently has experienced a surge of attention.[27−32] For example, MFM-300(Al) and MFM-601(Zr) showed promising results for selective SO_2 adsorption and outstanding robustness.[33−35] Previously, we had examined MIL-160(Al), which exhibited an excellent ideal adsorbed solution theory (IAST) selectivity of 128 at 293 K and 1 bar for SO_2/CO_2 gas mixtures (10:90 v/v).[36]

For the use of MOFs in the selective adsorption of SO_2 traces below 500 ppm, the low pressure ($p < 0.01$ bar) SO_2 uptake is more relevant compared to the overall capacity reached at ambient pressure. Currently, the designed synthesis of porous adsorbents for highly selective removal of SO_2 from flue gas is still challenging and more endeavors are necessary to elucidate the underlying principles for optimal MOF SO_2 adsorbents. A model of potential factors influencing the selective SO_2 adsorption of an adsorbent is visualized in Figure 1.

So far, it is still a matter of discussion as to which factors constitute high SO_2 uptakes at low pressures ($p < 0.01$ bar).[37] In this work, we elucidate small pore widths and NH_2-substituents as critical MOF parameters to achieve high quantities in low-pressure SO_2 adsorption by focusing on Al- and Zr-MOFs, which are generally regarded as rather hydrothermally stable.[38−41] Also the determination of IAST-selectivities for SO_2/CO_2 gas mixtures provides a first indication for the separation performance of a given material. Overall, the results should allow designing MOFs to remove low SO_2 concentrations from $N_2/CO_2/SO_2$ gas mixtures.

■ EXPERIMENTAL SECTION

Materials and Methods. All reagents were purchased from commercial vendors and used without further purification. The MOFs were synthesized according to the published literature or were purchased (Table S1). The MOF identity was established by positively matching the powder X-ray diffractograms (PXRD) with the simulation from published cif-structure files and by a porosity analysis of the nitrogen sorption isotherms (see the Supporting Information for details).

Powder X-ray diffraction (PXRD) measurements were performed on a Bruker D2 Phaser with a Cu Kα-cathode source ($\lambda = 1.54182$; 30 kV, 10 mA) at room temperature. The finely ground samples were measured in the $5° < 2\theta < 50°$ range at a scan rate of 40 s deg^{-1} using a flat, low background silicon sample holder. N_2 gas adsorption for the Brunauer−Emmett−Teller (BET) surface area and porosity characterization was performed on a Quantachrome Autosorb 6 automatic gas adsorption analyzer. This instrument is not optimized to analyze very small micropores, and hence, a small number of data points are seen in the N_2 sorption isotherms in Figures S22−S33. At the same time, the MOFs in this work are already well characterized from the literature, and we note that our BET surface area and pore volume results agree very well (within experimental error) with the literature values. SO_2 and CO_2 sorption isotherms were measured on a Quantachrome Autosorb iQ MP.

Before each gas sorption experiment, the samples were activated according to the literature (≤3 h of degassing at ≤393 K and a ~5 × 10^{-3} mbar vacuum). The gases (He, N_2, SO_2, CO_2) were of ultrahigh purity (99.999%). The standard temperature and pressure (STP) volumes at 293.15 K and 101.325 kPa are reported in all cases according to the recommendation of the National Institute of Standards and Technology (NIST). The N_2 adsorption experiments were performed within a pressure range of 0.005−1 bar at 77 K, the SO_2 sorption experiments from 0.001 to 1 bar (0.95 ± 0.007 bar) at 293 K, and CO_2 sorption experiments from 0.001 to 1 bar (0.95 ± 0.005 bar). A Dräger Pac 6000 electrochemical SO_2 sensor with a measuring range of 0.1−100 ppm was used for leakage testing and maintaining safe work conditions.

■ RESULTS AND DISCUSSION

Four Zr- and eight Al-MOFs were investigated in this work and are presented in Scheme 1. Structural details are given in Section S2. The SO_2 sorption isotherms of these 12 MOFs were measured volumetrically up to 0.96 bar at 293 K. For clarity in the presentation of the SO_2 sorption isotherm diagrams, we will discuss Zr-MOFs and Al-MOFs separately.

SO_2 Adsorption by Zr-MOFs. All of the four representative Zr-MOFs have Zr_6 nodes albeit with different ligand connectivity numbers of 12, 8, or 6 for Zr-Fum, DUT-67(Zr), and NU-1000 or MOF-808, respectively.

Zr-fumarate (Zr-Fum) shows a good SO_2 affinity, already at 0.11 bar, with an SO_2 uptake of 3.1 mmol·g^{-1}, which increases to a maximum of 4.9 mmol·g^{-1} at 1 bar (Figure 2). MOF-808 and

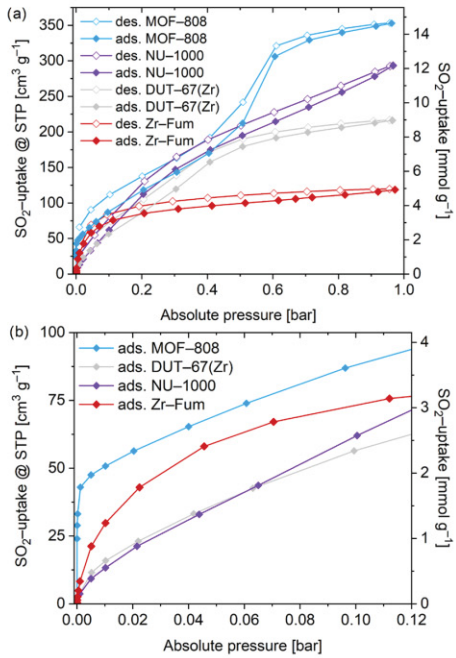

Figure 2. SO_2 sorption isotherms (293 K) of examined Zr-MOFs: (a) 0.001−1 bar and (b) 0.001−0.12 bar.

DUT-67(Zr) both exhibit two-step SO_2 adsorption isotherms (Figure 2a). In MOF-808, the first adsorption step finishes at 0.01 bar with an SO_2 uptake of 2.1 mmol·g^{-1}, followed by a moderate uptake in the pressure range of 0.01−0.5 bar up to 8.8 mmol·g^{-1}. The second step ends at 0.6 bar with an SO_2 uptake of 12.7 mmol·g^{-1}, followed by a saturation stage with a maximum of 14.6 mmol·g^{-1} at 1 bar.

Both DUT-67(Zr) and Zr-MOF NU-1000 exhibit moderate SO_2 adsorption capabilities in the low-pressure range with SO_2 uptakes of 0.7 and 0.6 mmol·g^{-1} at 0.01 bar as well as 2.3 and 2.6

https://doi.org/10.1021/acsami.1c06003
ACS Appl. Mater. Interfaces 2021, 13, 29137−29149

Table 1. Characteristics of Examined Materials in this Work and the Results of SO_2 Adsorption at 293 K

material	BET-surface area[d] [$m^2\,g^{-1}$]	total pore volume[d] [$cm^3\,g^{-1}$]	pore width[d] [Å]	SO_2 uptake [$mmol\cdot g^{-1}$] at 0.01 bar	0.1 bar	1 bar	SO_2/CO_2 IAST selectivity[d] at SO_2/CO_2 molar ratio 0.01[d]	0.1[d]	0.5[d]
Zr-Fum	600	0.290	4.8; 5.6; 7.4[42]	1.2	3.1	4.9	53	46	41
MOF-808	1990	0.749	4.8; 18.4[42]	2.1	3.6	14.6	48	66	370
DUT-67(Zr)	1260	0.544	8.8; 16.6[42]	0.7	2.3	9.0	22	22	37
NU-1000	1740	1.196	12; 29[43]	0.6	2.6	12.2	16	17	22
MIL-53(Al)	1450	0.706	8.5[e44]	0.4	3.3	10.5	17	22	43
NH_2-MIL-53(Al)	620	0.358	7.3[45]	2.0	4.3	8.0	41	42	56
Al-Fum	970	0.447	5.8[46]	1.0	4.1	7.5	34	35	36
MIL-53(tdc)(Al)	1000	0.415	8[47]	0.6	5.0	6.9	24	48	83
CAU-10-H	600	0.258	6[48]	1.2	3.7	4.8	29	27	25
MIL-96(Al)	530	0.237	~4; ~11, 11[49]	1.2	3.7	6.5	7	7	8
MIL-100(Al)	1890	0.824	25; 29[50]	0.4	2.5	16.3	17	18	38
NH_2-MIL-101(Al)	1770	1.001	25; 34[51]	1.5	3.6	17.3	29	20	16

[a]Ideal adsorbed solution theory (IAST) selectivity at 1 bar. See Section S4 for the CO_2 sorption data. [b]BET surface areas were calculated from five adsorption points of N_2 adsorption isotherm data within $0.05 < pp_0^{-1} < 0.2$. Values were rounded with the estimated standard deviation $\pm$ 50 $m^2\,g^{-1}$. [c]Total pore volumes were calculated from the experimental N_2 sorption data at $0.85 < pp_0^{-1} < 0.95$, depending on the isotherm shape. For details, see Section S3.3. [d]Pore widths as given in the literature. [e]Large pore form.

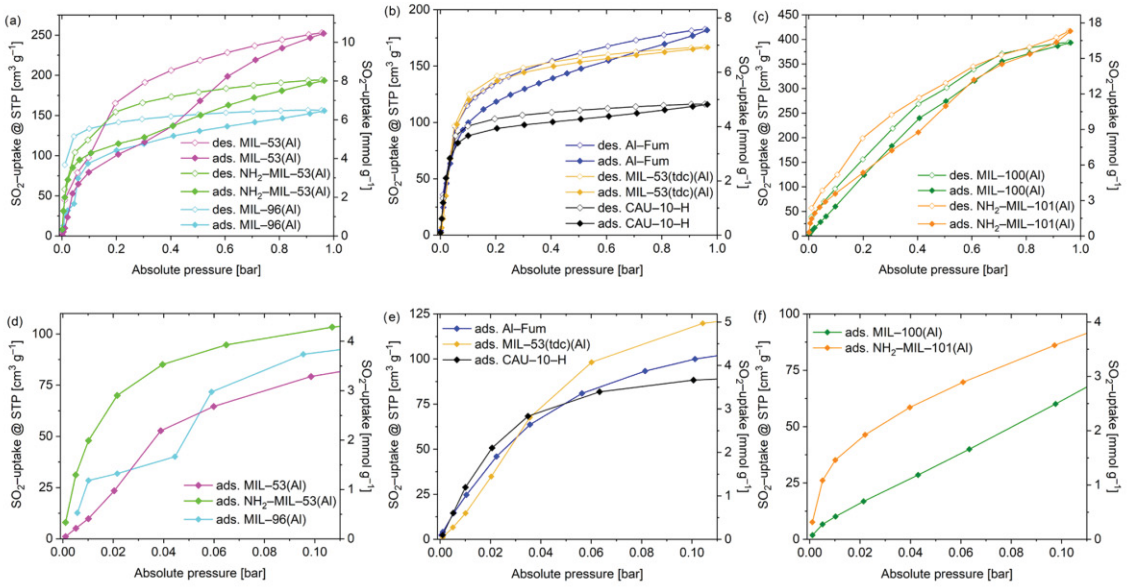

Figure 3. SO_2 sorption isotherms (293 K) of examined Al-MOFs: (a−c) 0.001−1 bar and (d−f) 0.001−0.11 bar.

$mmol\cdot g^{-1}$ at 0.1 bar, respectively (Table 1). DUT-67(Zr) shows a slight adsorption step at ~0.3 bar and a further increase until a maximum SO_2 uptake of 9.0 $mmol\cdot g^{-1}$. The SO_2 adsorption isotherm of NU-1000 increases rather steadily with a maximum SO_2 uptake of 12.2 $mmol\cdot g^{-1}$ at 1 bar and 293 K (in agreement with the isotherm in ref S2). The saturation uptake could not be reached in NU-1000 due to its micro- and mesoporosity with pore diameters of ~12 and ~29 Å for the triangular and hexagonal pore cross sections, respectively.[43]

Although all four Zr-MOFs have a bi- or multimodal pore size distribution (Table 1), we assign the observation of a two-step SO_2 adsorption in MOF-808 and DUT-67 to the simultaneous smaller (4.8 and 8.8 Å) and larger (16.6 and 18.4 Å) micropore diameters in the frameworks.[42] The two MOFs, Zr-Fum and MOF-808, with a significantly higher low-pressure uptake feature an equally smallest pore width (both 4.8 Å). The smaller pore width of DUT-67(Zr) is 8.8 Å and that of NU-1000 is 12 Å.[42] For a high low-pressure SO_2 adsorption, this suggests an optimal pore diameter of ~4 to <8 Å, as will be further discussed in the Porosity−Adsorption Relationships section.

SO_2 Adsorption by Al-MOFs. The eight representative Al-MOFs differ in their pore structures with 5 out of 8 having square to rhombic channels and infinite-chain SBUs. The infinite building units (here the Al-μ-OH-chain) and thus the resulting MOFs are known to show better thermal stability in comparison to frameworks with the same metal ions and the type of ligand but with discrete building units.[53]

https://doi.org/10.1021/acsami.1c06003
ACS Appl. Mater. Interfaces 2021, 13, 29137−29149

The Al-MOFs, MIL-53(Al), NH_2-MIL-53(Al), Al-Fum, MIL-53(tdc)(Al), and CAU-10-H, have one-dimensional channels with nearly square to rhombic cross sections of 5.8−8.5 Å. MIL-53(Al) and NH_2-MIL-53(Al) differ from the other MOFs by their reversible breathing behavior with the adsorption of guest molecules.[44,54] The complex structure of MIL-96(Al) consists of an isolated, not accessible pore A and "zig-zag" channels connecting the larger B and the smaller pore C.[49,55] MIL-100(Al) and NH_2-MIL-101(Al) have 3D pore networks of spherical mesopores of diameter ≥25 Å connected by smaller windows.

The SO_2 adsorption isotherms of MIL-53(Al) and NH_2-MIL-53(Al) (Figure 3a,d) show SO_2 uptakes to 3.3 and 4.3 mmol·g^{-1}, respectively, at 0.1 bar, which is followed by a flattening of the adsorption. Noteworthy is the rather steep increase for NH_2-MIL-53(Al) up to 0.01 bar, which will be discussed together with NH_2-MIL-101(Al). Further at 0.3−0.4 bar, both frameworks show second adsorption steps, which lead to maximum SO_2 uptakes of 10.5 and 8.0 mmol·g^{-1} at 1 bar for MIL-53(Al) and NH_2-MIL-53(Al), respectively. As mentioned above, this second adsorption step can be explained by a structure transition (breathing) from a narrow pore (np) into a large pore (lp) form, which significantly enhances the accessible space within the frameworks. The pronounced hysteresis observed in both desorption isotherms is additional evidence for phase transitions.

Previously, Liu et al.[23] and Yang et al.[56] have reported reversible phase transition upon SO_2 capture of the frameworks FMOF-2 and MFM-520, respectively. In FMOF-2, the transition can be described as a breathing mechanism, whereas, for MFM-520, an unexpected periodic-to-aperiodic structure transition was observed.

The SO_2 isotherm of MIL-96(Al) (Figure 3a,d) features two distinct adsorption steps in the low-pressure range (up to 0.1 bar). The first step finishes at 0.01 bar with an SO_2 uptake of 1.2 mmol·g^{-1}, followed by a second step starting at 0.05 bar with an SO_2 uptake of up to 3.7 mmol·g^{-1} at 0.1 bar followed by a saturation stage with a maximum SO_2 uptake of 6.5 mmol·g^{-1} at 1 bar. The stepwise adsorption reflects the complex pore structure of MIL-96(Al), which exhibits an isolated cavity A with a diameter of 11 Å and two further cavities B ∼ 11 Å and C ∼ 4 Å, which are connected and form zig-zag channels.[49] The type H2 desorption hysteresis is further evidence of a more complex pore structure in which network effects are important. The very steep desorption branch, which is a characteristic feature of H2(a) loops, can be attributed either to pore-blocking/percolation in a narrow range of pore necks or to cavitation-induced evaporation.[57]

Further, we investigated Al-MOFs with similar channel structures to MIL-53(Al), albeit more rigid, that is, without an established breathing behavior and of nearly square cross section. The SO_2 adsorption isotherms of Al-Fum, MIL-53(tdc)(Al), and CAU-10-H (Figure 3b,e) feature a similar behavior for the low-pressure range with SO_2 uptakes of 4.1, 5.0, and 3.7 mmol·g^{-1} at 0.1 bar and maximum uptake of 7.5, 6.9, and 4.8 mmol·g^{-1} at 1 bar, respectively.

CAU-10-H is isostructural to previously investigated MIL-160, which showed promising properties for a potential application in FGD processes.[36] Our results for CAU-10-H are consistent with the work reported recently by Alejandre et al.[58] The low-pressure range, up to 0.1 bar, covers 76% of the total uptake capacity in the case of CAU-10-H, which would be beneficial for pressure swing adsorption.

SO_2 adsorption in MIL-100(Al) and NH_2-MIL-101(Al) (Figure 3c,f) takes place over the whole pressure range without reaching the saturation stage at 1 bar, similar to NU-1000 (Figure 2). Again, this is due to the large pore sizes in the mesopore region. In the absence of smaller micropores, MIL-100(Al) shows one of the lowest SO_2 adsorptions at low pressures; however, with increasing pressure, it surpasses most materials examined in this work, with a total capacity of 16.3 mmol·g^{-1} at 1 bar.

The amino-functionalized MOF NH_2-MIL-101(Al) shows an initial steep increase up to ∼0.01 bar, very similar to NH_2-MIL-53(Al) (Figure 3d,f). An enhanced SO_2 uptake at low pressures was seen with amino functionalization for both NH_2-MIL-53(Al) and NH_2-MIL-101(Al) compared to their closely related frameworks, MIL-53(Al) and MIL-100(Al), respectively (Figure 3c,f). This early increase in uptake of the two NH_2-functionalized MOFs is much steeper than what is seen in this pressure range for the other Al-MOFs (cf. Figure 3d−f), which suggests its origin in the NH_2 group. This is in agreement with similar observations for the MOFs NH_2/-MIL-125(Ti)[59] and also coincides with findings for NH_2-UiO-66 exhibiting higher heat of adsorption values near zero coverage and a higher SO_2/CO_2 selectivity, compared to the parent UiO-66.[60] From a simulation of mmen-MIL-101(Cr) (mmen = *N,N′*-dimethylethylenediamine), the SO_2 adsorption sites were found to be transferred from Cr(III) in MIL-101(Cr) to the NH-amino groups. The lone-pair electrons from N interact with the S(SO_2) atom that has a partial positive charge. The mmen-NH groups form hydrogen bonds to O(SO_2), of the same SO_2 molecule, with distances of 1.92 and 2.27 Å as the predominant adsorption site.[61]

One gram of NH_2-MIL-53(Al) and NH_2-MIL-101(Al) corresponds to 4.5 or 1.5 mmol of the formula unit, respectively (cf. formula unit in Scheme 1) or to 4.5 mmol NH_2-bdc. Thus, at 0.01 bar, when the SO_2 uptake slope decreases, the ratios are ∼2 SO_2/4.5 NH_2-bdc in NH_2-MIL-53(Al) and ∼1.5 SO_2/4.5 NH_2-bdc in NH_2-MIL-101(Al). This suggests that two adjacent NH_2-groups can bind one SO_2 through two NH···OSO···HN hydrogen bonds in a high-affinity site. For NH_2-MIL-101(Al), the SO_2 uptake passes 3.6 mmol·g^{-1} at 0.1 bar and continues with relatively steady adsorption and reaches, albeit at no saturation yet, a maximum uptake of 17.3 mmol·g^{-1} at 1 bar, which is one of the highest reported in the literature (for a comprehensive compilation of literature data regarding SO_2 adsorption in MOFs, see Table S8). Ibarra et al. have recently investigated SO_2 adsorption in MIL-101(Cr) in which the bdc ligand was partially substituted with tetrafluoro-1,4-benzenedicarboxylate (4F-bdc) and showed a roughly similar isotherm shape to the isoreticular NH_2-MIL-101(Al) but with slightly higher SO_2 adsorption capacity with SO_2 uptakes of 4.6 and 18.4 mmol·g^{-1} at 0.1 and 1 bar, respectively, at 298 K and featured exceptional stability against SO_2.[62]

We do not see an effect of aqua ligands at the SBU for an enhanced SO_2 uptake at low pressure since MIL-100(Al) and NH_2-MIL-101(Al) with the same $\{Al_3(\mu_3\text{-}O)(OH)(H_2O)_2(O_2C\text{-})_6\}$ SBU behave quite differently (Figure 3f). The former has the lowest SO_2 uptakes of up to 0.1 bar of all Al-MOFs. This is not to say that there would be no effect of aqua ligands or adsorbed water for other things being equal.

Ibarra et al. could observe enhanced SO_2 adsorption in the MFM-300 series related to small amounts of pre-adsorbed EtOH.[28] Also, Li et al. predicted enhanced SO_2 adsorption for MIL-160 with 0.3% pre-absorbed water.[63]

https://doi.org/10.1021/acsami.1c06003
ACS Appl. Mater. Interfaces 2021, 13, 29137−29149

The terminal metal-OH and metal-bridging μ/μ_3-OH-groups can also significantly contribute to the SO_2 adsorption performance since these groups enter in hydrogen bonding/electrostatic interactions with SO_2 ($M\text{-}O^{\delta-}\text{–}H^{\delta+}\cdots O^{\delta-}{=}S^{\delta+}{=}O^{\delta-}$)[28,33,36,62] In our chosen Zr- and Al-MOFs, all examples feature these OH groups. In situ inelastic neutron scattering and density functional theory (DFT) calculations on the SO_2 adsorption in MFM-300(Al)[33] and in situ synchrotron PXRD studies for SO_2 in MFM-601(Zr)[64] revealed metal-OH···O=S=O hydrogen bonds for the first adsorbed SO_2 molecules. Other than that, the effect of μ-OH-groups regarding SO_2 adsorption is rarely examined in the literature. In the DFT Calculations section, we present potential binding sites of SO_2 in the representative MOFs, Zr-Fum and Al-Fum, which affirm the significant contribution of metal-OH···O=S=O interactions.

Porosity–Adsorption Relationships. The accessible surface area and the total accessible pore volume are often taken as the two prime MOF characteristics governing gas adsorption. Plots of the SO_2 uptake at 1 bar against the BET-surface area and pore volume (Figure 4a,b) show a reasonably linear correlation for most MOFs. Noteworthy outliers in the surface area correlation are NH_2-MIL-101(Al), MIL-100(Al), and NH_2-MIL-53(Al) with a higher than expected uptake based on the surface area. For NH_2-MIL-101(Al) and MIL-100(Al), their high total pore volume from micro- and mesopores gives rise to the higher uptake. The higher than expected SO_2 uptake for the flexible MOF, NH_2-MIL-53(Al), may be traced to a different extent of breathing with SO_2 at 293 K and N_2 at 77 K (where the latter yielded the accessible surface area and pore volume).

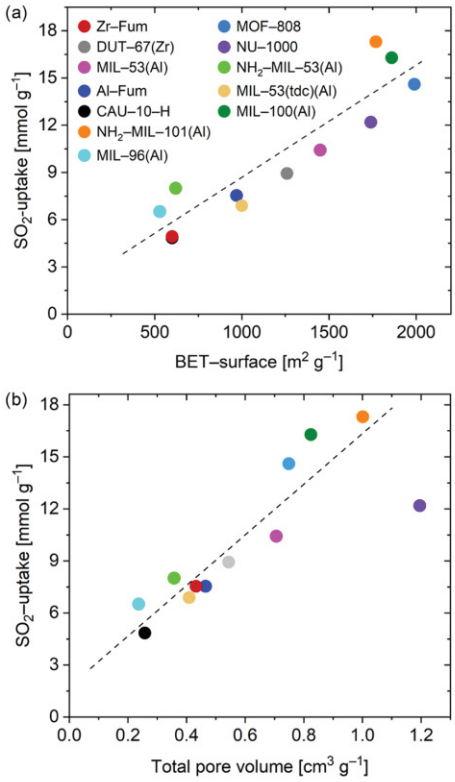

Figure 4. SO_2 uptake (1 bar, 293 K) vs (a) BET-surface area and (b) total pore volume. The dashed line is a trend line as a guide to the eye.

An outlier to significantly lower uptake in the uptake–pore volume relation is the Zr-MOF NU-1000, which has the highest total pore volume, even more than MIL-100(Al) and NH_2-MIL-101(Al), and is predominantly mesoporous. N_2 sorption studies with *t*-plot analysis yielded micro-to-total pore volume ratios ($cm^3\ g^{-1}/cm^3\ g^{-1}$) of 0.21/1.20 for NU-1000, 0.55/0.82 for MIL-100(Al), and 0.61/1.00 for NH_2-MIL-101(Al) (Table S2). The total pore volume represents a limit for the maximum capacity but the SO_2 adsorption isotherm of NU-1000 at 1 bar still has a high positive slope and is far from leveling off, which indicates an adsorption curve far from saturation, which will be reached only at higher pressures. Evidently, a primarily mesoporous material can be positioned below the linear trend line of the uptake–total pore volume dependence.

However, flue gas desulfurization or SO_2 gas sensors operate at low partial pressures of SO_2. When it comes to the desired high uptake at low pressure, there is no longer a surface area or total pore volume correlation. The low-pressure uptake at 0.01 and 0.1 bar is clearly independent of surface area (Figure S35). Instead, the uptake and isotherm characteristics in the low-pressure region (Figure S34) must be correlated with the SO_2 affinity of the materials. By fitting the SO_2 adsorption isotherms with an appropriate model, the affinity constants can be obtained (Table S3 and Figures S39–S50). A high-affinity constant between the adsorbent and the adsorbate reflects a high gas uptake at low pressure, which is a type-I isotherm.

When the surface-specific SO_2 uptake, that is, the uptake at low pressures (0.01 and 0.1 bar) divided by the BET-surface area, is plotted against the pore limiting diameter (PLD), an obvious maximum is obtained (Figure 5). The surface-specific SO_2 uptake is obtained by normalization, i.e., division of the uptake through the surface area, which is necessary as the absolute value of the uptake at low pressure depends on the available surface area. The PLD is defined as the smallest diameter of a pore or pore window in a framework. The maximum of low-pressure uptake vs PLD suggests an optimal pore diameter in the range between ~4 and 8 Å.[30] The value of 4 Å agrees with the kinetic diameter of SO_2 (4.1 Å).[65] In this PLD range, one can assume the SO_2 molecule to have dispersive interactions with both ends of the molecule to the surface. Such local optima are known for adsorbent structures where the opposite Connolly surfaces are at a distance of the length of the

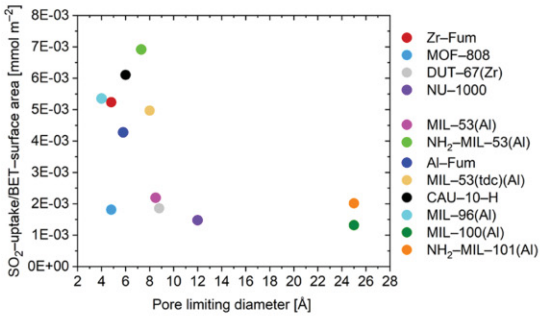

Figure 5. Surface-specific SO_2 uptake at 0.1 bar (293 K), which is the uptake at this pressure divided by the BET-surface area vs the pore limiting diameter (PLD). See Figure S36 for the surface-specific SO_2 uptake at 0.01 bar.

https://doi.org/10.1021/acsami.1c06003
ACS Appl. Mater. Interfaces 2021, 13, 29137–29149

adsorbed molecule, which can then simultaneously interact with the accessible surface at its opposite sides.[57] Grand-canonical-Monte Carlo (GCMC) simulations for a series of small-pore MOFs have shown a good correlation between the SO_2 uptake at reduced pressures (0.05 bar) and the heat of adsorption.[66]

A pore width of ~4 Å between the Connolly surfaces, i.e., the distance between probe-accessible surfaces of the opposite pore sides[57] allows the SO_2 molecule to have optimal multi-side dispersive interactions. The optimum range up to ~8 Å = 2 × 4 Å can be rationalized through the side-by-side interactions of two adjacent SO_2 molecules through (framework-)O═S···O═S═O(-framework) dipole−dipole interactions. The drop in the surface-specific uptake at larger pore sizes above 8 Å is then due to a change to "one-sided" interactions for the adsorbed SO_2 molecules with the uptake of further SO_2 molecules occurring solely through (framework-)O═S···O═S═O dipole−dipole interactions.[67] MOF-808 shows a somewhat low surface-specific SO_2 uptake at 0.1 bar, but, at an even smaller pressure of 0.01 bar, it has comparable good performance as Al-Fum (Figure S36).

From the conclusion that SO_2 will be preferentially adsorbed in the smallest pores at low pressures, one can also assume the micropore volume or the micropore surface area as the normalizing denominator for the surface-specific SO_2 uptake vs the PLD. The micropore surface area normalization is given in Figures S37 and S38 (at 0.1 and 0.01 bar, respectively). This SO_2 uptake normalization, however, then overenhances the uptake of the two amino-functionalized MOFs, NH_2-MIL-53(Al) and NH_2-MIL-101(Al). Thereby, the importance of amino groups is demonstrated at the same time. Yet, the very small micropore surface area of the largely mesoporous NH_2-MIL-101(Al) gives a small value in the denominator upon normalization, which together with the high uptake of NH_2-MIL-101(Al) then leads to an overall high SO_2 uptake even with the large PLD of about 25 Å (Figures S37 and S38). This would distort the conclusions drawn with respect to PLD.

In summary, the SO_2 adsorption isotherms of typical Zr- and Al-MOFs (Figures 2 and 3 for a combination, see Figure S34) show a wide range of shapes and uptake values in the relevant pressure regions. Once again, we note that a total SO_2 uptake at 1 bar, here found between ~5 and 17 mmol·g^{-1} at 293 K, is less meaningful when aiming for an application in SO_2 separation processes where SO_2 represents only a small volume fraction (<1000 ppm) of the gas mixture. Instead, the noted low-pressure uptake up to ~0.1 bar is more important.

IAST Selectivity. The ideal adsorbed solution theory (IAST) model is a method that gives first estimations on the mixed gas adsorption behavior of an adsorbent based on data gained from single-gas adsorption experiments. IAST-based estimations are most suitable when the following conditions are fulfilled: (i) the same accessible surface area is available to all adsorbates, (ii) low pressures (≤1 bar), and (iii) similar polarity of adsorbates.[68] IAST selectivities in this work were calculated with the "3P sim" software (see the Supporting Information) by fitting the adsorption isotherm data points with the dual-site Langmuir Sips model (DSLS) (Figures S39−S50). Parameters are given in Table S2.

CO_2 can be regarded as the main competitor to SO_2 for a potential adsorptive separation during flue gas desulfurization. IAST selectivities for SO_2/CO_2 gas mixtures for selected MOFs are displayed in Figure 6 (see Table 1 and Figure S51 for all MOFs).

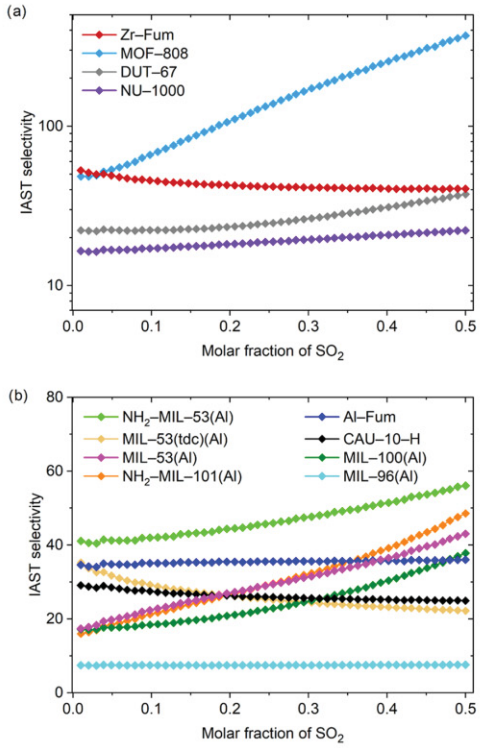

Figure 6. Calculated SO_2/CO_2 IAST selectivity dependence on the molar fraction of SO_2 in the range of 0.01−0.5 at 293 K and 1 bar: (a) Zr-MOFs and (b) Al-MOFs.

The highest calculated SO_2/CO_2 IAST selectivities at 1 bar and low SO_2 mol fraction of 0.01 (1% or 10.000 ppm SO_2) were 53, 48, 41, and 34 for Zr-Fum, MOF-808, NH_2-MIL-53(Al), and Al-Fum, respectively (Table 1). These MOFs had all shown an early steep SO_2 uptake (Figures 2b and 3d), which is one understandable prerequisite for a high SO_2/CO_2 IAST selectivity at a low molar fraction of SO_2 together with a low CO_2 uptake at low pressure (see Table S4).

Isosteric Enthalpy of Adsorption. The isosteric enthalpy of adsorption (ΔH_{ads}) for SO_2 was determined for the representative MOFs, Zr-Fum, Al-Fum, and NH_2-MIL-53(Al), by applying a virial analysis on adsorption isotherm data measured between 293 and 303 K (Figure 7; for details see Section S6.2). The isosteric enthalpy of adsorption near zero coverage (ΔH^0_{ads}) in Zr-Fum is −49 kJ mol^{-1}, whereas Al-Fum and NH_2-MIL-53(Al) exhibit values of −42 and −67 kJ mol^{-1}, respectively. At maximum loading, ΔH_{ads} decreases to −16, −30, and −58 kJ mol^{-1} for Zr-Fum, Al-Fum, and NH_2-MIL-53(Al), respectively. The values of ΔH^0_{ads} can be compared with the DFT-calculated highest binding energies (see below). For Zr-Fum and Al-Fum, the ΔH^0_{ads} value is of the same order of magnitude as in the previously investigated Zr-MOFs (−48 and −51 kJ mol^{-1} for MFM-600[64] and NU-1000,[52] respectively) and Al-MOFs (−42 and −42.8 kJ mol^{-1} for MIL-160[36] and CAU-10-H,[58] respectively). The overall higher adsorption enthalpy for NH_2-MIL-53(Al) can be explained by the strong interaction of the amino group with the polarizable SO_2 molecule.

https://doi.org/10.1021/acsami.1c06003
ACS Appl. Mater. Interfaces 2021, 13, 29137−29149

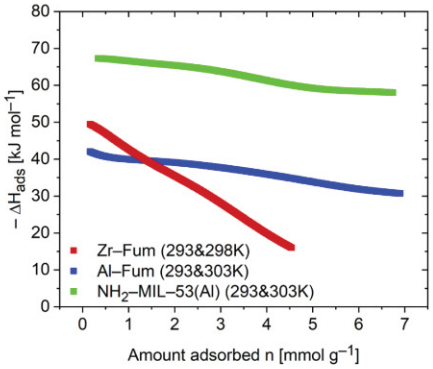

Figure 7. Isosteric enthalpy of adsorption of SO_2 for Zr-Fum, Al-Fum, and NH_2-MIL-53(Al) determined by virial analysis applied on SO_2 adsorption isotherm data measured at temperatures between 293 and 303 K. Computational details are given in the Supporting Information, Section S7.2.

Stability Test toward Dry and Moist SO_2. FGD materials must endure harsh conditions of humid SO_2, containing the moderately strong and quite corrosive sulfurous acid in equilibrium. Though MOFs are often stable toward dry SO_2, many of them degrade when moisture is present.[59] Also, the presence of water could partially shift the adsorption of SO_2 from physisorption to weak chemisorption, which impacts the regeneration of an adsorbent.[11] Therefore, in this study, we tested the stability of all materials after both dry and humid SO_2 exposure conditions (Section S3). To assess the stability, the changes of the PXRD patterns (Figures S10–S21) were examined qualitatively, while changes of the BET-surface area and the total pore volume after exposure were used as the primary quantitative parameters (Figures S22–S33 and 8). It is

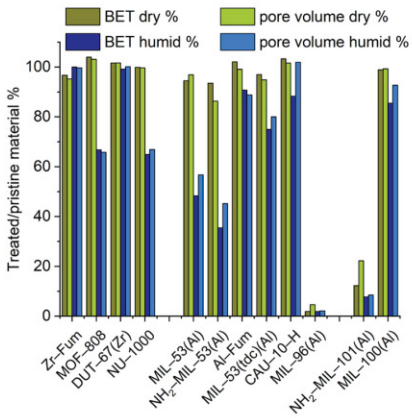

Figure 8. Relative (treated/pristine) BET-surface area and total pore volume of investigated MOFs after dry and humid SO_2 exposure.

worth mentioning that distinct changes in the PXRD pattern, after dry or humid SO_2 exposure, were rarely observed. More significant and indicative of framework degradation were losses in surface area for some MOFs. Hence, a combination of diffraction and adsorption experiments is always recommended. Moreover, we note that the distinction between framework degradation and irreversible adsorption is not trivial. However, in materials with potential applicability for FGD, neither framework degradation nor irreversible SO_2 adsorption is preferable. An overview of the results from BET-surface analyses and accessible pore volume, by relating treated/pristine samples, is presented in Figure 8.

Under dry SO_2 exposure, NH_2-MIL-100(Al) and MIL-96(Al) had already demonstrated a major loss of porosity, and thus were deemed SO_2-unstable. Interestingly, the dry SO_2 exposure during ≤10 h did not strongly affect the majority of examined materials (≥90% retained BET-surface area and pore volume). In contrast, under humid SO_2 exposure during 5 h, most MOFs showed a noticeable decrease in accessible porosity. After humid SO_2 exposure, the surface areas of MIL-53(Al) and NH_2-MIL-53(Al) decreased by more than 50%, while NU-1000, MOF-808, Al-Fum, MIL-53(tdc), CAU-10-H, and MIL-100(Al) showed less significant losses in surface area (≥50–90% retained BET-surface area and pore volume). Only Zr-Fum and DUT-67(Zr) showed good performance in both stability tests without a noticeable decrease in porosity. Both MOFs previously showed good water stability also under acidic conditions.[40,69]

DFT Calculations. For the investigation and illustration of the possible binding sites of SO_2, we applied dispersion-corrected DFT (DFT-D) calculations on model frameworks of the three example MOFs—Zr-Fum, Al-Fum, and NH_2-MIL-53(Al). Distances between the oxygen atom of the SO_2 molecule and hydrogen atoms of the framework above 2.8 Å[70] were not viewed as (O/C–)H···O bonds, as the distances between the SO_2 sulfur atom and oxygen atoms of the MOF were above 4 Å. For computational details, see Section S7.

Zr-Fum. With the discrete secondary building units in Zr-Fum, a cluster approach is appropriate. To mimic the local pore environment in Zr-Fum, three different cluster models, each being neutral, were isolated from its crystal structure (Figure 9).

Hydroxido-Centered Model 1. An isolated $[Zr_6(\mu_3\text{-O})(\mu_3\text{-OH})(Hfum)_3(O_2CH)_9]$ cluster with three mono-deprotonated fumarate^{1-} ligands surrounding a μ_3-OH group by spanning the three edges of a triangular face of the Zr_6 octahedron was used to model part of the pore cavity (Figure 9a). Out of the 12 bridging fumarate^{2-} ligands around a Zr_6 cluster in Zr-Fum, nine ligands were replaced by formiate ligands, $^{-}O_2CH$, each spanning a Zr···Zr edge of the Zr_6 octahedron. This ensured the electro-neutrality of the cluster model.

Metal-Centered Model 2. An isolated $[Zr_6(\mu_3\text{-O})(\mu_3\text{-OH})(Hfum)_4(O_2CH)_8]$ cluster with four fumarate^{1-} ligands surrounding a metal vertex by spanning the four edges around a Zr corner of the Zr_6 octahedron was used (Figure 9b).

Oxido-Centered Model 3. The $[Zr_6(\mu_3\text{-O})(\mu_3\text{-OH})(Hfum)_3(O_2CH)_9]$ cluster is similar to model 1, except that the three fumarate^{1-} ligands now surround a μ_3-O group (Figure 9c,d).

Four main binding sites for SO_2 are found in the optimized cluster models of Zr-Fum (Figure 9). In binding site 1 of the hydroxido-centered model 1, the O atom of SO_2 interacts with the H atom of the μ_3-OH group. This $OH^{\delta+}\cdots{}^{\delta-}OS$ hydrogen bonding interaction with the optimized H···O distance of 1.88 Å is supplemented by an electrostatic interaction at a distance of 3.33 Å between the fum-carboxylate O atom and the $^{\delta+}S$ atom of SO_2 as well as (fum)C···S dispersion interactions. This site has the highest binding energy of −51.5 kJ mol^{-1} of all found four higher-energy binding sites. The value is close to the experimental enthalpy of adsorption near zero coverage

https://doi.org/10.1021/acsami.1c06003
ACS Appl. Mater. Interfaces 2021, 13, 29137−29149

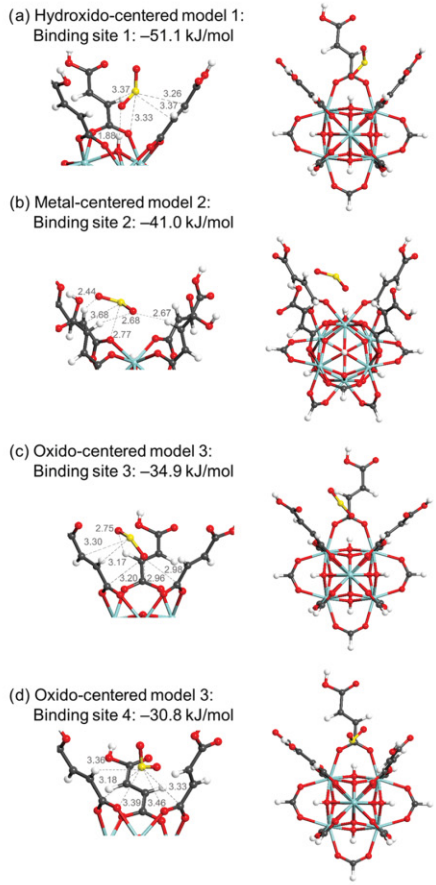

Figure 9. DFT-simulated higher-energy binding sites of SO_2 in Zr-Fum. Left: Close-up of potential SO_2 binding sites with closest contacts (in Å) between the SO_2 molecule to nearby framework atoms depicted by dashed lines. Right: Complete cluster model of SO_2 in Zr-Fum. See the text for a description of models 1−3.

(ΔH^0_{ads}) in Zr-Fum of −49 kJ mol^{-1} (cf. Figure 7). In binding site 2 of the metal-centered model 2, there are multiple weak (fum)CH$^{\delta+}$... $^{\delta-}$OS interactions (2.44−2.67 Å) together with the electronic attraction between CO$^{\delta-}$...$^{\delta+}$S (2.77 Å), as well as the fum···SO_2 dispersion interactions. Together, this gives site 2 a binding energy of −41.0 kJ mol^{-1}. The next lower-energy binding sites 3 and 4 exist in the oxido-centered model 3. Their lower binding energies of −34.9 and −30.9 kJ mol^{-1}, compared to sites 1 and 2, derive from a longer/weaker (fum)CH$^{\delta+}$...$^{\delta-}$OS contact of 2.75 Å (site 3) and longer/weaker CO$^{\delta-}$...$^{\delta+}$S contacts of 3.39−3.46 Å (site 4) as well as weaker (fum)C···S dispersion interactions than seen for sites 1 and 2, respectively.

Al-MOFs. For Al-Fum and NH_2-MIL-53(Al), with their infinite secondary building units $\{Al(\mu\text{-}OH)(O_2C\text{-})_2\}_n$, unit cells were generated from their respective crystal structures instead of a cluster model as in Zr-Fum. Figures S56 and S57 depict geometries and structure parameters of the plane wave DFT-D3-optimized Al-MOFs. The free optimized structures exhibit near-parallel alignment of the linker units with 90° O−Al−O angles, while the constrained structures are slightly more distorted. In the constrained structures, the parameters were fixed according to the crystal structure data. We also note variations in the optimized cell vector lengths and angles with respect to the crystal structure parameters. In Al-Fum, the *b*-vector lengthens by ca 0.9 Å, while the respective *a*- and *c*-vectors shorten by 0.1 and 0.2 Å. The β-angle widens by ca. 5°. For NH_2-MIL-53(Al), we observe a lengthening in the *b*- and *a*-vectors of ca. 0.5 and 0.15 Å, respectively, and a shortening of 0.3 Å in the *c*-vector. The overall cell volume is mostly preserved in the optimized vacuum structure of Al-Fum. NH_2-MIL-53(Al) has a ca. 3% larger cell size after full relaxation. Optimization of a single SO_2 molecule within the structures partially results in further contraction along the *c*-axis in Al-Fum and additional lengthening along *b* in NH_2-MIL-53(Al), indicating the breathing capability of both MOFs at low pressures (Figures 10 and 11). Interestingly, most of the computed high-energy binding modes (1−3) show this contraction along *c* and expansion along *b*.

The predominant noncovalent binding mode in sites 1−4 in Al-Fum (Figure 10a−e) can be traced to OH$^{\delta+}$...$^{\delta-}$OS hydrogen bonding interactions of SO_2 with the μ-OH bridge and H···O distances from 1.98 to 2.82 Å. The binding site 1 (Figure 10a) with −51.1 kJ mol^{-1} and with the shortest H···O distance is energetically close to binding sites 2 (−49.5 kJ mol^{-1}) and 3 (−48.6 kJ mol^{-1}). In the latter two sites, the small pores of Al-Fum allow the interaction of two μ-OH bridges from the opposite pore walls with the same SO_2 molecule via OH$^{\delta+}$...$^{\delta-}$OSO$^{\delta-}$...$^{\delta+}$HO hydrogen bonds (Figure 10b,c). The experimental enthalpy of adsorption near zero coverage (ΔH^0_{ads}) in Al-Fum was −42 kJ mol^{-1} (cf. Figure 7).

In the two lower-energy binding sites 4a and 4b of equal energy (−41.0 kJ mol^{-1}), again SO_2 interacts with the framework through OH$^{\delta+}$...$^{\delta-}$OS and a (fum)CH$^{\delta+}$...$^{\delta-}$OS hydrogen bond in site 4a, while weaker H···O hydrogen bonding is observed in site 4b (Figure 10d,e). Additional (fum)CO$^{\delta-}$...$^{\delta+}$$SO_2$ contacts as well as (fum)C···OSO dispersion interactions lead to the energy differentiation between the binding sites in Figure 10.

From the fully relaxed optimization of NH_2-MIL-53(Al) with one SO_2 molecule, we obtained at least four binding sites with binding energies ranging from −67.3 to −49.1 kJ mol^{-1} (Figure 11a−d). Binding site 1 (Figure 11a) has the highest binding energy (−67.3 kJ mol^{-1}), and it is dominated by NH$^{\delta+}$...$^{\delta-}$OS hydrogen bonding and HN$^{\delta-}$...$^{\delta+}$SO electrostatic attractive interactions between $-NH_2$ groups from two independent BDC-NH_2 linkers. The value is again close to the experimental enthalpy of adsorption near zero coverage (ΔH^0_{ads}) in NH_2-MIL-53(Al) of −67 kJ mol^{-1} (cf. Figure 7). Binding site 2 (Figure 11b) has a slightly lower binding energy (−58.2 kJ mol^{-1}). Here, SO_2 mainly binds to C_6-π from bdc-NH_2 through C_6-$\pi^{\delta-}$...$^{\delta+}$SO interactions with C_6-π···S distances between 2.99 and 3.19 Å. For binding site 3 (Figure 11c) with a binding energy of −55.1 kJ mol^{-1}, we note a NH$^{\delta+}$...$^{\delta-}$OS hydrogen bond, COO$^{\delta-}$...$^{\delta+}$SO electrostatic interactions, and weak CH$^{\delta+}$...$^{\delta-}$OS interactions as cooperating effects, trapping SO_2 within the pores of NH_2-MIL-53(Al). The shortest distances between SO_2 and the ligands (NH$^{\delta+}$...$^{\delta-}$OS = 1.99 Å and CH$^{\delta+}$...$^{\delta-}$OS = 2.56 Å) in site 3 are between ligands on different Al atoms. Binding site 4 (Figure 11d) has the lowest binding energy (−49.1 kJ mol^{-1}); besides C6-$\pi^{\delta-}$...$^{\delta+}$SO and NH$^{\delta+}$...$^{\delta-}$OS interactions, an additional OH$^{\delta+}$...$^{\delta-}$OS hydrogen bond between μ-OH and SO_2 contributes to the adsorption of SO_2.

https://doi.org/10.1021/acsami.1c06003
ACS Appl. Mater. Interfaces 2021, 13, 29137−29149

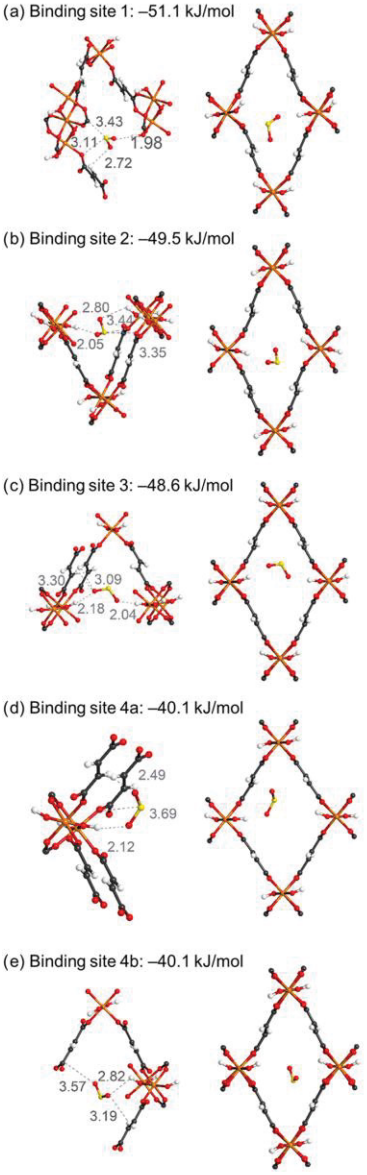

Figure 10. DFT-simulated higher-energy binding sites of SO_2 in Al-Fum. Left: Close-up of potential SO_2 binding sites with closest contacts (in Å) between the SO_2 molecule to nearby framework atoms depicted by dashed lines. Right: Cross-sectional model of SO_2 in Al-Fum. See the text for a description of the model.

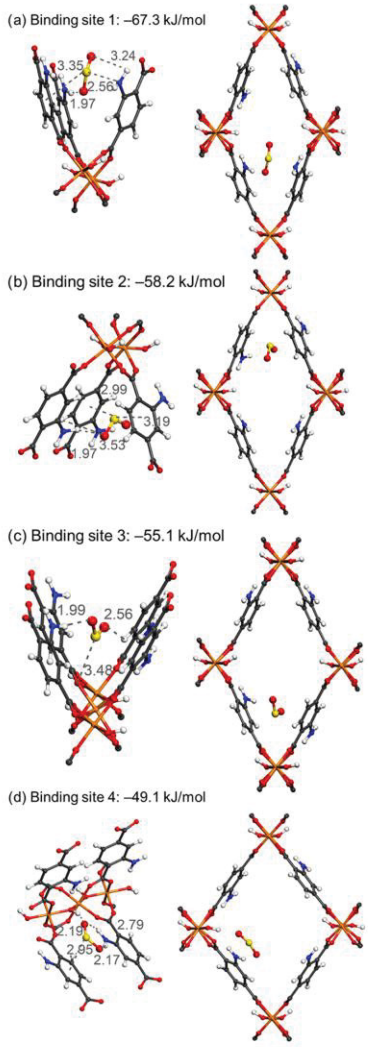

Figure 11. DFT-simulated higher-energy binding sites of SO_2 in NH_2-MIL-53(Al). Left: Close-up of potential SO_2 binding sites with closest contacts in Å between the SO_2 molecule to nearby framework atoms depicted by dashed lines. Right: Cross-sectional model of SO_2 in NH_2-MIL-53(Al). See the text for a description of the model.

It should be noted that the free relaxation of Al-Fum and NH_2-MIL-53(Al) cells for each binding site can give an additional contribution to the binding energy.

Further, we simulated SO_2 adsorption isotherms for Al-Fum in the pressure range of 0.01−1 bar at 293 K (Figure S58) using the GCMC program Cassandra (for computational details, see Section S7.3). The simulations were performed using either a fully relaxed geometry or the fixed cell parameters of the crystal structure data and by setting the Lennard-Jones parameter ε for aluminum either to 254.12 K (100%) or zero, allowing only electrostatic interactions with this atom type. The best agreement with our experimental data was achieved with the fixed geometry and $\varepsilon(\mathrm{Al}) = 0$, which somewhat underestimated the SO_2 adsorption capability or with the approach using the relaxed structure and $\varepsilon(\mathrm{Al}) = 100\%$, which overestimated the SO_2 adsorption capability of Al-Fum.

The simulated isotherm data for Al-Fum was also used to model the pore filling in Al-Fum by a GCMC approach and is displayed in the form of single snapshots related to a defined pressure or as a movie, with a time-lapse over the complete pressure range (Figure S59 and Supporting Movies: SI-Al-Fum-2 kPa and SI-Al-Fum-0.05−100 kPa). Within the snapshots (e.g., at 2 and 3 kPa), it is observed that some pores are empty,

https://doi.org/10.1021/acsami.1c06003
ACS Appl. Mater. Interfaces 2021, 13, 29137−29149

while nearby pores are already filled with multiple SO_2 molecules. This could be an indication of uneven filling of the pores, which might be caused by intermolecular dipole−dipole interactions of the SO_2 adsorptive process. It is recognized that the dipole moment of SO_2 plays an important role in the adsorption process with the pore filling occurring by (framework-)O═S···O═S═O and (framework-)O═S═O···S═O dipole−dipole interactions, forming SO_2 chains or clusters. However, this observation could also be assigned to "artifacts/background noise" of the randomized Monte-Carlo simulations and thus needs further investigations.

■ CONCLUSIONS

Four Zr- and eight Al-MOFs, most of which are frequently investigated prototypical MOFs, were examined for their SO_2 adsorption capability to identify factors that influence the activity of SO_2 separations from CO_2 by MOFs. A strong correlation between the SO_2 uptake and BET-surface area and pore volume, at 1 bar and 293 K, was observed for all materials independent of their pore structure. Especially, MOFs featuring narrow pores with pore diameters between ∼4 and 8 Å yielded high SO_2 affinities.

Also, amino groups at the linker tend to be advantageous for tuning SO_2 affinity. Among all tested MOFs, NH_2-MIL-53(Al), which combines both of the aforementioned properties, showed the highest SO_2 affinity and excellent low-pressure adsorption performance.

The chemical stability of MOFs vs acidic gases such as SO_2 over a prolonged time (10 h) and in the presence of moisture (for 5 h) presents a fundamental problem. Among the selected and proven water-stable Zr- and Al-MOFs, only Zr-Fum and DUT-67(Zr) could be called stable, while the other MOFs showed more or less loss of porosity, especially under the simultaneous presence of SO_2 and H_2O. Interestingly, PXRD patterns were less indicative of framework degradation than losses in surface area (porosity). This suggests that degradation at the pore mouths leads to pore blocking, thereby leaving the inner framework of the MOF crystallites intact, albeit inaccessible.

Theoretical calculations on Zr-Fum, Al-Fum, and NH_2-MIL-53(Al) point also to metal-bridging μ-OH- and NH_2-groups in the SBU or at the linker as an important component of primary binding sites for $-OH^{\delta+}\cdots^{\delta-}OSO$ and $-NH^{\delta+}\cdots^{\delta-}OSO$ hydrogen bonding interactions with binding energies of −50 kJ mol^{-1} and above. At the same time, a low CO_2 affinity is required for trace SO_2 separation from flue gases. Calculated IAST selectivities for the highly SO_2-affine MOFs, Zr-Fum, MOF-808, NH_2-MIL-53(Al), reached values above 40 for SO_2/CO_2 binary gas mixtures and low SO_2 mol fraction of 0.01 (1% or 10.000 ppm SO_2) at 1 bar.

In the end, this work not only gives a compilation of potential MOFs for possible use in adsorptive flue gas desulfurization processes but also offers guidelines to design new adsorbents for this important application.

■ ASSOCIATED CONTENT

Supporting Information

The Supporting Information is available free of charge at https://pubs.acs.org/doi/10.1021/acsami.1c06003.

Synthesis of MOFs; additional MOF structure figures; powder X-ray diffractograms; gas sorption isotherms and measurement details; isotherm fitting and simulation parameters; details on DFT and GCMC calculations and simulations; and comparison of SO_2 sorption literature data (PDF)

SI-Al-Fum-2 kPa (Movie) (MP4)

SI-Al-Fum-0.05−100 kPa (Movie) (MP4)

■ AUTHOR INFORMATION

Corresponding Authors

Oliver Weingart − *Institut für Theoretische Chemie und Computerchemie, Heinrich-Heine-Universität Düsseldorf, 40225 Düsseldorf, Germany*; Email: oliver.weingart@hhu.de

Christoph Janiak − *Institut für Anorganische Chemie und Strukturchemie, Heinrich-Heine-Universität Düsseldorf, 40225 Düsseldorf, Germany; Hoffmann Institute of Advanced Materials, Shenzhen Polytechnic, Shenzhen 518055, China*; orcid.org/0000-0002-6288-9605; Email: janiak@hhu.de

Authors

Philipp Brandt − *Institut für Anorganische Chemie und Strukturchemie, Heinrich-Heine-Universität Düsseldorf, 40225 Düsseldorf, Germany*

Shang-Hua Xing − *Institut für Anorganische Chemie und Strukturchemie, Heinrich-Heine-Universität Düsseldorf, 40225 Düsseldorf, Germany; Hoffmann Institute of Advanced Materials, Shenzhen Polytechnic, Shenzhen 518055, China*

Jun Liang − *Institut für Anorganische Chemie und Strukturchemie, Heinrich-Heine-Universität Düsseldorf, 40225 Düsseldorf, Germany; Hoffmann Institute of Advanced Materials, Shenzhen Polytechnic, Shenzhen 518055, China*

Gülin Kurt − *Institut für Anorganische Chemie und Strukturchemie, Heinrich-Heine-Universität Düsseldorf, 40225 Düsseldorf, Germany*

Alexander Nuhnen − *Institut für Anorganische Chemie und Strukturchemie, Heinrich-Heine-Universität Düsseldorf, 40225 Düsseldorf, Germany*

Complete contact information is available at: https://pubs.acs.org/10.1021/acsami.1c06003

Notes

The authors declare no competing financial interest.

■ ACKNOWLEDGMENTS

The authors thank Dr. István Boldog for constructive discussions and his overall support. This work was supported by the Deutsche Forschungsgemeinschaft (DFG)—396890929/GRK 2482.

■ REFERENCES

(1) Várhelyi, G. Continental and Global Sulfur Budgets-I. Anthropogenic SO_2 Emissions. *Atmos. Environ.* **1985**, *19*, 1029−1049.

(2) International Energy Agency. *World Energy Outlook 2019*; OECD Publishing: Paris, 2019.

(3) Likens, G. E.; Driscoll, C. T.; Buso, D. C. Long-Term Effects of Acid Rain: Response and Recovery of a Forest Ecosystem. *Science* **1996**, *272*, 244−246.

(4) Gregory, K.; Webster, C.; Durk, S. Estimates of Damage to Forests in Europe due to Emissions of Acidifying Pollutants. *Energy Policy* **1996**, *24*, 655−664.

(5) Reiss, R.; Anderson, E. L.; Cross, C. E.; Hidy, G.; Hoel, D.; McClellan, R.; Moolgavkar, S. Evidence of health impacts of sulfate-and nitrate-containing particles in ambient air. *Inhalation Toxicol.* **2007**, *19*, 419−449.

(6) Srivastava, R. K.; Jozewicz, W. Flue Gas Desulfurization: The State of the Art. *J. Air Waste Manage. Assoc.* **2001**, *51*, 1676−1688.

(7) Rao, A. B.; Rubin, E. S. A Technical, Economic, and Environmental Assessment of Amine-Based CO_2 Capture Technology for Power Plant Greenhouse Gas Control. *Environ. Sci. Technol.* **2002**, *36*, 4467−4475.
(8) Ding, S.; Liu, F.; Shi, X.; Liu, K.; Lian, Z.; Xie, L.; He, H. Significant Promotion Effect of Mo Additive on a Novel Ce−Zr Mixed Oxide Catalyst for the Selective Catalytic Reduction of NO_x with NH_3. *ACS Appl. Mater. Interfaces* **2015**, *7*, 9497−9506.
(9) Goo, J. H.; Irfan, M. F.; Kim, S. D.; Hong, S. C. Effects of NO_2 and SO_2 on Selective Catalytic Reduction of Nitrogen Oxides by Ammonia. *Chemosphere* **2007**, *67*, 718−723.
(10) Kohl, A. L.; Nielsen, R. *Gas Purification*; Gulf Professional: Houston, TX, 1997.
(11) Hanif, M. A.; Ibrahim, N.; Abdul Jalil, A. Sulfur Dioxide Removal: An Overview of Regenerative Flue Gas Desulfurization and Factors affecting Desulfurization Capacity and Sorbent Regeneration. *Environ. Sci. Pollut. Res.* **2020**, *27*, 27515−27540.
(12) Evans, J. D.; Garai, B.; Reinsch, H.; Li, W.; Dissegna, S.; Bon, V.; Senkovska, I.; Fischer, R. A.; Kaskel, S.; Janiak, C.; Stock, N.; Volkmer, D. Metal−organic frameworks in Germany: From synthesis to function. *Coord. Chem. Rev.* **2019**, *380*, 378−418.
(13) Suh, M. P.; Park, H. J.; Prasad, T. K.; Lim, D. W. Hydrogen Storage in Metal Organic Frameworks. *Chem. Rev.* **2012**, *112*, 782−835.
(14) Sumida, K.; Rogow, D. L.; Mason, J. A.; McDonald, T. M.; Bloch, E. D.; Herm, Z. R.; Bae, T.-H.; Long, J. R. Carbon Dioxide Capture in Metal-Organic Frameworks. *Chem. Rev.* **2012**, *112*, 724−781.
(15) He, Y.; Zhou, W.; Qian, G.; Chen, B. Methane Storage in Metal-Organic Frameworks. *Chem. Soc. Rev.* **2014**, *43*, 5657−5678.
(16) Britt, D.; Tranchemontagne, D.; Yaghi, O. M. Metal-Organic Frameworks with High Capacity and Selectivity for Harmful Gases. *Proc. Natl. Acad. Sci. U.S.A.* **2008**, *105*, 11623−11627.
(17) Bobbitt, N. S.; Mendonca, M. L.; Howarth, A. J.; Islamoglu, T.; Hupp, J. T.; Farha, O. K.; Snurr, R. Q. Metal-Organic Frameworks for the Removal of Toxic Industrial Chemicals and Chemical Warfare Agents. *Chem. Soc. Rev.* **2017**, *46*, 3357−3385.
(18) Wang, H.; Lustig, W. P.; Li, J. Sensing and Capture of Toxic and Hazardous Gases and Vapors by Metal-Organic Frameworks. *Chem. Soc. Rev.* **2018**, *47*, 4729−4756.
(19) Han, X.; Yang, S.; Schröder, M. Porous Metal-Organic Frameworks as Emerging Sorbents for Clean Air. *Nat. Rev. Chem.* **2019**, *3*, 108−118.
(20) Jurado-Vázquez, T.; Sánchez-González, E.; Campos-Reales-Pineda, A. E.; Islas-Jácome, A.; Lima, E.; González-Zamora, E.; Ibarra, I. A. MFM-300: From Air Pollution Remediation to Toxic Gas Detection. *Polyhedron* **2019**, *157*, 495−504.
(21) Martínez-Ahumada, E.; López-Olvera, A.; Jancik, V.; Sánchez-Bautista, J. E.; González-Zamora, E.; Martis, V.; Williams, D. R.; Ibarra, I. A. MOF Materials for the Capture of Highly Toxic H_2S and SO_2. *Organometallics* **2020**, *39*, 883−915.
(22) Islamoglu, T.; Chen, Z.; Wasson, M. C.; Buru, C. T.; Kirlikovali, K. O.; Afrin, U.; Mian, M. R.; Farha, O. K. Metal-Organic Frameworks against Toxic Chemicals. *Chem. Rev.* **2020**, *120*, 8130−8160.
(23) Fernandez, C. A.; Thallapally, P. K.; Motkuri, R. K.; Nune, S. K.; Sumrak, J. C.; Tian, J.; Liu, J. Gas-Induced Expansion and Contraction of a Fluorinated Metal−Organic Framework. *Cryst. Growth Des.* **2010**, *10*, 1037−1039.
(24) Thallapally, P. K.; Motkuri, R. K.; Fernandez, C. A.; McGrail, B. P.; Behrooz, G. S. Prussian Blue Analogues for CO_2 and SO_2 Capture and Separation Applications. *Inorg. Chem.* **2010**, *49*, 4909−4915.
(25) Glover, T. G.; Peterson, G. W.; Schindler, B. J.; Britt, D.; Yaghi, O. MOF-74 Building Unit has a Direct Impact on Toxic Gas Adsorption. *Chem. Eng. Sci.* **2011**, *66*, 163−170.
(26) Tan, K.; Canepa, P.; Gong, Q.; Liu, J.; Johnson, D. H.; Dyevoich, A.; Thallapally, P. K.; Thonhauser, T.; Li, J.; Chabal, Y. J. Mechanism of Preferential Adsorption of SO_2 into Two Microporous Paddle Wheel Frameworks $M(bdc)(ted)_{0.5}$. *Chem. Mater.* **2013**, *25*, 4653−4662.
(27) Tchalala, M. R.; Bhatt, P. M.; Chappanda, K. N.; Tavares, S. R.; Adil, K.; Belmabkhout, Y.; Shkurenko, A.; Cadiau, A.; Heymans, N.; Weireld, G.; Maurin, G.; Salama, K. N.; Eddaoudi, M. Fluorinated MOF Platform for Selective Removal and Sensing of SO_2 from Flue Gas and Air. *Nat. Commun.* **2019**, *10*, No. 1328.
(28) Zárate, J. A.; Sánchez-González, E.; Williams, D. R.; González-Zamora, E.; Martis, V.; Martínez, A.; Balmaseda, J.; Maurin, G.; Ibarra, I. A. High and Energy-Efficient Reversible SO_2 Uptake by a Robust Sc(III)-Based MOF. *J. Mater. Chem. A* **2019**, *7*, 15580−15584.
(29) Domínguez-González, R.; Rojas-León, I.; Martínez-Ahumada, E.; Martínez-Otero, D.; Lara-García, H. A.; Balmaseda-Era, J.; Ibarra, I. A.; Percástegui, E. G.; Jancik, V. UNAM-1: A Robust Cu I and Cu II Containing 3D-hydrogen-Bonded Framework with Permanent Porosity and Reversible SO_2 Sorption. *J. Mater. Chem. A* **2019**, *7*, 26812−26817.
(30) Zhang, Y.; Zhang, P.; Yu, W.; Zhang, J.; Huang, J.; Wang, J.; Xu, M.; Deng, Q.; Zeng, Z.; Deng, S. Highly Selective and Reversible Sulfur Dioxide Adsorption on a Microporous Metal-Organic Framework via Polar Sites. *ACS Appl. Mater. Interfaces* **2019**, *11*, 10680−10688.
(31) Walton, I.; Chen, C.; Rimsza, J. M.; Nenoff, T. M.; Walton, K. S. Enhanced Sulfur Dioxide Adsorption in UiO-66 Through Crystal Engineering and Chalcogen Bonding. *Cryst. Growth Des.* **2020**, *20*, 6139−6146.
(32) Chen, Z.; Wang, X.; Cao, R.; Idrees, K. B.; Liu, X.; Wasson, M. C.; Farha, O. K. Water-Based Synthesis of a Stable Iron-Based Metal−Organic Framework for Capturing Toxic Gases. *ACS Mater. Lett.* **2020**, *2*, 1129−1134.
(33) Yang, S.; Sun, J.; Ramirez-Cuesta, A. J.; Callear, S. K.; David, W. I. F.; Anderson, D. P.; Newby, R.; Blake, A. J.; Parker, J. E.; Tang, C. C.; Schröder, M. Selectivity and Direct Visualization of Carbon Dioxide and Sulfur Dioxide in a Decorated Porous Host. *Nat. Chem.* **2012**, *4*, 887−894.
(34) Carter, J.; Morris, C.; Godfrey, H. G. W.; Day, S. J.; Potter, J.; Thompson, S. P.; Tang, C.; Yang, S.; Schröder, M. Long-Term Stability of MFM-300(Al) Towards Toxic Air Pollutants. *ACS Appl. Mater. Interfaces* **2020**, *12*, 42949−42954.
(35) Carter, J. H.; Han, X.; Moreau, F. Y.; da Silva, I.; Nevin, A.; Godfrey, H. G. W.; Tang, C. C.; Yang, S.; Schröder, M. Exceptional Adsorption and Binding of Sulfur Dioxide in a Robust Zirconium-Based Metal-Organic Framework. *J. Am. Chem. Soc.* **2018**, *140*, 15564−15567.
(36) Brandt, P.; Nuhnen, A.; Lange, M.; Möllmer, J.; Weingart, O.; Janiak, C. Metal−Organic Frameworks with Potential Application for SO_2 Separation and Flue Gas Desulfurization. *ACS Appl. Mater. Interfaces* **2019**, *11*, 17350−17358.
(37) Brandt, P.; Nuhnen, A.; Öztürk, S.; Kurt, G.; Liang, J.; Janiak, C. Comparative Evaluation of Different MOF and Non-MOF Porous Materials for SO_2 Adsorption and Separation Showing the Importance of Small Pore Diameters for Low-Pressure Uptake. *Adv. Sustainable Syst.* **2021**, *5*, No. 2000285.
(38) Low, J. J.; Benin, A. I.; Jakubczak, P.; Abrahamian, J. F.; Faheem, S. A.; Willis, R. R. Virtual high throughput screening confirmed experimentally: porous coordination polymer hydration. *J. Am. Chem. Soc.* **2009**, *131*, 15834−15842.
(39) Sun, Y.; Spieß, A.; Jansen, C.; Nuhnen, A.; Gökpinar, S.; Wiedey, R.; Ernst, S.-J.; Janiak, C. Tunable LiCl@UiO-66 composites for water sorption-based heat transformation applications. *J. Mater. Chem. A* **2020**, *8*, 13364−13375.
(40) Burtch, N. C.; Jasuja, H.; Walton, K. S. Water Stability and Adsorption in Metal-Organic Frameworks. *Chem. Rev.* **2014**, *114*, 10575−10612.
(41) Ding, M.; Cai, X.; Jiang, H.-L. Improving MOF Stability: Approaches and Applications. *Chem. Sci.* **2019**, *10*, 10209−10230.
(42) Furukawa, H.; Gándara, F.; Zhang, Y.-B.; Jiang, J.; Queen, W. L.; Hudson, M. R.; Yaghi, O. M. Water Adsorption in Porous Metal-Organic Frameworks and Related Materials. *J. Am. Chem. Soc.* **2014**, *136*, 4369−4381.
(43) Islamoglu, T.; Otake, K.-i.; Li, P.; Buru, C. T.; Peters, A. W.; Akpinar, I.; Garibay, S. J.; Farha, O. K. Revisiting the Structural Homogeneity of NU-1000, a Zr-Based Metal−Organic Framework. *CrystEngComm* **2018**, *20*, 5913−5918.
(44) Loiseau, T.; Serre, C.; Huguenard, C.; Fink, G.; Taulelle, F.; Henry, M.; Bataille, T.; Férey, G. A Rationale for the Large Breathing of

the Porous Aluminum Terephthalate (MIL-53) Upon Hydration. *Chem. – Eur. J.* **2004**, *10*, 1373−1382.
(45) Gascon, J.; Aktay, U.; Hernandezalonso, M.; Vanklink, G.; Kapteijn, F. Amino-Based Metal-Organic Frameworks as Stable, Highly Active Basic Catalysts. *J. Catal.* **2009**, *261*, 75−87.
(46) Alvarez, E.; Guillou, N.; Martineau, C.; Bueken, B.; Van de Voorde, B.; Le Guillouzer, C.; Fabry, P.; Nouar, F.; Taulelle, F.; de Vos, D.; Chang, J. S.; Cho, K. H.; Ramsahey, N.; Devic, T.; Daturi, M.; Maurin, G.; Serre, C. The Structure of the Aluminum Fumarate Metal-Organic Framework A520. *Angew. Chem.* **2015**, *127*, 3735−3739.
(47) Tschense, C. B. L.; Reimer, N.; Hsu, C.-W.; Reinsch, H.; Siegel, R.; Chen, W.-J.; Lin, C.-H.; Cadiau, A.; Serre, C.; Senker, J.; Stock, N. New Group 13 MIL-53 Derivates based on 2,5-Thiophenedicarboxylic Acid. *Z. Anorg. Allg. Chem.* **2017**, *643*, 1600−1608.
(48) Teo, H. W. B.; Chakraborty, A. Water Adsorption on Various Metal Organic Frameworks. *IOP Conf. Ser.: Mater. Sci. Eng.* **2017**, *272*, No. 012019.
(49) Benzaqui, M.; Pillai, R. S.; Sabetghadam, A.; Benoit, V.; Normand, P.; Marrot, J.; Menguy, N.; Montero, D.; Shepard, W.; Tissot, A.; Martineau-Corcos, C.; Sicard, C.; Mihaylov, M.; Carn, F.; Beurroies, I.; Llewellyn, P. L.; De Weireld, G.; Hadjiivanov, K.; Gascon, J.; Kapteijn, F.; Maurin, G.; Stenou, N.; Serre, C. Revisiting the Aluminum Trimesate-Based MOF (MIL-96): From Structure Determination to the Processing of Mixed Matrix Membranes for CO_2 Capture. *Chem. Mater.* **2017**, *29*, 10326−10338.
(50) Jeremias, F.; Khutia, A.; Henninger, S. K.; Janiak, C. MIL-100(Al, Fe) as water adsorbents for heat transformation purposes—a promising application. *J. Mater. Chem.* **2012**, *22*, 10148−10151.
(51) Navarro-Sánchez, J.; Almora-Barrios, N.; Lerma-Berlanga, B.; Ruiz-Pernía, J. J.; Lorenz-Fonfria, V. A.; Tuñón, I.; Martí-Gastaldo, C. Translocation of Enzymes into a Mesoporous MOF for Enhanced Catalytic Activity under Extreme Conditions. *Chem. Sci.* **2019**, *10*, 4082−4088.
(52) Gorla, S.; Díaz-Ramírez, M. L.; Abeynayake, N. S.; Kaphan, D. M.; Williams, D. R.; Martis, V.; Lara-García, H. A.; Donnadieu, B.; Lopez, N.; Ibarra, I. A.; Montiel-Palma, V. Functionalized NU-1000 with an Iridium Organometallic Fragment: SO_2 Capture Enhancement. *ACS Appl. Mater. Interfaces* **2020**, *12*, 41758−41764.
(53) Mouchaham, G.; Wang, S.; Serre, C. The Stability of Metal-Organic Frameworks. In *Metal-Organic Frameworks: Applications in Separations and Catalysis*; García, H.; Navalon, S., Eds.; Wiley-VCH: Weinheim, 2018.
(54) Alhamami, M.; Doan, H.; Cheng, C.-H. A Review on Breathing Behaviors of Metal-Organic-Frameworks (MOFs) for Gas Adsorption. *Materials* **2014**, *7*, 3198−3250.
(55) Loiseau, T.; Lecroq, L.; Volkringer, C.; Marrot, J.; Férey, G.; Haouas, M.; Taulelle, F.; Bourrelly, S.; Llewellyn, P. L.; Latroche, M. MIL-96, a Porous Aluminum Trimesate 3D Structure Constructed from a Hexagonal Network of 18-Membered Rings and μ_3-Oxo-Centered Trinuclear Units. *J. Am. Chem. Soc.* **2006**, *128*, 10223−10230.
(56) Li, J.; Zhou, Z.; Han, X.; Zhang, X.; Yan, Y.; Li, W.; Smith, G. L.; Cheng, Y.; McCormick McPherson, L. J.; Teat, S. J.; Frogley, M. D.; Rudić, S.; Ramirez-Cuesta, A. J.; Blake, A. J.; Sun, J.; Schröder, M.; Yang, S. Guest-Controlled Incommensurate Modulation in a Meta-Rigid Metal-Organic Framework Material. *J. Am. Chem. Soc.* **2020**, *142*, 19189−19197.
(57) Thommes, M.; Kaneko, K.; Neimark, A. V.; Olivier, J. P.; Rodríguez-Reinoso, F.; Rouquerol, J.; Sing, K. S. W. Physisorption of gases, with special reference to the evaluation of surface area and pore size distribution (IUPAC Technical Report). *Pure Appl. Chem.* **2015**, *87*, 1051−1069.
(58) Zárate, J. A.; Domínguez-Ojeda, E.; Sánchez-González, E.; Martínez-Ahumada, E.; López-Cervantes, V. B.; Williams, D. R.; Martis, V.; Ibarra, I. A.; Alejandre, J. Reversible and Efficient SO_2 Capture by a Chemically stable MOF CAU-10: Experiments and Simulations. *Dalton Trans.* **2020**, *49*, 9203−9207.
(59) Mounfield, W. P.; Han, C.; Pang, S. H.; Tumuluri, U.; Jiao, Y.; Bhattacharyya, S.; Dutzer, M. R.; Nair, S.; Wu, Z.; Lively, R. P.; Sholl, D. S.; Walton, S. W. Synergistic Effects of Water and SO_2 on Degradation of MIL-125 in the Presence of Acid Gases. *J. Phys. Chem. C* **2016**, *120*, 27230−27240.
(60) Li, Z.; Liao, F.; Jiang, F.; Liu, B.; Ban, S.; Chen, G.; Sun, C.; Xiao, P.; Sun, Y. Capture of H_2S and SO_2 from trace sulfur containing gas mixture by functionalized UiO-66(Zr) materials: A molecular simulation study. *Fluid Phase Equilib.* **2016**, *427*, 259−267.
(61) Zhang, Z.; Yang, B.; Ma, H. Aliphatic amine decorating metal−organic framework for durable SO_2 capture from flue gas. *Sep. Purif. Technol.* **2021**, *259*, No. 118164.
(62) Martínez-Ahumada, E.; Díaz-Ramírez, M. L.; Lara-García, H. A.; Williams, D. R.; Martis, V.; Jancik, V.; Lima, E.; Ibarra, I. A. High and Reversible SO_2 Capture by a Chemically Stable Cr(III)-Based MOF. *J. Mater. Chem. A* **2020**, *8*, 11515−11520.
(63) Liu, J.-X.; Li, J.; Tao, W.-Q.; Li, Z. 3. Al-Based Metal-Organic Framework MFM-300 and MIL-160 for SO_2 Capture: A Molecular Simulation Study. *Fluid Phase Equilib.* **2021**, *536*, No. 112963.
(64) Carter, J. H.; Han, X.; Moreau, F. Y.; da Silva, I.; Nevin, A.; Godfrey, H. G. W.; Tang, C. C.; Yang, S.; Schröder, M. Exceptional Adsorption and Binding of Sulfur Dioxide in a Robust Zirconium-Based Metal−Organic Framework. *J. Am. Chem. Soc.* **2018**, *140*, 15564−15567.
(65) Li, J.-R.; Kuppler, R. J.; Zhou, H.-C. Selective Gas Adsorption and Separation in Metal-Organic Frameworks. *Chem. Soc. Rev.* **2009**, *38*, 1477−1504.
(66) Song, X.-D.; Wang, S.; Hao, C.; Qiu, J.-S. Investigation of SO_2 Gas Adsorption in Metal−Organic Frameworks by Molecular Simulation. *Inorg. Chem. Commun.* **2014**, *46*, 277−281.
(67) Lowell, S.; Shields, J. E.; Thomas, M. A.; Thommes, M. Adsorption Isotherms. In *Characterization of Porous Solids and Powders: Surface Area, Pore Size and Density*; Springer International Publishing: Cham, 2004; pp 11−14.
(68) Cessford, N. F.; Seaton, N. A.; Düren, T. Evaluation of Ideal Adsorbed Solution Theory as a Tool for the Design of Metal-Organic Framework Materials. *Ind. Eng. Chem. Res.* **2012**, *51*, 4911−4921.
(69) Bon, V.; Senkovska, I.; Evans, J. D.; Wöllner, M.; Hölzel, M.; Kaskel, S. Insights into the Water Adsorption Mechanism in the Chemically Stable Zirconium-Based MOF DUT-67 − a Prospective Material for Adsorption-Driven Heat Transformations. *J. Mater. Chem. A* **2019**, *7*, 12681−12690.
(70) Desiraju, G. R.; Steiner, T. The Weak Hydrogen Bond. In *IUCr Monograph on Crystallography*; Oxford Science: Oxford, 1999; Vol. 9.

https://doi.org/10.1021/acsami.1c06003
ACS Appl. Mater. Interfaces 2021, 13, 29137−29149

Supporting Information

Zirconium and Aluminum MOFs for Low-Pressure SO_2 Adsorption and Potential Separation: Elucidating the Effect of Small Pores and NH_2-Groups

Philipp Brandt,[†] Shang-Hua Xing,[†,‖] Jun Liang,[†,‖], Gülin Kurt,[†] Alexander Nuhnen,[†] Oliver Weingart,[*,§] Christoph Janiak[*,†,‖]

[†] Institut für Anorganische Chemie und Strukturchemie, Heinrich-Heine-Universität Düsseldorf, Universitätsstraße 1, 40225 Düsseldorf, Germany

[‖] Hoffmann Institute of Advanced Materials, Shenzhen Polytechnic, 7098 Liuxian Blvd, Nanshan District, Shenzhen, China

[§] Institut für Theoretische Chemie und Computerchemie, Heinrich-Heine-Universität Düsseldorf, Universitätsstraße 1, 40225 Düsseldorf, Germany

Email addresses: p.brandt@hhu.de; shanghua.xing@hhu.de; liangj956@nenu.edu.cn; guelin.kurt@hhu.de; alexander.nuhnen@hhu.de; ; oliver.weingart@hhu.de; janiak@hhu.de

Content

S1 MOF Syntheses

Materials: All reagents were commercially purchased and used without any further purification. Examined materials were synthesized according to the literature (Table S1) or were commercially purchased. Examined Materials were synthesized according to the literature (Table S1).

Table S1. Synthesis references of prepared MOF materials and activation conditions.

Material	Synthesis	Purchased	Activation conditions
Zr-Fum	Behrens *et al.*[1]	-	12 h; 120 °C
MOF-808	Hwang *et al.*[2]	-	12 h; 120 °C
DUT-67(Zr)	Stock *et al.*[3]	-	12 h; 150 °C
NU-1000	Farha *et al.*[4]	-	12 h; 120 °C
MIL-53(Al)	Kim *et al.*[5]	-	12 h; 180 °C
NH_2-MIL-53(Al)	Guo *et al.*[6]	-	12 h; 150 °C
Al-Fum	-	Sigma-Aldrich	12 h; 120 °C
MIL-53(Al)(tdc)	Janiak *et al.*[7]	-	12 h; 150 °C
CAU-10-H	Stock *et al.*[8]	-	12 h; 180 °C
MIL-96(Al)	Latroche *et al.*[9]	-	12 h; 150 °C
MIL-100(Al)	Li *et al.*[10]	-	12 h; 120 °C
NH_2-MIL-101(Al)	Kapteijin *et al.*[11]	-	12 h; 150 °C

S1.1 Literature-based MOF Syntheses

Zirconium-fumarate (Zr-Fum) was synthesized according to the literature.[1] $ZrCl_4$ (0.517 mmol, 0.1204 g, 1 eq) and fumaric acid (1.550 mmol, 3 eq) were dissolved in 20 mL of N,N-dimethylformamide (DMF) in a 100 mL Schott glass bottle. Formic acid (15.5 mmol, 0.585 mL, 30 eq) was added as a modulator. The glass bottle was Teflon-capped and heated in an oven at 120 °C for 24 h. The resulting white precipitate was washed with 10 mL of DMF and 2 x 10 mL of ethanol, respectively. The washing process in ethanol was carried out under stirring and heating at 70 °C for 1 h. The white precipitate was centrifuged off and dried at room temperature overnight.

MOF-808 was synthesized according to the literature.[2] $ZrOCl_2 \cdot 8H_2O$ (1.57 mmol, 0.506 g) and trimesic acid (1,3,5-H_3btc) (1,58 mmol, 0.331 g) were dissolved in a mixture of 27 mL of DMF and 30 mL of formic acid. The reaction mixture was placed in an 80 mL Teflon-lined stainless-steel autoclave and heated in an oven at 135 °C for 48 h. The resulting white precipitate was centrifuged off and washed with 40 mL of DMF and 45 mL of ethanol for 24 h, respectively. The respective solvents were exchanged twice during the washing procedure. The precipitate was collected by centrifugation and dried in an oven at 80 °C overnight.

DUT-67(Zr) was synthesized according to the literature.[3] $ZrOCl_2 \cdot 8H_2O$ (4.00 mmol, 1.289 g and 2,5-thiophenedicarboxylic acid (2,5-H_2-tdc) (2.66 mmol, 0.459 g) were dissolved in 10 mL of water and 10 mL of acetic acid in a 35 mL microwave tube. The resulting mixture was heated in a microwave oven at 95 °C for 1 h. The white precipitate was collected by centrifugation and washed with 2 x 15 mL of an aqueous sodium acetate solution (0.1 mol/L) and 15 mL of water, respectively. Finally, the precipitate was dried in an oven at 95 °C overnight.

NU-1000 was synthesized according to the literature.[4] $ZrOCl_2 \cdot 8H_2O$ (15.1 mmol, 4.85 g) and benzoic acid (1.1 mol, 135 g) were added in a 1 L Pyrex-bottle and dissolved under sonication in 300 mL of DMF. The reaction mixture was heated in an oven at 100 °C for 1 h. In the meantime, in a 500 mL Pyrex-bottle the ligand 4,4',4",4'"-(pyrene-1,3,6,8-tetrayl)tetrabenzoic acid (H_4TBAPy) (2.9 mmol, 2.0g) was dissolved in 100 mL of DMF under sonication and heated in an oven at 100 °C for 1 h. Then the H_4TBAPy solution was poured in the 1 L bottle containing the zirconium precursor. The two solutions were well mixed and placed in an oven at 120 °C for 16 h resulting in a yellow precipitate. After cooling to room temperature, the mother solution was centrifuged off in 6 x 50 mL centrifugation tubes. The precipitate was soaked in fresh DMF (45 mL each) for 2 h and then centrifuged off. This procedure was repeated two times. The precipitate was transferred in a 1 L Pyrex-bottle and 650 mL of DMF and 25 mL of an 8 mol/L HCl aqueous solution were added and mixed accurately. The mixture was heated in an oven at 100 °C for 16 h. After cooling to room temperature, the mother solution was centrifuged off in 6 x 50 mL centrifugation tubes. The precipitate was soaked in fresh DMF (45 mL each) for 2 h and then centrifuged off. Then the precipitate was soaked in fresh acetone (45 mL each) for 12 h during that time the acetone was replaced two times. After the final separation of solid and solution, the solid was dried in a vacuum oven at 80 °C for 12 h.

NH_2-MIL-53(Al) was synthesized according to the literature.[6] $AlCl_3 \cdot 6H_2O$ (1.584 mmol, 0.3824 g) and 2-aminoterephthalic acid (1.551 mmol, 0.2809 g) are dissolved in 14.5 mL of DMF and 0.5 mL water. The solution was placed in a Teflon-lined stainless-steel autoclave and heated in an oven at 150 °C for 24 h. The precipitate was separated from the mother solution by centrifugation and then soaked in 20 mL fresh DMF and heated in an oven at 150 °C for 24 h. This procedure was repeated one time. Then the precipitate was washed with 30 mL acetone and centrifuged off. This procedure was repeated two times. After final centrifugation, the precipitate was dried in air for three days.

MIL-53(tdc)(Al) was synthesized according to the literature.[7] $Al_2(SO_4)_3 \cdot 18\ H_2O$ (3.58 mmol, 2.386 g and 2,5-thiophenedicarboxylic acid (2,5-H_2-tdc) (3.14 mmol, 0.540g) are dissolved in a mixture of H_2O and DMF (4:1, 20.1 mL: 5.02 mL) in a 50 mL round bottom flask. The mixture was heated under reflux at 135 °C for 24 h. The resulting white precipitate was separated from the mother solution by centrifugation and redispersed in 40 mL of water. This procedure was repeated two times. A fourth washing step was applied by re-dispersing the precipitate in 40 mL of water which then was heated under reflux for 3 h. After final centrifugation, the precipitate was dried in a vacuum oven at 60 °C for 24 h.

CAU-10-H was synthesized according to the literature.[8] $Al_2(SO_4)_3 \cdot 18H_2O$ (1.20 mmol, 0.800 g) and isophthalic acid (1,3-H_2-bdc) (1.20 mmol, 0.200 g) are mixed in 1 mL of DMF and 4 mL of water. This mixture was placed in a 50 mL Teflon-lined steel autoclave and heated in an oven at 135 °C for 12 h. After cooling to room temperature, the resulting white precipitate was collected by centrifugation. Then the solid was re-dispersed in 20 mL of water and stirred for 5 h. After centrifugation, the solid was dried in air overnight.

MIL-96(Al) was synthesized according to the literature.[9] $Al(NO_3)_3 \cdot 9H_2O$ (3.508 mmol, 1.316 g) and trimesic acid (1,3,5-H_2-btc) are dissolved in 5 mL of water. The solution (pH = 1) was placed in a 10 mL Teflon-lined steel autoclave. The autoclave was sealed and heated in an oven at 210 °C for 24 h. After cooling to room temperature, the white precipitate was recovered by centrifugation and washed with 2 x 20 mL of water. After the final centrifugation, the precipitate was dried in air overnight.

MIL-100(Al) was synthesized according to the literature.[10] $Al(NO_3)_3 \cdot 9H_2O$ (3.543 mmol, 1.329 g) and trimesic acid (1,3,5-H_2-btc) (2.93 mmol, 0.616 g) and SAPO-34 (2.40 mmol, 0.142 g) were dissolved in 20 mL of water in a 35 mL quartz vessel. The vessel was sealed and heated in a microwave oven at 190 °C (150 W and an autogenic pressure of 20 bar) for 10 min. After cooling to room temperature, the resulting white precipitate was collected by centrifugation. Then the solid was washed and centrifuged with 3 x 40 mL of DMF and 3 x 40 mL of ethanol, respectively. Finally, the precipitate was dried in a vacuum oven at 60 °C for 3 days.

NH_2-MIL-101(Al) was synthesized according to the literature.[11] $AlCl_3 \cdot 6H_2O$ (2.222 mmol, 0.510 g) and 2-aminoterephthalic acid (3.093 mmol, 0.560 g) were dissolved in 25 mL of DMF and placed in a 50 mL Teflon-lined steel autoclave. After sealing, the autoclave was heated in an oven at 130 °C for 72 h. After cooling to room temperature, the resulting yellow precipitate was separated from the mother solution by centrifugation and then washed with 3 x 30 mL of acetone. Then the solid was again recovered by centrifugation and re-dispersed and refluxed in 50 mL of methanol for 20 h. After the final centrifugation, the precipitate was dried in a vacuum oven at 100 °C.

S1.2 Modified or Alternative Synthesis

MIL-53(Al) was synthesized with modification to the literature.[5] $AlCl_3 \cdot 6H_2O$ (0.67 mmol, 163 mg) and 1,4-benzenedicarboxylic acid (0.99 mmol, 165 mg) are dissolved in 9.58 mL of DMF and left standing for 24 h. The mixture was transferred in a 100 mL Teflon-lined steel autoclave and heated in an oven at 180 °C for 72 h yielding a white powder. The precipitate was separated from the mother solution by centrifugation and then soaked in 10 mL of fresh DMF and heated in an oven at 110 °C for 24 h. This procedure was repeated one time. After final centrifugation, the precipitate was dried in a vacuum oven at 100 °C for 24 h.

S2 MOF structures

The following sections of the framework structures were drawn with the program Diamond [12] based on the noted Cambridge crystallographic data center (CCDC) cif-files from the Cambridge Structure Database. A distinct pore cavity is depicted by a sphere and its diameter given. For a channel-type cavity the dimensions of the cross-section are given. The given distances take the van der Waals surface of the adsorbent into account.

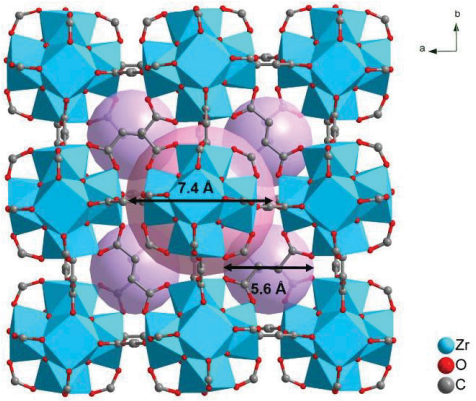

Figure S1. Section of the framework structure and pore size of Zr-Fum (CCDC 1002678).[13]

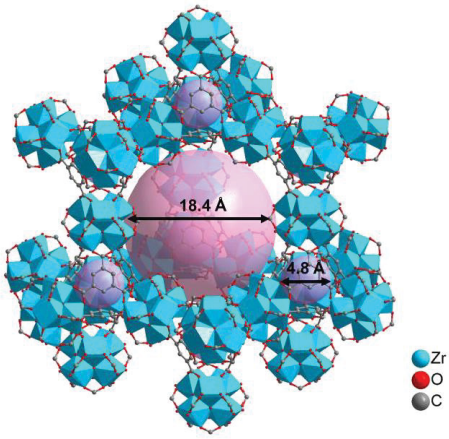

Figure S2. Section of the framework structure and pore size of MOF-808 (CCDC 1002672).[13]

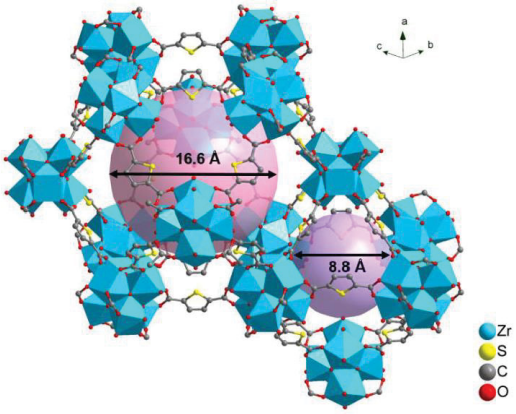

Figure S3. Section of the framework structure and pore size of DUT-67(Zr) (CCDC 902898).[14]

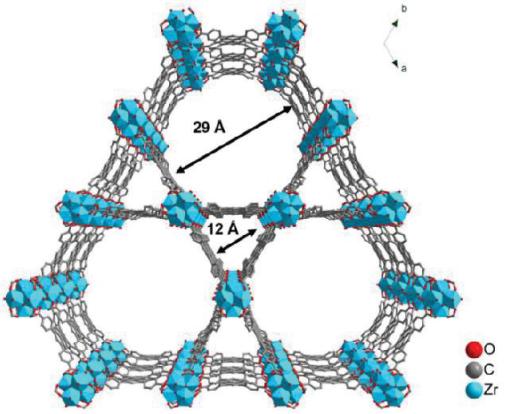

Figure S4. Section of the framework structure and pore size of NU-1000 (CCDC 955328)[15]

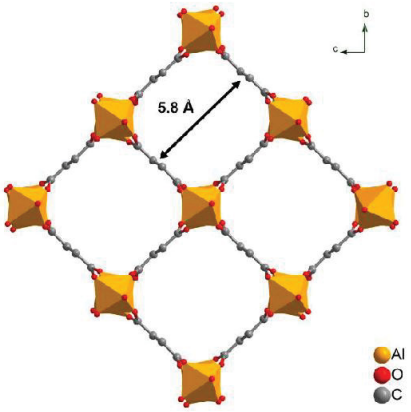

Figure S5. Section of the framework structure and pore size of Al-Fum (CCDC 1051975)[16] and isostructureal MIL-53(Al), NH_2-MIL-53(Al) and MIL-53(tdc)(Al).

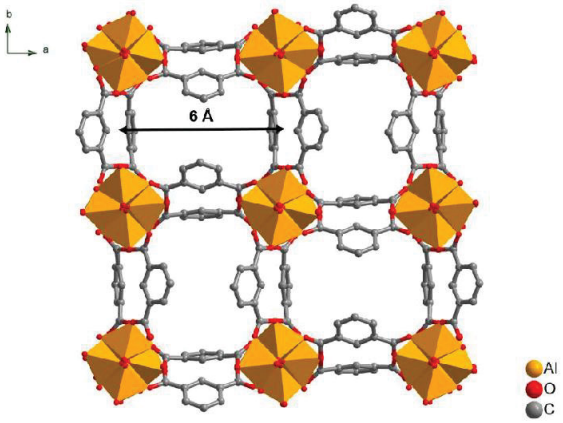

Figure S6. Section of the framework structure and pore size of CAU-10-H (CCDC 1454066).[17]

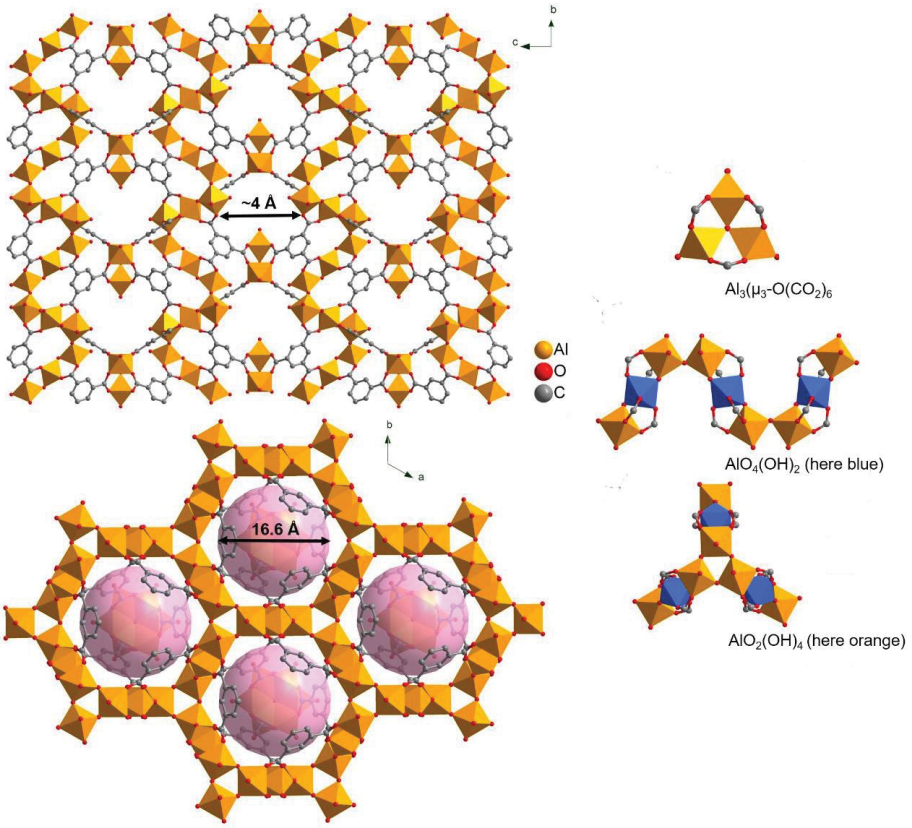

Figure S7. Section of the framework structure and pore size of MIL-96(Al) (CCDC 622598)[9]

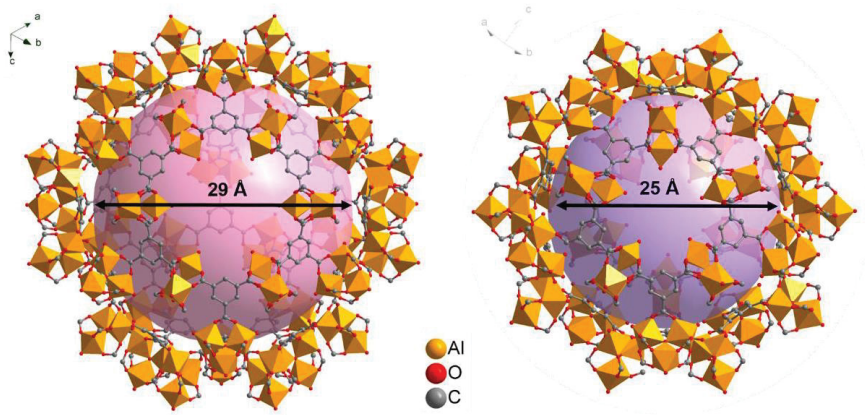

Figure S8. Section of the framework structure and pore size of MIL-100(Al) (CCDC 789872)[18] and isostructural NH_2-MIL-101(Al).

S3 Characterization of Materials as-Synthesized, After Dry SO_2 and Humid SO_2 Exposure

The characterization was done on the as-synthesized materials and on the materials after dry and humid SO_2 exposure to check for the stability against SO_2 and SO_2/H_2O.

The stability tests were carried out as follows: Before and after stability tests for dry and humid SO_2 exposure all MOFs were activated as described in Table S1, SI. For dry exposure, the volumetric SO_2 ad- and desorption measurement was taken and the sample was characterized again by PXRD and N_2 sorption after the SO_2-isotherm measurement. For humid SO_2 exposure, a controlled airflow of 2 L min^{-1} was bubbled through a sodium hydrogen sulfite solution (0.4 g $Na_2S_2O_5$ in 100 mL of water) in a Schlenk round bottom flask to transport gaseous SO_2 into a humidity chamber (desiccator vessel). The experimental setup is shown in Figure S9. To ensure a largely constant SO_2 concentration in the exposure chamber, the setup was constructed with a 3-way valve for the possibility to divert the gas flow. The SO_2 was either directed to the chamber or diverted to the exhaust if there was sufficient SO_2 in the chamber. The desiccator was equipped with a crystallizing dish filled with saturated sodium chloride solution (80 mL, giving a relative humidity (RH) of 75%) and the sample (50 mg). The RH and the amount of SO_2 in the desiccator was monitored with a hygrometer (VWR TH300 hygrometer) and an SO_2-sensor (Dräger Pac 6000 electrochemical sensor), respectively. Materials were exposed to a humid SO_2 environment at room temperature with 75 ± 6% RH and 35 ± 5 ppm SO_2 for 5 h.

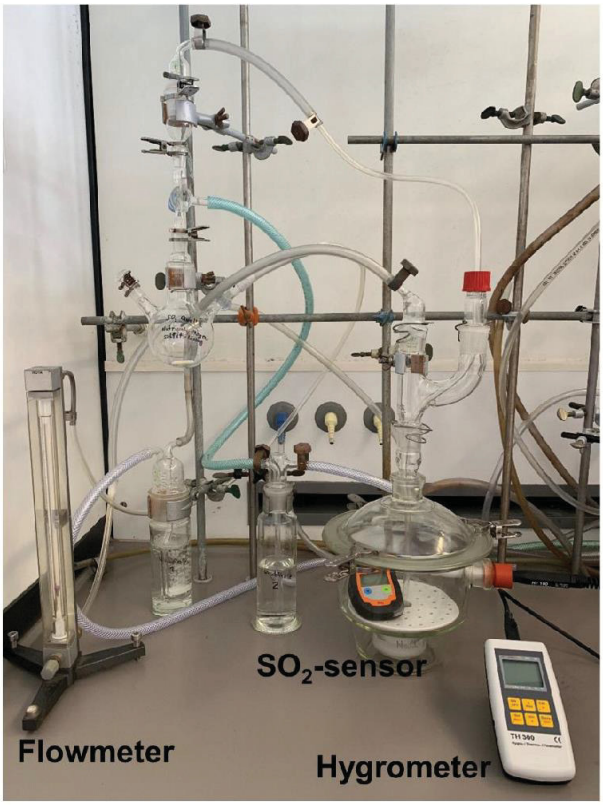

Figure S9. Setup for humid SO_2 exposure experiments.

S3.1 Powder X-ray Diffraction

Powder X-ray diffraction (PXRD) measurements were performed on a Bruker *D2 Phaser* (300 W, 30 kV, 10 mA) at ambient temperatures. As radiation source a Cu-Kα-cathode (λ = 1.54182 Å) between 5° < 2Θ < 50° was used. Diffraction patterns were obtained using a silicon "low background" sample holder.

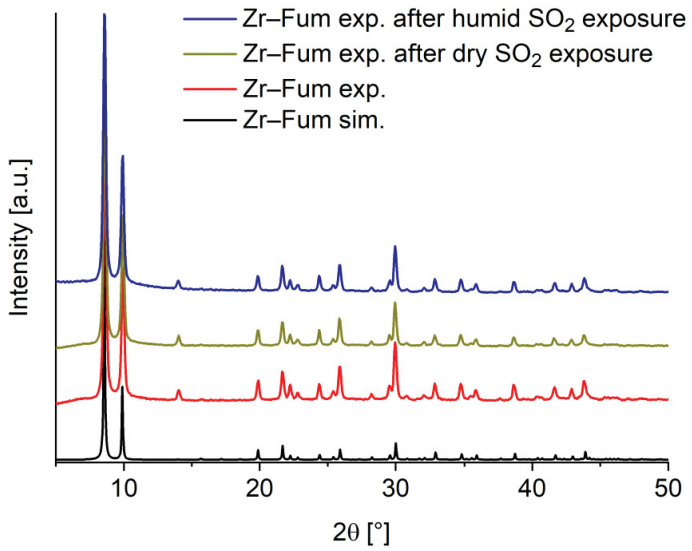

Figure S10. Comparison of PXRD patterns of Zr-Fum (simulation based on crystal structure data, CCDC 1002678, Reference 13).

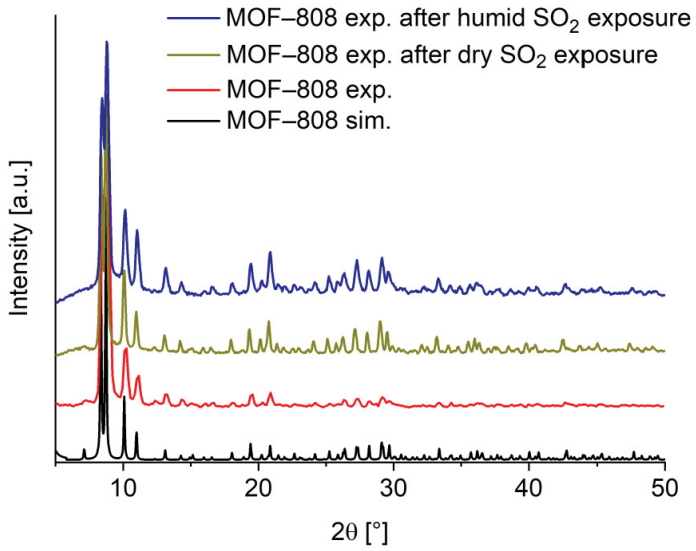

Figure S11. Comparison of PXRD patterns of MOF-808 (simulation based on crystal structure data, CCDC 1002672, Reference 13).

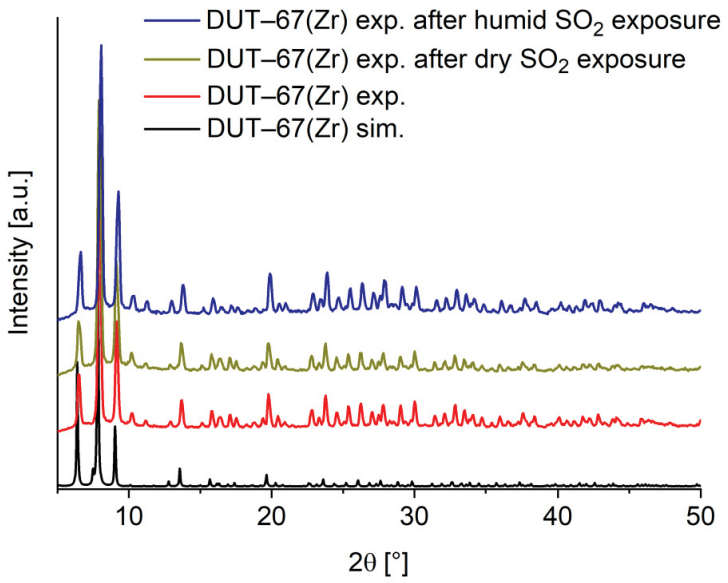

Figure S12. Comparison of PXRD patterns of DUT-67(Zr) (simulation based on crystal structure data, CCDC 902898, Reference 14).

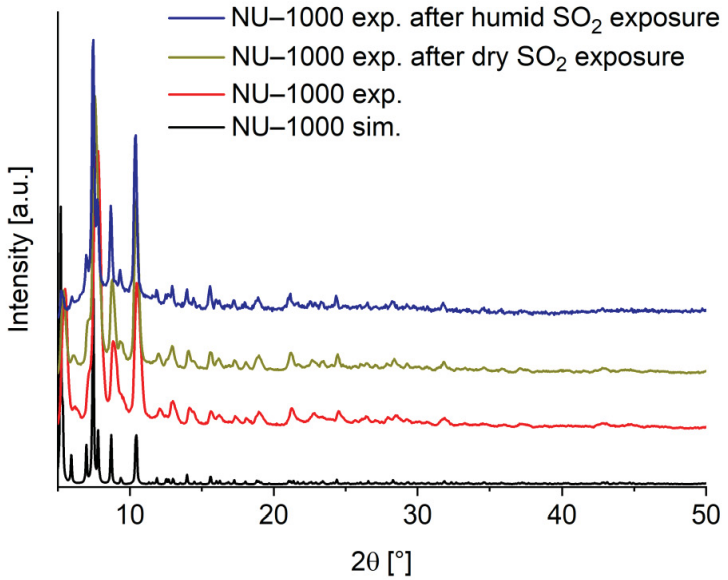

Figure S13. Comparison of PXRD patterns of NU-1000 (simulation based on crystal structure data, CCDC 955328, Reference 15).

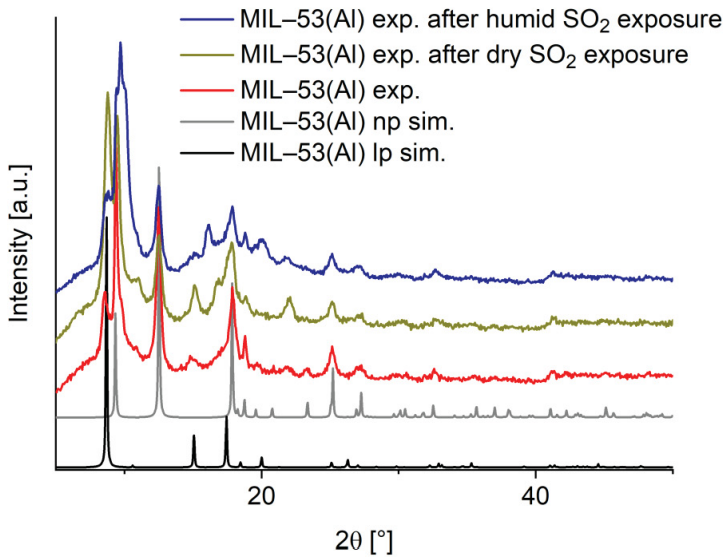

Figure S14. Comparison of PXRD patterns of MIL-53(Al) (simulation MIL-53(Al) ***l****arge* ***p****ore* or ***n****arrow* ***p****ore*, based on crystal structure data, CCDC 220476 and 220477, respectively, Reference 19).

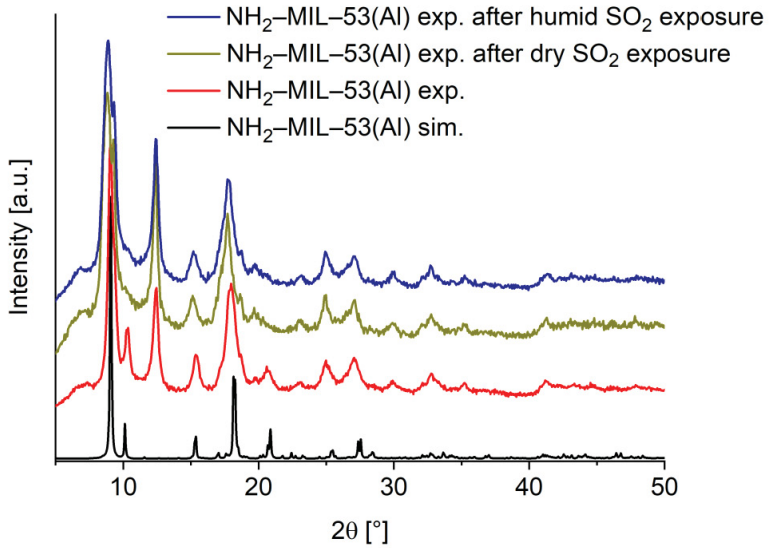

Figure S15. Comparison of PXRD patterns of NH_2-MIL-53(Al) (simulation based on crystal structure data, CCDC 901254, Reference 20).

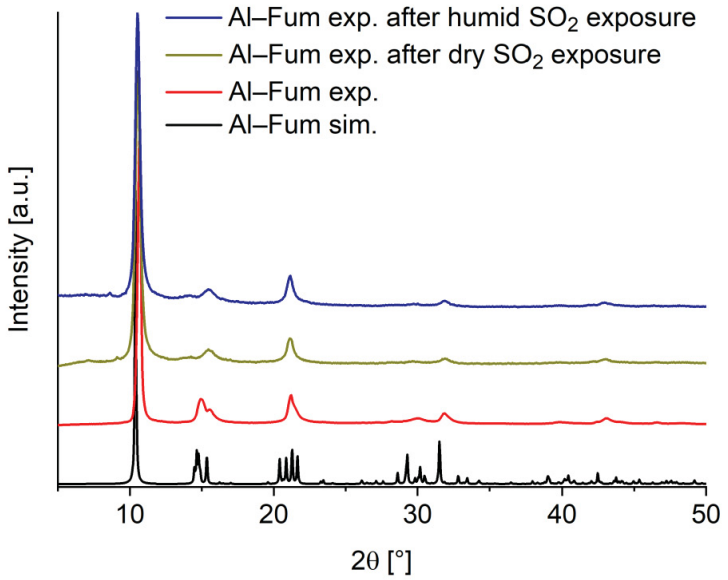

Figure S16. Comparison of PXRD patterns of Al-Fum (simulation based on crystal structure data, CCDC 1051975, Reference 16).

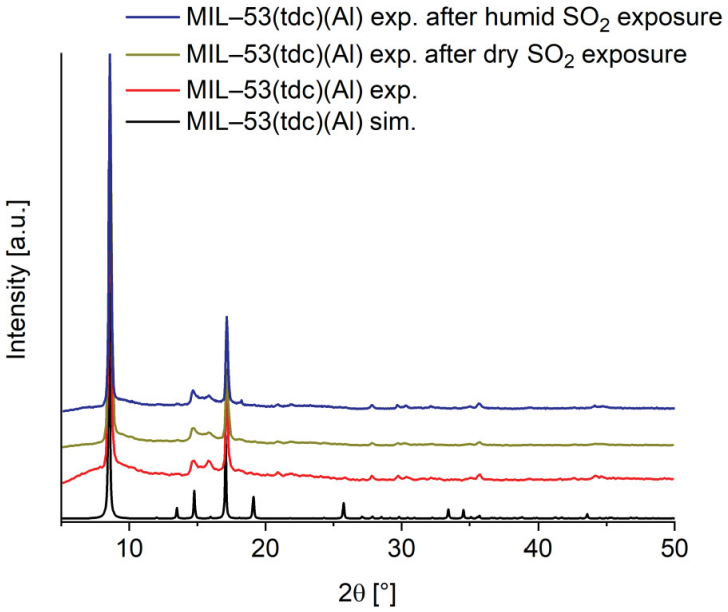

Figure S17. Comparison of PXRD patterns of MIL-53 (tdc)(Al) (simulation based on crystal structure data, which was generously provided by Serre and co-workers).

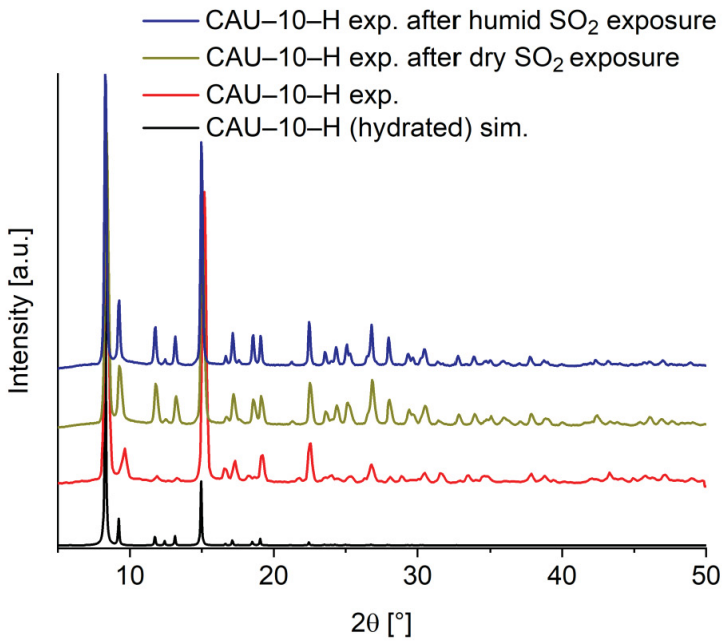

Figure S18. Comparison of PXRD patterns of CAU-10-H (simulation based on crystal structure data, CCDC 1454066, Reference 17).

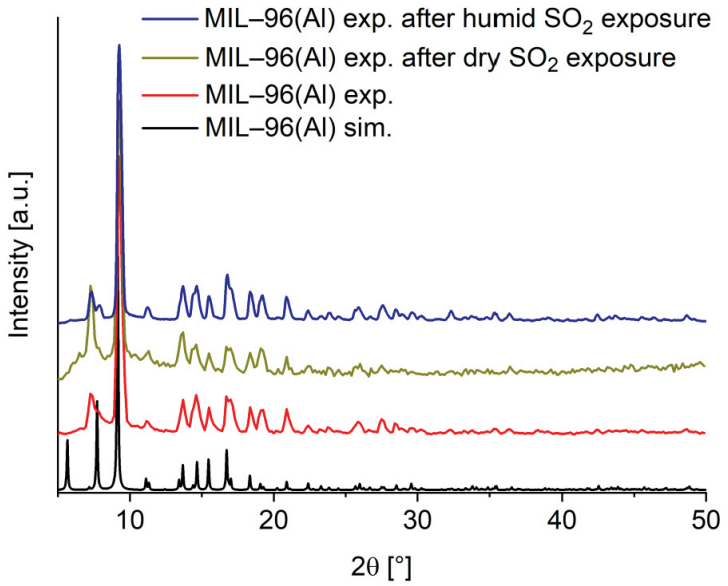

Figure S19. Comparison of PXRD patterns of MIL-96(Al) (simulation based on crystal structure data, CCDC 902898, Reference 9).

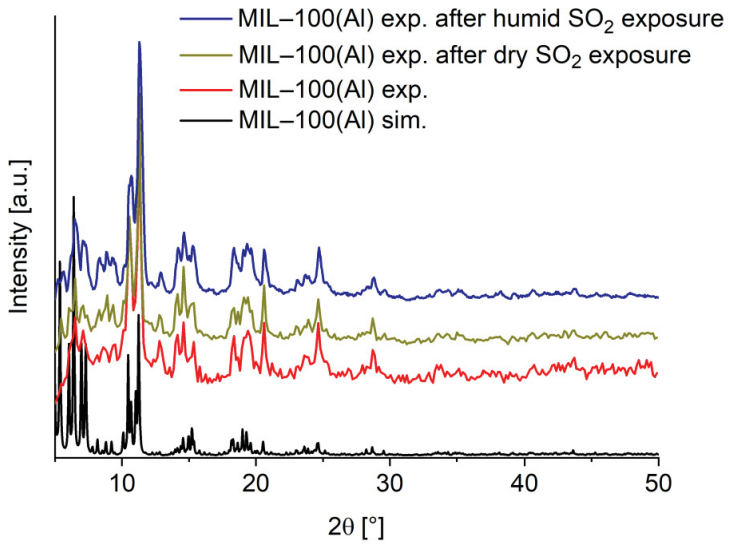

Figure S20. Comparison of PXRD patterns of MIL-100(Al) (simulation based on crystal structure data, CCDC 789872, Reference 18).

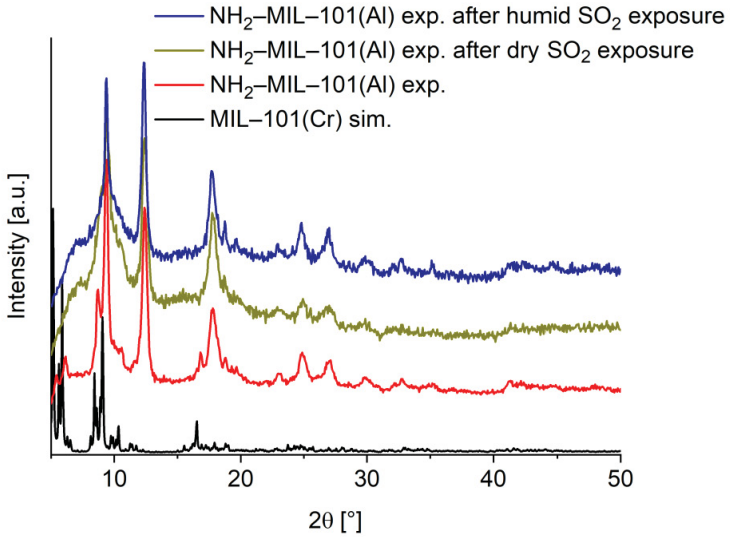

Figure S21. Comparison of PXRD patterns of NH_2-MIL-101(Al) (simulation based on crystal structure data, CCDC 605510, Reference 21).

S3.2 Nitrogen Adsorption

N_2-sorption isotherms were measured on an *Autosorb 6* (QUANTACHROME, Odelzhausen, Germany) instrument at 77 K within a pressure range of 0.005-1 bar. Before each experiment, the samples were activated for at least 12 hours and at a minimum of 393 K under a vacuum of less than $5 \cdot 10^{-3}$ mbar.

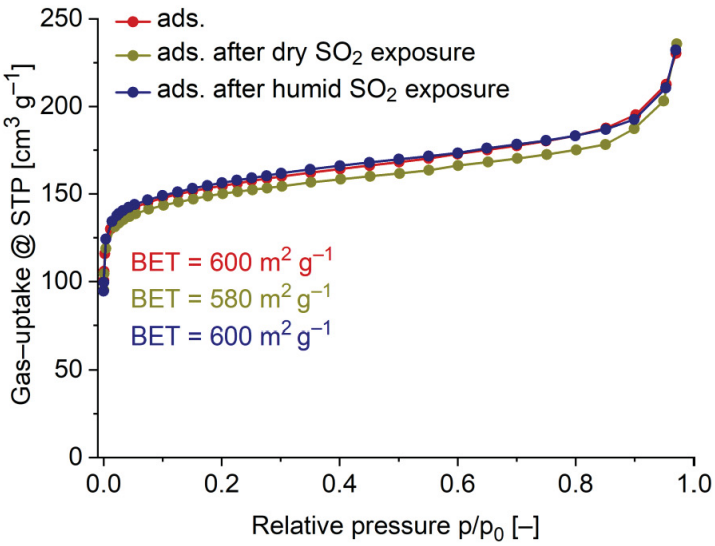

Figure S22: N_2-adsorption isotherms (77 K) of Zr-Fum.

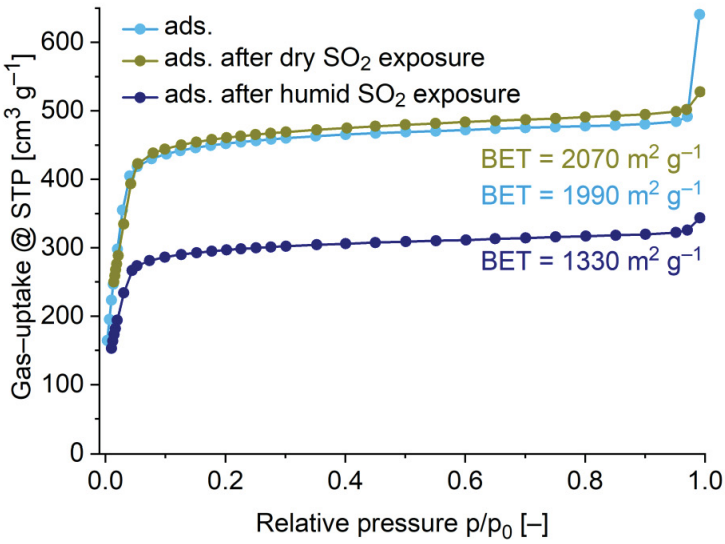

Figure S23. N_2-adsorption isotherms (77 K) of MOF-808.

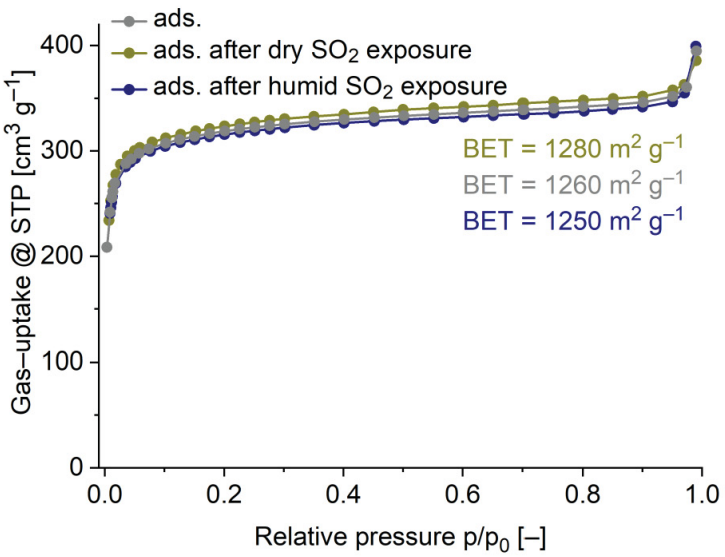

Figure S24. N_2-adsorption isotherms (77 K) of DUT-67(Zr).

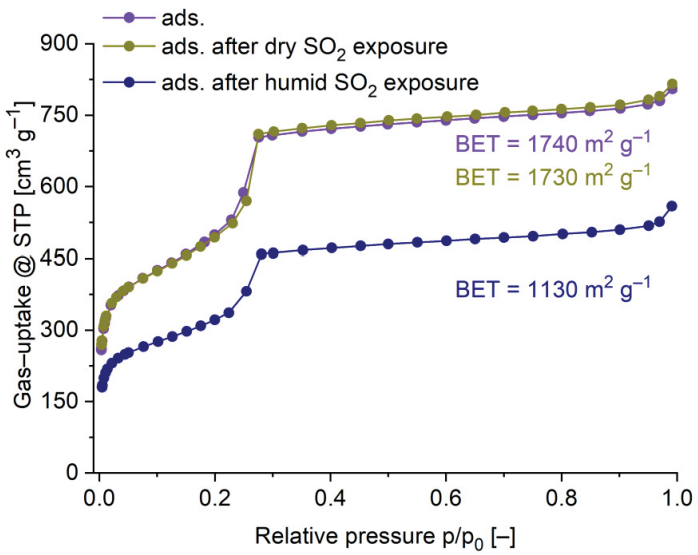

Figure S25. N_2-adsorption isotherms (77 K) of NU-1000.

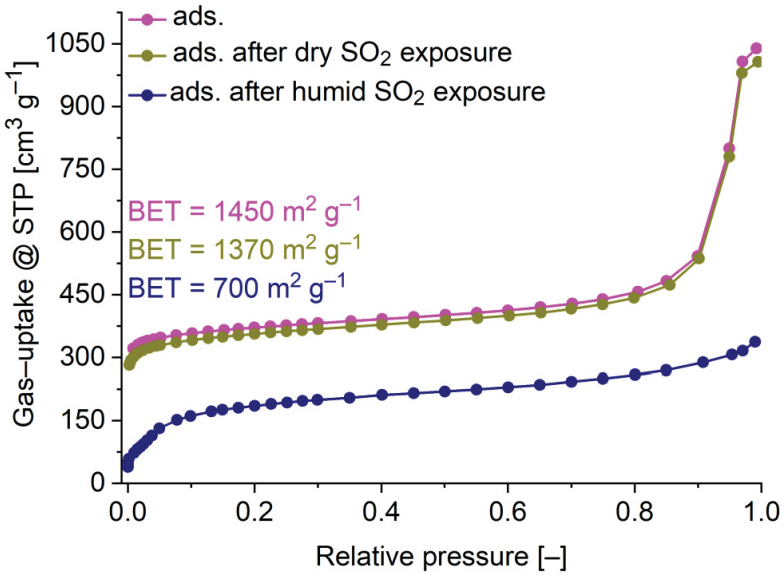

Figure S26. N_2-adsorption isotherms (77 K) of MIL-53(Al).

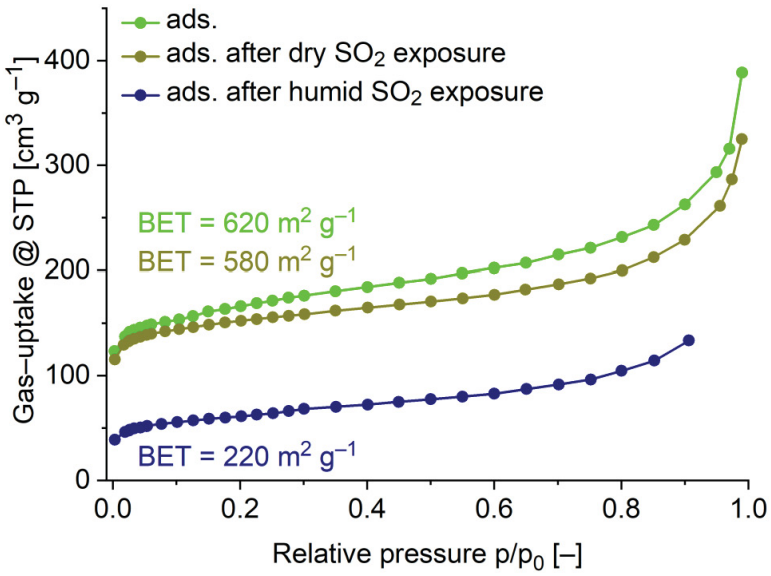

Figure S27. N_2-adsorption isotherms (77 K) of NH_2-MIL-53(Al).

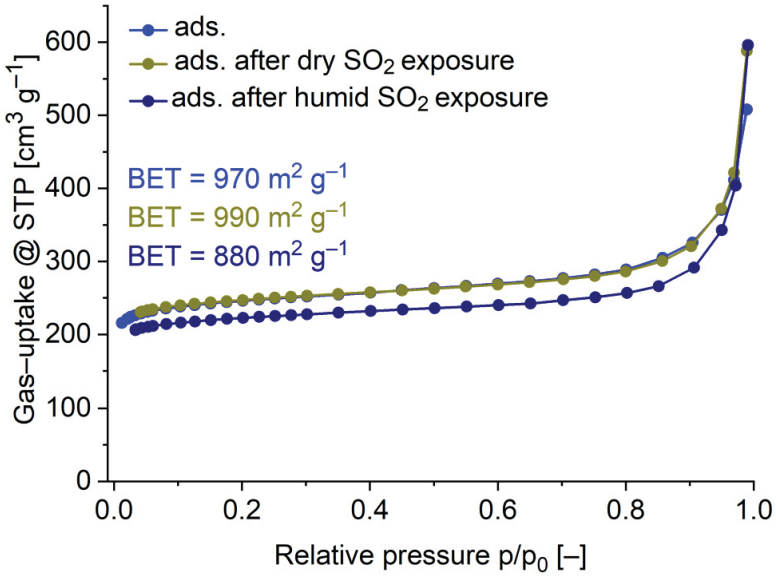

Figure S28. N_2-adsorption isotherms (77 K) of Al-Fum.

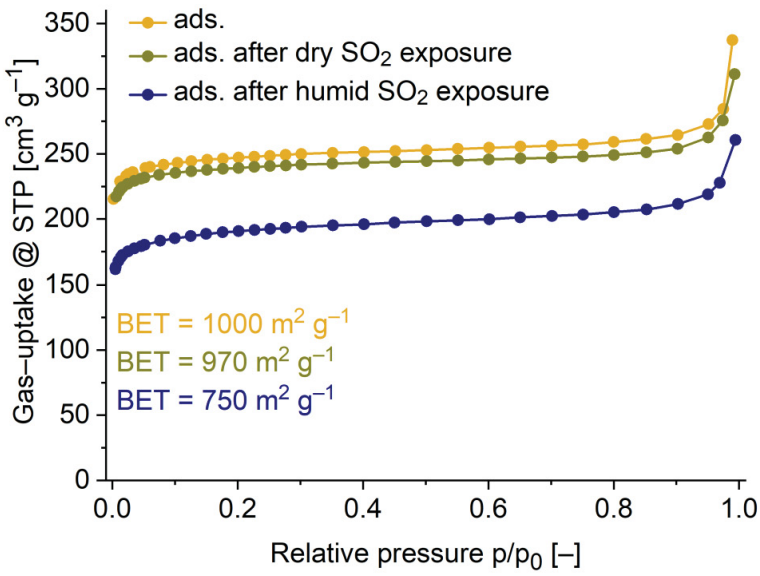

Figure S29. N_2-adsorption isotherms (77 K) of MIL-53(tdc)(Al).

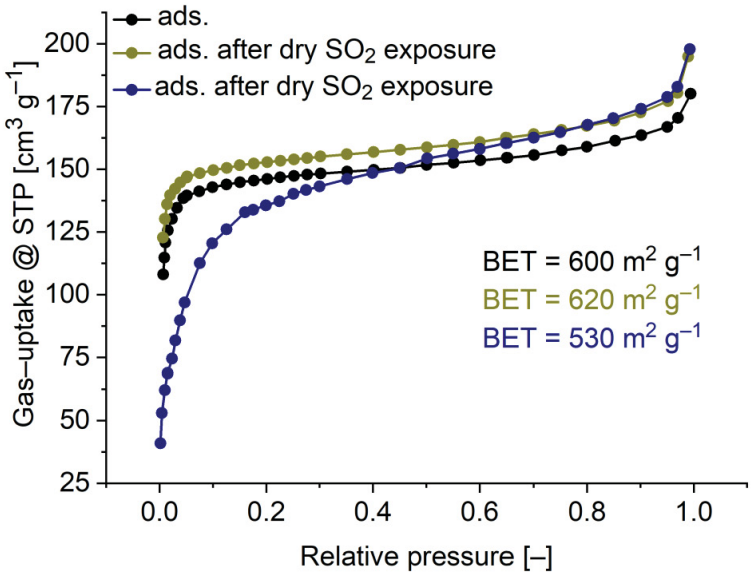

Figure S30. N_2-adsorption isotherms (77 K) of CAU-10-H.

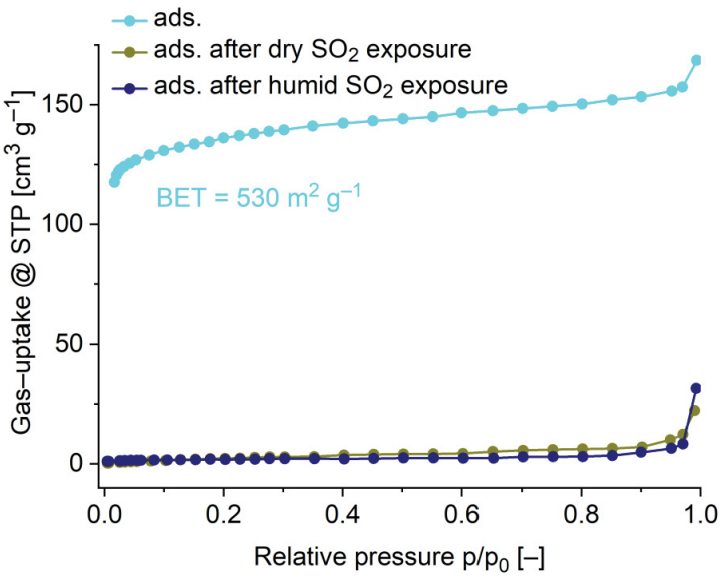

Figure S31. N_2-adsorption isotherms (77 K) of MIL-96(Al).

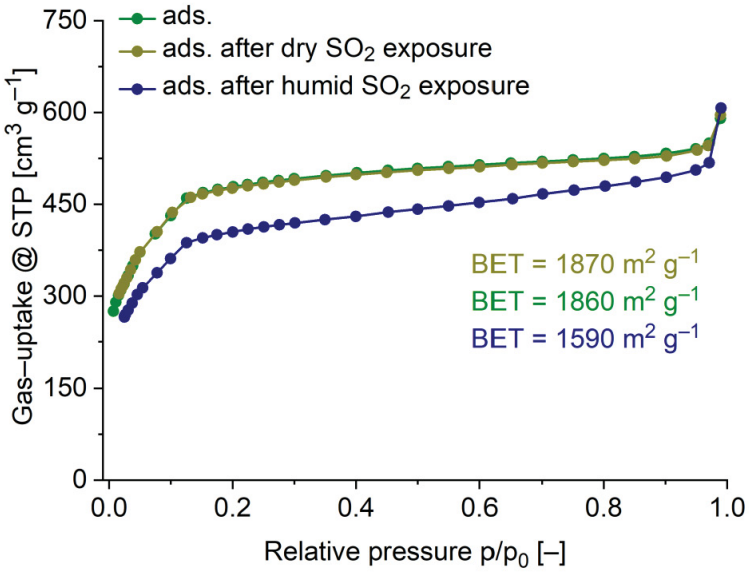

Figure S32. N_2-adsorption isotherms (77 K) of MIL-100(Al).

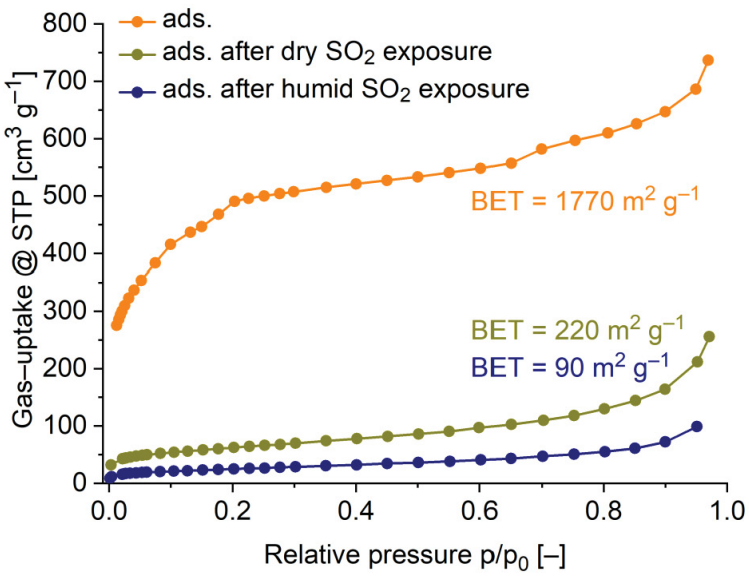

Figure S33. N_2-adsorption isotherms (77 K) of NH_2-MIL-101(Al).

Table S2. Micropore properties of investigated MOFs obtained by t-plot analysis.

Material	Micro BET-surface area [m^2 g^{-1}]	BET-surface area [m^2 g^{-1}]	Micropore volume [cm^3 g^{-1}]	Total pore volume [cm^3 g^{-1}]
Zr-Fum	480	600	0.189	0.290
MOF-808	1740	1990	0.593	0.749
DUT-67(Zr)	1050	1260	0.403	0.544
NU-1000	510	1740	0.205	1.196
MIL-53(Al)	1190	1450	0.463	0.706
NH_2-MIL-53(Al)	373	620	0.150	0.358
Al-Fum	820	970	0.319	0.447
MIL-53(tdc)(Al)	940	1000	0.362	0.415
CAU-10-H	550	600	0.203	0.258
MIL-96(Al)	450	530	0.175	0.237
MIL-100(Al)	1420	1890	0.548	0.824
NH_2-MIL-101(Al)	360	1770	0.603	1.001

S4 SO_2 Sorption Studies

S4.1 Method

Before each experiment samples were activated for at least 3 hours and at a minimum of 393 K under vacuum < $5 \cdot 10^{-3}$ mbar. All used gases (He, SO_2, CO_2, N_2) were of ultra-high purity (UHP grade 5.0, 99.999%) and the STP volumes at 293.15 K and 101.325 kPa are given according to the NIST standards. SO_2 and CO_2 sorption experiments were performed on an *Autosorb iQ MP* (QUANTACHROME, Odelzhausen, Germany) instrument within a pressure range of 0.001-1 bar and 293 K. For safety precautions of toxic SO_2, a *Dräger Pac 6000* SO_2-detector (0-100 ppm in 0.1 ppm steps) was used in close range to the sorption-device.

SO_2-sorption experiments with our setup involve some limitations emerging from the corrosive nature of the SO_2-adsorptive. The Quantachrome *iQ MP* device was equipped with Viton® gaskets. The chemical compatibility of gasket materials is available in ref. 22. For these Viton® gaskets each SO_2-sorption run had to be completed within a maximum time of 10 h. This time limit was specified by the company Quantachrome to prevent damage to the gaskets. After this time the system had to be regenerated by flushing with nitrogen. Irreversible swelling of the SO_2 adsorbing gaskets in the measurement device, which could cause leaks in the system, had to be prevented by setting the measurement time to this maximum (10 h) to meet safety precautions and to protect the device. Then, after each measurement, the gas line was flushed with N_2 several times and remained under N_2 atmosphere for at least 12 h to regenerate the gaskets. In the case of long equilibration times upon adsorption and desorption we decided to collect the adsorption data points as complete as possible with long-enough equilibration times at the expense that for desorption, fewer data points could be measured. This compromise then led to incomplete, i.e. not-closed desorption branches, which however are solely due to the experimental boundary conditions and cannot be interpreted in terms of decomposition or chemisorption. Also the pressure range from ~0.05 to 0.5 bar was measured with a larger spacing of data points to lower the total measurement time. This may have prevented in a few cases to clearly show the formation of adsorption steps of MOFs with bi- or multimodal pore size distributions. However, if the individual pore sizes of a given material do not differ significantly a potential adsorption step is difficult to be observed anyhow, especially when the measurement temperature is 30 K above the boiling point of the adsorbate, where adsorbent-adsorbate interactions are already weaker.

S4.2 Combination Figures of SO_2 Adsorption Isotherms

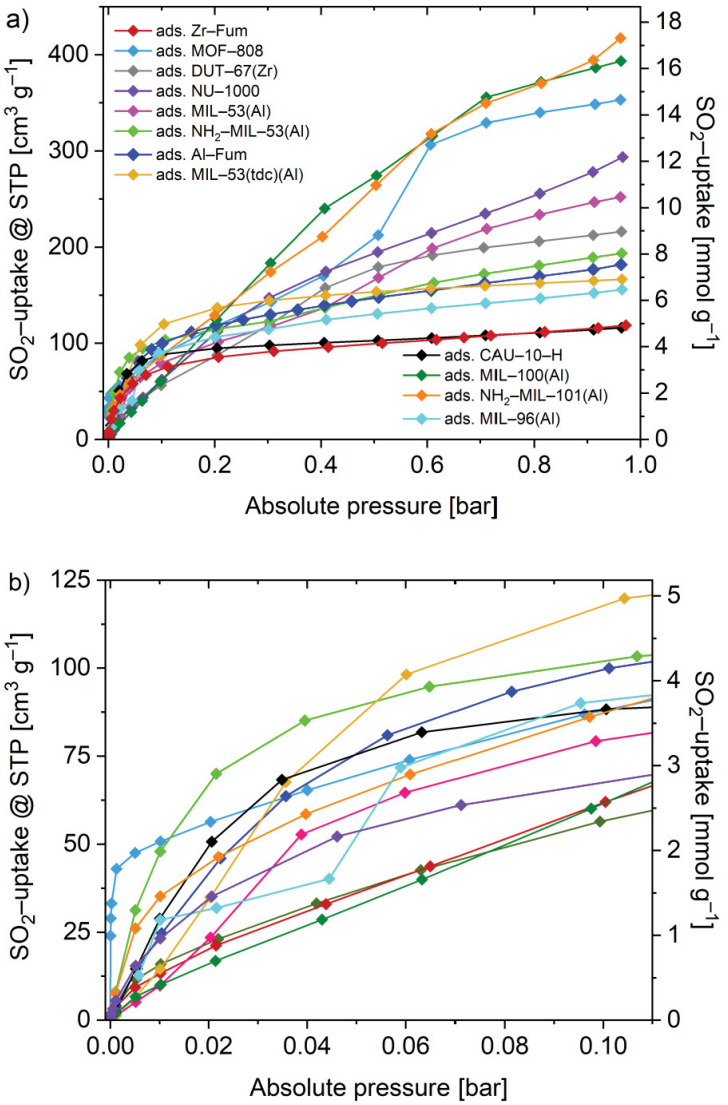

Figure S34. Overlay of the SO_2 adsorption isotherms (293 K) for all examined materials (a) 0.001-1 bar, (b) 0.001-0.11 bar.

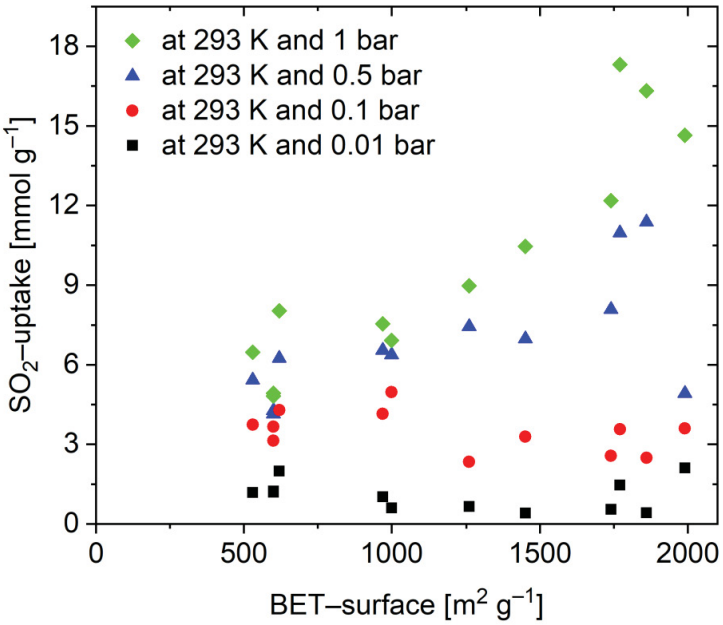

Figure S35. SO_2 uptake at different pressures vs BET surface area (293 K). The MOF correlation for the green data points (diamonds) can be seen in Figure 4a in the main text.

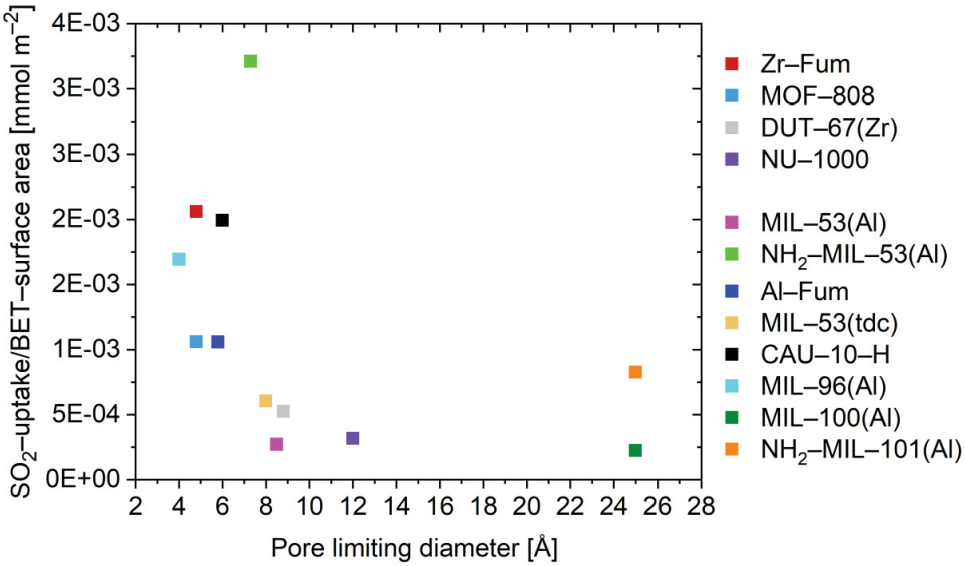

Figure S36. Surface-specific SO_2 uptake at 0.01 bar (293 K), which is the uptake at this pressure divided by the BET-surface area *vs* the pore limiting diameter (PLD). The surface-specific SO_2 uptake at 0.1 bar is shown in Figure 5 in the main text.

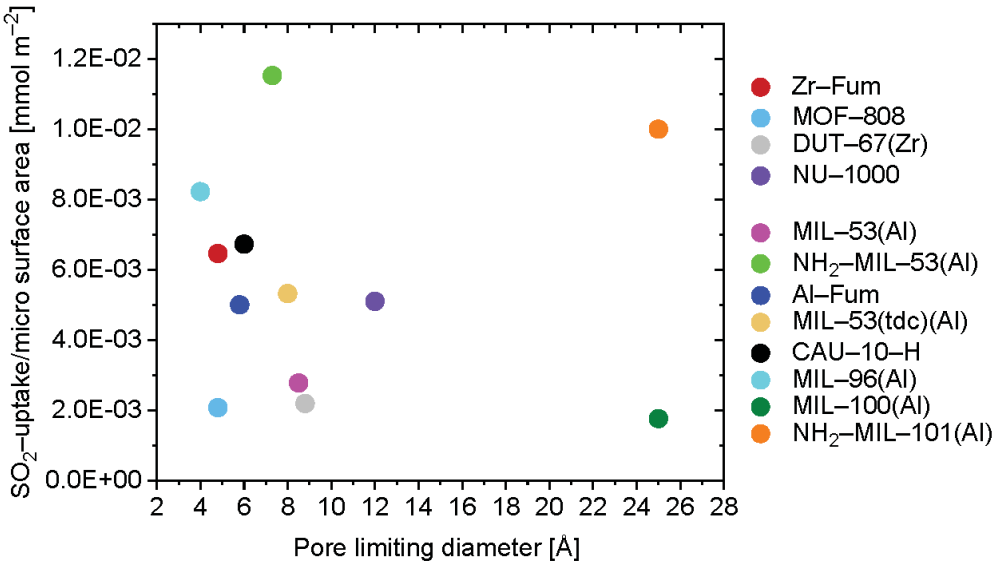

Figure S37. Micropore surface-specific SO_2 uptake at 0.1 bar (293 K), which is the uptake at this pressure divided by the micro-surface area vs the pore limiting diameter (PLD).

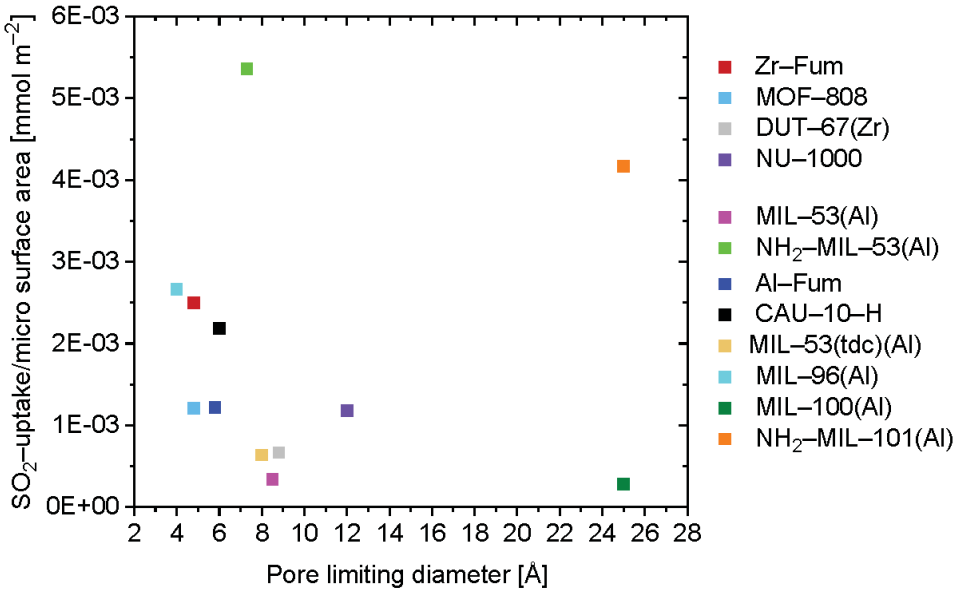

Figure S38. Micropore surface-specific SO_2 uptake at 0.01 bar (293 K), which is the uptake at this pressure divided by the micro-surface area vs the pore limiting diameter (PLD).

S5 SO_2 and CO_2 Sorption and Isotherm Fitting

The measurement of adsorption isotherms of both SO_2 and CO_2 under the same conditions are used to examine sorption capacity and affinity and are further used to calculate the IAST-selectivity. Fitting-simulations were calculated using 3P sim software.[23] We applied several commonly used models (eq. 1-6) on our isotherm data. The best comparability for two adsorption isotherms is obtained by applying the same model on both isotherm data. Fitting parameters are shown in Table S3.

Freundlich: $$q_{eq} = K \cdot p^t \quad (1)$$

Langmuir: $$q_{eq} = \frac{q_{max} \cdot K \cdot p}{1 + K \cdot p} \quad (2)$$

Sips: $$q_{eq} = \frac{q_{max} \cdot (K \cdot p)^t}{1 + (K \cdot p)^t} \quad (3)$$

Toth: $$q_{eq} = \frac{q_{max} \cdot K \cdot p}{(1 + (K \cdot p)^t)^{1/t}} \quad (4)$$

DSL: $$q_{eq} = q_{max1} \frac{\cdot K_1 \cdot p}{1 + K_1 \cdot p} + q_{max2} \frac{\cdot K_2 \cdot p}{1 + K_2 \cdot p} \quad (5)$$

DSLSips $$q_{eq} = q_{\max} \left(\frac{\cdot K_1 \cdot p}{1 + K_1 \cdot p} + \frac{\cdot (K_2 \cdot p)^t}{(1 + K_2 \cdot p)^t} \right) \quad (6)$$

q_{eq}= amount adsorbed [mmol/g]

q_{max} = maximum adsorption capacity [mmol/g]

K = affinity constant for adsorption [1/bar]

p = pressure [kPa]

t = index of heterogeneity

The Sips model represents a combination of the Langmuir and the Freundlich model. This becomes apparent when K or p approaches 0 and the model is reduced to a Freundlich equation whereas for homogeneous materials with t = 1 concentrations it is reduced to the Langmuir equation.[24]

Table S3: Dual-site Langmuir Sips fitting parameters used for the calculation of SO_2/CO_2 IAST-selectivities.

Material	Gas	Model [a]	R^2	Affinity const. 1 [1/bar]	Max. loading [mmol/g]	Affinity const. 2 [1/bar]	Heterogeneity exponent
Zr-Fum	SO_2	DSLS	0.999	26.915	4.00	1.250	3.00
	CO_2	DSLS	0.999	1.838	1.899	0.740	1.766
MOF-808	SO_2	DSLS	0.979	14.563	7.426	1.850	11.300
	CO_2	DSLS	0.999	1.563	1.840	0.845	2.658
DUT-67	SO_2	DSLS	0.999	10.109	4.721	2.618	3.536
	CO_2	DSLS	0.999	1.286	1.895	0.490	1.978
NU-1000	SO_2	DSLS	0.999	2.115	15.504	0.678	4.878
	CO_2	DSLS	0.999	0.269	3.749	0.395	1.138
MIL-53(Al)	SO_2	DSLS	0.999	13.539	5.683	1.706	4.427
	CO_2	DSLS	0.998	0.412	1.888	2.999	0.918
NH_2-MIL-53(Al)	SO_2	DSLS	0.999	71.635	4.769	1.459	2.386
	CO_2	DSLS	0.999	5.504	2.115	1.114	2.067
Al-Fum	SO_2	DSLS	0.999	22.007	5.932	0.706	2.038
	CO_2	DSLS	0.999	0.094	3.659	1.247	1.184
MIL-53(tdc)(Al)	SO_2	DSLS	0.991	17.375	7.193	0.757	12.418
	CO_2	DSLS	0.999	0.313	4.918	0.498	1.218
CAU-10-H	SO_2	DSLS	0.996	43.002	4.445	0.6032	3.864
	CO_2	DSLS	0.999	1.077	2.461	1.170	1.212
MIL-96(Al)	SO_2	DSLS	0.993	23.949	5.930	0.587	2.860
	CO_2	DSLS	0.999	4.692	2.760	1.334	1.446
MIL-100(Al)	SO_2	DSLS	0.999	2.851	10.554	2.030	2.265
	CO_2	DSLS	0.999	0.999	1.583	0.842	2.056
NH_2-MIL-101(Al)	SO_2	DSLS	0.998	7.669	9.375	1.743	4.294
	CO_2	DSLS	0.999	0.400	2.690	1.251	0.721

[a] DSLS _ Dual-site Langmuir SIPS. The number of three decimal digits are needed for the IAST selectivity calculation. Rounding to one decimal digit (as in Table 2, main text) leads to significant deviations in the IAST values.

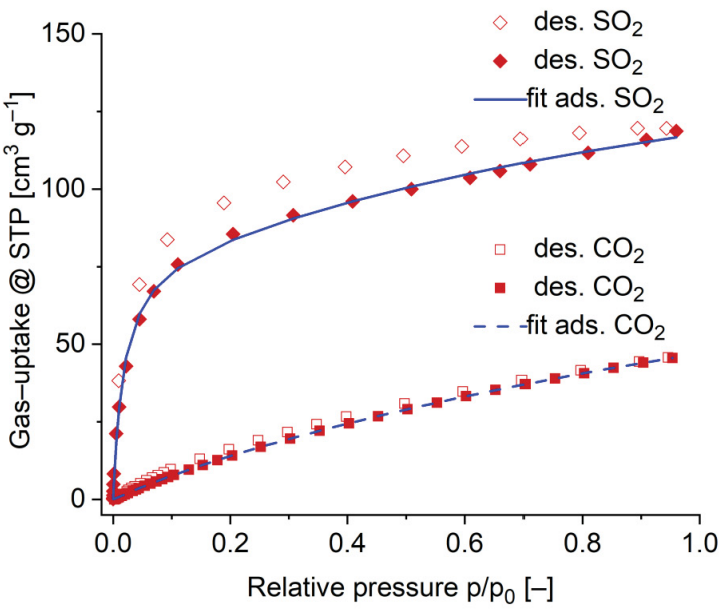

Figure S39. Experimental SO_2- (rhombs) and CO_2- (squares) sorption isotherm and fitted SO_2- (line) and CO_2- (dashed line) adsorption isotherm of Zr-Fum at 293 K.

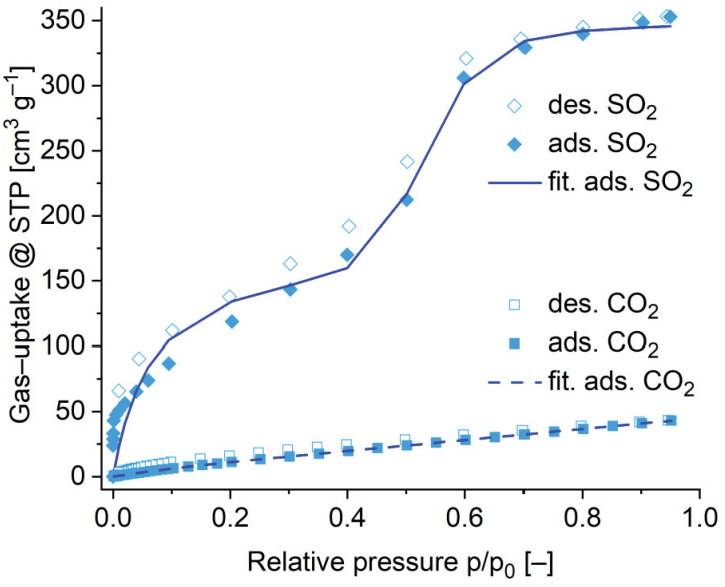

Figure S40. Experimental SO_2- (rhombs) and CO_2- (squares) sorption isotherm and fitted SO_2- (line) and CO_2- (dashed line) adsorption isotherm of MOF-808 at 293 K.

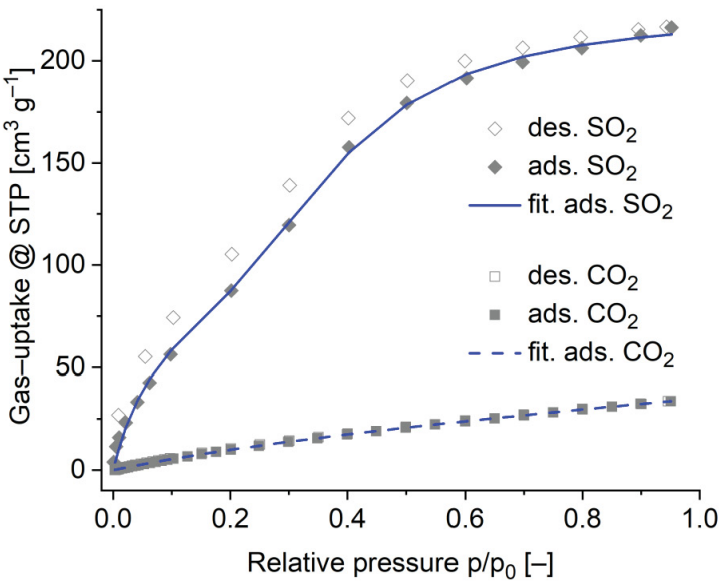

Figure S41. Experimental SO_2- (rhombs) and CO_2- (squares) sorption isotherm and fitted SO_2- (line) and CO_2- (dashed line) adsorption isotherm of DUT-67(Zr) at 293 K.

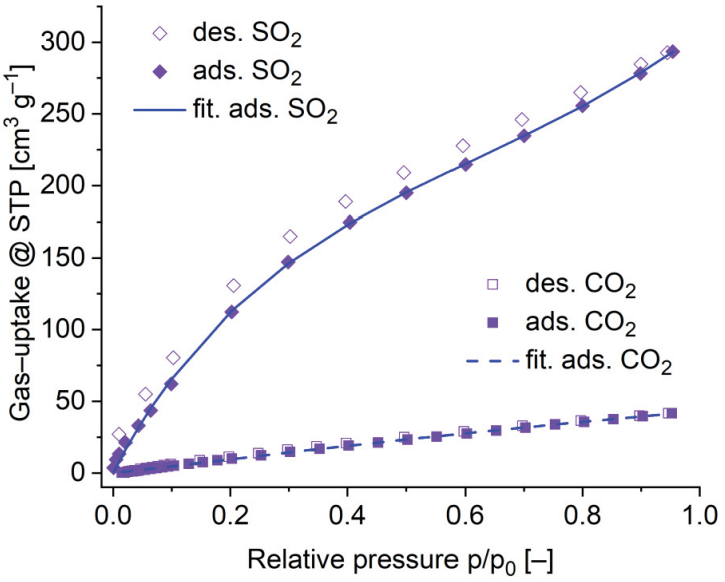

Figure S42. Experimental SO_2- (rhombs) and CO_2- (squares) sorption isotherm and fitted SO_2- (line) and CO_2- (dashed line) adsorption isotherm of NU-1000 at 293 K.

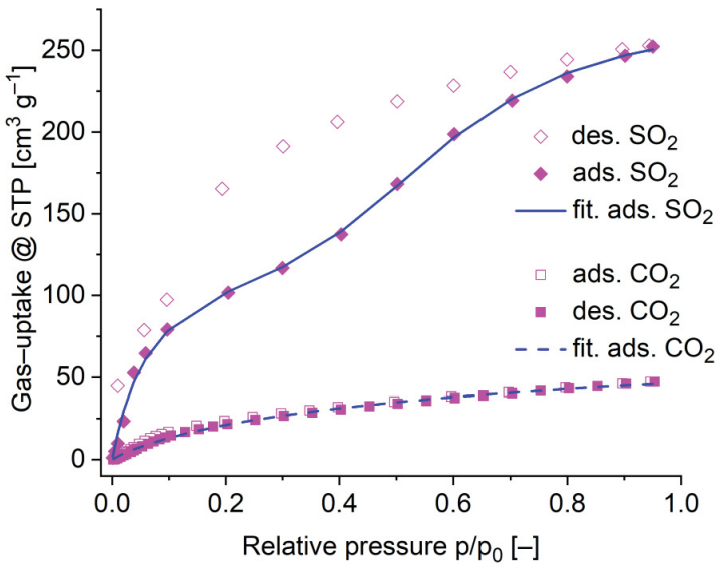

Figure S43. Experimental SO_2- (rhombs) and CO_2- (squares) sorption isotherm and fitted SO_2- (line) and CO_2- (dashed line) adsorption isotherm of MIL-53(Al) at 293 K.

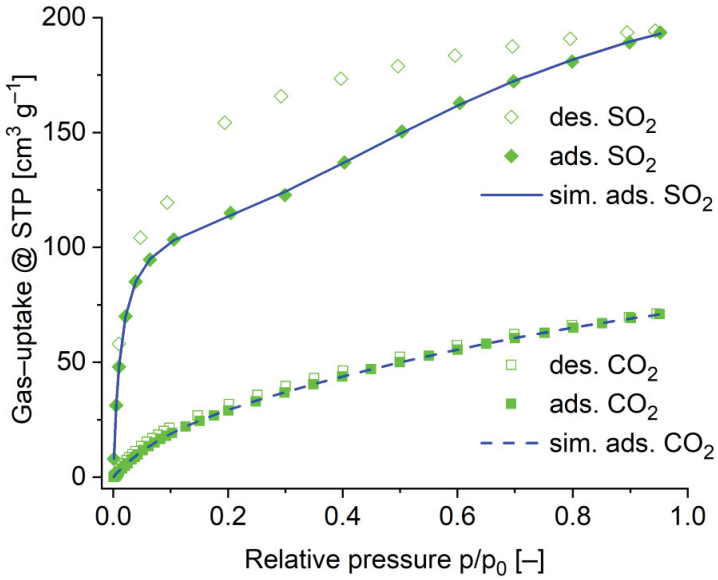

Figure S44. Experimental SO_2- (rhombs) and CO_2- (squares) sorption isotherm and fitted SO_2- (line) and CO_2- (dashed line) adsorption isotherm of NH_2-MIL-53(Al) at 293 K.

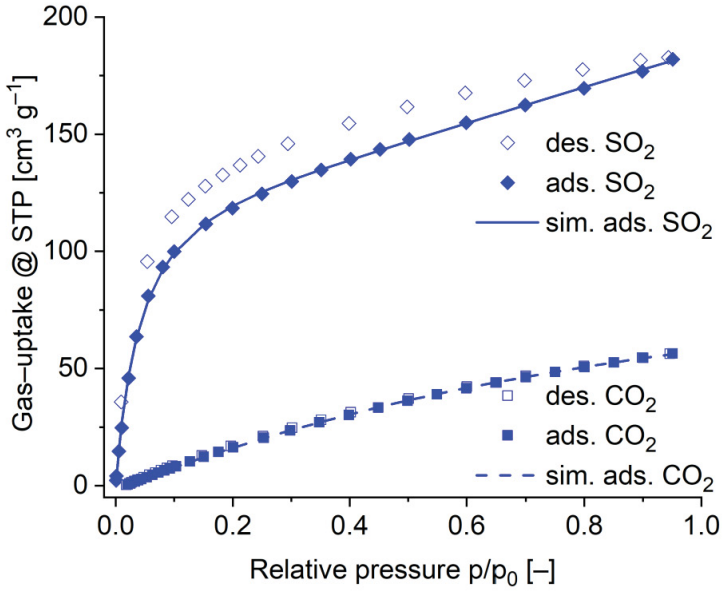

Figure S45. Experimental SO_2- (rhombs) and CO_2- (squares) sorption isotherm and fitted SO_2- (line) and CO_2- (dashed line) adsorption isotherm of Al-Fum at 293 K.

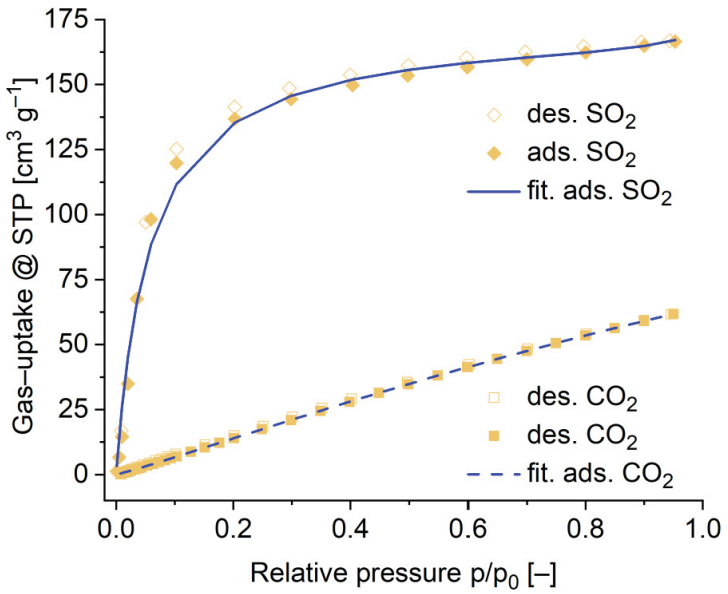

Figure S46. Experimental SO_2- (rhombs) and CO_2- (squares) sorption isotherm and fitted SO_2- (line) and CO_2- (dashed line) adsorption isotherm of MIL-53(tdc)(Al) at 293 K.

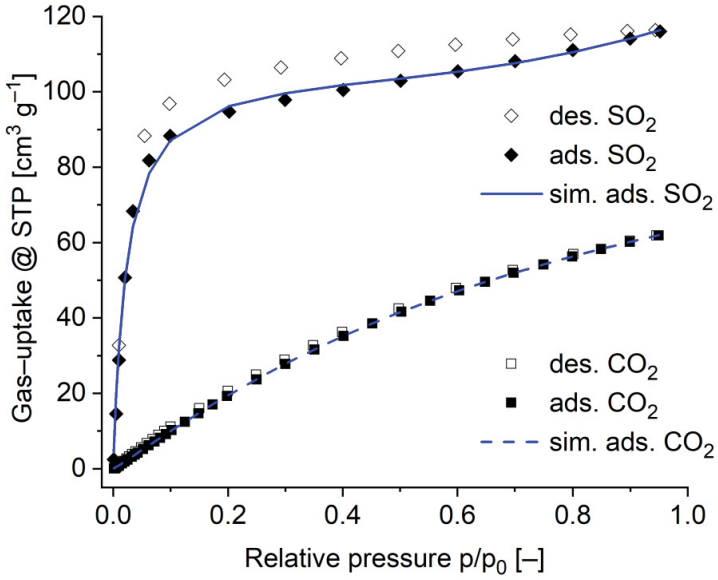

Figure S47. Experimental SO_2- (rhombs) and CO_2- (squares) sorption isotherm and fitted SO_2- (line) and CO_2- (dashed line) adsorption isotherm of CAU-10-H at 293 K.

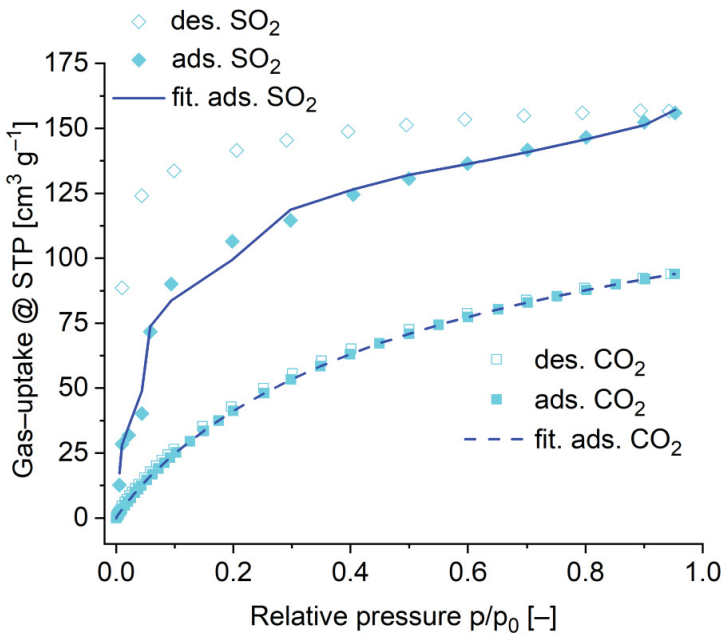

Figure S48. Experimental SO_2- (rhombs) and CO_2- (squares) sorption isotherm and fitted SO_2- (line) and CO_2- (dashed line) adsorption isotherm of MIL-96(Al) at 293 K.

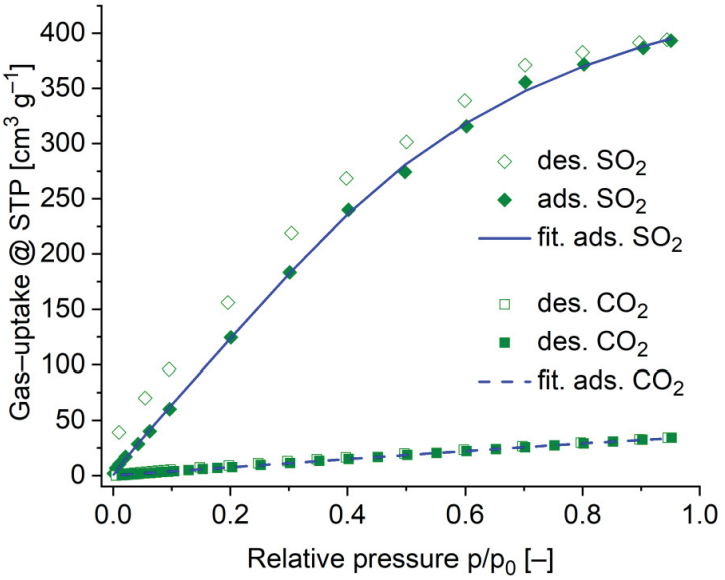

Figure S49. Experimental SO_2- (rhombs) and CO_2- (squares) sorption isotherm and fitted SO_2- (line) and CO_2- (dashed line) adsorption isotherm of MIL-100(Al) at 293 K.

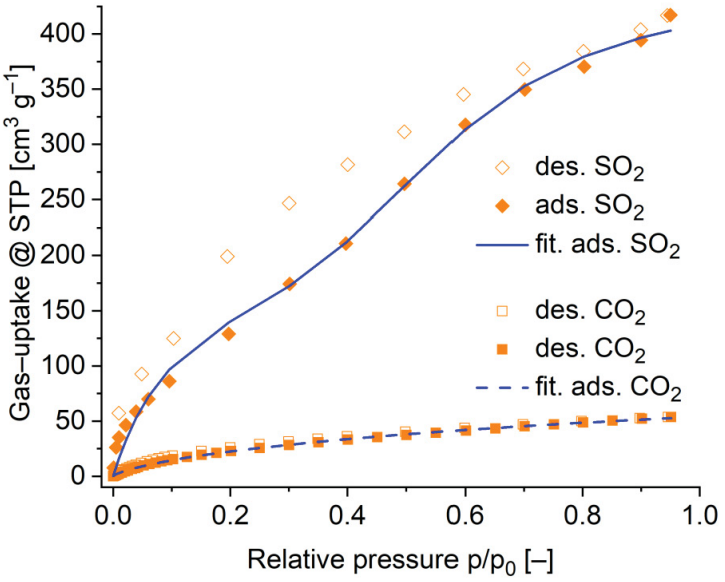

Figure S50. Experimental SO_2- (rhombs) and CO_2- (squares) sorption isotherm and fitted SO_2- (line) and CO_2- (dashed line) adsorption isotherm of NH_2-MIL-101(Al) at 293 K.

S6 Computational Details

S6.1 Ideal Adsorbed Solution Theory, IAST-Selectivity

Selectivities of SO_2 over CO_2 in Table S4 were calculated from fitted isotherm data (Table S3) of experimentally measured isotherms at 293 K. The 3P sim software (3P Instruments, Germany, version 1.1.0.7) calculates the maximal loadings of each gas depending on the given mole fraction. IAST selectivities S of binary gas mixtures were calculated using equation 7, where x_i represents the absorbed gas amount and y_i the mole fraction of each adsorptive.

$$S = \frac{x_1/x_2}{y_1/y_2} \qquad (7)$$

Table S4. Gas uptake values of SO_2 and CO_2 isotherms measured at 293 K and the resulting SO_2/CO_2 IAST selectivity values.

Material	SO_2 uptake [mmol g^{-1}] at			CO_2uptake [mmol g^{-1}] at			SO_2/CO_2 IAST selectivity at SO_2/CO_2 molar ratio		
	0.01 bar	0.1 bar	0.5 bar	0.01 bar	0.1 bar	0.5 bar	0.01	0.1	0.5
Zr-Fum	1.2	3.1	4.1	0.05	0.3	1.2	53	46	41
MOF-808	2.1	3.6	8.8	0.03	0.3	1.0	48	66	370
DUT-67(Zr)	0.7	2.3	7.4	0.02	0.2	0.9	22	22	37
NU-1000	0.6	2.6	8.1	0.004	0.2	1.0	16	17	22
MIL-53(Al)	0.4	3.3	7.0	0.07	0.6	1.4	17	22	43
NH_2-MIL-53(Al)	2.0	4.3	6.2	0.1	0.8	2.1	41	42	56
Al-Fum	1.0	4.1	6.1	0.02	0.3	1.5	34	35	36
MIL-53(tdc)(Al)	0.6	5.0	6.5	0.03	0.3	1.4	24	48	83
CAU-10-H	1.2	3.7	4.3	0.03	0.4	1.7	29	27	25
MIL-96(Al)	1.2	3.7	5.4	0.1	1.0	3.0	7	7	8
MIL-100(Al)	0.4	2.5	10.3	0.003	0.2	0.8	17	18	38
NH_2-MIL-101(Al)	1.5	3.6	11.0	0.09	0.6	1.6	29	20	16

Calculated SO_2/CO_2 IAST-selectivities for all examined materials are presented in Figure S51. MOF-808 demonstrates superior affinity and adsorption capacity for SO_2 over CO_2 with a gas-uptake of 97.3 and 16.8 cm^3 g^{-1} at $p/p_0 = 0.1$ (293 K), respectively. This gap in gas adsorption (SO_2/CO_2) is increased when moving to elevated pressures of 0.5 bar, resulting in high IAST-selectivities in the range of 48-370. The unusual drastic increase of IAST-selectivity for MOF-808 reflects the pronounced SO_2 adsorption step at p/p_0 = ~0.5 bar, observed for this MOF. NH_2-MIL-53(Al) and MIL-53(Al) show IAST-selectivities between 41-56 and 17-43. Note that the additional SO_2 capacity, gathered by the transition from the *np* to the *lp* form of NH_2-MIL-53(Al), is probably not exploitable for SO_2/CO_2 separation processes since after the pore

opening of the MOF it is expected that the adsorbed amount of CO_2 is also enhanced. A summary of IAST-selectivity values is also given in Table 1 in the main text.

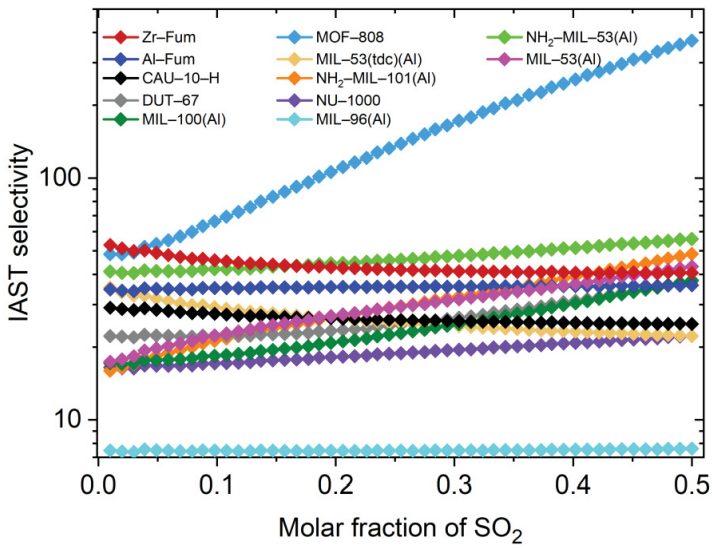

Figure S51. The calculated SO_2/CO_2 IAST selectivity dependence on the molar fraction of SO_2 in the range of 0.01-0.5 (293 K, 1 bar).

S6.2 Enthalpy of Adsorption *via* Virial Analysis

$$p = n \cdot exp\left(\sum_{i=0}^{m} C_i\, n^i\right) \tag{8}$$

In eqn. (8) C_0 is a constant for the adsorbate–adsorbent interaction, C_1, C_2, etc. are constants for the double, triple, etc. interactions in the adsorbent field. The constants C_i depend on temperature and the heat of adsorption Q_{st} (not to be mistaken as the enthalpy of adsorption, since $\Delta H_{ads} = -Q_{st}$) is given as eqn. (9).

$$Q_{st}(n) = \left(\sum_{i=0}^{m} \frac{dC_i}{dT} RT^2 n^i\right) \tag{9}$$

The equation for the global fit used for viral analysis is given as eqn. (10).

$$\ln p = \ln n + \frac{1}{T}\sum_{i=0}^{m} a_i n^i + \sum_{i=0}^{m} b_i n^i \tag{10}$$

From the virial fit, $\Delta H_{ads}(n)$ is then calculated by multiplying the ideal gas constant R with the sum of the a_i coefficients multiplied by the uptake n to the power of i, according to eqn. (11).

$$\Delta H_{ads}(n) = R \cdot \sum_{i=0}^{m} a_i n^i \tag{11}$$

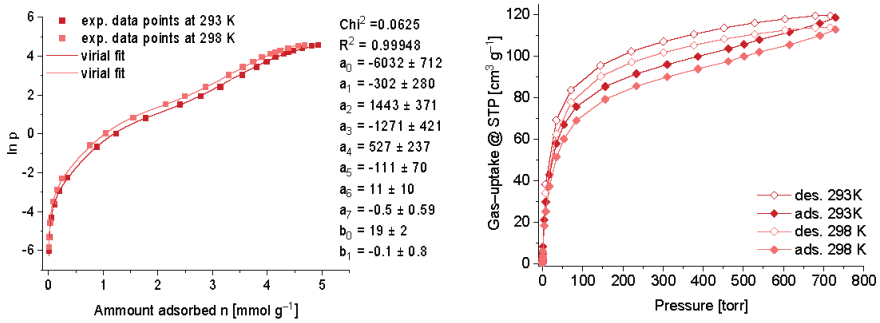

Figure S52. Virial analysis for SO_2 adsorption isotherms of Zr-Fum at 293 K and 298 K with the fitting parameters (virial coefficients) a_i and b_i.

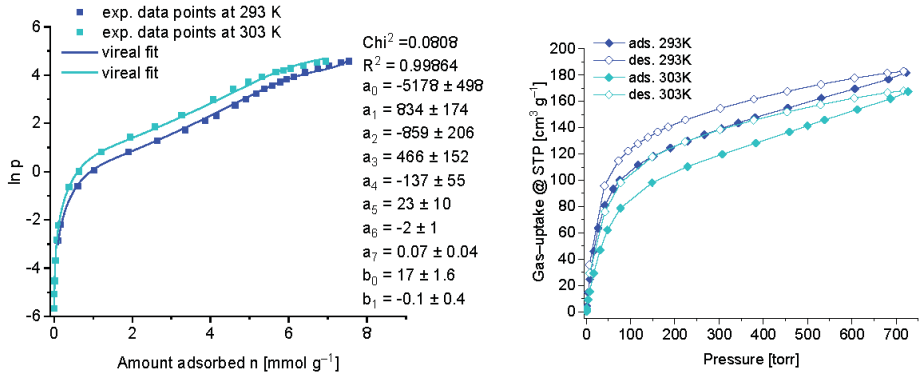

Figure S53. Virial analysis for SO_2 adsorption isotherms of Al-Fum at 293 K and 303 K with the fitting parameters (virial coefficients) a_i and b_i.

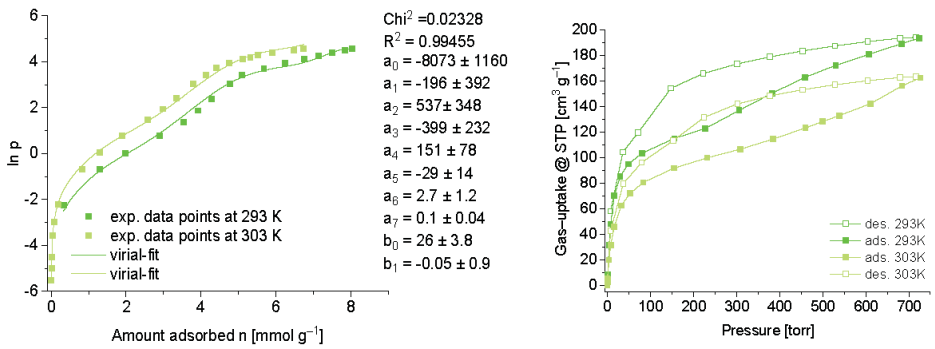

Figure S54. Virial analysis for SO_2 adsorption isotherms of NH_2-MIL-53(Al) at 293 K and 303 K with the fitting parameters (virial coefficients) a_i and b_i.

S7 DFT Calculations

We used two different approaches to locate possible binding sites and binding energies for Zr-Fum and Al-Fum *via* density functional theory (DFT) calculation simulations. The reason for these different approaches is found in the nature of the framework structures. Zr-Fum forms octahedral metal clusters which are suitable for a modeling approach using a single SBU together with attached ligands. Contrary Al-Fum forms infinite $\{Al(OH)(O_2C\text{-})_2\}$ chains. When the Al-chain is cut and subsequently optimized the former linear chain undergoes significant deformation. Thus, for Al-Fum, the more complex periodic approach is more suitable to locate binding sites of potential guest molecules.

S7.1 DFT Calculations for Zr-Fum

DFT calculations were performed with Becke, three-parameter, Lee-Yang-Parr (B3LYP) functional by using the Gaussian 16 software.[25] We used three model systems (Figure S55) which were derived from the crystal structure of Zr-Fum (CCDC no. 1002678, Refcode BOHKAM), and which resemble the different local environments of the pore surface cavity pockets around the $\{Zr_6(\mu_3\text{-}O)(\mu_3OH)(O_2C\text{-})_{12}\}$ cluster. Hydrogen atoms were added to no-longer metal-binding carboxyl groups of now terminal fumarate ligands. For less computation time and costs, the linkers which were not part of the cavity pockets were simplified to terminal formiate, HCOO-groups . Each model was set as the initial configuration for geometry optimization by the B3LYP-D3 method.[26] The double-ζ basis set LANL2DZ was used for Zr-atoms and the 6-311G** basis set was used for non-metal atoms (C, H, O and S). In structure optimization, the Zr atoms, as well as the outside carbon atoms of linkers, were fixed according to their coordination position in the experimental crystal structure.

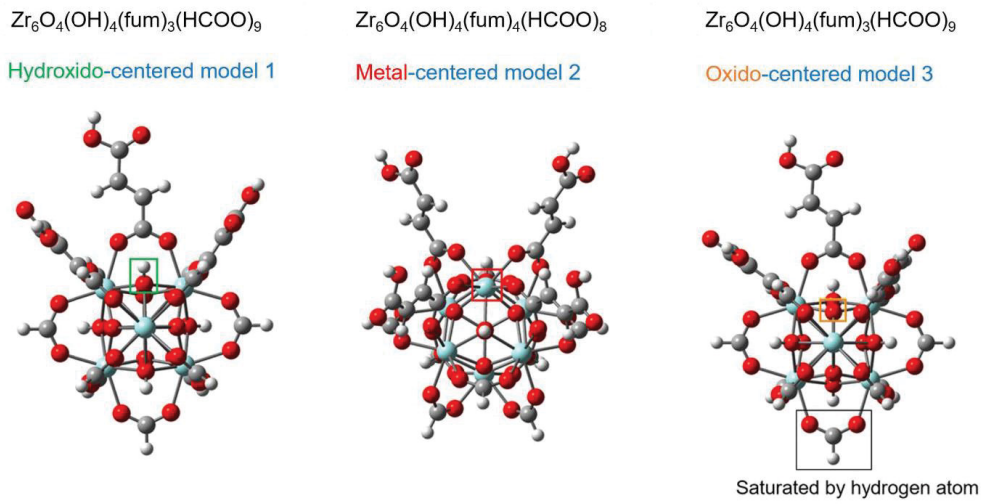

Figure S55. Simplified models of Zr-Fum to determine SO_2 binding sites *via* DFT calculations.

The SO_2 molecule was manually placed on each of the optimized Zr-Fum configurations with a different site at various positions, and then the fully relaxed optimizations of the SO_2···Zr-Fum models were performed. The binding energies of the SO_2 molecule with Zr-Fum were calculated by the dispersion corrected B3LYP-D3 functional along with 6-311G**. The basis set superposition error (BSSE) was corrected by the counterpoise method.[27] Thus, the binding energy is given by eq. 12.

$$\Delta E = E_{MOF/SO2} - (E_{MOF} + E_{SO2}) + E_{BSSE} \qquad (12)$$

Table S5. Calculated binding energies for potential SO_2 binding sites in Zr-Fum.

Binding-site	Model	MOF···SO_2 [Hartree-energy]	MOF [Hartree-energy]	SO_2 [Hartree-energy]	BSSE [Hartree-energy]	Binding energy [kJ mol^{-1}]
1	Hydroxide-centered	-4503.590028	-3954.904287	-548.658202	0.007925	-51.5
2	Metal-centered	-4769.654488	-4220.971984	-548.658326	0.008571	-41.0
3	Oxido-centered	-4503.583418	-3954.904096	-548.658454	0.007562	-34.9
4	Oxido-centered	-4503.582641	-3954.904443	-548.658485	0.007982	-30.8

Table S6. Representative non–covalent bonds between the Zr-Fum framework and SO_2 molecules, and binding energies based on DFT calculations.

Interaction	Contact distance [Å]	Binding energy [kJ mol^{-1}]
model 1: Binding site 1		–51.5
OH···OSO	1.88	
(fum)C···SO_2	3.26	
	3.37	
	3.37	
(fum)O···SO_2	3.33	
model 2: Binding site 2		–41.0
(fum)H ··OSO	2.44	
	2.67	
	2.68	
(fum)O···SO_2	2.77	
(fum)C ···SO_2	3.68	
model 3: Binding site 3		–34.9
(fum)H···OSO	2.75	
(fum)C···OSO	2.96	
	2.98	
	3.20	
(fum)C ···SO_2	3.17	
	3.30	
model 3: Binding site 4		–30.8
(fum)C ···SO_2	3.18	
	3.33	
(fum)H···SO_2	3.36	
(fum)O···SO_2	3.39	
	3.46	

S7.2 DFT Calculations for Al-MOFs

Quantum mechanical calculations for the Al-MOFs Al-Fum and NH_2-MIL-53(Al) alone and with adsorbed SO_2 were performed using DFT and the Quantum-Espresso software.[28] The crystal structure of Al-Fum/NH_2-MIL-53(Al) served as starting geometry. Oxygen atoms belonging to guest water molecules in Al-Fum were removed, and hydrogen atoms were added to the fumarate linker carbon atoms and oxygen atoms forming OH-bridges, which were not reported in the cif-structure file. The structures of Al-Fum and NH_2-MIL-53(Al) were geometry-optimized using the Broyden-Fletcher-Goldfarb-Shanno (BFGS) scheme, ultrasoft Rappe-Rabe-Kaxiras-Joannopoulos(RRKJ)–type pseudopotentials and the generalized gradient approximation (GGA) with Perdew-Burke-Enzerhof (PBE) exchange-correlation. To account for dispersion effects, the semi-empirical Grimme D3-correction scheme was applied.[29] Calculations were performed using the Monkhorst pack scheme with a 2 x 2 x 2 k-point mesh, an energy cutoff of 70 Rydberg and a charge cutoff of 700 Rydberg. Geometry optimizations were performed by (a) allowing the cell parameter to fully relax and (b) by fixing the cell parameters to the experimental values. After geometry optimization of the fully-relaxed Al-Fum/NH_2-MIL-53(Al) structure (a), SO_2 was placed at various locations and the geometries were allowed to fully relax. To compute the binding energy of SO_2, we optimized a single SO_2 molecule in an empty cell of the same size as the Al-Fum/NH_2-MIL-53(Al) structure and under the same conditions stated before. The binding energy was then obtained as the difference between the sum of energies of Al-Fum/NH_2-MIL-53(Al) and SO_2 and the energy of Al-Fum/NH_2-MIL-53(Al) including the adsorbed SO_2 molecule.

Freely optimized structure (both PBE-D3) Constrained structure

Freely optimized structure	Constrained structure
a = 6.7581	a = 6.8419
b = 12.9714	b = 12.0877
c = 14.3752	c = 14.2070
α = 90.00°	α = 90.00°
β = 128.11°	β = 122.55°
γ = 90.00°	γ = 90.00°
V= 6691.4262 bohr³	V= 6683.7687 bohr³
E = 0.00 kJ/mol	E= 71.65 kJ/mol

Figure S56. Geometries and structure parameters of DFT-D3 optimized Al-Fum.

Freely optimized structure (both PBE-D3) Constrained structure

a = 6.8078
b = 16.8583
c = 13.0258
α = 89.97°
β = 90.29°
γ = 89.66°
V= 10088.1575 bohr³
E = 0.00 kJ/mol

a= 6.6425
b = 16.3870
c = 13.3679
α = 90.00°
β = 90.00°
γ = 90.00°
V= 9819.5325 bohr³
E= 19.80 kJ/mol

Figure S57. Geometries and structure parameters of DFT-D3 optimized NH_2-MIL-53(Al).

Table S7. Representative non–covalent bonds between the Al-Fum framework and SO_2 molecules, and binding energies based on DFT calculations.

Bond type	Contact distance [Å]	Binding energy [kJ mol^{-1}]
Binding site 1		–51.1
OH···OSO	1.98	
(fum)H···OSO	2.72	
(fum)O···SO_2	3.11	
(fum)C···SO_2	3.43	
Binding site 2		–49.5
OH···OSO	2.05	
	2.80	
(fum)O···SO_2	3.35	
	3.44	
Binding site 3		–48.8
OH···OSO	2.04	
	2.18	
(fum)H···OSO	3.09	
	3.30	
Binding site 4a		–41.0
OH···OSO	2.12	
(fum)H ··OSO	2.49	
(fum)O···SO_2	3.69	
Binding site 4b		–41.0
OH···OSO	2.82	
(fum)H ··OSO	3.19	
(fum)O···OSO	3.57	

Table S8. Representative non–covalent bonds between the NH_2-MIL-53(Al) framework and SO_2 molecules, and binding energies based on DFT calculations.

Bond type	Contact distance [Å]	Binding energy [kJ mol^{-1}]
Binding site 1		–67.3
NH···OSO	1.97	
	3.24	
N···SO_2	2.56	
C_6-π ··SO_2	3.35	
Binding site 2		–58.2
NH···OSO	1.97	
C_6-π ··SO_2	2.99	
	3.19	
(BDC)H ·· OSO	3.53	
Binding site 3		–55.1
NH···OSO	1.99	
(BDC)H···OSO	2.58	
(BDC)O···SO_2	3.48	
Binding site 4		–49.1
NH···OSO	2.17	
	2.79	
C_6-π ··OSO	2.95	
OH···OSO	2.19	

S7.3 Monte-Carlo-simulations of adsorption isotherms

Atomic partial charges for the DFT-optimized structures (a) and (b) of Al-Fum were generated with the REPEAT method[30] and the CP2K program.[31] Atoms were described using DZVP-MOLOPT-GTH basis sets and corresponding GTH-PBE pseudopotentials. Simulations of SO_2-adsorption isotherms were performed with the program Cassandra[32] using a fixed 7x4x4 supercell and Lennard-Jones parameters from the Universal Force-Field (UFF)[33] for C, H and O atoms and UFF4MOF parameters [34] for Al. The SO_2-molecule was described as a rigid entity using the parameter set developed by Ketko et al.[35] For each model, additional simulations were performed where the Lennard-Jones parameter ε was set to zero for all Al atoms, thus allowing only electrostatic interactions with this atom type. A similar strategy was successfully applied by Borges et al. to obtain water adsorption isotherms in MOFs containing Al.[36,37] Adsorption isotherm simulations were conducted in the Grand-Canonical ensemble at 293 K with $2x10^7$ Monte-Carlo steps for equilibration and production phases. The chemical potential of SO_2 was determined for each pressure point using the Peng-Robinson equation of state.[38]

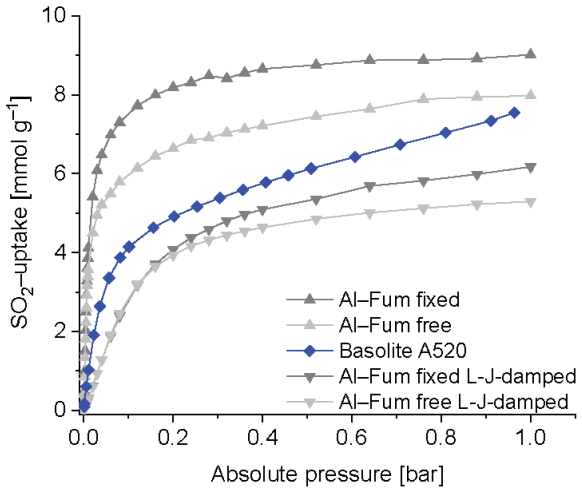

Figure S58. SO_2-adsorption of Al-Fum at 293 K: fixed structure (dark gray), freely optimized structure (light gray). Lennard-Jones interactions of aluminum are considered to 100 % (triangles pointing upwards) or 0 % (triangles pointing downwards).

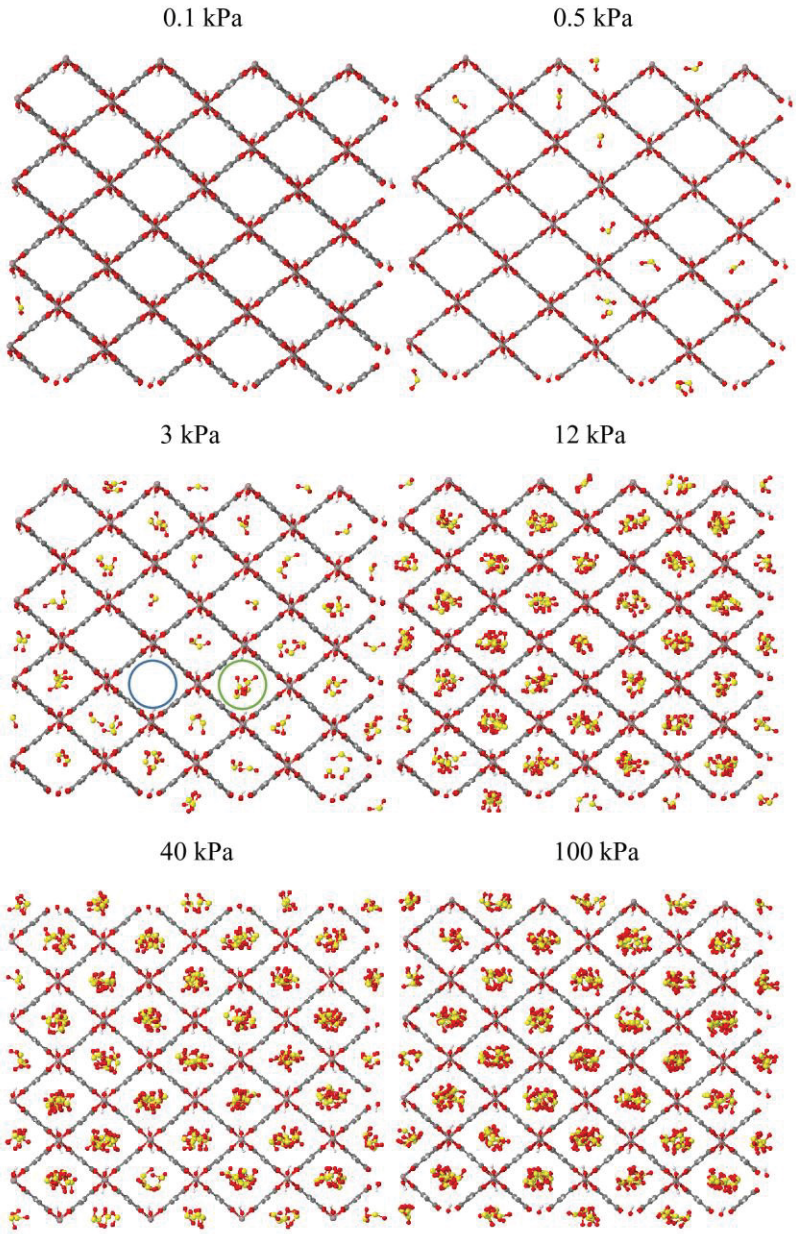

Figure S59. Snapshots of the pore filling of SO_2 in Al-Fum at 0.1-100 kPa and 293 K. The circles for 3 kPa emphasize the empty (blue) and multiple-SO_2-filled pores (green)

S8 Comparison with Literature

Table S9. Comparison of SO_2 sorption data from this work with the literature.

Material	SO_2-uptake [mmol·g^{-1}]			Temp. [K]	BET [m^2 g^{-1}]	Total pore-volume [cm^3 g^{-1}]	Pore width [Å]	Lit.
	0.01 bar	0.1 bar	1 bar					
Zr-Fum	1.3	2.9	6.5	293	600	0.290	4.8; 5.6; 7.4[13]	this work
MOF-808	2.1	3.6	14.6	293	1190	0.749	4.8; 18.4[13]	this work
DUT-67(Zr)	0.7	2.3	9.0	293	1260	0.535	8.8; 16.6[13]	this work
NU-1000	0.6	2.6	12.2	293	1740	1.196	12; 29[39]	this work
MIL-53(Al)	0.4	3.3	10.5	293	1450	0.706	8.5[40]	this work
NH_2-MIL-53(Al)	2.0	4.3	8.0	293	1120	0.358	7.3[41]	this work
Al-Fum	1.0	4.1	7.5	293	970	0.447	5.8[16]	this work
MIL-53(tdc)(Al)	0.6	5.0	6.9	293	1000	0.415	8[7]	this work
CAU-10-H	1.2	3.7	4.8	293	600	0.258	6[42]	this work
MIL-100(Al)	0.4	2.5	16.3	293	1890	0.824	25; 29[43]	this work
NH_2-MIL-101(Al)	1.5	3.6	17.3	293	1770	1.001	25; 34[44]	this work
MIL-96(Al)	1.2	3.7	6.5	293	530	0.237	~4; ~11; 11[45]	this work
MIL-160	4.2	5.5	7.2	293	1170	0.460	5	49
NH_2-MIL-125(Ti)	3.0	7.9	10.8	293	1560	0.651	5-8[46]	49
MOF-177	0.3	1.0	25.7	293	4100	1.51	10.6-11.8[47,48]	49
MFM-202a	-	3.0	10.2	298	2220	-	-	50
MFM-300(Al)	-	-	7.7[a]	293	1370	0.375[b]	5.7	51, 52
MFM-300(In)	-	-	8.28	298	1071	0.419	-	53
MFM-300(Al)-MW	7.2	8.6	-	283	1272	0.58	5	54
MFM-305	-	5.1[a]	7.0	298	779	0.372	6.2	55
MFM-305-CH_3	-	4.4[a]	5.2	298	256	0.184	5.2	55
MFM-600	-	~3[a]	5.0	298	2281	-	-	56
MFM-601	-	~8[a]	12.3	298	3644	-	-	56
MFM-170	-	~6[a]	17.5	298	2408	0.88	12.8; 14.2;15.9	57
MFM-170-H_2O	-	-	13.0	298	2003	-	-	57
NU-1000	-	2.1	10.9	298	1970	-	-	58
MIL-101(Cr)-4F	~1.3[a]	4.6	18.4	298	2176	1.19		59
CAU-10-H	-	3.9	4.47	298	630	0.25	6[42]	60
MOF-505	-	-	12.9[a]	298	2216	0.73	8.3; 10.1	61
Fe-soc-MOF	-	7.3	11.7	298	1470	0.58		62
MIL-125(Ti)	-	3[a]	9.8[a]	298	1527	-	-	63
SIFSIX-1-Cu	3.43	8.74	11.01	298	-	-	-	64
SIFSIX-2-Cu-i	4.16	6.01	6.90	298	630	-	-	64
[Zn_2(oxo-dihbac)$_2$ (bipy)]	-	-	10.9	293	47/275[b]	0.059[b]/ 0.098[b]	4.5-6.5, 8	65
Ni(bdc)(ted)$_{0.5}$	-	4.54	9.97	298	1783	0.74	7.8	66
Zn(bdc)(ted)$_{0.5}$	-	-	4.41	298	1888	0.84	7.8	66
Mg-MOF-74	-	6.44	8.60	298	1206	-	-	66, 67
Ni-DMOF-TM	-	-	4.8[a]	298	940	0.459	-	68
UNAM-1	0.4[a]	1.6[a]	3.5	298	522	-	-	69

KAUST-8	-	2.3[a]	2.9[a]	298	250			70
KAUST-7	-	2.1[a]	2.6[a]	298	280			70
ELM-12	-	1.95	2.73	298	706	0.26	4.3-6.1	71
$Co_3[Co(CN)_6]_2$	-	-	2.5	298	712	-	-	72
$Zn_3[Co(CN)_6]_2$	-	-	1.8	298	700	-	-	72
FMOF-2	-	-	2.2	298	378	-	-	73

[a] read from isotherm, [b] from CO_2 sorption data (273 K)

References

(1) Wißmann, G.; Schaate, A.; Lilienthal, S.; Bremer, I.; Schneider, A. M.; Behrens, P. Modulated Synthesis of Zr-Fumarate MOF. *Microporous Mesoporous Mater.* **2012**, *152*, 64–70.

(2) Valekar, A. H.; Cho, K.-H.; Chitale, S. K.; Hong, D.-Y.; Cha, G.-Y.; Lee, U.-H.; Hwang, D. W.; Serre, C.; Chang, J.-S.; Hwang, Y. K. Catalytic Transfer Hydrogenation of Ethyl Levulinate to γ-Valerolactone over Zirconium-based Metal–Organic Frameworks. *Green Chem.* **2016**, *18*, 4542–4552.

(3) Reinsch, H.; Waitschat, S.; Chavan, S. M.; Lillerud, K. P.; Stock, N. A Facile "Green" Route for Scalable Batch Production and Continuous Synthesis of Zirconium MOFs. *Eur. J. Inorg. Chem.* **2016**, *2016*, 4490–4498.

(4) Wang, T. C.; Vermeulen, N. A.; Kim, I. S.; Martinson, A. B. F.; Stoddart, J. F.; Hupp, J. T.; Farha, O. K. Scalable Synthesis and Post-Modification of a Mesoporous Metal-Organic Framework called NU-1000. *Nat. Protoc.* **2016**, *11*, 149–162.

(5) Kim, J.; Kim, W. Y.; Ahn, W.-S. Amine-functionalized MIL-53(Al) for CO_2/N_2 Separation: Effect of Textural Properties. *Fuel* **2012**, *102*, 574–579.

(6) Cheng, X.; Zhang, A.; Hou, K.; Liu, M.; Wang, Y.; Song, C.; Zhang, G.; Guo, X. Size- And Morphology-Controlled NH_2-MIL-53(Al) prepared in DMF-Water mixed solvents. *Dalton Trans* **2013**, *42*, 13698–13705.

(7) Tannert, N.; Ernst, S.-J.; Jansen, C.; Bart, H.-J.; Henninger, S. K.; Janiak, C. Evaluation of the Highly Stable Metal–Organic Framework MIL-53(Al)-TDC (TDC = 2,5-thiophenedicarboxylate) as a new and promising adsorbent for heat transformation applications. *J. Mater. Chem. A* **2018**, *6*, 17706–17712.

(8) Reinsch, H.; van der Veen, M. A.; Gil, B.; Marszalek, B.; Verbiest, T.; de Vos, D.; Stock, N. Structures, Sorption Characteristics, and Nonlinear Optical Properties of a New Series of Highly Stable Aluminum MOFs. *Chem. Mater.* **2013**, *25*, 1, 17–26.

(9) Loiseau, T.; Lecroq, L.; Volkringer, C.; Marrot, J.; Férey, G.; Haouas, M.; Taulelle, F.; Bourrelly, S.; Llewellyn, P. L.; Latroche, M. MIL-96, a Porous Aluminum Trimesate 3D Structure Constructed from a Hexagonal Network of 18-Membered Rings and μ_3-Oxo-Centered Trinuclear Units. *J. Am. Chem. Soc.* **2006**, *128*, 10223–10230.

(10) Qiu, M.; Guan, Q.; Li, W. Controllable Assembly of Al-MIL-100 via an Inducing Occupied Effect and Ist Selective Adsorption Activity. *Cryst. Growth Des.* **2016**, *16*, 3639–3646.

(11) Serra-Crespo, P.; Ramos-Fernandez, E. V.; Gascon, J.; Kapteijn, F. Synthesis and Characterization of an Amino Functionalized MIL-101(Al); Separation and Catalytic Properties. *Chem. Mater.* **2011**, *23*, 2565–2572.

(12) K. Brandenburg, *DIAMOND*, Version 4.5; Crystal and Molecular Structure Visualization; Crystal Impact – K. Brandenburg & H. Putz Gbr., Bonn, Germany, 2009–2020.

(13) Furukawa, H.; Gándara, F.; Zhang, Y.-B.; Jiang, J.; Queen, W. L.; Hudson, M. R.; Yaghi, O. M. Water Adsorption in Porous Metal-Organic Frameworks and Related Materials. *J. Am. Chem. Soc.* **2014**, *136*, 4369–4381.

(14) Bon, V.; Senkovska, I.; Baburin, I. A.; Kaskel, S. Zr- and Hf-Based Metal–Organic Frameworks: Tracking Down the Polymorphism. *Cryst. Growth Des.* **2013**, *13*, 1231–1237.

(15) Mondloch, J. E.; Bury, W.; Fairen-Jimenez, D.; Kwon, S.; DeMarco, E. J.; Weston, M. H.; Sarjeant, A. A.; Nguyen, S. T.; Stair, P. C.; Snurr, R. Q.; Farha, O. K.; Hupp, J. T. Vapor-Phase Metalation by Atomic Layer Deposition in a Metal-Organic Framework. *J. Am. Chem. Soc.* **2013**, *135*, 10294–10297.

(16) Alvarez, E.; Guillou, N.; Martineau, C.; Bueken, B.; Van de Voorde, B.; Le Guillouzer, C.; Fabry, P.; Nouar, F.; Taulelle, F.; de Vos, D. Chang, J. S.; Cho, K. H.; Ramsahey, N.; Devic, T.; Daturi, M.; Maurin, G.; Serre, C. The Structure of the Aluminum Fumarate Metal-Organic Framework A520. *Angew. Chem.* **2015**, *127*, 3735–3739.

(17) Fröhlich, D.; Pantatosaki, E.; Kolokathis, P. D.; Markey, K.; Reinsch, H.; Baumgartner, M.; van der Veen, M. A.; Vos, D. E. de; Stock, N.; Papadopoulos, G. K.; Henninger, S. K.; Janiak, C. Water Adsorption Behaviour of CAU-10-H: A thorough Investigation of its Structure–Property Relationships. *J. Mater. Chem. A* **2016**, *4*, 11859–11869.

(18) Volkringer, C.; Popov, D.; Loiseau, T.; Férey, G.; Burghammer, M.; Riekel, C.; Haouas, M.; Taulelle, F. Synthesis, Single-Crystal X-ray Microdiffraction, and NMR Characterizations of the Giant Pore Metal-Organic Framework Aluminum Trimesate MIL-100. *Chem. Mater.* **2009**, *21*, 5695–5697.

(19) Loiseau, T.; Serre, C.; Huguenard, C.; Fink, G.; Taulelle, F.; Henry, M.; Bataille, T.; Férey, G. A Rationale for the Large Breathing of the Porous Aluminum Terephthalate (MIL-53) Upon Hydration. *Chem. Eur. J.* **2004**, *10*, 1373–1382.

(20) Chin, J. M.; Chen, E. Y.; Menon, A. G.; Tan, H. Y.; Hor, A. T. S.; Schreyer, M. K.; Xu, J. Tuning the Aspect Ratio of NH_2-MIL-53(Al) Microneedles and Nanorodsvia Coordination Modulation. *CrystEngComm* **2013**, *15*, 654–657.

(21) Lebedev, O. I.; Millange, F.; Serre, C.; van Tendeloo, G.; Férey, G. First Direct Imaging of Giant Pores of the Metal−Organic Framework MIL-101. *Chem. Mater.* **2005**, *17*, 6525–6527.

(22) https://www.coleparmer.com/chemical-resistance, retrieved November 3rd 2020.

(23) 3P INSTRUMENTS, 3P sim, Version 1.1.0.7, *Simulation and Evaluation Tool for mixSorb*, 3P INSTRUMENTS 2018.

(24) Turiel, E.; Perez-Conde, C.; Martin-Esteban, A. Assessment of the Cross-Reactivity and Binding Sites Characterisation of a Propazine-Imprinted Polymer Using the Langmuir-Freundlich Isotherm. *Analyst* **2003**, *128*, 137–141.

(25) Frisch, M. J.; Trucks, G. W.; Schlegel, H. B.; Scuseria, G. E.; Robb, M. A.; Cheeseman, J. R.; Scalmani, G.; Barone, V.; Petersson, G. A.; Nakatsuji, H.; Li, X.; Caricato, M.; Marenich, A. V.; Bloino, J.; Janesko, B. G.; Gomperts, R.; Mennucci, B.; Hratchian, H. P.; Ortiz, J. V.; Izmaylov, A. F.; Sonnenberg, J. L.; Williams-Young, D.; Ding, F.; Lipparini, F.; Egidi, F.; Goings, J.; Peng, B.; Petrone, A.; Henderson, T.; Ranasinghe, D.; Zakrzewski, V. G.; Gao, J.; Rega, N.; Zheng, G.; Liang, W.; Hada, M.; Ehara, M.; Toyota, K.; Fukuda, R.; Hasegawa, J.; Ishida, M.; Nakajima, T.; Honda, Y.; Kitao, O.; Nakai, H.; Vreven, T.; Throssell, K.; Montgomery, J. A., Jr.; Peralta, J. E.; Ogliaro, F.; Bearpark, M. J.; Heyd, J. J.; Brothers, E. N.; Kudin, K. N.; Staroverov, V. N.; Keith, T. A.; Kobayashi, R.; Normand, J.; Raghavachari, K.; Rendell, A. P.; Burant, J. C.; Iyengar, S. S.; Tomasi, J.; Cossi, M.; Millam, J. M.; Klene, M.; Adamo, C.; Cammi, R.; Ochterski, J. W.; Martin, R. L.; Morokuma, K.; Farkas, O.; Foresman, J. B.; Fox, D. J.Fox. *Gaussian 16, Revision A.03*; Gaussian, Inc., Wallingford CT, 2016.

(26) Grimme, S; Antony, J.; Ehrlich, S.; Krieg, H. *J. Chem. Phys.* **2010**, *132*, 154104–154122.

(27) Boys, S. F.; Bernardi, F. *Mol. Phys.* **1970**, *19*, 553–566.

(28) Giannozzi, P.; Baroni, S.; Bonini, N.; Calandra, M.; Car, R.;Cavazzoni, C.; Ceresoli, D.; Chiarotti, G. L.; Cococcioni, M.; Dabo, I.; Dal Corso, A.; de Gironcoli, S.; Fabris, S.; Fratesi, G.; Gebauer, R.; Gerstmann, U.; Gougoussis, C.; Kokalj, A.; Lazzeri, M.; Martin-Samos, L.; Marzari, N.; Mauri, F.; Mazzarello, R.; Paolini, S.; Pasquarello, A.; Paulatto, L.; Sbraccia, C.; Scandolo, S.; Sclauzero, G.; Seitsonen, A. P.; Smogunov, A.; Umari, P.; Wentzcovitch, R. M.

QUANTUM ESPRESSO: A Modular and Open-Source Software Project for Quantum Simulations of Materials. *J. Phys.: Condens. Matter* **2009**, *21*, 395502, 1-19.

(29) Grimme, S. Semiempirical GGA-Type Density Functional Constructed with a Long-Range Dispersion Correction. *J. Comput. Chem.* **2006**, *27*, 1787–1799.

(30) Gabrieli, A.; Sant, M.; Demonties, P.; Suffritti, G. B. Partial Charges in Periodic Systems: Improving Electrostatic Potential (ESP) Fitting via Total Dipole Fluctuations and Multiframe Approaches. *J. Chem. Theory Comput.* **2015**, *11*, 3829-3843.

(31) Kühne, T. D., Iannuzzi, M., Del Ben, M., Rybkin, V. V, Seewald, P., Stein, F., Laino, T., Khaliullin, R. Z., Schütt, O., Schiffmann, F., Golze, D., Wilhelm, J., Chulkov, S., Bani-Hashemian, M. H., Weber, V., Borštnik, U., Taillefumier, M., Jakobovits, A. S., Lazzaro, A., Pabst, H.; Müller, T.; Schade, R.; Guidon, M.; Adermatt, S.; Holmberg, N.; Schenter, G. K.; Hehn, A.; Bussy, A.; Belleflamme, F.; Tabacchi, G.; Glöß, A.; Lass, M.; Bethune, I.; Mundy, C. J.; Plessl, C.; Watkins, M.; VandeVondele, J. CP2K: An electronic structure and molecular dynamics software package - Quickstep: Efficient and accurate electronic structure calculations. *J. Chem. Phys.* **2020**, *152*, 194103.

(32) Shah, J. K., Marin-Rimoldi, E., Mullen, R. G., Keene, B. P., Khan, S., Paluch, A. S., Rai, N., Romanielo, L. L., Rosch, T. W., Yoo, B.; Maginn, E. J. Cassandra: An open source Monte Carlo package for molecular simulation. *J. Comput. Chem.* **2017**, *38*, 1727–1739.

(33) Rappe, A. K., Casewit, C. J., Colwell, K. S., Goddard, W. A.; Skiff, W. M. UFF, a Full Periodic Table Force Field for Molecular Mechanics and Molecular Dynamics imulations. *J. Am. Chem. Soc.* **1992**, *114*, 10024–10035.

(34) Coupry, D. E., Addicoat, M. A.; Heine, T. Extension of the Universal Force Field for Metal–Organic Frameworks. *J. Chem. Theory Comput.* **2016**, *12*, 5215–5225.

(35) Ketko, M. H., Kamath, G.; Potoff, J. J. Development of an Optimized Intermolecular Potential for Sulfur Dioxide. *J. Phys. Chem. B* **2011**, *115*, 4949–4954.

(36) Cadiau, A., Lee, J. S., Damasceno Borges, D., Fabry, P., Devic, T., Wharmby, M. T., Martineau, C., Foucher, D., Taulelle, F., Jun, C.-H., Hwang, Y. K., Stock, N., De Lange, M. F., Kapteijn, F., Gascon, J., Maurin, G., Chang, J.-S.; Serre, C. Design of Hydrophilic Metal Organic Framework Water Adsorbents for Heat Reallocation. *Adv. Mater.* **2015**, *27*, 4775–4780.

(37) Damasceno Borges, D., Maurin, G.; Galvão, D. S. Design of Porous Metal-Organic Frameworks for Adsorption Driven Thermal Batteries. *MRS Adv.* **2017**, *2*, 519–524.

(38) Peng, D.-Y.; Robinson, D. B. A New Two-Constant Equation of State. *Ind. Eng. Chem. Fundam.* **1976**, *15*, 59–64.

(39) Islamoglu, T.; Otake, K.-I.; Li, P.; Buru, C. T.; Peters, A. W.; Akpinar, I.; Garibay, S. J.; Farha, O. K. Revisiting the Structural Homogeneity of NU-1000, a Zr-Based Metal–Organic Framework. *CrystEngComm* **2018**, *20*, 5913–5918.

(40) Loiseau, T.; Serre, C.; Huguenard, C.; Fink, G.; Taulelle, F.; Henry, M.; Bataille, T.; Férey, G. A Rationale for the Large Breathing of the Porous Aluminum Terephthalate (MIL-53) Upon Hydration. *Chem. Eur. J.* **2004**, *10*, 1373–1382.

(41) Gascon, J.; Aktay, U.; Hernandezalonso, M.;Vanklink, G.; Kkapteijn, F. Amino-Based Metal-Organic Frameworks as Stable, Highly Active Basic Catalysts. *J. Catal.* **2009**, *261*, 75–87.

(42) Teo, H. W. B.; Chakraborty, A. Water Adsorption on Various Metal Organic Frameworks. *IOP Conf. Ser.: Mater. Sci. Eng.* **2017**, *272*, 1–5.

(43) Jeremias, F.; Khutia, A.; Henninger, S. K.; Janiak, C. MIL-100(Al, Fe) as water adsorbents for heat transformation purposes—a promising application. *J. Mater. Chem.* **2012**, *22*, 10148–10151.

(44) Navarro-Sánchez, J.; Almora-Barrios, N.; Lerma-Berlanga, B.; Ruiz-Pernía, J. J.; Lorenz-Fonfria, V. A.; Tuñón, I.; Martí-Gastaldo, C. Translocation of Enzymes into a Mesoporous MOF for Enhanced Catalytic Activity under Extreme Conditions. *Chem. Sci.* **2019**, *10*, 4082–4088.

(45) Benzaqui, M.; Pillai, R. S.; Sabetghadam, A.; Benoit, V.; Normand, P.; Marrot, J.; Menguy, N.; Montero, D.; Shepard, W.; Tissot, A.; Martineau-Corcos, C.; Sicard, C.; Milhaylov, M.; Carn, F.; Beurroies, I.; Llewellyn, P. L.; De Weireld, G.; Hadjiivanov, K.; Gascon. J.; Kapteijn, F.; Maurin, G; Steunou, N.; Serre, C. Revisiting the Aluminum Trimesate-Based MOF (MIL-96): From Structure Determination to the Processing of Mixed Matrix Membranes for CO_2 Capture. *Chem. Mater.* **2017**, *29*, 10326–10338.

(46) Fan, Y.-H.; Zhang, S.-W.; Qin, S.-B.; Li, X.-S.; Qi, S.-H. An Enhanced Adsorption of Organic Dyes onto NH_2 Functionalization Titanium-Based Metal-Organic Frameworks and the Mechanism Investigation. *Microporous Mesoporous Mater.* **2018**, *263*, 120–127.

(47) Saha, D.; Deng, S. Hydrogen Adsorption on Metal-Organic Framework MOF-177. *Tsinghua Sci. Technol.* **2010**, *15*, 363–376.

(48) Peterson, G. W.; Mahle, J.; Balboa, A.; Wagner, G.; Sewell, T.; Karwacki, C. J. Defense Technical Information Center: Fort Belvoir, VA, 2008.

(49) Brandt, P.; Nuhnen, A.; Lange, M.; Möllmer, J.; Weingart, O.; Janiak, C. Metal–Organic Frameworks with Potential Application for SO_2 Separation and Flue Gas Desulfurization. *ACS Appl. Mater. Interfaces* **2019**, *11*, 17350–17358.

(50) Yang, S.; Liu, L.; Sun, J.; Thomas, K. M.; Davies, A. J.; George, M. W.; Blake, A. J.; Hill, A. H.; Fitch, A. N.; Tang, C. C.; Schröder, M. Irreversible Network Transformation in a Dynamic Porous Host Catalyzed by Sulfur Dioxide. *J. Am. Chem. Soc.* **2013**, *135*, 4954–4957.
(51) Yang, S.; Sun, J.; Ramirez-Cuesta, A. J.; Callear, S. K.; David, W. I. F.; Anderson, D. P.; Newby, R.; Blake, A. J.; Parker, J. E.; Tang, C. C.; Schröder, M. Selectivity and Direct Visualization of Carbon Dioxide and Sulfur Dioxide in a Decorated Porous Host. *Nat. Chem.* **2012**, *4*, 887–894.
(52) Han, X.; Godfrey, H. G. W.; Briggs, L.; Davies, A. J.; Cheng, Y.; Daemen, L. L.; Sheveleva, A. M.; Tuna, F.; McInnes, E. J. L.; Sun, J.;Drathen, C.; George, M. W.; Ramirez-Cuesta, A. J.; Thomas, K. M.; Yang, S.; Schröder, M. Reversible Adsorption of Nitrogen Dioxide Within a Robust Porous Metal-Organic Framework. *Nat. Mater.* **2018**, *17*, 691–696.
(53) Savage, M.; Cheng, Y.; Easun, T. L.; Eyley, J. E.; Argent, S. P.; Warren, M. R.; Lewis, W.; Murray, C.; Tang, C. C.; Frogley, M. D.; Cinque, G.; Sun, J.; Rudić, S.; Murden, R. T.; Benham, M. J.; Fitch, A. N.; Blake, A. J.; Ramirez-Cuesta, A. J.; Yang, S.; Schröder, M. Selective Adsorption of Sulfur Dioxide in a Robust Metal-Organic Framework Material. *Adv. Mater.* **2016**, *28*, 8705–8711.
(54) Thomas-Hillman, I.; Stevens, L. A.; Lange, M.; Möllmer, J.; Lewis, W.; Dodds, C.; Kingman, S. W.; Laybourn, A. Developing a Sustainable Route to Environmentally Relevant Metal–Organic Frameworks: Ultra-Rapid Synthesis of MFM-300(Al) using Microwave Heating. *Green Chem.* **2019**, *21*, 5039–5045.
(55) Li, L.; da Silva, I.; Kolokolov, D. I.; Han, X.; Li, J.; Smith, G.; Cheng, Y.; Daemen, L. L.; Morris, C. G.; Godfrey, H. G. W.;Jacques, N. M.; Zhang. X.; Manuel. P.; Frogley. M. D.; Murray. C. A.; Ramirez-Cuesta, A. J.; Cinque, G. Tang, C. C.; Stepanov, A. G.; Yang, S.; Schröder, M. Post-Synthetic Modulation of the Charge Distribution in a Metal–Organic Framework for Optimal Binding of Carbon Dioxide and Sulfur Dioxide. *Chem. Sci.* **2019**, *10*, 1472–1482.
(56) Carter, J. H.; Han, X.; Moreau, F. Y.; da Silva, I.; Nevin, A.; Godfrey, H. G. W.; Tang, C. C.; Yang, S.; Schröder, M. Exceptional Adsorption and Binding of Sulfur Dioxide in a Robust Zirconium-Based Metal-Organic Framework. *J. Am. Chem. Soc.* **2018**, *140*, 15564–15567.
(57) Smith, G. L.; Eyley, J. E.; Han, X.; Zhang, X.; Li, J.; Jacques, N. M.; Godfrey, H. G. W.; Argent, S. P.; McCormick McPherson, L. J.; Teat, S. J.; Cheng, Y.; Frogley, M. D.; Cinque, G.; Day, S. J.; Tang, C. C.; Easun, T. L.; Rudić, S.; Ramires-Cuesta, A. J.; Yang, S.; Schröder,

M. Reversible Coordinative Binding and Separation of Sulfur Dioxide in a Robust Metal-Organic Framework with Open Copper Sites. *Nat. Mater.* **2019**, *18*, 1358–1365.

(58) Gorla, S.; Díaz-Ramírez, M. L.; Abeynayake, N. S.; Kaphan, D. M.; Williams, D. R.; Martis, V.; Lara-García, H. A.; Donnadieu, B.; Lopez, N.; Ibarra, I. A.; Montiel-Palma, V. Functionalized NU-1000 with an Iridium Organometallic Fragment: SO_2 Capture Enhancement. *ACS Appl. Mater. Interfaces* **2020**, *12*, 41758–41764.

(59) Martínez-Ahumada, E.; Díaz-Ramírez, M. L.; Lara-García, H. A.; Williams, D. R.; Martis, V.; Jancik, V.; Lima, E.; Ibarra, I. A. High and Reversible SO_2 Capture by a Chemically Stable Cr(III)-Based MOF. *J. Mater. Chem. A*, **2020**, *8*, 11515-11520.

(60) Zárate, J. A.; Domínguez-Ojeda, E.; Sánchez-González, E.; Martínez-Ahumada, E.; López-Cervantes, V. B.; Williams, D. R.; Martis, V.; Ibarra, I. A.; Alejandre, J. Reversible and Efficient SO_2 Capture by a Chemically stable MOF CAU-10: Experiments and Simulations. *Dalton Trans.* **2020**, *49*, 9203-9207.

(61) Song, X.-D.; Wang, S.; Hao, C.; Qiu, J.-S. Investigation of SO_2 Gas Adsorption in Metal–Organic Frameworks by Molecular Simulation. *Inorg. Chem. Commun.* **2014**, *46*, 277–281.

(62) Chen, Z.; Wang, X.; Cao, R.; Idrees, K. B.; Liu, X.; Wasson, M. C.; Farha, O. K. Water-Based Synthesis of a Stable Iron-Based Metal–Organic Framework for Capturing Toxic Gases. *ACS Materials Lett.* **2020**, 1129–1134.

(63) Mounfield, W. P.; Han, C.; Pang, S. H.; Tumuluri, U.; Jiao, Y.; Bhattacharyya, S.; Dutzer, M. R.; Nair, S.; Wu, Z.; Lively, R. P.; Sholl, D. S.; Walton, K. S. Synergistic Effects of Water and SO_2 on Degradation of MIL-125 in the Presence of Acid Gases. *J. Phys. Chem. C* **2016**, *120*, 27230–27240.

(64) Cui, X.; Yang, Q.; Yang, L.; Krishna, R.; Zhang, Z.; Bao, Z.; Wu, H.; Ren, Q.; Zhou, W.; Chen, B.; Xing, H. Ultrahigh and Selective SO_2 Uptake in Inorganic Anion-Pillared Hybrid Porous Materials. *Adv. Mater.* **2017**, *29*, 1606929.

(65) Glomb, S.; Woschko, D.; Makhloufi, G.; Janiak, C. Metal-Organic Frameworks with Internal Urea-Functionalized Dicarboxylate Linkers for SO_2 and NH_3 Adsorption. *ACS Appl. Mater. Interfaces* **2017**, *9*, 37419–37434.

(66) Tan, K.; Canepa, P.; Gong, Q.; Liu, J.; Johnson, D. H.; Dyevoich, A.; Thallapally, P. K.; Thonhauser, T.; Li, J.; Chabal, Y. J. Mechanism of Preferential Adsorption of SO_2 into Two Microporous Paddle Wheel Frameworks $M(bdc)(ted)_{0.5}$. *Chem. Mater.* **2013**, *25*, 4653–4662.

(67) Grant Glover, T.; Peterson, G. W.; Schindler, B. J.; Britt, D.; Yaghi, O. M. MOF-74 Building Unit has a Direct Impact on Toxic Gas Adsorption. *Chem. Eng. Sci.* **2011**, *66*, 163–170.

(68) Hungerford, J.; Bhattacharyya, S.; Tumuluri, U.; Nair, S.; Wu, Z.; Walton, K. S. DMOF-1 as a Representative MOF for SO_2 Adsorption in Both Humid and Dry Conditions. *J. Phys. Chem. C* **2018**, *122*, 23493–23500.

(69) Domínguez-González, R.; Rojas-León, I.; Martínez-Ahumada, E.; Martínez-Otero, D.; Lara-García, H. A.; Balmaseda-Era, J.; Ibarra, I. A.; Percástegui, E. G.; Jancik, V. UNAM-1: a Robust Cu I and Cu II containing 3D-Hydrogen-Bonded Framework with Permanent Porosity and Reversible SO_2 Sorption. *J. Mater. Chem. A* **2019**, *7*, 26812–26817.

(70) Tchalala, M. R.; Bhatt, P. M.; Chappanda, K. N.; Tavares, S. R.; Adil, K.; Belmabkhout, Y.; Shkurenko, A.; Cadiau, A.; Heymans, N.; Weireld, G. Maurin. G.; Salama, K. N.; Eddaoudi. M. Fluorinated MOF Platform for Selective Removal and Sensing of SO_2 from Flue Gas and Air. *Nat. Commun.* **2019**, *10*, 1328,1–10.

(71) Zhang, Y.; Zhang, P.; Yu, W.; Zhang, J.; Huang, J.; Wang, J.; Xu, M.; Deng, Q.; Zeng, Z.; Deng, S. Highly Selective and Reversible Sulfur Dioxide Adsorption on a Microporous Metal-Organic Framework via Polar Sites. *ACS Appl. Mater. Interfaces* **2019**, *11*, 10680–10688.

(72) Thallapally, P. K.; Motkuri, R. K.; Fernandez, C. A.; McGrail, B. P.; Behrooz, G. S. Prussian Blue Analogues for CO_2 and SO_2 Capture and Separation Applications. *Inorg. Chem.* **2010**, *49*, 4909–4915.

(73) Fernandez, C. A.; Thallapally, P. K.; Motkuri, R. K.; Nune, S. K.; Sumrak, J. C.; Tian, J.; Liu, J. Gas-Induced Expansion and Contraction of a Fluorinated Metal–Organic Framework. *Cryst. Growth Des.* **2010**, *10*, 1037–1039.

3.2 Comparative Evaluation of Different MOF and Non-MOF Porous Materials for SO_2 Adsorption and Separation Showing the Importance of Small Pore Diameters for Low–Pressure Uptake

Philipp Brandt, Alexander Nuhnen, Seçil Öztürk, Gülin Kurt, Jun Liang, Christoph Janiak

Adv. Sustainable Syst. **2021**, *5*, 2000285

DOI: 10.1002/adsu.202000285, Referenz [153]

Diese Studie beschäftigt sich mit der Untersuchung von SO_2-Adsorptionseigenschaften von prototypischen MOF Materialien und vergleicht diese mit Vertretern klassischerer poröser Materialklassen wie z.B. Zeolith, Silicagel, Aktivkohle oder kovalente triazinbasierte Netzwerke (CTF). Einzelgassorptionsmessungen wurden dazu genutzt, Rückschlüsse auf Einflussfaktoren der Materialeigenschaften bezüglich SO_2 ziehen zu können. Unabhängig von der Mikroporenstruktur und etwaiger Oberflächenmodifikationen der porösen Netzwerke, konnte ein linearer Zusammenhang zwischen zugänglicher Oberfläche und der SO_2-Adsorption bei 293 K und 1 bar beobachtet werden. Weiter zeigte sich, dass Netzwerke mit kleinen Mikroporen, entsprechend einem Durchmesser von ~4 – 8 Å, eine erhöhte SO_2-Aufnahme im Niedrigdruckbereich aufweisen. Die an den kinetischen Durchmesser von SO_2 (4,1 Å) angepassten Porengrößen scheinen eine effizientere Packung des Adsorptivs und starke SO_2···Porenwand Interaktionen zu ermöglichen.

In Bezug auf SO_2/CO_2-IAST-Selektivitäten bei SO_2-Molfraktionen von 0,01 und 1 bar konnten für MOF-Materialien Werte zwischen 41 und 34 erreicht werden, während die Selektivitätswerte für andere Materialklassen zwischen 265 und 9 schwankten. Unter zusätzlicher Berücksichtigung der Stabilität gegenüber feuchtem SO_2 zeigten CTF-1 und SAPO-34 die mitunter besten Ergebnisse.

Anteile an der Veröffentlichung:

- Idee, Konzept, experimentelle Arbeiten im Labor, Durchführung der Analytik (bis auf unten gelistete Ausnahmen)
- Aufarbeitung der Ergebnisse, Verfassung des Manuskripts und das Erstellen der Abbildungen und Tabellen. Korrektur durch Herrn Prof. Dr. Christoph Janiak.
- Synthese und Charakterisierung der Materialien mit Unterstützung von Frau Gülin Kurt, Frau Dr. Seçil Öztürk, Herrn Dr. Alexander Nuhnen und Herrn. Dr. Jun Liang.

RESEARCH ARTICLE

ADVANCED SUSTAINABLE SYSTEMS
www.advsustainsys.com

Comparative Evaluation of Different MOF and Non-MOF Porous Materials for SO_2 Adsorption and Separation Showing the Importance of Small Pore Diameters for Low-Pressure Uptake

*Philipp Brandt, Alexander Nuhnen, Seçil Öztürk, Gülin Kurt, Jun Liang, and Christoph Janiak**

Dedicated to Prof. Wolfgang Kaim on the occasion of his 70th birthday

The search for adsorbents for flue gas desulfurization processes is a current interest. For the first time, a comparative experimental study of SO_2 adsorption by porous materials including the prototypical metal–organic frameworks NH_2-MIL-101(Cr), Basolite F300 (Fe-1,3,5-BTC), HKUST-1 (Cu-BTC), the zeolitic imidazolate frameworks (ZIF)-8, ZIF-67, the alumosilicate Zeolite Y, the silicoaluminumphosphate (SAPO)-34, Silica gel 60, the covalent triazine framework (CTF)-1, and the active carbon Ketjenblack is carried out. Microporous materials with pore sizes in the range of 4–8 Å or with nitrogen heterocycles are found to be optimal for SO_2 uptake in the low-pressure range. The SO_2 uptake capacity at 1 bar correlates with the Brunauer-Emmett-Teller-surface area and pore volume rather independently of the surface microstructure. Zeolite Y and SAPO-34 are stable toward humid SO_2. The materials Zeolite Y and CTF-1(600) show the most promising SO_2/CO_2 selectivity results with an ideal adsorbed solution theory selectivity in the range of 265–149 and 63–43 with a mole fraction of 0.01–0.5 SO_2, respectively, at 293 K and 1 bar.

1. Introduction

Over 85% of the global energy is still generated from the burning of fossil fuels leading to the emission of exhaust fumes, containing CO_2, NO_x, and SO_2.[1,2] For example, 43% of total SO_2 emissions (62.7 Mt in 2018) are related to coal combustion (27.0 Mt in 2018).[3] Emission of the toxic and acidic anhydrate gas SO_2 is harmful to the biosphere and to human health both through air pollution and the formation of acid rain.[4,5]

The classic separation of SO_2 from flue gases is done by wet limestone-scrubbing or treatment by amine-based absorbents.[6] Flue gases generated by heavy oil- or coal combustion typically contain 500–3000 ppm of SO_2, which can be reduced by up to 95% using these established methods.[7] Importantly, traces of SO_2 of <500 ppm remain in the flue gas and are emitted into the atmosphere. Also, this residual SO_2 inactivates CO_2 adsorbents or poisons selective NO_x-oxidation catalysts.[8–10] A further decrease of the SO_2 content in flue gases is therefore of high economic and environmental importance. Reversible SO_2 physisorption by porous materials is seen as a means to achieve a further SO_2 reduction in flue gases.

Currently, the SO_2 adsorption with metal–organic frameworks (MOFs) experiences high interest.[11–27] Metal–organic frameworks are typically microporous metal-ligand coordination networks with uniform porosity, low density, and high tunability through the organic linker, that is, the metal-bridging ligand.[28] MOFs are actively studied in the role of adsorbents (particularly N_2, H_2, CO_2, CH_4, etc.) for prospective gas storage and gas separation[29–31] or the capture of toxic and polluting gases.[32–38] Yet, MOFs are often not of high chemical and hydrothermal stability.[39] An advantage of MOFs is clearly their designability, in particular their controllable pore size and modifiable pore surface is unmatched, yet, other porous materials may also feature good SO_2 uptake characteristics.

The main components of a typical flue gas mixture are N_2 or CO_2 with a minor part of SO_2 (500–3000 ppm).[7] Superior affinity to SO_2 over CO_2 and N_2, which conditions high selectivity, is essential for reaching high efficiency of separation. A promising material should also possess a high SO_2 single-gas

P. Brandt, Dr. A. Nuhnen, S. Öztürk, G. Kurt, Dr. J. Liang, Prof. C. Janiak
Institut für Anorganische und Analytische Chemie
Heinrich-Heine-Universität Düsseldorf
Düsseldorf 40204, Germany
E-mail: janiak@uni-duesseldorf.de
Dr. J. Liang, Prof. C. Janiak
Hoffmann Institute of Advanced Materials
Shenzhen Polytechnic
7098 Liuxian Blvd, Nanshan District, Shenzhen 518055, China
The ORCID identification number(s) for the author(s) of this article can be found under https://doi.org/10.1002/adsu.202000285.

DOI: 10.1002/adsu.202000285

adsorption capacity in the low-pressure range without appreciable hysteresis. The overall potential of an SO_2 adsorbent depends also on stability and recyclability. SO_2 sorption materials should withstand corrosive conditions under dry and humid SO_2 exposure without a decrease in adsorption capability.[40] Further, the reversibility of the SO_2 adsorption at near room temperatures and energy-efficient recovery is crucial.[41] The prospective porous materials for reversible physisorption should be microporous (d_{pore} < 2 nm), as adsorption should occur at low pressures to secure the removal of the relevant trace amounts of SO_2 from flue gases.[41]

In view of the current high interest on the physisorption of SO_2 with MOFs we are critically comparing here selected MOFs with other selected porous materials, namely the alumosilicate Zeolite Y, the silicoaluminumphosphate (SAPO)-34, Silica gel 60, the covalent triazine framework (CTF)-1, and the active carbon Ketjenblack. The collected SO_2 adsorption data were used to verify existing simulation calculations[42–44] and assess the materials for their capabilities to remove low SO_2 concentrations from $N_2/CO_2/SO_2$ gas mixtures, with quantitative assessment of SO_2/CO_2 selectivities using the ideal adsorbed solution theory (IAST) model. Furthermore, the relative stabilities toward dry and humid SO_2 gas were determined via a follow-up porosity and powder X-ray diffraction pattern analysis.

2. Results and Discussion

We selected the MOFs NH_2-Matériaux de l'Institut Lavoisier (MIL)-101(Cr)[45,46], Basolite F300[47,48] (also named Fe-1,3,5-benzenetricarboxylate (BTC)), Hong Kong University of Science and Technology (HKUST)-1[49,50] (also named Cu-BTC), the zeolitic imidazolate frameworks (ZIF)-8,[51,52] and ZIF-67[53,54] which can all be considered highly prototypical and which are intensely investigated toward application-oriented properties (see the Supporting Information for information on their structure). From the other porous material classes Zeolite Y,[55] the silicoaluminum phosphate SAPO-34,[56] Silica gel 60, the carbon–nitrogen framework CTF-1[57] (covalent triazine framework), and the active carbon Ketjenblack were investigated for SO_2 physisorption. Ketjenblack is a form of active carbon with high electroconductivity and a broad pore size distribution with a somewhat more ordered structure compared to other active carbons.[58,59] With this selection of materials we aim to cover a broad range of properties, e.g., pore size, functionality, open metal sites, etc. for comparative purposes (see Section S1, Supporting Information, for details). The MOFs NH_2-MIL-101(Cr), HKUST-1, ZIF-8, and ZIF-67 were synthesized according to literature procedures and their identity was established by powder X-ray diffractometry (PXRD) and porosity analysis from nitrogen sorption isotherms (see the Supporting Information for details). The materials Basolite F300, Zeolite Y, SAPO-34, Silica gel 60, and Ketjenblack were purchased from commercial sources (see the Supporting Information for further information).

The individual SO_2 adsorption isotherms were measured at 293 K (**Figures 1** and **2**, for a combination, see Figure S22, Supporting Information) and the corresponding data together with the porosity characteristics from nitrogen sorption isotherms is given in **Table 1**. For clarity in the SO_2 sorption isotherm diagrams we will present and discuss the MOF and the non-MOF materials separately.

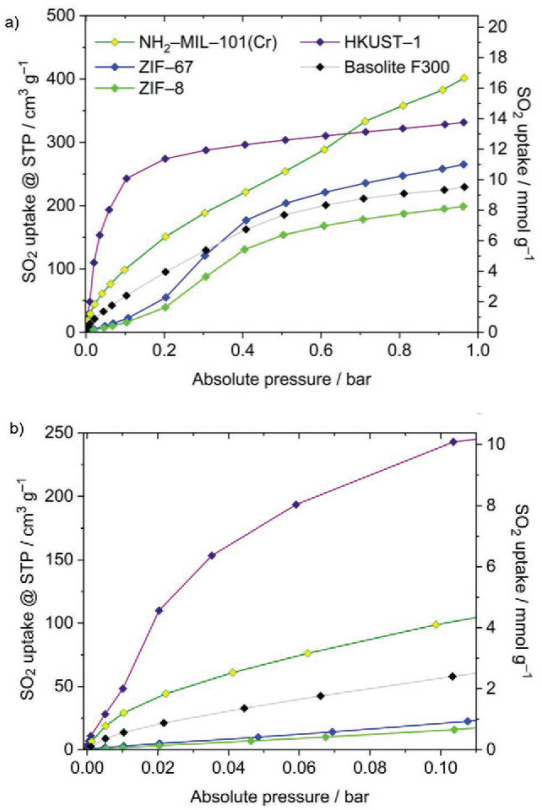

Figure 1. SO_2 adsorption isotherms (293 K) of the examined MOF materials: a) 0.001–1 bar and b) 0.001–0.11 bar. SO_2 desorption isotherms are omitted for clarity and are displayed in Figures S23–S29 in the Supporting Information.

2.1. SO_2 Adsorption by MOF Materials

The amino-functionalized MOF NH_2-MIL-101(Cr) shows a moderate rise in SO_2 uptake in the pressure range from 0.001 to 0.1 bar with an SO_2 uptake of 4.1 mmol g^{-1} at 0.1 bar. The SO_2 isotherm reflects a steady increase up to ambient pressures with a maximum SO_2 uptake of 16.7 mmol g^{-1} at 1 bar without reaching a saturation stage. The adsorption isotherm is far from leveling off at 1 bar. This can be explained by relatively large micropores with a diameter of 15.4 and 19.9 Å for NH_2-MIL-101(Cr) (vide infra).[70]

The amino functionalization of the MOFs was chosen as a possible factor, favoring adsorption of SO_2, interpretable both as an interaction between basic and acidic species or as an interaction between polar species with enhanced dipole–dipole interactions.[19] Interestingly, however, NH_2-MIL-101(Cr) shows no surface-specific enhancement of SO_2 uptake, i.e., the uptake per unit of the Brunauer-Emmett-Teller (BET) surface (see below),

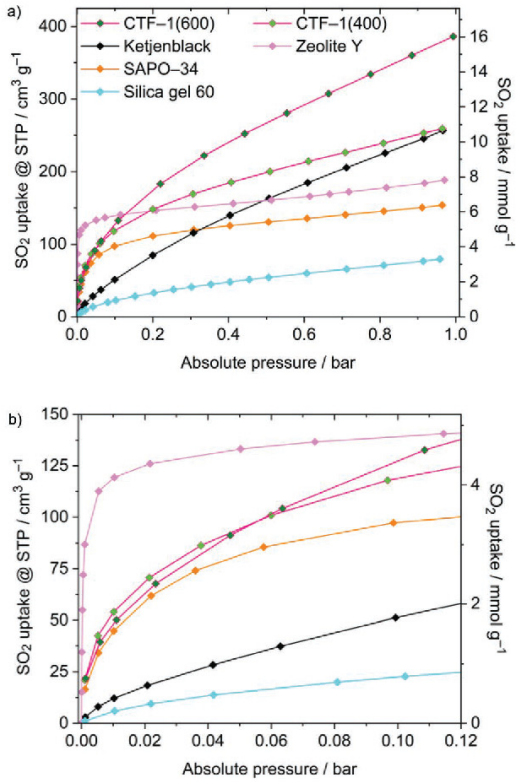

Figure 2. SO_2 adsorption isotherms (293 K) of the examined non-MOF materials: a) 0.001–1 bar and b) 0.001–0.12 bar. SO_2 desorption isotherms are omitted for clarity and are displayed in Figures S23–S29 in the Supporting Information.

compared to other materials in this study. Ibarra et al. recently investigated SO_2 adsorption in the fluorinated MIL-101(Cr)4-F which shows a roughly similar isotherm shape to the isoreticular amino-functionalized frameworks but with slightly higher SO_2 adsorption capacity with uptakes of 4.6 and 18.4 mmol g^{-1} at 0.1 and 1 bar, respectively, at 298 K and features exceptional stability against SO_2.[71] This is in agreement with a smaller enthalpy of adsorption near zero coverage, $\Delta H^0_{ads} = -36$ kJ mol^{-1} for NH_2-MIL-101(Cr) (Figure S35, Supporting Information) than $\Delta H^0_{ads} = -54$ kJ mol^{-1} for MIL-101(Cr)4-F.[71]

Basolite F300 shows somewhat lower SO_2 adsorption over the whole pressure range than NH_2-MIL-101(Cr), reaching 9.5 mmol g^{-1} at 1 bar.

The SO_2 isotherm of HKUST-1 features a single sharp increase in uptake to 10.1 mmol g^{-1} at 0.1 bar, followed by a fast transition to near saturation with a maximum SO_2 uptake of 13.8 mmol g^{-1} at 1 bar (a type-Ib isotherm by the International Union of Pure and Applied Chemistry (IUPAC) classification).[72] To the best of our knowledge HKUST-1 shows one of the highest SO_2 capacities with a type-I isotherm under ambient temperature and pressure ever reported. The remarkable uptake of HKUST-1 can be explained by the abundance of open metal sites (coordinatively unsaturated copper sites).[73] Our experimental results are in good agreement with simulation calculations for SO_2 in HKUST-1 carried out by Song et al. (sim./exp. at 298/293 K at 0.05 bar = ≈0.9/0.8 mmol g^{-1} or 1 bar = ≈15/13.8 mmol g^{-1})[44] where absolute values deviate only slightly due to differences in accessible surface area. However, in subsequent stability tests, HKUST-1 showed no sustained stability (see below).

ZIF-8 and ZIF-67 both feature an unusual "S"-shaped (IUPAC type-V isotherm)[72] adsorption isotherm, with an initial stage at ≤ ≈0.1 bar where the adsorption is very low. The delayed SO_2 uptake for ZIF-8 was previously predicted by Sun et al. and Song et al. by simulation calculations and is in good agreement

Table 1. SO_2 adsorption data and porosity characteristics at 293 K.

Material	Formula	SO_2 uptake [mmol g^{-1}] at			BET[a] [m^2 g^{-1}]	Total pore vol.[b] [cm^3 g^{-1}]	Pore width[c] [Å]	SO_2/CO_2 selectivity[d] at SO_2/CO_2 molar ratio		
		0.01 bar	0.1 bar	1 bar				0.01	0.1	0.5
NH_2-MIL-101(Cr)	$[Cr_3(O)(OH)(NH_2\text{-bdc})_3(H_2O)_2]$	1.2	4.1	16.7	2290	1.16	15.4, 19.9[70]	34	30	30
Basolite F300; Fe(BTC)	n.a.	0.6	2.4	9.5	1070	0.49	18–22[60]	n.d.	n.d.	n.d.
HKUST-1	$[Cu_3(1,3,5\text{-btc})_2(H_2O)_3]$	2.0	10.1	13.8	1490	0.61	5, 11, 14[61]	41	36	28
ZIF-8	$Zn(2\text{-MeIm})_2$	0.1	0.7	8.2	1820	0.80	3.4, 11.4[75]	n.d.	n.d.	n.d.
ZIF-67	$Co(2\text{-MeIm})_2$	0.1	0.9	11.0	1980	0.69	3.4, 11.4[75]	n.d.	n.d.	n.d.
Zeolite Y (NaY)	n.a.	5.0	5.8	7.7	930	0.33	7.4, 13.7[62]	265	180	149
SAPO-34	n.a.	1.9	4.0	6.4	720	0.28	≈5[63]	42	36	33
Silica gel 60	n.a.	0.2	0.9	3.3	540	0.75	≈10–100, av. 60[64]	n.d.	n.d.	n.d.
CTF-1(400)	Ideally $(C_8H_4N_2)_x$	2.2	4.9	10.8	980	0.46	≈6–25[65,66]	62	40	27
CTF-1(600)	Ideally $(C_8H_4N_2)_x$	2.1	5.5	16.0	2060	1.20	≈8–35[66,67]	63	46	43
Ketjenblack	Ideally C	0.5	2.1	10.7	1410	1.24	≈20–80, av. 40[68,69]	9	10	14

[a]BET areas were calculated from five adsorption points of the N_2 isotherms within $0.05 < p\,p_0^{-1} < 0.2$. Values were rounded according to the estimated standard deviation of ±20 m^2 g^{-1}; [b]Total pore volumes were calculated from experimental N_2 sorption data at $p\,p_0^{-1} = 0.85$–0.95, depending on the isotherm shape. For details see Section S2.3 in the Supporting Information; [c]Pore widths as given in the literature; [d]See Section S2.5 in the Supporting Information for the CO_2 sorption data. The MOFs Basolite F300, ZIF-8, ZIF-67, and Silica gel 60 did not show an appreciable SO_2 uptake at low pressure, hence the SO_2/CO_2 selectivities were not determined (n.d.).

with our experimental results.[43,44] The observation of "S"-isotherm shapes can be explained by the small pore entrance diameter of 3.4 Å[74,75] for both ZIF-8 and ZIF-67 and hence steric hindrance for the passage of SO_2 (kinetic diameter of 4.1 Å).[76]

The gate-opening effect occurring in both ZIFs, where the methyl groups of the ligand rotate due to the swinging of the imidazolate rings,[77] is the reason for the delayed rise in SO_2 adsorption occurs at ≈0.3 bar for both ZIF-8 and ZIF-67. The maximum SO_2 uptake reaches 8.2 and 11.0 mmol g^{-1} at 1 bar, respectively.

2.2. SO_2 Adsorption by Non-MOF Zeolite Y, SAPO-34, Silica Gel 60, CTF-1, and Ketjenblack

From all examined materials the previously investigated Zeolite Y[78–80] shows the highest affinity toward SO_2 with exceptional uptake of 5.0 mmol g^{-1} even at 0.01 bar (65% of the 1 bar capacity) with a fast transition into near saturation and maximum SO_2 uptake of 7.7 mmol g^{-1} at 1 bar.

SAPO-34 shows a type-Ib SO_2 adsorption isotherm with an uptake of 4.0 mmol g^{-1} at 0.1 bar, followed by a saturation stage with a maximum SO_2 uptake of 6.4 mmol g^{-1} at 1 bar. The adsorption differences in Zeolite Y and SAPO-34 which have a broadly similar structure correlate rather well with the difference in surface area and pore volume. The high early uptake of both materials can be traced to their small pore sizes which favor multiple SO_2-pore wall interactions (see below).

Silica gel 60 demonstrated a steady linear rise of SO_2 adsorption reaching an uptake of 3.3 mmol g^{-1} at 1 bar, which is the lowest value in this comparative study. The effect could be explained by the combination of relatively low surface area and large pore sizes of the chiefly mesoporous Silica gel, which worsens the efficiency of the host–guest interactions. The saturation stage should be reached at pressures exceeding 1 bar.

The two covalent triazine frameworks (CTFs) CTF-1(400) and CTF-1(600) are synthesized at 400 and 600 °C, respectively. CTF-1(400) and CTF-1(600) show steep uptake steps with 4.9 and 5.5 mmol g^{-1} adsorbed at 0.1 bar, followed by a nearly linear uptake reaching the values of 10.8 and 16.0 mmol g^{-1} at 1 bar, respectively. Ketjenblack has a nearly linear uptake over the whole pressure range and arrives at an uptake of 10.7 mmol g^{-1} at 1 bar. Neither of the three carbon materials reaches the saturation at 1 bar. Especially, the isotherms for CTF-1(600) and Ketjenblack still have a high positive slope and are far from leveling off at 1 bar. The superior affinity of the CTFs to SO_2 compared to Ketjenblack is likely due to the presence of smaller pore sizes in the former and more importantly due to stronger dipole–dipole interaction between the triazine and nitrile nitrogen atoms and SO_2. The nitrogen atoms are primarily heteroarylic, but residual, unreacted terminal nitrile groups are also present.[81]

2.3. Structure–Adsorption Relationships

The surface area and the total accessible pore volume could be taken as the two primary factors governing the total SO_2 adsorption at 1 bar. The SO_2 uptake of all examined materials at 293 K

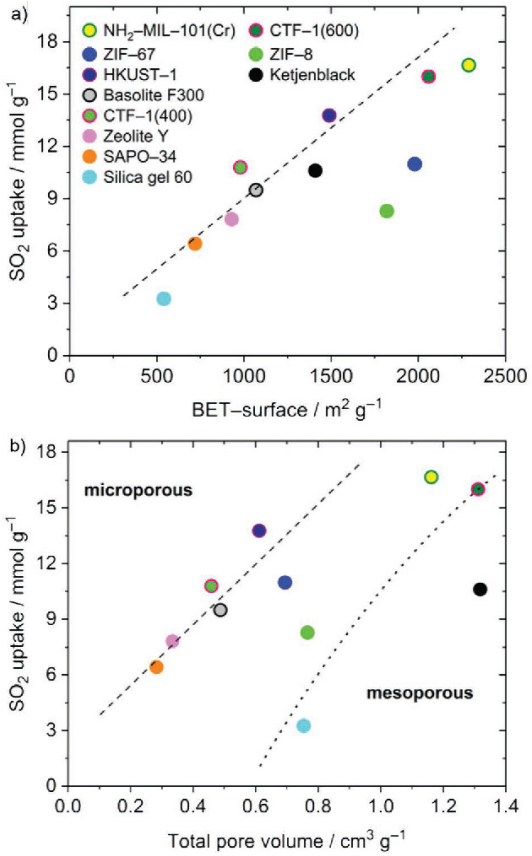

Figure 3. SO_2 uptake (1 bar, 293 K) versus a) BET-surface area and b) total accessible pore volume (both determined by N_2 adsorption at 77 K). The dashed trend lines are a guide to the eye. The dotted line in (b) separates the micro- and mesoporous materials.

and 1 bar is plotted against the BET-surface area and the pore volume in **Figure 3**. The examined materials differ significantly in terms of chemical composition and surface microstructure, nevertheless, the microporous materials without diffusion restriction show a reasonable correlation between SO_2 uptake and BET-surface area and total pore volume (Figure 3).

The two microporous ZIFs are noteworthy outliers in the uptake-surface area and pore volume correlation. This can be explained with the noted small pore window diameter of 3.4 Å[74,75] and steric hindrance for the passage of SO_2. Above the threshold or gate-opening pressure of ≈0.3 bar, the SO_2 molecules could enter the pores. The two ZIFs are microporous materials with no mesopores. However, when probing the BET surface area, the smaller N_2 molecule with its kinetic diameter of 3.64 Å can more effectively cover the surface and fill the 11.4 Å diameter pore, than the larger SO_2 molecule with its kinetic diameter of 4.1 Å. Part of the pore surface and volume will remain inaccessible or empty with SO_2 due to steric hindrance from nearby adsorbates. A geometric estimate suggests that about 6 SO_2 molecules may fit into the 11.4 pore, while about 15 N_2 molecules can fill the same space. This effect of inaccessible surface is

especially pronounced in pores wider than the molecule length, but not wide enough for unrestrained surface coverage.

Also, the uptake of NH_2-MIL-101(Cr), CTF-1(600), Ketjenblack, and Silica gel 60 is lower than expected from their surface area or pore volume which corresponds to the not reached saturation stage at 1 bar (see their above sorption isotherms). The total pore volume represents the limit for the maximum capacity. This is why the (partially) mesoporous materials are positioned below the linear trend line of the uptake versus surface area and pore volume dependence. The larger pores are not completely filled as the adsorption curve is far from saturation (in terms of an idealized Langmuir curve). The saturation uptake is only reached at pressures higher than 1 bar. The pore filling of such larger mesopores would have to occur by (framework-)O=S···O=S=O and (framework-)O=S=O···S=O dipole–dipole interactions, forming SO_2 chains or clusters. The dipole moment of SO_2 plays an important role in the adsorption process. In mesopores only part of the adsorbed SO_2 can interact with the surface. If in addition the surface of the mesoporous materials has only low affinity sites (e.g., Ketjenblack, Silica gel 60) then this contributes to the not reached saturation.

Most applications, including flue gas desulfurization or gas sensors, are restricted to gas mixtures with low partial pressures of SO_2. The optimization of the material performance at low pressures (≤ 0.1 bar) is therefore essential, whereas the total accessible pore volume should only be nonlimiting, i.e., only a certain threshold for the minimal uptake should be guaranteed. For the targeted low-pressure region, it is evident that there is no correlation between low-pressure SO_2 uptake and BET surface area (Figure S30, Supporting Information) and there is also no correlation of the SO_2 uptake to the micropore volume (Figure S31, Supporting Information).

For a high gas uptake at low pressure, that is a type-I isotherm, there must be a high affinity between the adsorbent and the adsorbate. At low pressure, the adsorption affinity is synonymous with the uptake as long as the latter is not limited by surface area or accessible volume. The SO_2 adsorption isotherms of the materials were fitted with a Langmuir (LAI) or dual-site Langmuir (DSL) model yielding the affinity constants given in **Table 2**. The remarkably high initial SO_2 affinity constant of Zeolite Y (2739 bar^{-1}) correlates with the higher initial uptake compared to SAPO-34 or CTF-1(400/600) with less steep uptake und thus yielding lower SO_2 affinity constants (95, 143, and 115 bar^{-1}, respectively).

Table 2. Fitting parameters for SO_2/CO_2 IAST-selectivities at 293 K.

Material[a)]	Gas	Model[b)]	Affinity const. [bar^{-1}]
NH_2-MIL-101(Cr)	SO_2	DSL	46.0
	CO_2	DSL	9.6
HKUST-1	SO_2	LAI	22.0
	CO_2	LAI	0.4
SAPO-34	SO_2	DSL	95.1
	CO_2	DSL	5.5
Zeolite Y	SO_2	DSL	2739
	CO_2	DSL	9.3
CTF-1(400)	SO_2	DSL	143.3
	CO_2	DSL	6.1
CTF-1(600)	SO_2	DSL	115.3
	CO_2	DSL	10.5
Ketjenblack	SO_2	LAI	0.9
	CO_2	LAI	0.4

[a)]Basolite F300, ZIF-8, ZIF-67, and Silica gel 60 were not included in the IAST calculations for their low SO_2 uptakes at low pressures. The correlation coefficients for the isotherm fits were >0.996; [b)]DSL = Dual-site Langmuir; LAI = Langmuir.

There is an optimum (or local optima) of pore size and pore shape for a given molecule. For example, one local optimum for a linear gas molecule with a length of L_{ads} is an adsorbent structure with opposite surfaces at a distance of L_{ads} between the Connolly surface, i.e., probe the accessible surface of the opposite sides.[72] This ensures optimal dispersive interactions with both ends of the molecule to the surface and this model is often used for computations.

The results of this study support the existence of an optimal pore size[18,26] for a high adsorption affinity of SO_2 at low pressures. The existence of such optimum is clearly visible by the maximum in the distribution of the surface-specific SO_2 uptake at 0.01 bar and 0.1 bar (293 K) against the pore limiting diameter (PLD), shown in **Figure 4**. As the absolute value of the uptake at low pressure depends on the surface area, it was normalized by division through the surface area, giving the surface-specific SO_2 uptake.

The PLD is the smallest diameter of a pore or window, present in a framework. The optimum pore width would be ≈4–8 Å, as found in HKUST-1, Zeolite Y, SAPO-34, and CTF-1(400). Porous materials with such pore widths exhibit a surface-specific SO_2 uptake larger than 1×10^{-3} or 5×10^{-3} mmol m^{-2} at 0.01 or 0.1 bar, respectively. In contrast, materials with pores outside the above pore criteria exhibit a surface-specific SO_2 uptake smaller than 0.5×10^{-3} or 2×10^{-3} mmol m^{-2} at 0.01 or 0.1 bar, respectively.

Grand-canonical Monte Carlo (GCMC) simulations for SO_2 sorption in MOFs, among them HKUST-1 and ZIF-8, also indicated that the amount of SO_2 adsorbed at 1 bar correlated neither well with the surface area nor with the total accessible pore volume. Instead, a good correlation of SO_2 uptake was found with the heat of adsorption in small pore ($d_{pore} \geq 4$ Å) materials at 0.05 bar pressure.[44]

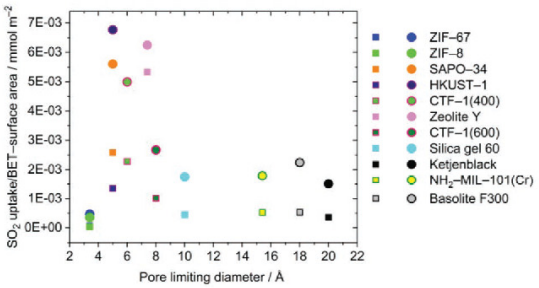

Figure 4. Surface specific SO_2 uptake (i.e., the total uptake divided/normalized by the BET-surface area) at 0.01 bar (squares) and 0.1 bar (circles) versus the pore limiting diameter. Note that for Silica Gel 60, CTF-1, and Ketjenblack only the smallest pore diameter is indicated and these materials have a broad pore size distribution (Table 1).

Furthermore, studies on NH_2-MIL-125(Ti) and $[Zn_2(L1)_2(bpe)]$ indicate a positive effect of nitrogen functionalization to enhance the SO_2 affinity at low pressures.[26,82] The effect could be operating here for CTF-1(400), CTF-1(600), and NH_2-MIL-101(Cr) and partially offset the (expected) lower uptake from the larger pore diameters.

In situ inelastic neutron scattering and density functional theory (DFT) calculations of SO_2 at manchester framework material (MFM)-300(Al)[19] and in situ synchrotron PXRD studies on MFM-601(Zr)[83] had shown that stronger SO_2 anchor points are also metal-OH groups as the hydrogen-bonding sites (metal-OH···O=S=O) for the first SO_2 molecules. Here NH_2-MIL-101(Cr) and most likely Basolite F300 feature metal-OH anchor points. Also, the open metal sites in HKUST-1 are strong binding sites. However, in situ SO_2 sorption synchrotron single-crystal X-ray diffraction experiments on the Cu(II) paddle-wheel MOF MFM-170 gave the open Cu^{2+} sites only as the secondary adsorption sites, where the SO_2 molecule binds to in an end-on mode Cu···O=S=O with 2.3(1) Å and an occupancy of only 0.67. Upon desorption the diffraction data under a dynamic vacuum at 298 K left the Cu^{2+}-bound SO_2 with an occupancy of 0.09 which suggests that due to the Jahn–Teller effect the Cu-O=S=O bonding is weak so that it is almost entirely desorbed on the reduction of pressure.[21] On the other hand, ZIF-8 and ZIF-67 neither have metal-OH nor open metal sites, contributing to a low affinity, besides the low uptake due to the gate-opening effect (vide supra).

2.4. IAST Selectivity

CO_2 is the main competitor of SO_2 regarding the binding to the adsorbent during the flue gas desulfurization. The SO_2/CO_2 selectivity, which is crucial for the separation of gas mixtures, was assessed with the IAST model for some of the most promising materials using binary SO_2/CO_2 mixtures. IAST-based estimations are adequate when the conditions of low relative pressures, similar polarity, as well as close molecular volumes of the components of the gas mixture, are fulfilled.[84]

The calculation of IAST-selectivities was performed by fitting the adsorption isotherm data points (Figures S23–S29 and Table S2, Supporting Information) using the "3P sim" software (parameters in Table S3, Supporting Information).[85]

The dependence of the calculated SO_2/CO_2 IAST-selectivities on the mole fraction of SO_2 (1 bar, 293 K) for all the examined materials are shown in **Figure 5**. Along with the order of Zeolite Y, CTF-1(600), CTF-1(400), SAPO-34, and HKUST-1 with SO_2/CO_2 IAST-selectivities from 265, 63, 62, 42, and 41 these materials demonstrated the highest selectivities at 0.01 (10.000 ppm) molar fraction of SO_2 (293 K and 1 bar). It is interesting that at a higher SO_2 molar fraction of 0.5, the respective values become 149, 43, 27, 33, and 28 (293 K and 1 bar), i.e., the order changes somewhat. Overall, Zeolite Y shows the most promising result regarding the capture of SO_2 from flue gas mixtures since it provides a high SO_2/CO_2 selectivity and its type-I isotherm should allow a relatively small pressure interval for pressure swing adsorption processes.

Although, HKUST-1 shows decent SO_2/CO_2 selectivity of 41 at a 0.01 molar fraction of SO_2, previously, Yaghi et al. and

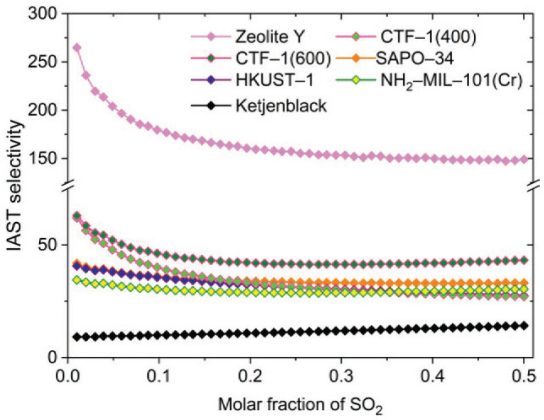

Figure 5. SO_2/CO_2 IAST selectivity dependence on the molar fraction of SO_2 in the range of 0.01–0.5 (293 K, 1 bar).

Jones et al. used HKUST-1 in breakthrough experiments in which the material showed no significant retention of SO_2.[32,86] Furthermore, a decreasing IAST-selectivity of HKUST-1 toward even lower SO_2 partial pressures than 0.01 indicates that the material might not be able to separate trace amounts of SO_2. Noteworthy, HKUST-1 had the highest calculated selectivity for NO_x from GCMC simulations on a broad range of porous materials, including MOFs, ZIFs and zeolites with respect to a gas mixture of CO_2, N_2, O_2, SO_2, and NO_x.[43]

Despite the high surface area of Ketjenblack the low affinity to SO_2 results in its unremarkable SO_2/CO_2 IAST-selectivity of 9 at a 0.01 molar fraction of SO_2 (293 K and 1 bar).

2.5. Stability Test toward Dry and Moist SO_2

Stability tests of investigated materials were carried out with both dry and humid SO_2 (the experimental methodology is given in the Supporting Information). From thermogravimetric analysis the porous materials show an initial water loss from their pores, but the frameworks are stable to 300 °C (Figures S32 and S33, Supporting Information). Humid SO_2, containing the moderately strong and quite corrosive sulfurous acid in equilibrium, reflects much better the real-world conditions in a potential sequestration application. The change of the BET-surface area and the total pore volume after SO_2 exposure during the specified time was used as the primary stability indicator parameters (**Figure 6** and Figures S11–S21, Supporting Information), while changes of the PXRD patterns were examined qualitatively (Figures S4–S10, Supporting Information). Note that the influence of humid SO_2 exposure was mainly examined for materials that demonstrated both notable stability under dry SO_2 exposure and remarkable SO_2 affinity. While ZIF-8, ZIF-67, and Silica gel 60 were very stable toward dry SO_2 (Figure 6), their affinity was low, hence neither of the three was subjected to humid SO_2 anymore. It is worth mentioning that changes in the PXRD pattern were less prominent upon decomposition which is why a combination of diffraction and adsorption experiments is always recommended.

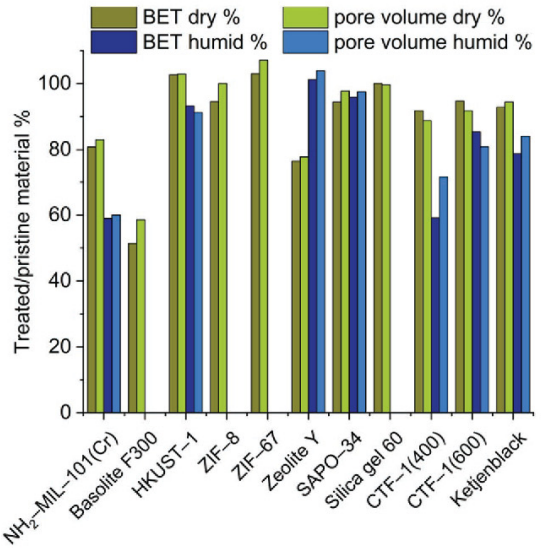

Figure 6. The relative (treated/pristine) BET surface area and total pore volume of investigated porous materials after dry and humid SO_2 exposure.

The dry SO_2 exposure during ≤10 h did not affect the majority of examined materials strongly (Figure 6). Most materials retained more than 90% of the BET-surface area and pore volume, in comparison to the untreated material. However, the amino-functionalized MOF NH_2-MIL-101(Cr) as well as Basolite F300 demonstrated a major loss of porosity and were deemed SO_2-unstable. We note that the parent MOF to NH_2-MIL-101(Cr), namely MIL-101(Cr) is also not stable toward SO_2 which was explained by its comparatively hydrophilic nature.[71] We suggest that both NH_2-MIL-101(Cr) and Basolite F300 are unstable because the SO_2 can interact with the metal-aqua and hydroxido ligand M-OH_2 and M-OH (Figure S1, Supporting Information), which are still present in both metal-cluster secondary building units (SBUs) after activation at 120 °C. Such an interaction can form sulfurous acid or hydrogen sulfite which may break the metal-carboxylate bonds with formation of metal-sulfite and the conjugated acid of the ligand. Mounfield et al. have performed in situ IR experiments on MIL-125 which confirmed the presence of bisulfite species and, in combination with computational simulations of formation energies of these adsorbed species, indicated that the degradation of the framework. The degradation likely proceeds through a reaction involving water, the dissociation of water or sulfurous or the combined reaction of sulfurous acid and water. Sulfurous acid, H_2SO_3 can be formed from SO_2 with humidity inside the MOF.[87]

Under humid SO_2 exposure (35 ± 5 ppm) during 5 h SAPO-34 showed nearly no change in porosity and could be considered stable under both dry and humid conditions (Figure 6). CTF-1(600), Ketjenblack and surprisingly, HKUST-1 demonstrated moderate surface area loss under the humid-SO_2 exposure conditions. CTF-1(400) showed a more severe loss in surface area and pore volume toward humid SO_2. When HKUST-1 was subjected to a humid SO_2 exposure time of 8 and 24 h a drastic degradation of the framework structure became visible in subsequent PXRD and N_2 adsorption analysis (Figures S6 and S13, Supporting Information). Concerning, the initial higher stability of HKUST-1 in comparison to usually regarded more stable NH_2-MIL-101(Cr) and Basolite F300 we refer again to the SBUs with their reactive metal-carboxylate bonds. The principle difference in the three SBUs is that the metal-aqua and -hydroxido ligands M-OH_2 and M-OH in NH_2-MIL-101(Cr) and Basolite F300 are normally bound ligands where reaction with the SO_2 under formation of reactive sulfurous acid or hydrogen sulfite can occur (Figure S1, Supporting Information). Whereas in HKUST-1, the aqua ligand on d^9-Cu(II) is subject to the Jahn–Teller distortion with an elongated Cu–O distance and weaker interaction (Figure S2, Supporting Information). This Cu-aqua ligand is easily removed upon activation. Further, sulfurous acid, which may still form, will also bind much weaker to Cu and thereby interact much slower with the Cu-carboxylate bonds.

Furthermore, SO_2 is also a strong reducing agent and may reduce the metal atoms in the MOFs to a lower valent state, such as Cr(II), Fe(II), and Cu(I). Upon reduction, the metal-carboxylate bonding can change more drastically, for example, high-spin d^4-Cr(II) is also subject to Jahn–Teller distortion. In this regard, it is interesting to note that in activated HKUST-1 it was observed through the spectroscopic investigation of adsorbed CO_2, CO, or NO that Cu(I) is present and coexists with Cu(II). Obviously, in HKUST the oxidation state of copper can be reduced to Cu(I) by redox treatments, using vacuum and/or reducing gases at different temperatures, albeit without noticeable framework degradation.[88–91] Hence, a higher "redox stability" could also be an explanation for the higher kinetic stability of HKUST-1 compared to the MIL frameworks.

A special case is Zeolite Y which exhibited better stability performance under humid exposure conditions than toward dry SO_2 (Figure 6). In the case of Zeolite Y, the accessibility and the location of the Na^+ counter cations to the anionic alumosilicate framework contribute largely to the adsorption properties of this material.[92] Polar molecules, like water, can induce cation redistribution and thus change adsorption properties, e.g., selectivity and capacity, significantly.[93,94] So, it might be the case that preadsorbed water blocks or rather changes the accessibility for SO_2 in our experiment.

3. Conclusions

Five prototypical MOF materials were compared with six representatives of other classes of porous materials regarding their SO_2 adsorption capabilities. A strong correlation between the SO_2 uptake at 1 bar and 293 K and BET-surface area and pore volume was observed for all microporous materials, independently of their surface microstructure. The highest affinity constants toward SO_2 at low partial pressures (0.01–0.1 bar) were registered for materials featuring pores with diameters of ≈4–8 Å, and aromatic nitrogen atoms (e.g. CTFs).

The calculated IAST-selectivities for SO_2 over CO_2 were in the range of 9–265 (at 0.01–0.5 molar fraction of SO_2), with the highest selectivity over the whole range given by Zeolite Y. Also, remarkable selectivities at low pressure were demonstrated by

CTF-1(400/600), which reflect the benefit of weakly basic acrylic nitrogens as more affine adsorption sites. When the stability toward humid SO_2 is further taken into consideration, this then leaves CTF-1(600), and SAPO-34 as the most promising materials for realistic use (i.e., humid conditions). The results of this work should raise the awareness for well-known porous material classes in the competition with currently advocated MOFs for SO_2 adsorption.

4. Experimental Section

Materials: The examined materials were synthesized according to published methods or obtained commercially (see Table S1, Supporting Information).

Gas Adsorption: BET characterization was performed on a Quantachrome *Autosorb 6* automatic gas adsorption analyzer (further instrument). SO_2 and CO_2 isotherms were measured on a Quantachrome *Autosorb iQ MP* instrument. Before each experiment, the samples were activated according to the literature (but at least 3 h of degassing and a temperature of not less than 393 K) and a $\approx 5 \times 10^{-3}$ mbar vacuum. All gases (He, N_2, SO_2, CO_2) were of ultrahigh purity (99.999%). The standard temperature and pressure volumes at 293.15 K and 101.325 kPa are reported according to the recommendation of the National Institute of Standards and Technology. The N_2 adsorption experiments for the BET surface area and pore volume determination were performed within a pressure range of 0.005–1 bar at 77 K. The SO_2 sorption experiments were performed within a pressure range of 0.001–1 bar (0.96 ± 0.007 bar) and 293 K. A Dräger *Pac 6000* electrochemical SO_2 sensor with a measuring range of 0.1–100 ppm was used for leakage testing and maintaining safe work conditions.

Powder X-Ray Diffraction: The PXRD measurements were performed on a Bruker *D2 Phaser* with a Cu-K_α-cathode source (λ = 1.54182; 30 kV, 10 mA) at room temperature. The finely ground samples were measured in the range of $5° < 2\theta < 50°$ using a low background silicon sample holder.

Thermogravimetric Analysis (TGA): TGA was performed on a Netzsch Thermo-Microbalance Apparatus TG 209 F3 Tarsus, at a heating rate of 10 K min^{-1} under a nitrogen flow. Samples were not activated before the measurement.

Stability Tests toward Dry and Moist SO_2: For the determination of the material stability under SO_2 exposure the change in BET surface area (N_2 sorption) and crystallinity (PXRD) were examined. Samples were activated as described above.

Stability tests toward dry SO_2 were carried out as the above SO_2 ad- and desorption isotherm measurement by exposing the sample between 8 h to less than 10 h under a variable pressure of 0.001–1 bar. Afterward the stability was assessed by the identity or changes in the PXRD and BET surface area and porosity.

Stability tests toward humid SO_2 were done in a self-constructed exposure chamber (Figure S2, Supporting Information), which contained a vessel of saturated sodium chloride solution (80 mL) to set a relative humidity (RH) of 75%. The chamber was filled with humid SO_2 by bubbling air through a solution of sodium hydrogen sulfite ($Na_2S_2O_5$ dissolved in water). The generated SO_2 concentration and the RH-value in the chamber were monitored by a Dräger *Pac 6000* SO_2 sensor and a *VWR TH300* hygrometer, respectively. The exposure was done at room temperature under an atmosphere containing 35 ± 5 ppm SO_2 and of 75 ± 6% RH humidity for 5 h. Experimental details and setup can be found in Section S2.1 in the Supporting Information.

Supporting Information

Supporting Information is available from the Wiley Online Library or from the author.

Acknowledgements

Open access funding enabled and organized by Projekt DEAL.

Conflict of Interest

The authors declare no conflict of interest.

Data Availability Statement

Research data are not shared.

Keywords

active carbon, adsorption, metal–organic frameworks, MOFs, porous materials, sulfur dioxide, zeolites

Received: December 10, 2020
Revised: January 12, 2021
Published online: February 11, 2021

[1] D. Gielen, R. Gorini, N. Wagner, R. Leme, L. Gutierrez, G. Prakash, E. Asmelash, L. Janeiro, G. Gallina, G. Vale, L. Sani, X. Casals, R. Ferroukhi, B. Parajuli, M. Renner, C. Garcia-Banos, J. Feng, *Global Energy Transformation: A Roadmap to 2050, IRENA*, Abu Dhabi **2019**.
[2] M. Maurya, J. K. Singh, *J. Phys. Chem. C* **2018**, *122*, 14654.
[3] F. Birol, L. Cozzi, T. Gould, S. Bouckaert, T.-Y. Kim, K. McNamara, B. Wanner, C. McGlade, P. Olejarnik, Z. Adam, L. Arboleya Sarazola, Y. Arsalane, B. Baruah, S. Bennett, M. Cappannelli, O. Chen, A. Contejean, H. Cisse Coulibaly, D. Crow, D. D'Ambrosio, A. Dasgupta, J. C. Donovan, M. Dos Santos, L. Gallarati, T. Goodson, L. Y. Lee, J. Liu, W. Matsumura, Y. Nobuoka, S. Papapanagiotou, C. Pavarini, D. Perugia, A. Petropoulos, A. Rouget, M. Ruiz de Chavez Velez, A. Schröder, G. Sondak, L. Staas, A. Toril, M. Waldron, M. A. Walton, W. Yu, P. Zeniewski, *International Energy Agency, World Energy Outlook 2019*, OECD Publishing, Paris **2019**.
[4] G. E. Likens, D. T. Driscoll, D. C. Buso, *Science* **1996**, *272*, 244.
[5] K. Gregory, C. Webster, S. Durk, *Energy Policy* **1996**, *24*, 655.
[6] R. K. Srivastava, W. Jozewicz, *J. Air Waste Manage. Assoc.* **2011**, *51*, 1676.
[7] J.-Y. Lee, T. C. Keener, Y. J. Yang, *J. Air Waste Manage. Assoc.* **2012**, *59*, 725.
[8] A. B. Rao, E. S. Rubin, *Environ. Sci. Technol.* **2002**, *36*, 4467.
[9] J. H. Goo, M. F. Irfan, S. D. Kim, S. C. Hong, *Chemosphere* **2007**, *67*, 718.
[10] S. Ding, F. Liu, X. Shi, K. Liu, Z. Lian, L. Xie, H. He, *ACS Appl. Mater. Interfaces* **2015**, *7*, 9497.
[11] P. K. Thallapally, R. K. Motkuri, C. A. Fernandez, B. P. McGrail, G. S. Behrooz, *Inorg. Chem.* **2010**, *49*, 4909.
[12] K. Tan, P. Canepa, Q. Gong, J. Liu, D. H. Johnson, A. Dyevoich, P. K. Thallapally, T. Thonhauser, J. Li, Y. J. Chabal, *Chem. Mater.* **2013**, *25*, 4653.
[13] T. Grant Glover, G. W. Peterson, B. J. Schindler, D. Britt, O. Yaghi, *Chem. Eng. Sci.* **2011**, *66*, 163.
[14] X. Han, S. Yang, M. Schröder, *Nat. Rev. Chem.* **2019**, *3*, 108.
[15] T. Jurado-Vázquez, E. Sánchez-González, A. E. Campos-Reales-Pineda, A. Islas-Jácome, E. Lima, E. González-Zamora, I. A. Ibarra, *Polyhedron* **2019**, *157*, 495.

[16] J. A. Zárate, E. Sánchez-González, D. R. Williams, E. González-Zamora, V. Martis, A. Martínez, J. Balmaseda, G. Maurin, I. A. Ibarra, *J. Mater. Chem. A* **2019**, *7*, 15580.
[17] R. Domínguez-González, I. Rojas-León, E. Martínez-Ahumada, D. Martínez-Otero, H. A. Lara-García, J. Balmaseda-Era, I. A. Ibarra, E. G. Percástegui, V. Jancik, *J. Mater. Chem. A* **2019**, *7*, 26812.
[18] Y. Zhang, Z. Chen, X. Liu, Z. Dong, P. Zhang, J. Wang, Q. Deng, Z. Zeng, S. Zhang, S. Deng, *Ind. Eng. Chem. Res.* **2019**, *59*, 874.
[19] S. Yang, J. Sun, A. J. Ramirez-Cuesta, S. K. Callear, W. I. F. David, D. P. Anderson, R. Newby, A. J. Blake, J. E. Parker, C. C. Tang, M. Schröder, *Nat. Chem.* **2012**, *4*, 887.
[20] X. Han, H. G. W. Godfrey, L. Briggs, A. J. Davies, Y. Cheng, L. L. Daemen, A. M. Sheveleva, F. Tuna, E. J. L. McInnes, J. Sun, C. Drathen, M. W. George, A. J. Ramirez-Cuesta, K. M. Thomas, S. Yang, M. Schröder, *Nat. Mater.* **2018**, *17*, 691.
[21] G. L. Smith, J. E. Eyley, X. Han, X. Zhang, J. Li, N. M. Jacques, H. G. W. Godfrey, S. P. Argent, L. J. McCormick McPherson, S. J. Teat, Y. Cheng, M. D. Frogley, G. Cinque, S. J. Day, C. C. Tang, T. L. Easun, S. Rudić, A. J. Ramirez-Cuesta, S. Yang, M. Schröder, *Nat. Mater.* **2019**, *18*, 1358.
[22] S. Yang, L. Liu, J. Sun, K. M. Thomas, A. J. Davies, M. W. George, A. J. Blake, A. H. Hill, A. N. Fitch, C. C. Tang, M. Schröder, *J. Am. Chem. Soc.* **2013**, *135*, 4954.
[23] M. Savage, Y. Cheng, T. L. Easun, J. E. Eyley, S. P. Argent, M. R. Warren, W. Lewis, C. Murray, C. C. Tang, M. D. Frogley, G. Cinque, J. Sun, S. Rudić, R. T. Murden, M. J. Benham, A. N. Fitch, A. J. Blake, A. J. Ramirez-Cuesta, S. Yang, M. Schröder, *Adv. Mater.* **2016**, *28*, 8705.
[24] V. Chernikova, O. Yassine, O. Shekhah, M. Eddaoudi, K. N. Salama, *J. Mater. Chem. A* **2018**, *6*, 5550.
[25] X. Cui, Q. Yang, L. Yang, R. Krishna, Z. Zhang, Z. Bao, H. Wu, Q. Ren, W. Zhou, B. Chen, H. Xing, *Adv. Mater.* **2017**, *29*, 1606929.
[26] P. Brandt, A. Nuhnen, M. Lange, J. Möllmer, O. Weingart, C. Janiak, *ACS Appl. Mater. Interfaces* **2019**, *11*, 17350.
[27] Z. Chen, X. Wang, R. Cao, K. B. Idrees, X. Liu, M. C. Wasson, O. K. Farha, *ACS Mater. Lett.* **2020**, *2*, 1129.
[28] C. Janiak, J. K. Vieth, *New J. Chem.* **2010**, *34*, 2366.
[29] M. P. Suh, H. J. Park, T. K. Prasad, D. W. Lim, *Chem. Rev.* **2012**, *112*, 782.
[30] K. Sumida, D. L. Rogow, J. A. Mason, T. M. McDonald, E. D. Bloch, Z. R. Herm, T.-H. Bae, J. R. Long, *Chem. Rev.* **2012**, *112*, 724.
[31] Y. He, W. Zhou, G. Qian, B. Chen, *Chem. Soc. Rev.* **2014**, *43*, 5657.
[32] D. Britt, D. Tranchemontagne, O. M. Yaghi, *Proc. Natl. Acad. Sci. U. S. A.* **2008**, *105*, 11623.
[33] N. S. Bobbitt, M. L. Mendonca, A. J. Howarth, T. Islamoglu, J. T. Hupp, O. K. Farha, R. Q. Snurr, *Chem. Soc. Rev.* **2017**, *46*, 3357.
[34] H. Wang, W. P. Lustig, J. Li, *Chem. Soc. Rev.* **2018**, *47*, 4729.
[35] E. Martínez-Ahumada, A. López-Olvera, V. Jancik, J. E. Sánchez-Bautista, E. González-Zamora, V. Martis, D. R. Williams, I. A. Ibarra, *Organometallics* **2020**, *39*, 883.
[36] T. Islamoglu, Z. Chen, M. C. Wasson, C. T. Buru, K. O. Kirlikovali, U. Afrin, M. R. Mian, O. K. Farha, *Chem. Rev.* **2020**, *120*, 8130.
[37] X. Shi, X. Zhang, F. Bi, Z. Zheng, L. Sheng, J. Xu, Z. Wang, Y. Yang, *J. Mol. Liq.* **2020**, *316*, 113812.
[38] X. Zhang, Y. Yang, L. Song, J. Chen, Y. Yang, Y. Wang, *J. Hazard. Mater.* **2019**, *365*, 597.
[39] a) J. J. Low, A. I. Benin, P. Jakubczak, J. F. Abrahamian, S. A. Faheem, R. R. Willis, *J. Am. Chem. Soc.* **2009**, *131*, 15834. b) K. Leus, T. Bogaerts, J. De Decker, H. Depauw, K. Hendrickx, H. Vrielinck, V. Van Speybroeck, P. Van Der Voort, *Microporous Mesoporous Mater.* **2016**, *226*, 110.
[40] M. R. Tchalala, P. M. Bhatt, K. N. Chappanda, S. R. Tavares, K. Adil, Y. Belmabkhout, A. Shkurenko, A. Cadiau, N. Heymans, G. Weireld, G. Maurin, K. N. Salama, M. Eddaoudi, *Nat. Commun.* **2019**, *10*, 1.
[41] Y. Zhang, P. Zhang, W. Yu, J. Zhang, J. Huang, J. Wang, M. Xu, Q. Deng, Z. Zeng, S. Deng, *ACS Appl. Mater. Interfaces* **2019**, *11*, 10680.
[42] D. Bahamon, A. Díaz-Márquez, P. Gamallo, L. F. Vega, *Chem. Eng. J.* **2018**, *342*, 458.
[43] W. Sun, L.-C. Lin, X. Peng, B. Smit, *AIChE J.* **2014**, *60*, 2314.
[44] X.-D. Song, S. Wang, C. Hao, J.-S. Qiu, *Inorg. Chem. Commun.* **2014**, *46*, 277.
[45] S. Bernt, V. Guillerm, C. Serre, N. Stock, *Chem. Commun.* **2011**, *47*, 2838.
[46] Y. Lin, C. Kong, L. Chen, *RSC Adv.* **2012**, *2*, 6417.
[47] G. Majano, O. Ingold, M. Yulikov, G. Jeschke, J. Pérez-Ramírez, *CrystEngComm* **2013**, *15*, 9885.
[48] A. Dhakshinamoorthy, M. Alvaro, P. Horcajada, E. Gibson, M. Vishnuvarthan, A. Vimont, J.-M. Grenèche, C. Serre, M. Daturi, H. Garcia, *ACS Catal.* **2012**, *2*, 2060.
[49] S. S.-Y. Chui, S. M.-F. Lo, J. P. H. Charmant, A. Guy Orpen, I. D. Williams, *Science* **1999**, *283*, 1148.
[50] M. Hartmann, S. Kunz, D. Himsl, O. Tangermann, S. Ernst, A. Wagener, *Langmuir* **2008**, *24*, 8634.
[51] a) X.-C. Huang, Y.-Y. Lin, J.-P. Zhang, X.-M. Chen, *Angew. Chem., Int. Ed.* **2006**, *45*, 1557. b) K. S. Park, Z. Ni, A. Côté, J. Y. Choi, R. Huang, F. J. Uribe-Romo, H. K. Chae, M. O'Keeffe, O. M. Yaghi, *Proc. Natl. Acad. Sci. U. S. A.* **2006**, *103*, 10186.
[52] Y. Hu, Z. Liu, J. Xu, Y. Huang, Y. Song, *J. Am. Chem. Soc.* **2013**, *135*, 9287.
[53] Q. Shi, Z. Chen, Z. Song, J. Li, J. Dong, *Angew. Chem., Int. Ed.* **2011**, *50*, 672.
[54] G. Zhong, D. Liu, J. Zhang, *J. Mater. Chem. A* **2018**, *6*, 1887.
[55] A. Srinivasan, M. W. Grutzeck, *Environ. Sci. Technol.* **1999**, *33*, 1464.
[56] B. M. Lok, C. A. Messina, R. L. Patton, R. T. Gajek, T. R. Cannan, E. M. Flanigen, *J. Am. Chem. Soc.* **1984**, *106*, 6092.
[57] P. Kuhn, M. Antonietti, A. Thomas, *Angew. Chem., Int. Ed.* **2008**, *47*, 3450.
[58] S. Kuroda, N. Tobori, M. Sakuraba, Y. Sato, *J. Power Sources* **2003**, *119–121*, 924.
[59] X. Qian, L. Jin, D. Zhao, X. Yang, S. Wang, X. Shen, D. Rao, S. Yao, Y. Zhou, X. Xi, *Electrochim. Acta* **2016**, *192*, 346.
[60] X. Hu, X. Lou, C. Li, Y. Ning, Y. Liao, Q. Chen, E. S. Mananga, M. Shen, B. Hu, *RSC Adv.* **2016**, *6*, 114483.
[61] S. D. Worrall, M. A. Bissett, P. I. Hill, A. P. Rooney, S. J. Haigh, M. P. Attfield, R. A. W. Dryfe, *Electrochim. Acta* **2016**, *222*, 361.
[62] C. A. C. Perez, N. S. de Resende, V. M. M. Salim, M. Schmal, *J. Phys. Chem. C* **2017**, *121*, 2755.
[63] H. Shi, *RSC Adv.* **2015**, *5*, 38330.
[64] D. Dutta, S. Chatterjee, K. T. Pillai, P. K. Pujari, B. N: Ganguly, *Chem. Phys.* **2005**, *312*, 319.
[65] S. Dey, S. Bügel, S. Sorribas, A. Nuhnen, A. Bhunia, J. Coronas, C. Janiak, *Front. Chem.* **2019**, *7*, 693.
[66] S. Öztürk, Y.-X. Xiao, D. Dietrich, B. Giesen, J. Barthel, J. Ying, Y.-X. Yang, C. Janiak, *Beilstein J. Nanotechnol.* **2020**, *11*, 770.
[67] Y. Zhao, K. X. Yao, B. Teng, T. Zhang, Y. Han, *Energy Environ. Sci.* **2013**, *6*, 3684.
[68] G. Wang, G. Sun, Q. Wang, S. Wang, J. Guo, Y. Gao, Q. Xin, *J. Power Sources* **2008**, *180*, 176.
[69] C. Mani-Lata, C. Hussakan, G. Panomsuwan, *J. Compos. Sci.* **2020**, *4*, 121.
[70] D. Jiang, L. L. Keenan, A. D. Burrows, K. J. Edler, *Chem. Commun.* **2012**, *48*, 12053.
[71] E. Martínez-Ahumada, M. L. Díaz-Ramírez, H. A. Lara-García, D. R. Williams, V. Martis, V. Jancik, E. Lima, I. A. Ibarra, *J. Mater. Chem. A* **2020**, *8*, 11515.
[72] M. Thommes, K. Kaneko, A. V. Neimark, J. P. Olivier, F. Rodriguez-Reinoso, J. Rouquerol, K. S. W. Sing, *Pure Appl. Chem.* **2015**, *87*, 1051.

[73] Ü. Kökçam-Demir, A. Goldman, L. Esrafili, M. Gharib, A. Morsali, O. Weingart, C. Janiak, *Chem. Soc. Rev.* **2020**, *49*, 2751.
[74] H. Bux, F. Liang, Y. Li, J. Cravillon, M. Wiebcke, J. Caro, *J. Am. Chem. Soc.* **2009**, *131*, 16000.
[75] W. Ma, Q. Jiang, P. Yu, L. Yang, L. Mao, *Anal. Chem.* **2013**, *85*, 7550.
[76] J.-R. Li, R. J. Kuppler, H.-C. Zhou, *Chem. Soc. Rev.* **2009**, *38*, 1477.
[77] M. E. Casco, Y. Q. Cheng, L. L. Daemen, D. Fairen-Jimenez, E. V. Ramos-Fernández, A. J. Ramirez-Cuesta, J. Silvestre-Albero, *Chem. Commun.* **2016**, *52*, 3639.
[78] R. M. Barrer, A. F. Denny, *J. Chem. Soc.* **1964**, 4684.
[79] S. G. Deng, Y. S. Lin, *Ind. Eng. Chem. Res.* **1995**, *34*, 4063.
[80] A. Sultana, D. D. Habermacher, C. E. A. Kirschhock, J. A. Martens, *Appl. Catal., B* **2004**, *48*, 65.
[81] L. Manying, G. Liping, J. Shangbin, T. Bien, *J. Mater. Chem. A* **2019**, *7*, 5153.
[82] S. Glomb, D. Woschko, G. Makhloufi, C. Janiak, *ACS Appl. Mater. Interfaces* **2017**, *9*, 37419.
[83] J. H. Carter, X. Han, F. Y. Moreau, I. da Silva, A. Nevin, H. G. W. Godfrey, C. C. Tang, S. Yang, M. Schröder, *J. Am. Chem. Soc.* **2018**, *140*, 15564.
[84] N. F. Cessford, N. A. Seaton, T. Düren, *Ind. Eng. Chem. Res.* **2012**, *51*, 4911.
[85] 3P INSTRUMENTS, 3P sim, Version 1.1.0.7, Simulation and Evaluation Tool for mixSorb, 3P INSTRUMENTS **2018**.
[86] G. W. Peterson, J. A. Rossin, J. B. DeCoste, K. L. Killops, M. Browe, E. Valdes, P. Jones, *Ind. Eng. Chem. Res.* **2013**, *52*, 5462.
[87] W. P. Mounfield, C. Han, S. H. Pang, U. Tumuluri, Y. Jiao, S. Bhattacharyya, M. R. Dutzer, S. Nair, Z. Wu, R. P. Lively, D. S. Sholl, K. S. Walton, *J. Phys. Chem. C* **2016**, *120*, 27230.
[88] C. Prestipino, L. Regli, J. G. Vitillo, F. Bonino, A. Damin, C. Lamberti, A. Zecchina, P. L. Solari, K. O. Kongshaug, S. Bordiga, *Chem. Mater.* **2006**, *18*, 1337.
[89] J. Szanyi, M. Daturi, G. Clet, D. R. Baer, C. H. Peden, *Phys. Chem. Chem. Phys.* **2012**, *14*, 4383.
[90] C. Chen, T. Wu, H. Wu, H. Liu, Q. Qian, Z. Liu, G. Yang, B. Han, *Chem. Sci.* **2018**, *9*, 8890.
[91] S. Bordiga, L. Regli, F. Bonino, E. Groppo, C. Lamberti, B. Xiao, P. S. Wheatley, R. E. Morris, A. Zecchina, *Phys. Chem. Chem. Phys.* **2007**, *9*, 2676.
[92] C. Beauvais, A. Boutin, A. H. Fuchs, *C. R. Chim.* **2005**, *8*, 485.
[93] A. Malka-Edery, K. Abdallah, P. Grenier, F. Meunier, *Adsorption* **2001**, *7*, 17.
[94] C. Mellot-Draznieks, J. Rodriguez-Carvajal, D. E. Cox, A. K. Cheetham, *Phys. Chem. Chem. Phys.* **2003**, *5*, 1882.

ADVANCED SUSTAINABLE SYSTEMS

Supporting Information

for *Adv. Sustainable Syst.*, DOI: 10.1002/adsu.202000285

Comparative Evaluation of Different MOF and Non-MOF Porous Materials for SO_2 Adsorption and Separation Showing the Importance of Small Pore Diameters for Low-Pressure Uptake

*Philipp Brandt, Alexander Nuhnen, Seçil Öztürk, Gülin Kurt, Jun Liang, and Christoph Janiak**

Supporting Information

Comparative Evaluation of Different MOF and non-MOF Porous Materials for SO_2 Adsorption and Separation Showing the Importance of Small Pore Diameters for Low-Pressure Uptake

Philipp Brandt,[a] Alexander Nuhnen,[a] Seçil Öztürk,[a] Gülin Kurt,[a] Jun Liang,[a,b] Christoph Janiak[*,a,b]*

[a] Institut für Anorganische Chemie und Strukturchemie, Heinrich-Heine-Universität Düsseldorf, Universitätsstraße 1, 40225 Düsseldorf, Germany

[b] Hoffmann Institute of Advanced Materials, Shenzhen Polytechnic, 7098 Liuxian Blvd, Nanshan District, Shenzhen, China

Email addresses: p.brandt@hhu.de; alexander.nuhnen@hhu.de, oeztues@uni-duesseldorf.de, guelin.kurt@uni-duesseldorf.de, liangj@uni-duesseldorf.de, janiak@hhu.de

Content

1 Materials

Table S1. Reference to synthesis or vendor of the materials.

Material	Synthesis	Purchase [a]	Activation conditions
NH_2-MIL-101(Cr)	Edler *et al.*[1]	-	12 h; 120 °C
Basolite F300	-	BASF	3 h; 120 °C
HKUST-1	Fan *et al.*[2]	-	12 h; 120 °C
ZIF-8	Ooi *et al.*[3]	-	12 h; 120 °C
ZIF-67	Carreon *et al.*[4]	-	12 h; 120 °C
Zeolite Y (NaY)	-	Alfa Aesar	12 h; 120 °C
Silica gel 60	-	Machery-Nagel-NAGEL	3 h; 120 °C
SAPO-34	-	Clariant AG	4 h; 120 °C
CTF-1(400)	Antonietti *et al.*[5]	-	12 h; 120 °C
CTF-1(600)	Antonietti *et al.*[5]	-	12 h; 120 °C
Ketjenblack (EC-600JD)	-	AkzoNobel	4 h; 120 °C

[a] Used without further purification.

NH_2-MIL-101(Cr) is a MOF which is like its parent MIL-101(Cr), with the empirical formula $[Cr_3(\mu_3\text{-}O)(bdc)_3(F,OH)(H_2O)_2]$ (bdc = benzene-1,4-dicarboxylate), considered moisture stable,[6] has micro- to mesopores and is frequently employed in various gas sorption studies, including CO_2,[7] and in catalysis,[8,9] Both MOFs are chromium-terephthalate based porous materials. The structure of both MOFs resembles the augmented MTN zeolite topology. MIL-101(Cr) is synthesized in quite harsh reaction conditions (220 °C in water). Thus, a fundamental water stability of this material can be expected and has been proven.[10]

Basolite F300 (Fe-BTC) is part of a series of MOFs, which has been commercialized by BASF.[11] The precise structure of Basolite F300 is unknown but it has a disordered framework of locally ordered units[12] and is related to the crystalline MOF structure of MIL-100(Fe) with the empirical formula 3D-$[Fe_3(O)(btc)_2(F,OH)(H_2O)_2]_2$ (btc = benzene-1,3,5-tricarboxylate, trimesate) which has received attention in literature with respect to its catalytic, gas separation and gas storage properties.[13] The porosity of MIL-100 originates from both 25 Å and 29 Å mesopores, which are accessible via 5.5 Å and 8.6 Å windows, respectively.[13] MIL-100(Fe) has been shown to be a hydrothermally very stable MOF and withstand repeated cyclic adsorption of water vapor.[14] Also, Fe-based materials are of relatively low cost and low toxicity.[12,15]

HKUST-1 (Cu-BTC or MOF-199), with the empirical formula $[Cu_3(btc)_2(H_2O)_3]_n$, is probably one of the most investigated MOFs. The porous framework of HKUST-1 is composed of Cu^{2+} cations as metal nodes and benzene-1,3,5-tricarboxylate (btc) anions as organic ligands.[16] The pseudo-octahedral coordination sphere of HKUST-1 includes paddle-wheel clusters formed by $Cu_2(OOC\text{-})_4$ units (Figure S2).[16,17,18] Cu^{2+} ions are coordinated by four oxygen atoms from the btc ligand and one oxygen atom in the axial position from a water ligand.[16] HKUST-1 comprises three kinds of pores and windows. Two larger cuboctahedral pores (11 Å and 14 Å), are accessible through square-shaped windows (9 Å).[16,19,20] Octahedral site cavities (5 Å) are connected to the main channels by triangular windows (3.5 Å).[16,14,21] Due to four benzene rings from the btc ligand these small pores have a more hydrophobic character.[22] Upon thermal or vacuum activation, water ligands coordinated at the secondary building unit (SBU) of HKUST-1 are removed creating coordinatively unsaturated metal sites (CUS, open metal sites, OMS).[17] These open Cu^{2+}-sites could bind to distinct guest molecules.[23]

Secondary building units of NH_2-MIL-101(Cr), MIL-100(Fe) and HKUST-1:

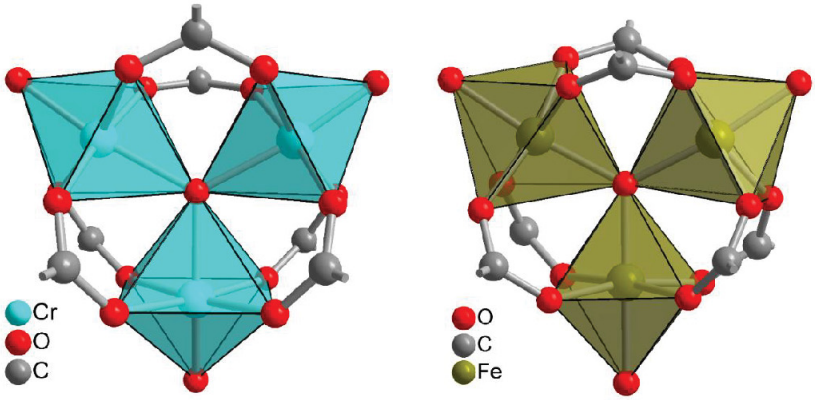

Figure S1. Secondary building unit (SBU) of MIL-101(Cr) and NH_2-MIL-101(Cr) (left) and MIL-100(Fe) (right). Basolite F300 (Fe-BTC) is the commercial variant of the prototypical MOF MIL-100(Fe). The outward-pointing three O atoms represent two aqua ligand (H_2O) and one hydroxido or fluorido ligand (OH/F), depending on the fluoride-free or fluoride-based synthesis. The latter cannot differentiated by crystal structure refinement as it is also disordered over all three positions. The SBU formulae are $\{Cr_3(\mu_3\text{-}O)(H_2O)_2(OH,F)(O_2C\text{-})_6\}$ and $\{Fe_3(\mu_3\text{-}O)(H_2O)_2(OH,F)(O_2C\text{-})_6\}$, respectively. Graphics have been drawn with the software DIAMOND [24] from the deposited cif-files under CCDC no. 605510, Refcode OCUNAK for MIL-101(Cr)[25] and CCDC no. 640536, Refcode CIGXIA for MIL-100(Fe).[13]

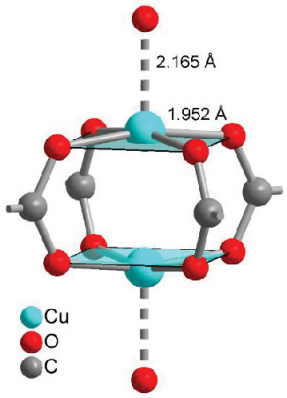

Figure S2. Secondary building unit (SBU) of HKUST-1 (Cu-btc) with its paddle-wheel structure of the square-pyramidal Cu atoms. The axially-oriented two O atoms represent two aqua ligand (H_2O) along the direction of the Jahn-Teller distortion of the d^9-Cu(II) atom. The given Cu-O distances underscore the weaker binding of the axial ligands. The SBU formula is $\{Cu_2(H_2O)_2(O_2C\text{-})_4\}$. Graphics have been drawn with the software DIAMOND [24] from the deposited cif-files under CCDC no. 112954, Refcode FIQCEN.[16]

ZIF-8/ ZIF-67 are two isostructural frameworks[26] with the empirical formula $[M(2\text{-MeIm})_2]$ (M = Zn, Co, 2-MeIm = 2-methylimidazolate) and are the parent MOFs of the "zeolithic imidazolate framework" series for the respective metal. ZIFs show great potential for several applications, in particular high-capacity storage and separation of gases, catalysis, sensing and optics.[27-34] ZIF-8 or ZIF-67 are composed of tetrahedrally nitrogen-coordinated Zn or Co atoms, respectively, and linked by 2-methylimidazolate ligands. ZIFs have structures similar to aluminosilicates (zeolites).[35] The

robustness and comparatively facile and inexpensive synthesis make ZIF-8 an ideal material for investigations on permanently porous 3D frameworks in general.[36]

Zeolite Y is the synthetic variant of the naturally occurring Faujasite (FAU-type) zeolites.[37] The framework structure of Zeolite Y consists of sodalite cages which are connected via channels of hexagonal prisms forming pores which are 7.4 Å and 13.4 Å in diameter.[38] The Si/Al ratio (~2.5) in Zeolite Y exceeds most other zeolite structures.[39] Zeolite Y is widely used as a catalyst in fluid catalytic cracking (FCC).[40,41]

SAPO-34 is a silicoaluminophosphate (SAPO) and the synthetic variant of the naturally occurring Chabazite (CHA-type) zeolite. During the synthesis, silicon is substituted with phosphorous forming $AlPO_4$ units.[42] Commonly used template molecules in the synthesis of SAPO-34 are tetraethylammonium hydroxide (TEA-OH) or morpholine.[43] SAPO-34 is a frequently used catalyst for methanol-to-olefin (MTO) conversion.[44,45]

Silica gel 60 is an amorphous silicon dioxide material which is generally used as drying agent or in standard separation processes like column chromatography.[46,47] The number 60 in the name silica gel 60 indicates the average pore size which has an overall range between 10-100 Å.[48]

CTFs (covalent triazine(-based) frameworks) were developed by Kuhn, Antonietti and Thomas *et al.* as porous organic materials with permanent porosity.[5,49-52] CTFs are nitrogen-containing aromatic polymer frameworks with triazine rings that exhibit high surface areas, porosity, thermal and chemical stability. CTFs are interesting because of advantages such as cheap and readily available starting materials, facile synthesis and a certain hydrophilicity. In addition, CTFs have been used in heterogeneous catalysis,[52] as catalytic support in liquid phase reactions,[53] for gas storage,[54] and separation of organic dyes.[55] CTFs can be synthesized through different methods and different reaction conditions that enable the tunability of their porosity and surface area.[5,56,57,58] The nitrogen moieties within the CTFs can provide coordination anchors or support for metal and other species.[59,60]

Ketjenblack (KB) is an electro-conductive carbon material that is suitable for many applications such as batteries, conductive coatings etc. It has very high specific surface area of 1400 m^2/g and excellent charge transfer properties. KB is an amorphous carbon with mesopores around 2-8 nm. When it is used as a component for composites, it can boost the overall performance of materials. KB has the same level of electro-conductivity as conventional carbon black but requires only 1/2 to 1/3 of the loading quantity in a composite. Because KB is effective at a lower loading quantity, it has less effect on the physical properties of the base resins or paint. Further, KB experiences minimal reduction in electro-conductivity when mixed with other materials.

2 Physical characterization of examined materials as-synthesized, after dry SO_2 and humid SO_2 exposure

2.1 Stability tests

Before and after stability tests for dry and humid SO_2 exposure all MOFs were activated as described. For dry exposure, the sample was characterized again after SO_2-isotherm measurement. For humid SO_2 exposure, a controlled airflow of 2 L min^{-1} was bubbled through a sodium hydrogen sulfite solution (0.4 g $Na_2S_2O_5$ in 100 mL water) in a Schlenk round bottom flask to transport gaseous SO_2 into a humidity chamber (desiccator vessel). The experimental setup is shown in Figure S3. To ensure a largely constant SO_2 concentration in the exposure chamber, the setup was constructed with a 3-way valve for the possibility to switch the route of gas flow. The SO_2 was either directed to the chamber or the exhaust air if there was sufficient SO_2 in the chamber. The desiccator was equipped with a crystallizing dish filled with saturated sodium chloride solution (80 mL, relative humidity (RH) 75%) and the sample (50 mg). The RH and the amount of SO_2 in the desiccator was monitored with a hygrometer (VWR TH300 hygrometer) and an SO_2-sensor (Dräger Pac 6000 electrochemical sensor), respectively. 7 materials were exposed to a humid SO_2 environment at room temperature with 75 ± 6% RH and 35 ± 5 ppm SO_2 for 5 h. The unit for humid SO_2 exposure is given by multiplying the concentration by the exposure time.

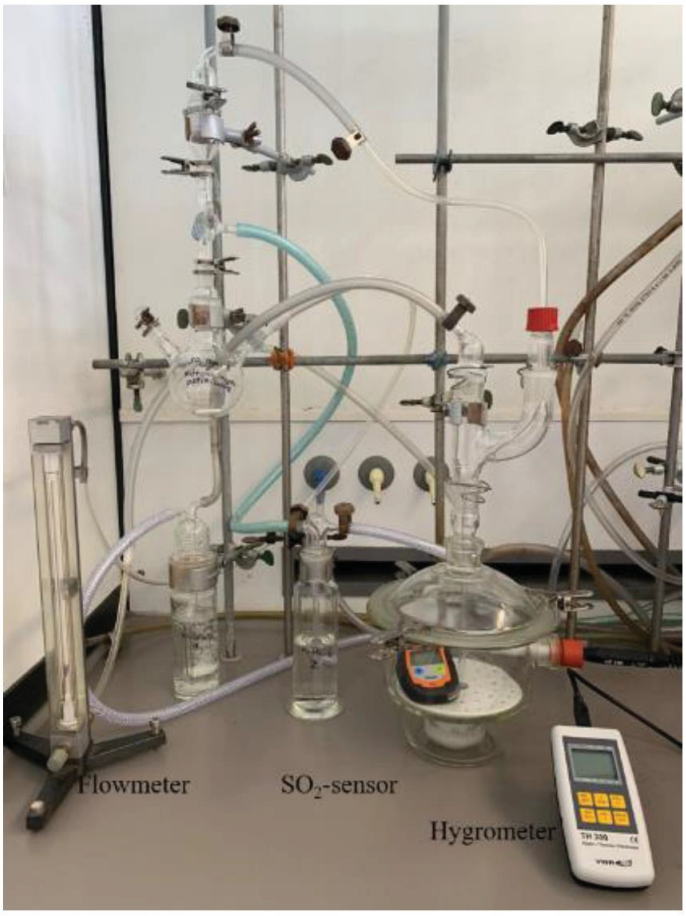

Figure S3. Setup for humid SO_2 exposure experiments.

2.2 Powder diffraction Experiments

Powder X-ray diffraction (PXRD) measurements were performed on a Bruker *D2 Phaser* (300 W, 30 kV, 10 mA) at ambient temperatures. As radiation source a Cu-Kα-cathode (λ = 1.54182 Å) between 5° < 2Θ < 50° was used. Diffraction patterns were obtained using a silicon "low background" sample holder.

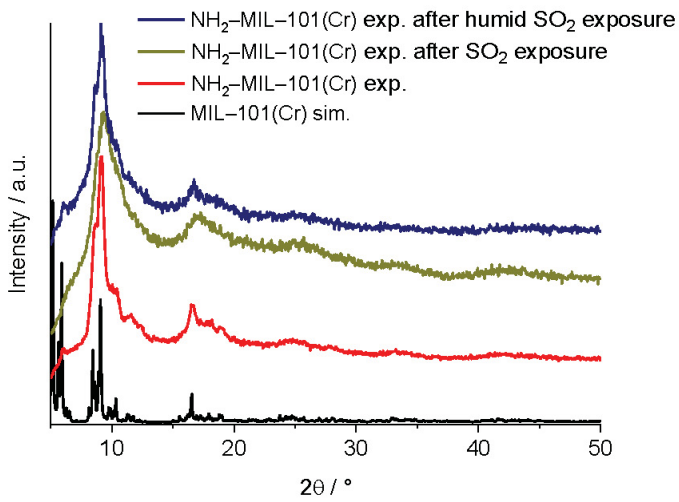

Figure S4. Comparison of experimental and simulated (sim.) PXRD patterns of NH_2-MIL-101(Cr) (simulation based on crystal structure data, CCDC 605510, Reference [61]).

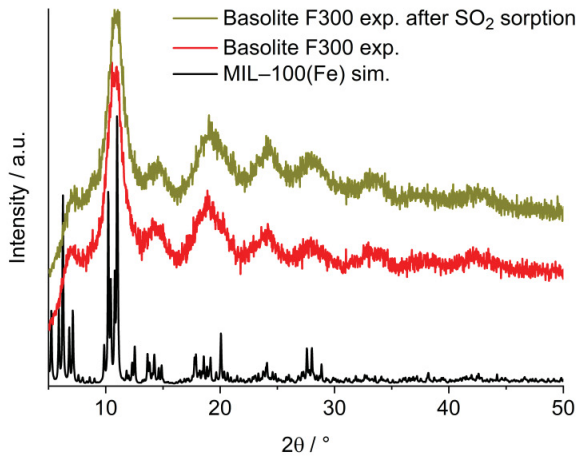

Figure S5. Comparison of experimental and simulated (sim.) PXRD patterns of Basolite F300 (simulation based on crystal structure data of MIL-100(Fe), CCDC 640536, Reference [13]).

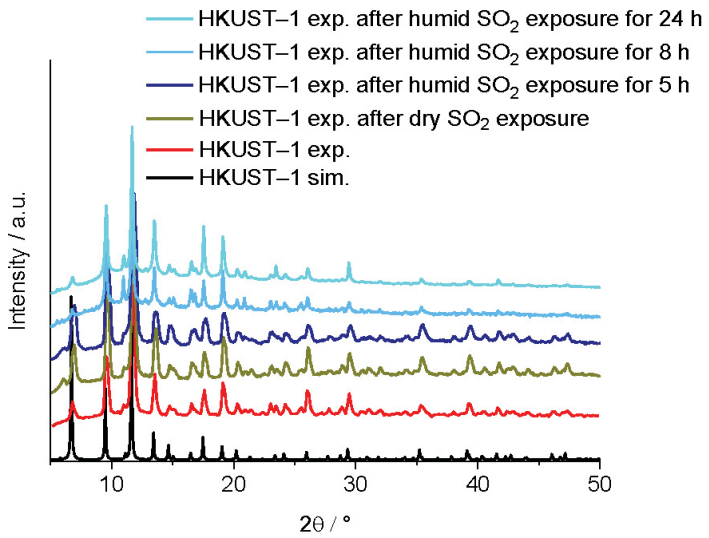

Figure S6. Comparison of experimental and simulated (sim.) PXRD patterns of HKUST-1 (simulation based on crystal structure data, CCDC 755080, Reference [62]).

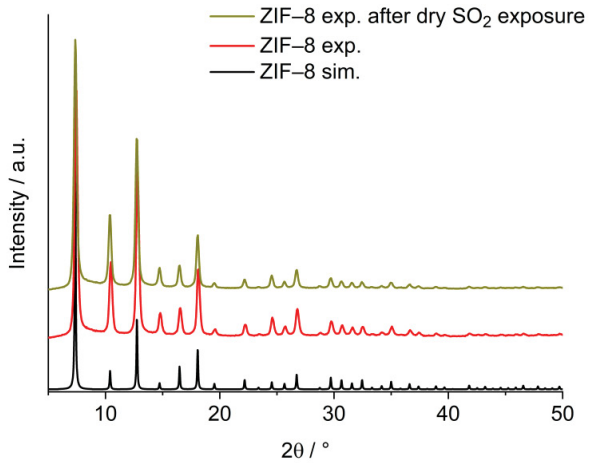

Figure S7. Comparison of experimental and simulated (sim.) PXRD patterns of ZIF-8 (simulation based on crystal structure data, CCDC 864309, Reference [63]).

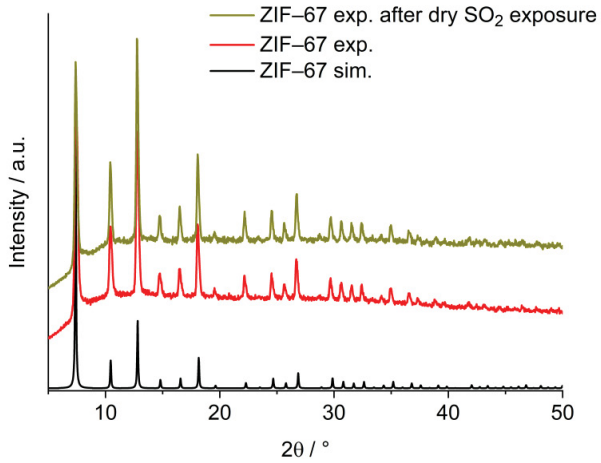

Figure S8. Comparison of experimental and simulated (sim.) PXRD patterns of ZIF-67 (simulation based on crystal structure data, CCDC 864309, Reference [64]).

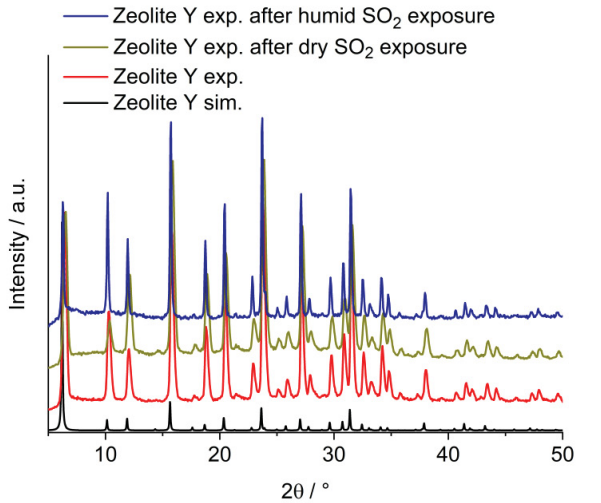

Figure S9. Comparison of experimental and simulated (sim.) PXRD patterns of Zeolite Y (simulation based on crystal structure data, Reference [38]).

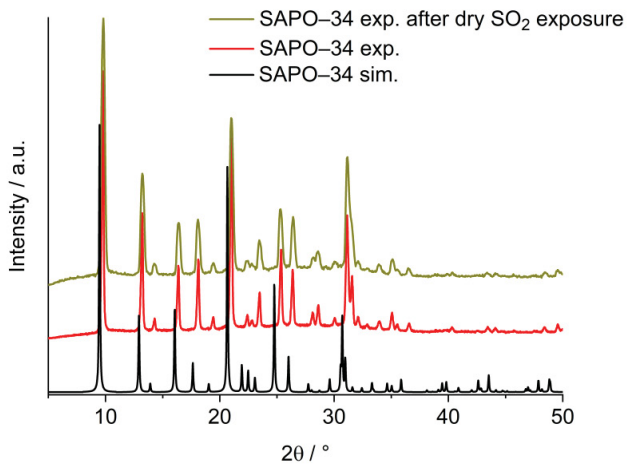

Figure S10. Comparison of experimental and simulated (sim.) PXRD patterns of SAPO-34 (simulation based on crystal structure data, CCDC 1582922, Reference [65]).

2.3 Gas sorption experiments

Before each experiment samples were activated for at least 3 hours and at a minimum temperature of 393 K under a vacuum of less than $5 \cdot 10^{-3}$ mbar. All used gases (He, SO_2, CO_2, N_2) were of ultra-high purity (UHP grade 5.0, 99.999%) and the STP volumes at 293.15 K and 101.325 kPa are given according to the NIST standards. N_2 sorption experiments were performed in a Quantachrome *Autosorb 6* (QUANTACHROME, Odelzhausen, Germany) instrument within a pressure range of 0.005-1 bar at 77 K. SO_2 and CO_2 Sorption experiments were performed on an *Autosorb iQ MP* (QUANTACHROME, Odelzhausen, Germany) instrument within a pressure range of 0.001-1 bar and 293 K. For safety precautions of toxic SO_2, a *Dräger Pac 6000* SO_2-detector (0-100 ppm in 0.1 ppm steps) was used in close range to the sorption-device.
SO_2-sorption experiments with our setup involve some limitations emerging from the corrosive nature of the SO_2-adsorptive. Each SO_2-sorption run had to be completed within a maximum time of 10 h. This time limit was specified by the company Quantachrome to prevent damage to the gaskets. After this time the system had to be regenerated by flushing with nitrogen. Irreversible swelling of the SO_2 adsorbing gaskets in the measurement device, which could cause leaks in the system, had to be prevented by setting the measurement time to this maximum (10 h) to meet safety precautions and to protect the device. Then, after each measurement, the gas line was flushed with N_2 several times and remained under N_2 atmosphere for at least 12 h to regenerate the gaskets. In the case of long equilibration times upon adsorption and desorption we decided to collect the adsorption data points as complete as possible with long-enough equilibration times at the expense that for desorption, fewer data points could be measured. This compromise then led to incomplete, i.e. not-closed desorption branches, which however are solely due to the experimental boundary conditions and cannot be interpreted in terms of decomposition or chemisorption.

2.4 N_2 sorption

N_2-sorption isotherms were measured on an *Autosorb 6* (QUANTACHROME, Odelzhausen, Germany) instrument at 77 K within a pressure range of 0.005-1 bar. Before each experiment samples were activated for at least 3 hours and at a minimum of 393 K under a vacuum of less than $5 \cdot 10^{-3}$ mbar.

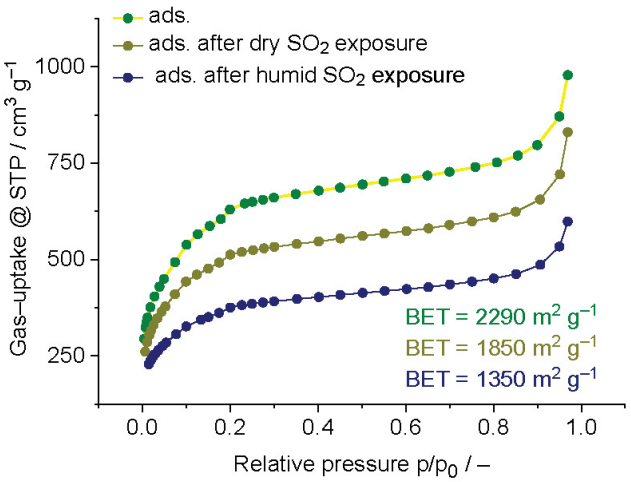

Figure S11. N_2-adsorption isotherms (77 K) of NH_2-MIL-101(Cr) before and after exposure to dry and humid SO_2.

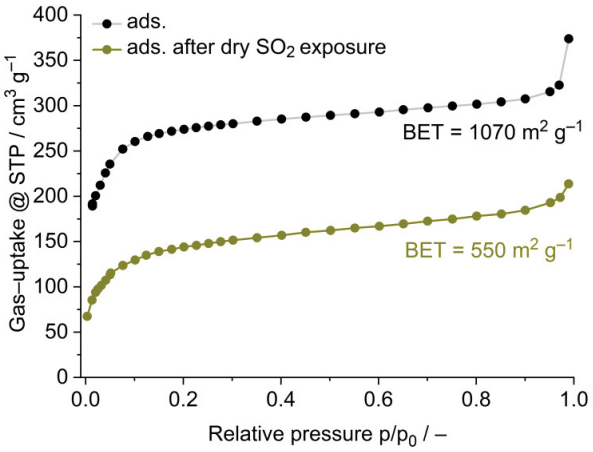

Figure S12. N_2-adsorption isotherms (77 K) of Basolite F300 before and after exposure to dry SO_2.

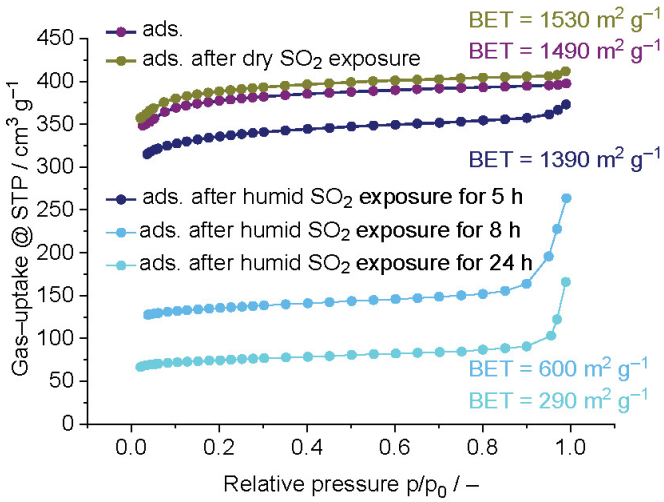

Figure S13. N_2-adsorption isotherms (77 K) of HKUST-1 before and after exposure to dry or humid SO_2.

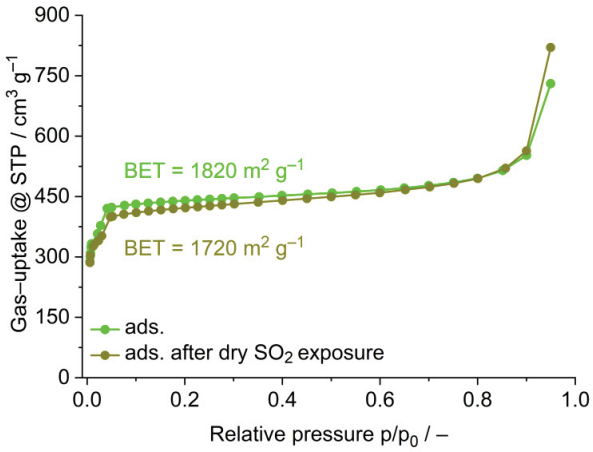

Figure S14. N_2-adsorption isotherms (77 K) of ZIF-8 before and after exposure to dry SO_2.

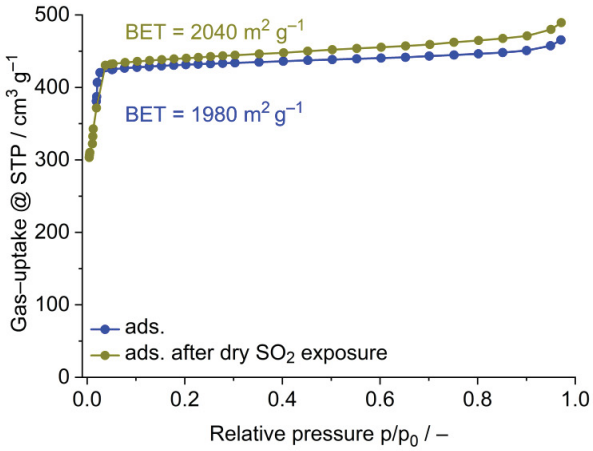

Figure S15. N_2-adsorption isotherms (77 K) of ZIF-67 before and after exposure to dry SO_2.

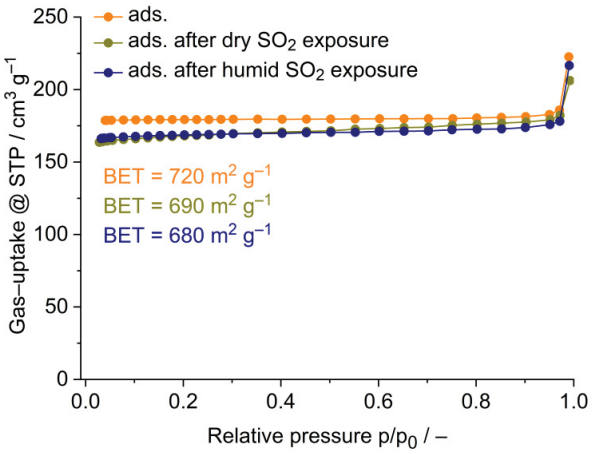

Figure S16. N_2-adsorption isotherms (77 K) of SAPO-34 before and after exposure to dry or humid SO_2.

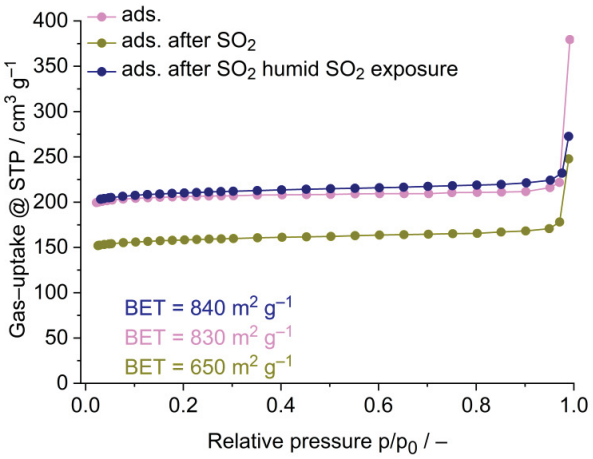

Figure S17. N_2-adsorption isotherms (77 K) of Zeolite Y before and after exposure to dry or humid SO_2.

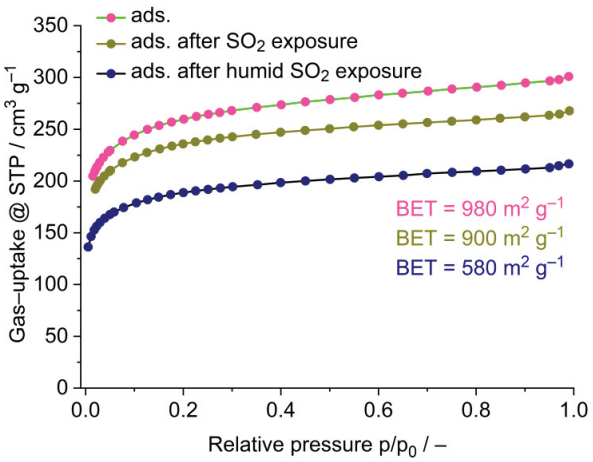

Figure S18. N_2-adsorption isotherms (77 K) of CTF-1(400) before and after exposure to dry or humid SO_2.

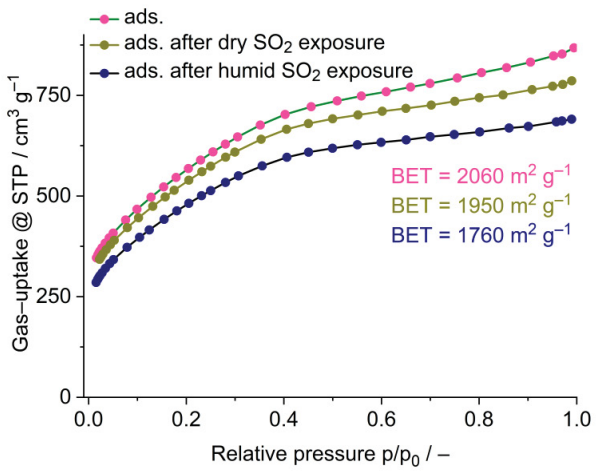

Figure S19. N_2-adsorption isotherms (77 K) of CTF-1(600) before and after exposure to dry or humid SO_2.

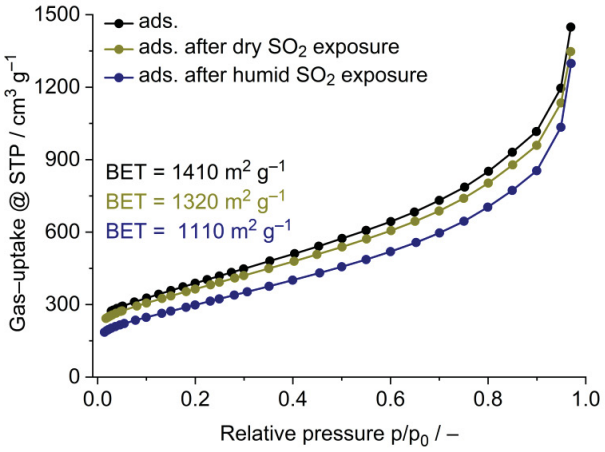

Figure S20. N_2-adsorption isotherms (77 K) of Ketjenblack before and after exposure to dry SO_2.

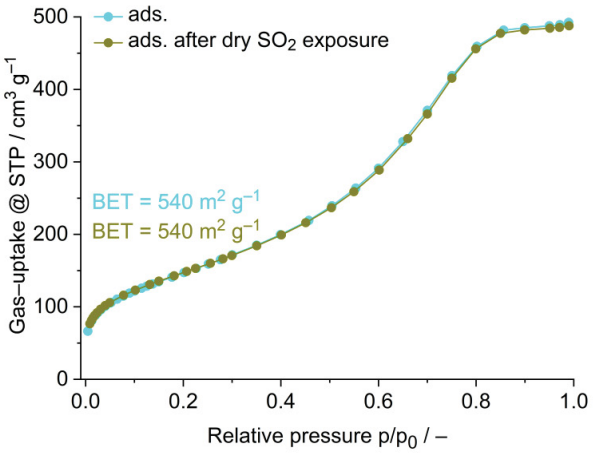

Figure S21. N_2-adsorption isotherms (77 K) of Silica gel 60 before and after exposure to dry SO_2.

2.5 SO_2 and CO_2-sorption and isotherm fitting

The measurement of adsorption isotherms of both SO_2 and CO_2 under the same conditions are used to examine sorption capacity and affinity and are further used to calculate the IAST-selectivity. SO_2 and CO_2 uptake values are given in Table S2 Fitting-simulations were calculated using 3P sim software.[66] We applied several commonly used models (eq. 1-6) on our isotherm data. Here the best fitting results are achieved by applying the Langmuir or Dual-site Langmuir (DSL) model. Fitting parameters are shown in Table S3.

Freundlich: $$q_{eq} = K \cdot p^t \quad (1)$$

Langmuir: $$q_{eq} = \frac{q_{max} \cdot K \cdot p}{1+K \cdot p} \quad (2)$$

Sips: $$q_{eq} = \frac{q_{max} \cdot K \cdot p^t}{1+K \cdot p^t} \quad (3)$$

Toth: $$q_{eq} = \frac{q_{max} \cdot K \cdot p}{(1+(K \cdot p)^t)^{1/t}} \quad (4)$$

DSL: $$q_{eq} = q_{max1} \frac{\cdot K_1 \cdot p}{1+K_1 \cdot p} + q_{max2} \frac{\cdot K_2 \cdot p}{1+K_2 \cdot p} \quad (5)$$

DSLSips $$q_{eq} = q_{\max} \left(\frac{\cdot K_1 \cdot p}{1+K_1 \cdot p} + \frac{\cdot (K_2 \cdot p)^t}{(1+K_2 \cdot p)^t} \right) \quad (6)$$

q_{eq}= amount adsorbed [mmol/g]

q_{max} = maximum adsorption capacity [mmol/g]

K = affinity constant for adsorption [1/bar]

p = pressure [kPa]

t = index of heterogeneity

The Sips model represents a combination of Langmuir and Freundlich model. This becomes apparent when K or p approaches 0 and the model is reduced to a Freundlich equation whereas for homogeneous materials with t = 1 concentrations it is reduced to the Langmuir equation.[67]

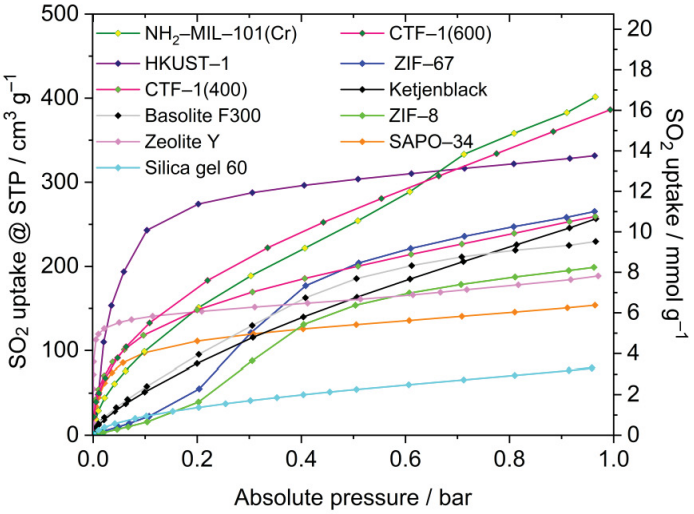

a)

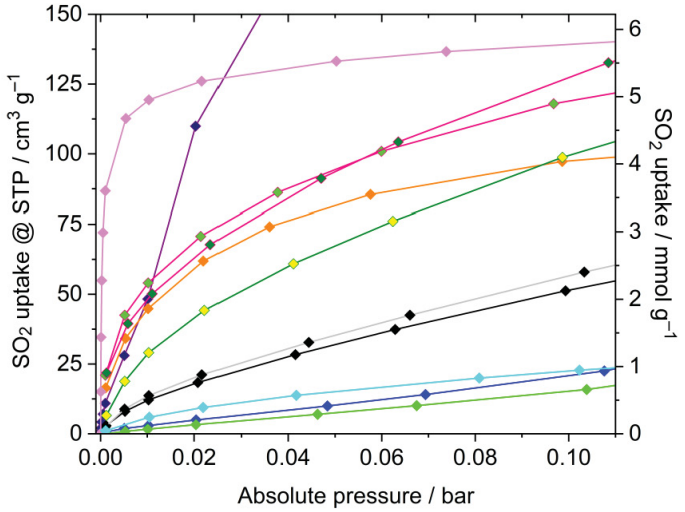

b)

Figure S22. Overlay of the SO_2 adsorption isotherms (293 K) for all examined materials (a) 0.001-1 bar, (b) 0.001-0.11 bar.

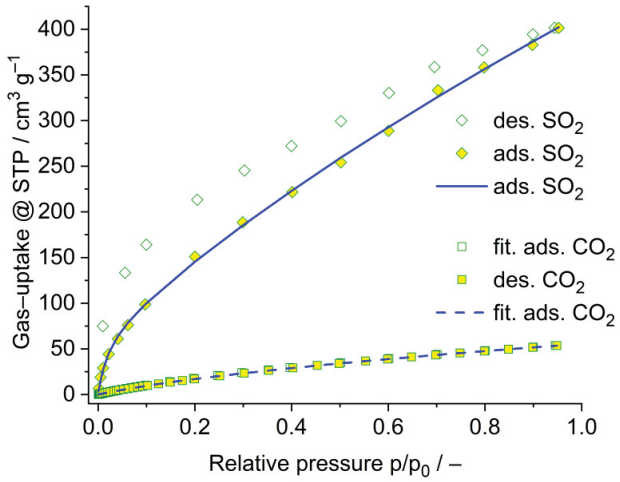

Figure S23. Experimental SO_2- (rhombs) and CO_2- (squares) sorption isotherm and fitted SO_2- (line) and CO_2- (dashed line) adsorption isotherm of NH_2-MIL-101(Cr) at 293 K.

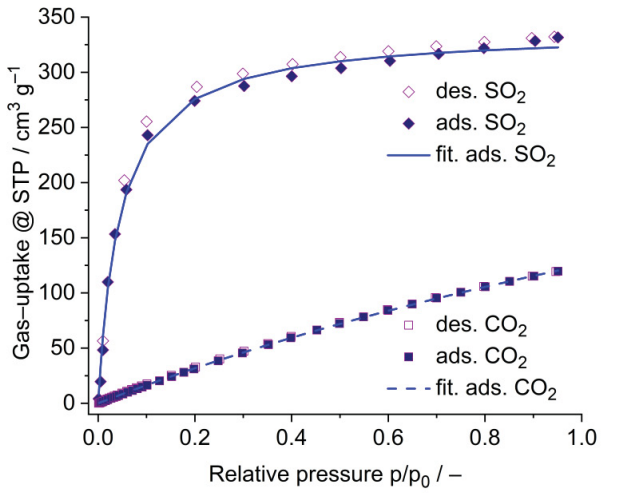

Figure S24. Experimental SO_2- (rhombs) and CO_2- (squares) sorption isotherm and fitted SO_2- (line) and CO_2- (dashed line) adsorption isotherm of HKUST-1 at 293 K.

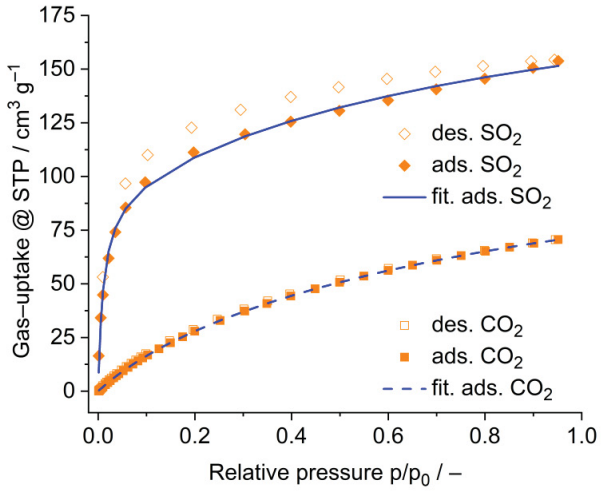

Figure S25. Experimental SO_2- (rhombs) and CO_2- (squares) sorption isotherm and fitted SO_2- (line) and CO_2- (dashed line) adsorption isotherm of SAPO-34 at 293 K.

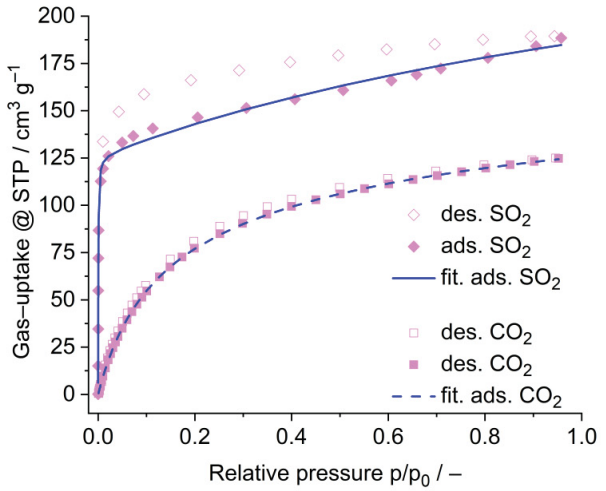

Figure S26. Experimental SO_2- (rhombs) and CO_2- (squares) sorption isotherm and fitted SO_2- (line) and CO_2- (dashed line) adsorption isotherm of Zeolite Y at 293 K.

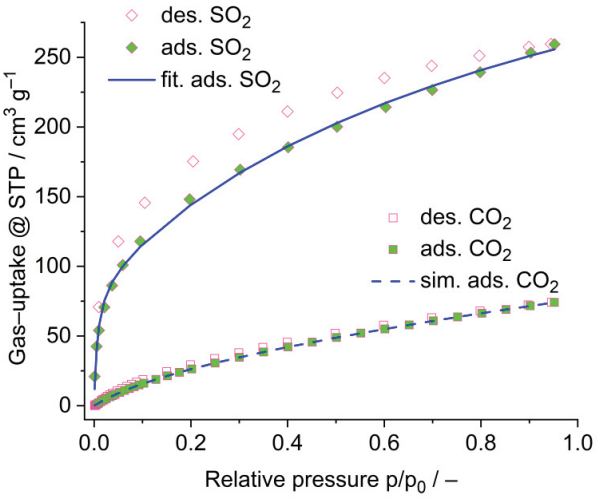

Figure S27. Experimental SO_2- (rhombs) and CO_2- (squares) sorption isotherm and fitted SO_2- (line) and CO_2- (dashed line) adsorption isotherm of CTF-1(400) at 293 K.

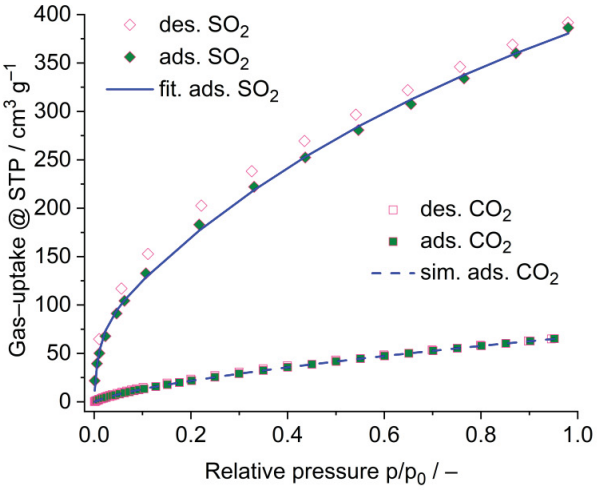

Figure S28. Experimental SO_2- (rhombs) and CO_2- (squares) sorption isotherm and fitted SO_2- (line) and CO_2- (dashed line) adsorption isotherm of CTF-1(600) at 293K.

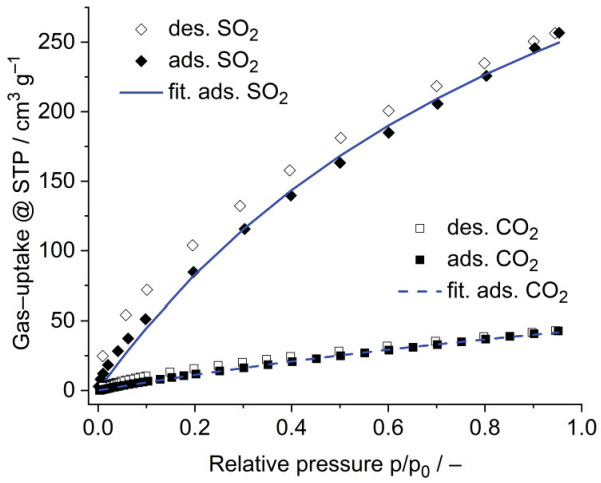

Figure S29. Experimental SO_2- (rhombs) and CO_2- (squares) sorption isotherm and fitted SO_2- (line) and CO_2- (dashed line) adsorption isotherm of Ketjenblack at 293K.

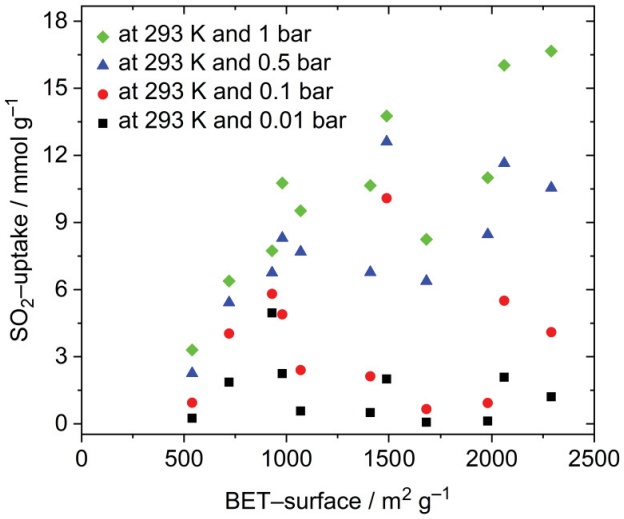

Figure S30. SO_2 uptake at different pressures vs BET surface area (293 K).

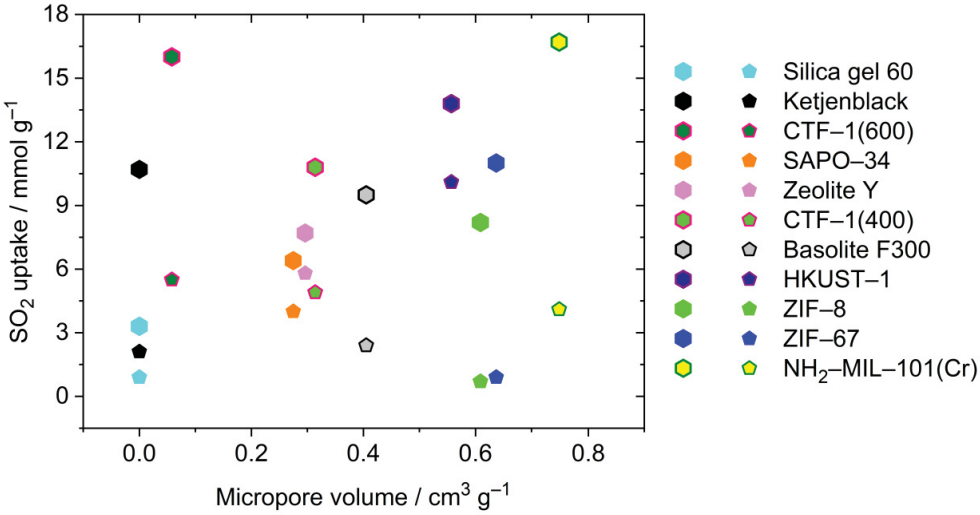

Figure S31. SO_2 uptake (293 K) at 1 bar indicated by hexagons and at 0.1 bar indicated by pentagons vs the micropore volume (determined by applying the t-plot method on N_2 adsorption data at 77 K at $p/p_0 \leq 0.3$).

2.6 Thermogravimetric analysis

TGA curves for NH_2-MIL-101(Cr) can be found in the Supporting Information to ref. [7] or in ref. [8].

Interpretation of the weight loss during thermogravimetric analysis: The first weight loss in the TGA curves, shown in Figure S32, can be assigned to the removal of water, from ambient humidity, and/or the removal of residual solvent out of the pores. MOF materials exhibit more limited thermal stability with decomposition of the organic frameworks at approximately 300 °C, whereas the covalent triazine frameworks CTF-1 (synthesized at 400 °C/600 °C) start with a significant weight loss at temperatures of over ~500 and ~700 °C, respectively and the zeolitic compounds, Zeolite Y and SAPO-34, withstand temperatures beyond 800 °C.

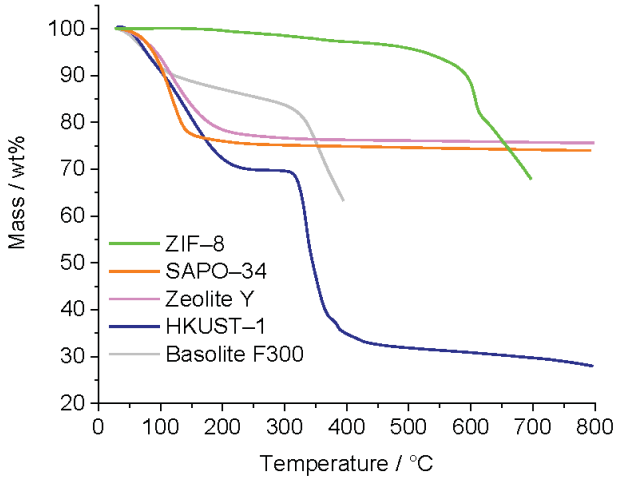

Figure S32. TGA curves measured under N_2-atmosphere, heating rate 10 K/min.

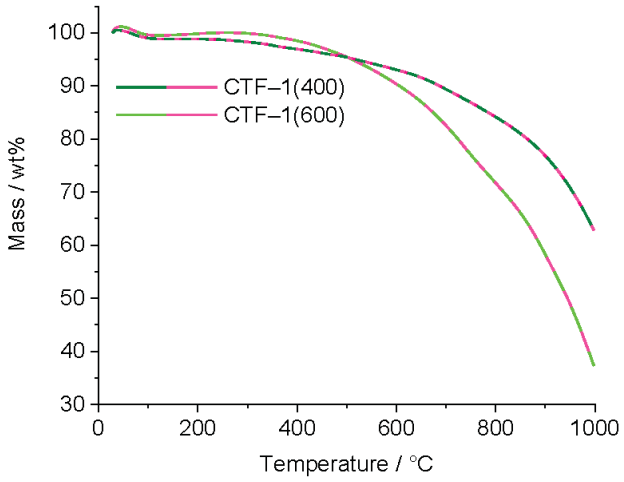

Figure S33. TGA curves measured under N_2-atmosphere, heating rate 5 K/min. Data replotted from the data obtained for the same samples used in ref. [68].

3 Enthalpy of adsorption for NH_2-MIL-101(Cr)

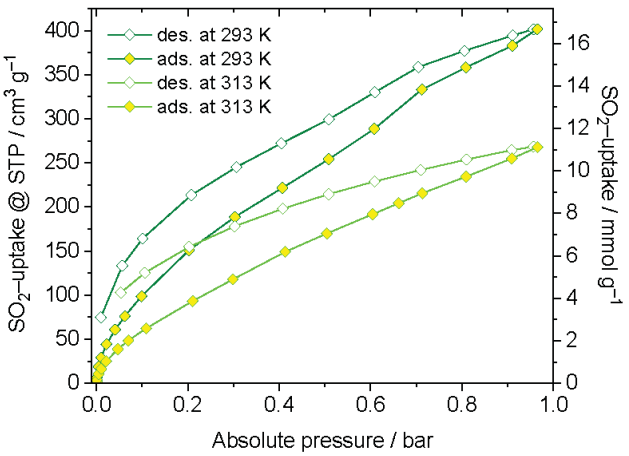

Figure S34. SO_2 sorption isotherms of NH_2-MIL-101(Cr) at 293 K and 313 K for the determination of the enthalpy of adsorption (see in Figure S34).

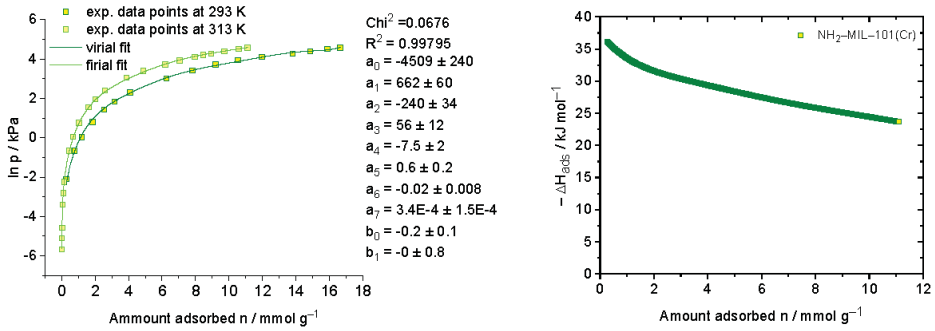

Figure S35. Left: Virial fit for the SO_2 adsorption isotherms of NH_2-MIL-101(Cr) at 293 K and 313 K and right enthalpy of adsorption ΔH_{ads} from the virial analysis SO_2 adsorption isotherms of of NH_2-MIL-101(Cr) at 293 K and 313 K. The isotherms were fitted from n_{min} = 0.28 mmol g^{-1}.

When comparing the slightly lower $\Delta H_{ads}(SO_2)$ of NH_2-MIL-101 (–36 kJ mol^{-1}) to MIL-101(Cr)-4F(1%) (–54 kJ mol^{-1}) the difference is possibly explained by the "pin" mechanism in which the fluorinated ligand leads to an SO_2 interaction with the Brønsted acid site (Cr-OH group in the SBU) and the Lewis acid site (open Cr^{3+} metal site in the SBU) thus also leading to a more efficient packing during SO_2 adsorption in MIL-101(Cr)-4F(1%).[69,70]

4 IAST-selectivity

Selectivities of SO_2 over CO_2 were calculated from fitted isotherm data of experimentally measured isotherms. The 3P sim software (3P Instruments, Germany, version 1.1.0.7) calculates the maximal loadings of each gas depending on the given mole fraction. IAST selectivities S of binary gas mixtures were calculated using equation 6, where x_i represents the absorbed gas amount and y_i the mole fraction of each adsorptive.

$$S = \frac{x_1/x_2}{y_1/y_2} \qquad (7)$$

Table S2. Gas uptake values of SO_2 and CO_2 isotherms measured at 293 K and the resulting SO_2/CO_2 IAST selectivity values.

Material	SO_2 uptake [mmol g^{-1}] at			CO_2uptake [mmol g^{-1}] at			SO_2/CO_2 selectivity at SO_2/CO_2 molar ratio		
	0.01 bar	0.1 bar	0.5 bar	0.01 bar	0.1 bar	0.5 bar	0.01	0.1	0.5
NH_2-MIL-101(Cr)	1.2	4.1	10.5	0.05	0.4	1.4	34	30	30
HKUST-1	2.0	10.1	12.6	0.1	0.7	3.0	41	36	28
Zeolite Y	5.0	5.8	6.7	0.4	2.3	4.4	265	180	149
SAPO-34	1.9	4.0	5.4	0.1	0.7	2.1	42	36	33
CTF-1(400)	2.2	4.9	8.3	0.1	0.7	2.0	62	40	27
CTF-1(600)	2.1	5.5	11.6	0.1	0.6	1.7	63	46	43
Ketjenblack	0.5	2.1	6.8	0.02	0.3	1.0	9	10	14

Table S3. Fitting Parameters for SO_2/CO_2 IAST-selectivities at 293 K. [a]

Material	Gas	Model [b]	R^2	Affinity const. [1/bar]	Max. loading [mmol/g]	Affinity const. 2 [1/bar]	Max. loading 2 [mmol/g]
NH_2-MIL-101(Cr)	SO_2	DSL	0.999	45.977	2.966	0.217	79.518
	CO_2	DSL	0.999	9.553	0.311	0.273	11.298
HKUST-1	SO_2	LAI	0.996	22.993	14.017	-	-
	CO_2	LAI	0.999	0.356	19.555	-	-
SAPO-34	SO_2	DSL	0.996	95.058	3.836	1.068	4.911
	CO_2	DSL	0.999	5.535	0.709	0.937	4.915
Zeolite Y	SO_2	DSL	0.996	2739	5.227	0.580	6.773
	CO_2	DSL	0.999	9.291	4.106	1.072	2.880
CTF-1(400)	SO_2	DSL	0.998	143.325	3.764	0.978	14.160
	CO_2	DSL	0.999	6.079	0.965	0.234	12.198
CTF-1(600)	SO_2	DSL	0.999	115.260	3.514	0.674	30.690
	CO_2	DSL	0.999	10.485	0.484	0.283	10.514
Ketjenblack	SO_2	LAI	0.996	0.901	22.275	-	-
	CO_2	LAI	0.999	0.390	6.367	-	-

[a] Basolite F300, ZIF-8, ZIF-67 and Silica Gel 60 were not included in the IAST calculations for their low SO_2 uptakes at low pressures. The number of three decimal digits are needed for the IAST selectivity calculation. Rounding to one decimal digit (as in Table 2, main text) leads to significant deviations in the IAST values. [b] DSL = Dual-site Langmuir; LAI = Langmuir.

5 Comparison with the literature

Table S4. Comparison of SO_2 sorption data from this work with the literature.

Material	SO_2-uptake [mmol g^{-1}]			Temp. [K]	BET [m^2 g^{-1}]	Total pore-volume [cm^3 g^{-1}]	Pore or window width [Å]	Lit.
	0.01 bar	0.1 bar	1 bar					
NH_2-MIL-101(Cr)	1.2	4.1	16.7	293	2290	1.162	15.4; 19.9[1]	this work
Basolite F300	0.6	2.4	9.5	293	1070	0.488	18-22[12]	this work
HKUST-1	2.0	10.1	13.8	293	1490	0.612	5; 11; 14[19]	this work
ZIF-8	0.1	0.7	8.2	293	1820	0.799	3.4; 11.4[71]	this work
ZIF-67	0.1	0.9	11.0	293	1980	0.694	3.4; 11.4[71]	this work
Zeolite Y	5.0	5.8	7.8	293	930	0.334	7.4, 13.7[38]	this work
SAPO-34	1.9	4.0	6.4	293	720	0.283	~5[72]	this work
Silica gel 60	0.2	0.9	3.3	293	540	0.754	~10-100[48]	this work
CTF-1(400)	2.2	4.9	10.8	293	980	0.459	~6-25[68,73]	this work
CTF-1(600)	2.1	5.5	16.0	293	2060	1.195	~8-35[68,74]	this work
Ketjenblack	0.5	2.1	10.7	293	1410	1.242	~20-80[75,76]	this work
MOF-177	0.3	1.0	25.7	293	4100	1.51	10.6-11.8[77,78]	79
NH_2-MIL-125(Ti)	3.0	7.9	10.8	293	1560	0.651	5-8[80]	79
MIL-160	4.2	5.5	7.2	293	1170	0.460	5	79
MIL-101(Cr)-4F	~1.3[a]	4.6	18.4	298	2176	1.19		69
MFM-170	-	~6[a]	17.5	298	2408	0.88	12.8,14.2, 15.9	81
MFM-170-H_2O	-	-	13.0	298	2003	-	-	81
MOF-505	-	-	12.9[a]	298	2216	0.73	8.3, 10.1	82
MFM-600	-	~3[a]	5.0	298	2281	-	-	83
MFM-601	-	~8[a]	12.3	298	3644	-	-	83
SIFSIX-1-Cu	3.43	8.74	11.01	298	-	-	-	84

SIFSIX-2-Cu-i	4.16	6.01	6.90	298	630	-	-	84
[Zn_2(oxo-dihbac)$_2$(bipy)]	-	-	10.9	293	47/275 [b]	0.059[b]/ 0.098[b]	4.5-6.5, 8	85
MFM-202a	-	3.0	10.2	298	2220	-	-	86
Ni(bdc)(ted)$_{0.5}$	-	4.54	9.97	298	1783	0.74	7.8	87
Zn(bdc)(ted)$_{0.5}$	-	-	4.41	298	1888	0.84	7.8	87
MIL-125(Ti)	-	3[a]	9.8[a]	298	1527	-	-	88
Mg-MOF-74	-	6.44	8.60	298	1206	-	-	87, 89
MFM-300(In)	-	-	8.28	298	1071	0.419	-	90
MFM-300(Al)	-	-	7.7[a]	293	1370	0.375[b]	5.7	91, 92
MFM-300(Al)-MW	7.2	8.6	-	283	1272	0.58	5	93
MFM-305	-	5.1[a]	7.0	298	779	0.372	6.2	94
MFM-305-CH_3	-	4.4[a]	5.2	298	256	0.184	5.2	94
NiDMOF-TM	-	-	4.8[a]	298	940	0.459	-	95
UNAM-1	0.4[a]	1.6[a]	3.5	298	522	-	-	96
KAUST-8	-	2.3[a]	2.9[a]	298	250			97
KAUST-7	-	2.1[a]	2.6[a]	298	280			97
Fe-soc-MOF		~9[a]	11.7	298	1470	0.58	-	98
ELM-12	-	1.95	2.73	298	706	0.26	4.3-6.1	99
$Co_3[Co(CN)_6]_2$	-	-	2.5	298	712	-	-	100
$Zn_3[Co(CN)_6]_2$	-	-	1.8	298	700	-	-	100
FMOF-2	-	-	2.2	298	378	-	-	101

[a] read from isotherm, [b] from CO_2 sorption data (273 K)

References

[1] D. Jiang, L. L. Keenan, A. D. Burrows, K. J. Edler, Synthesis and Post-Synthetic Modification of MIL-101(Cr)-NH_2 via a Tandem Diazotisation Process. *Chem. Comm.* **2012**, *48*, 12053–12055.

[2] N. Al-Janabi, P. Hill, L. Torrente-Murciano, A. Garforth, P. Gorgojo, F. Siperstein, X. Fan, Mapping the Cu-BTC Metal–Organic Framework (HKUST-1) Stability Envelope in the presence of Water Vapor for CO_2 Adsorption from Flue Gases. *Chem. Eng. J.* **2015**, *281*, 669–677.

[3] J. J. Beh, J. K. Lim, E. P. Ng, B. S. Ooi, Synthesis and Size Control of Zeolitic Imidazolate Framework-8 (ZIF-8): From the Perspective of Reaction Kinetics and Thermodynamics of Nucleation. *Mater. Chem. Phys.* **2018**, *216*, 393–401.

[4] X. Feng, M. A. Carreon, Kinetics of Transformation on ZIF-67 Crystals. *J. Cryst. Growth* **2015**, *418*, 158–162.

[5] P. Kuhn, A. Forget, D. Su, A. Thomas, M. Antonietti, From Microporous Regular Frameworks to Mesoporous Materials with Ultrahigh Surface Area: Dynamic Reorganization of Porous Polymer Networks. *J. Am. Chem. Soc.* **2008**, *130*, 13333–13337.

[6] A. Khutia, H. U. Rammelberg, T. Schmidt, S. Henninger, C. Janiak, Water sorption cycle measurements on functionalized MIL-101Cr for heat transformation application. *Chem. Mater.* **2013**, *25*, 790-798.

[7] A. Khutia, C. Janiak, Programming MIL-101Cr for selective and enhanced CO_2 adsorption at low pressure by postsynthetic amine functionalization. *Dalton Trans.* **2014**, *43*, 1338-1347.

[8] A. Herbst, A. Khutia, C. Janiak, Brønsted Instead of Lewis Acidity in Functionalized MIL-101Cr MOFs for Efficient Heterogeneous (nano-MOF) Catalysis in the Condensation Reaction of Aldehydes with Alcohols. *Inorg. Chem.* **2014**, *53*, 7319–7333.

[9] J. Chen, X. Zhang, X. Shi, F. Bi, Y. Yang, Y. Wang, Synergistic Effects of Octahedral TiO_2-MIL-101(Cr) with two Heterojunctions for Enhancing Visible-Light Photocatalytic Degradation of Liquid Tetracycline and Gaseous Toluene. *J. Colloid Interface Sci.* **2020**, *579*, 37–49.

[10] J. Ehrenmann, S. K. Henninger, C. Janiak, Water adsorption characteristics of MIL-101 for heat transformation applications of MOFs. *Eur. J. Inorg. Chem.* **2011**, 471–474.

[11] A. Dhakshinamoorthy, M. Alvaro, P. Horcajada, E. Gibson, M. Vishnuvarthan, A. Vimont, J.-M. Grenèche, C. Serre, M. Daturi, H. Garcia, Comparison of Porous Iron Trimesates Basolite F300 and MIL-100(Fe) As Heterogeneous Catalysts for Lewis Acid and Oxidation Reactions: Roles of Structural Defects and Stability. *ACS Catal.* **2012**, *2*, 2060–2065.

[12] X. Hu, X. Lou, C. Li, Y. Ning, Y. Liao, Q. Chen, E. S. Mananga, M. Shen, B. Hu, Facile synthesis of the Basolite F300-like nanoscale Fe-BTC framework and its lithium storage properties. *RSC Adv.* **2016**, *6*, 114483–114490.

[13] P. Horcajada, S. Surblé, C. Serre, D.-Y. Hong, Y.-K. Seo, J.-S. Chang, J.-M. Grenèche, I. Margiolaki, G. Férey, Synthesis and catalytic properties of MIL-100(Fe), an iron(III) carboxylate with large pores. *Chem. Commun.* **2007**, 2820–2822.

[14] F. Jeremias, A. Khutia, S. K. Henninger, C. Janiak, MIL-100(Al, Fe) as water adsorbents for heat transformation purposes—a promising application. *J. Mater. Chem.* **2012**, *22*, 10148–10151.

[15] F. Jeremias, S. K. Henninger, C. Janiak, Ambient pressure synthesis of MIL-100(Fe) MOF from homogeneous solution using a redox pathway. *Dalton Trans* **2016**, *45*, 8637–8644.

[16] S. S.-Y. Chui, S. M.-F. Lo, J. P. H. Charmant, A. G. Orpen, I. D. Williams, A chemically functionalizable nanoporous material. *Science* **1999**, *283*, 1148–1150.

[17] K. Schlichte, T. Kratzke, S. Kaskel, Improved Synthesis, Thermal Stability and Catalytic Properties of the Metal-Organic Framework Compound $Cu_3(BTC)_2$. *Microporous Mesoporous Mater.* **2004**, *73*, 81–88.

[18] P. Krawiec, M. Kramer, M. Sabo, R. Kunschke, H. Fröde, S. Kaskel, Improved Hydrogen Storage in the Metal-Organic Framework $Cu_3(BTC)_2$. *Adv. Eng. Mater.* **2006**, *8*, 293–296.

[19] S. D. Worrall, M. A. Bissett, P. I. Hill, A. P. Rooney, S. J. Haigh, M. P. Attfield, R. A.W. Dryfe, Metal-organic framework templated electrodeposition of functional gold nanostructures. *Electrochimica Acta* **2016**, *222*, 361–369.

[20] Q. Yang, C. Xue, C. Zhong, J.-F. Chen, Molecular Simulation of Separation of CO_2 from Flue Gases in CU-BTC Metal-Organic Framework. *AIChE J.* **2007**, *53*, 2832–2840.

[21] A. Perea-Cachero, J. Dechnik, R. Lahoz, C. Janiak, C. Téllez, J. Coronas, HKUST-1 Coatings on Laser-Microperforated Brass Supports for Water Adsorption. *CrystEngComm* **2017**, *19*, 1470–1478.

[22] P. Küsgens, M. Rose, I. Senkovska, H. Fröde, A. Henschel, S. Siegle, S. Kaskel, Characterization of Metal-Organic Frameworks by Water Adsorption. *Microporous Mesoporous Mater.* **2009**, *120*, 325–330.

[23] S. Loera-Serna, M. A. Oliver-Tolentino, M. de Lourdes López-Núñez, A. Santana-Cruz, A. Guzmán-Vargas, R. Cabrera-Sierra, H. I. Beltrán, J. Flores, Electrochemical Behavior of $[Cu_3(BTC)_2]$ Metal–Organic Framework: The Effect of the Method of Synthesis. *J. Alloys Compd.* **2012**, *540*, 113–120.

[24] K. Brandenburg, Diamond Version 4, Crystal and Molecular Structure Visualization, Crystal Impact - K. Brandenburg & H. Putz GbR, Bonn, Germany, 2009-2020.

[25] G. Férey, C. Mellot-Draznieks, C. Serre, F. Millange, J. Dutour, S. Surblé, I. Margiolaki, A Chromium Terephthalate-Based Solid with Unusually Large Pore Volumes and Surface Area. *Science* **2005**, *309*, 2040–2042.

[26] M. Erkartal, U. Erkilic, B. Tam, H. Usta, O. Yazaydin, J. T. Hupp, O. K. Farha, U. Sen, From 2-methylimidazole to 1,2,3-triazole: a Topological Transformation of ZIF-8 and ZIF-67 by Post-Synthetic Modification. *Chem. Commun.* **2017**, *53*, 2028–2031.

[27] X.-C. Huang, Y.-Y. Lin, J.-P. Zhang, X.-M. Chen, Ligand-Directed Strategy for Zeolite-Type Metal-Organic Frameworks: Zinc(II) Imidazolates with Unusual Zeolitic Topologies. *Angew. Chem. Int. Ed.* **2006**, *45*, 1557–1559.

[28] K. S. Park, Z. Ni, A. P. Côté, J. Y. Choi, R. Huang, F. J. Uribe-Romo, H. K. Chae, M. O'Keeffe, O. M. Yaghi, Exceptional Chemical and Thermal Stability of Zeolitic Imidazolate Frameworks. *PNAS* **2006**, *103*, 10186–10191.

[29] A. Phan, C. J. Doonan, F. J. Uribe-Romo, C. B. Knobler, M. O'Keeffe, O. M. Yaghi, Synthesis, Structure, and Carbon Dioxide Capture Properties of Zeolitic Imidazolate Frameworks. *Acc. Chem. Res.* **2010**, *43*, 58–67.

[30] J.-R. Li, R. J. Kuppler, H.-C. Zhou, Selective Gas Adsorption and Separation in Metal-Organic Frameworks. *Chem. Soc. Rev.* **2009**, *38*, 1477–1504.

[31] U. P. Tran, K. K. Le, N. T. Phan, Expanding Applications of Metal−Organic Frameworks: Zeolite Imidazolate Framework ZIF-8 as an Efficient Heterogeneous Catalyst for the Knoevenagel Reaction. *ACS Catal.* **2011**, *1*, 120–127.

[32] G. Zhong, D. Liu, J. Zhang, The application of ZIF-67 and its derivatives: adsorption, separation, electrochemistry and catalysts. *J. Mater. Chem. A* **2018**, *6*, 1887–1899.

[33] Y. Pan, Z. Lai Sharp, Separation of C2/C3 Hydrocarbon Mixtures by Zeolitic Imidazolate Framework-8 (ZIF-8) Membranes Synthesized in Aqueous Solutions. *Chem. Commun.* **2011**, 10275–10277.

[34] G. Lu, J. T. Hupp, Metal-Organic Frameworks as Sensors: a ZIF-8 Based Fabry-Pérot Device as a Selective Sensor for Chemical Vapors and Gases. *J. Am. Chem. Soc.* **2010**, *132*, 7832–7833.

[35] B. Chen, Z. Yang, Y. Zhu, Y. Xia, Zeolitic Imidazolate Framework Materials: Recent Progress in Synthesis and Applications. *J. Mater. Chem. A* **2014**, *2*, 16811–16831.

[36] J.-P. Zhang, A.-X. Zhu, R.-B. Lin, X.-L. Qi, X.-M. Chen, Pore Surface Tailored SOD-Type Metal-Organic Zeolites. *Adv. Mater.* **2011**, 1268–1271.

[37] A. Wolińska-Grabczyk and A. Jankowski, Membranes for Vapour Permeation, in *Pervaporation, Vapour Permeation and Membrane Distillation: Principles and Applications* (Eds A. Basile, A. Figoli, M. Khayet), Elsevier Science 2015, Burlington, pp. 145–175.

[38] C. A. C. Perez, N. S. de Resende, V. M. M. Salim, M. Schmal, Water Interaction in Faujasite Probed by in Situ X-ray Powder Diffraction. *J. Phys. Chem. C* **2017**, *121*, 2755–2761.

[39] W. Lutz, Zeolite Y: Synthesis, Modification, and Properties - A Case Revisited. *Adv. Mater. Sci. Eng.* **2014**, *2014*, 1–20.

[40] T. Li, H. Liu, Y. Fan, P. Yuan, G. Shi, X. T. Bi, X. Bao, Synthesis of Zeolite Y from Natural Aluminosilicate Minerals for Fluid Catalytic Cracking Application. *Green Chem.* **2012**, *14*, 3255.

[41] E. C. Vogt, B. M. Weckhuysen, Fluid Catalytic Cracking: Recent Developments on the Grand Old Lady of Zeolite Catalysis. *Chem. Soc. Rev.* **2015**, 7342–7370.

[42] J. Xu, K.-G. Haw, Z. Li, S. Pati, Z. Wang, S. Kawi, A Mini-Review on Recent Developments in SAPO-34 Zeolite Membranes and Membrane Reactors. *React. Chem. Eng.* **2021**, *6*, 52–66.

[43] T. Doan, K. Nguyen, P. Dam, T. H. Vuong, M. T. Le, H. P. Thanh, Synthesis of SAPO-34 Using Different Combinations of Organic Structure-Directing Agents. *J. Chem.* **2019**, *2019*, 1–10.

[44] J. Zhong, J. Han, Y. Wei, P. Tian, X. Guo, C. Song, Z. Liu, Recent Advances of the Nano-Hierarchical SAPO-34 in the Methanol-to-Olefin (MTO) Reaction and other Applications. *Catal. Sci. Technol.* **2017**, *7*, 4905–4923.

[45] M. Salmasi, S. Fatemi, S. J. Hashemi, MTO Reaction over SAPO-34 Catalysts Synthesized by Combination of TEAOH and Morpholine Templates and Different Silica Sources. *Sci. Iran* **2012**, *19*, 1632–1637.

[46] Y. Seo and S.-P. Kang, Enhancing CO2 Separation for Pre-Combustion Capture with Hydrate Formation in Silica Gel Pore Structure. *Chem. Eng. J.* **2010**, *161*, 308–312.

[47] S.-P. Kang, J. Lee, Y. Seo, Pre-Combustion Capture of CO2 by Gas Hydrate Formation in Silica Gel Pore Structure. *Chem. Eng. J.* **2013**, *218*, 126–132.

[48] D. Dutta, S. Chatterjee, K. T. Pillai, P. K. Pujari, B. N. Ganguly, Pore Structure of Silica Gel: a Comparative Study Through BET and PALS. *Chem. Phys.* **2005**, *312*, 319–324.

[49] P. Kuhn, M. Antonietti, A. Thomas, Porous, covalent triazine- based frameworks prepared by ionothermal synthesis. *Angew.Chem. Int. Ed.* **2008**, *47*, 3450-3453.

[50] P. Kuhn, A. Thomas, M. Antonietti, Toward tailorable porous organic polymer networks: a high-temperature dynamic polymerization scheme based on aromatic nitriles. *Macromolecules* **2009**, *42*, 319-326.

[51] M. J. Bojdys, J. Jeromenok, A. Thomas, M. Antonietti, Rational Extension of the Family of Layered, Covalent, Triazine-Based Frameworks with Regular Porosity. *Adv. Mater.* **2010**, *22*, 2202-2205.

[52] P. Katekomol, J. Roeser, M. Bojdys, J. Weber, A. Thomas, Covalent Triazine Frameworks Prepared from 1,3,5-Tricyanobenzene. *Chem. Mater.* **2013**, *25*, 1542-1548.

[53] C. E. Chan-Thaw, A. Villa, P. Katekomol, D. Su, A. Thomas, L. Prati, Covalent triazine framework as catalytic support for liquid phase reaction. *Nano Lett.* **2010**, *10*, 537-541.

[54] A. Bhunia, V. Vasylyeva, C. Janiak, From a supramolecular tetranitrile to a porous covalent triazine-based framework with high gas uptake capacities. *Chem. Commun.* **2013**, *49*, 3961-3963.

[55] W. Zhang, F. Liang, C. Li, L.-G. Qiu, Y.-P. Yuan, F.-M. Peng, X. Jiang, A.-J. Xie, Y.-H. Shen, J.-F. Zhu, Microwave-enhanced synthesis of magnetic porous covalent triazine-based framework composites for fast separation of organic dye from aqueous solution. *J. Hazard. Mater.* **2011**, *186*, 984-990.

[56] A. Bhunia, I. Boldog, A. Möller, C. Janiak, Highly stable nanoporous covalent triazine-based frameworks with an adamantane core for carbon dioxide sorption and separation. *J. Mater. Chem. A*, **2013**, *1*, 14990–14999.

[57] K. Wang, L. M. Yang, X. Wang, L. Guo, G. Cheng, C. Zhang, S. Jin, B. Tan, A. Cooper, Covalent Triazine Frameworks via a Low- Temperature Polycondensation Approach. *Angew. Chem. Int. Ed.* **2017**, *56*, 14149–14153.

[58] S. Ren, M. J. Bojdys, R. Dawson, A. Laybourn, Y. Z. Khimyak, D. J. Adams, A. I. Cooper, Porous, fluorescent, covalent triazine-based frameworks via room-temperature and microwave-assisted synthesis. *Adv. Mater.* **2012**, *24*, 2357–2361.

[59] J. Li, L. Zhang, X. Liu, N. Shang, S. Gao, C. Feng, C. Wang, Z. Wang, Pd nanoparticles supported on a covalent triazine-based framework material: an efficient and highly chemoselective catalyst for the reduction of nitroarenes. *New J. Chem.* **2018**, *42*, 9684–9689.

[60] P. Su, K. Iwase, T. Harada, K. Kamiya, S. Nakanishi, Covalent triazine framework modified with coordinatively-unsaturated Co or Ni atoms for CO2 electrochemical reduction. *Chem. Sci.* **2018**, *9*, 3941–3947.

[61] O. V. Lebedev, F. Millange, C. Serre, G. van Tendeloo, G. Férey, First Direct Imaging of Giant Pores of the Metal−Organic Framework MIL-101. *Chem. Mater.* **2005**, *17*, 6525–6527.

[62] S. Xiang, W. Zhou, J. M. Gallegos, Y. Liu, B. Chen, Exceptionally High Acetylene Uptake in a Microporous Metal-Organic Framework with Open Metal Sites. *J. Am. Chem. Soc.* **2009**, *131*, 12415–12419.

[63] W. Morris, C. J. Stevens, R. E. Taylor, C. Dybowski, O. M. Yaghi, M. A. Garcia-Garibay, NMR and X-ray Study Revealing the Rigidity of Zeolitic Imidazolate Frameworks. *J. Phys. Chem. C* **2012**, *116*, 13307–13312.

[64] H. T. Kwon, H.-K. Jeong, A. S. Lee, H. S. An, J. S. Lee, Heteroepitaxially Grown Geolitic Imidazolate Framework Membranes with Unprecedented Propylene/Propane Separation Performances. *J. Am. Chem. Soc.* **2015**, *137*, 12304–12311.

[65] N. Yan, L. Wang, X. Liu, P. Wu, T. Sun, S. Xu, J. Han, P. Guo, P. Tian, Z. Liu, A Novel Approach for Facilitating the Targeted Synthesis of Silicoaluminophosphates. *J. Mater. Chem. A* **2018**, *6*, 24186–24193.

[66] 3P INSTRUMENTS, 3P sim, Version 1.1.0.7, *Simulation and Evaluation Tool for mixSorb*, 3P INSTRUMENTS 2018.

[67] E. Turiel, C. Perez-Conde, A. Martin-Esteban, Assessment of the Cross-Reactivity and Binding Sites Characterisation of a Propazine-Imprinted Polymer Using the Langmuir-Freundlich Isotherm. *Analyst* **2003**, *128*, 137–141.

[68] S. Öztürk, Y.-X. Xiao, D. Dietrich, B. Giesen, J. Barthel, J. Ying, X.-Y. Yang, C. Janiak, Nickel Nanoparticles Aupported on a Covalent Triazine Framework as Electrocatalyst for Oxygen Evolution Reaction and Oxygen Reduction Reactions. *Beilstein J. Nanotechnol.* **2020**, *11*, 770–781.

[69] E. Martínez-Ahumada, M. L. Díaz-Ramírez, H. A. Lara-García, D. R. Williams, V. Martis, V. Jancik, E. Lima, I. A. Ibarra, High and Reversible SO_2 Capture by a Chemically Stable Cr(iii)-Based MOF. *J. Mater. Chem. A* **2020**, *8*, 11515–11520.

[70] M. L. Díaz-Ramírez, E. Sánchez-González, J. R. Álvarez, G. A. González-Martínez, S. Horike, K. Kadota, K. Sumida, E. González-Zamora, M.-A. Springuel-Huet, A. Gutiérrez-Alejandre, V. Jancik, S. Furukawa, S. Kitagawa, I. A. Ibarra, E. Lima, Partially Fluorinated MIL-101(Cr): from a Miniscule Structure Modification to a Huge Chemical Environment Transformation Inspected by 129 Xe NMR. *J. Mater. Chem. A* **2019**, *7*, 15101–15112.

[71] W. Ma, Q. Jiang, P. Yu, L. Yang, L. Mao, Zeolitic Imidazolate Framework-Based Electrochemical Biosensor for In Vivo Electrochemical Measurements. *Anal. Chem.* **2013**, *85*, 7550–7557.

[72] H. Shi, Organic Template-Free Synthesis of SAPO-34 Molecular Sieve Membranes for CO_2–CH_4 Separation. *RSC Adv.* **2015**, *5*, 38330–38333.

[73] S. Dey, S. Bügel, S. Sorribas, A. Nuhnen, A. Bhunia, J. Coronas, C. Janiak, Synthesis and Characterization of Covalent Triazine Framework CTF-1@Polysulfone Mixed Matrix Membranes and Their Gas Separation Studies. *Front. Chem.* **2019**, *7*, 693.

[74] Y. Zhao, K. X. Yao, B. Teng, T. Zhang, Y. Han, A Perfluorinated Covalent Triazine-Based Framework for Highly Selective and Water–Tolerant CO_2 Capture. *Energy Environ. Sci.* **2013**, *6*, 3684-3692.

[75] G. Wang, G. Sun, Q. Wang, S. Wang, J. Guo, Y. Gao, Q. Xin, Improving the DMFC Performance with Ketjen Black EC 300J as the Additive in the Cathode Catalyst GG.G. P*J. Power Sources* **2008**, *180*, 176–180.

[76] C. Mani-Lata, C. Hussakan, G. Panomsuwan, Fast and Facile Synthesis of Pt Nanoparticles Supported on Ketjen Black by Solution Plasma Sputtering as Bifunctional HER/ORR Catalysts. *J. Compos. Sci.* **2020**, *4*, 121.

[77] D. Saha, S. Deng, Hydrogen Adsorption on Metal-Organic Framework MOF-177. *Tsinghua Sci. Technol.* **2010**, *15*, 363–376.

[78] G. W. Peterson, J. Mahle, A. Balboa, G. Wagner, T. Sewell, C. J. Karwacki, Defense Technical Information Center: Fort Belvoir, VA, 2008.

[79] P. Brandt, A. Nuhnen, M. Lange, J. Möllmer, O. Weingart, C. Janiak, Metal–Organic Frameworks with Potential Application for SO_2 Separation and Flue Gas Desulfurization. *ACS Appl. Mater. Interfaces* **2019**, *11*, 17350–17358.

[80] Y.-H. Fan, S.-W. Zhang, S.-B. Qin, X.-S. Li, S.-H. Qi, An Enhanced Adsorption of Organic Dyes onto NH_2 Functionalization Titanium-Based Metal-Organic Frameworks and the Mechanism Investigation. *Microporous Mesoporous Mater.* **2018**, *263*, 120–127.

[81] G. L. Smith, J. E. Eyley, X. Han, X. Zhang, J. Li, N. M. Jacques, H. G. W. Godfrey, S. P. Argent, L. J. McCormick McPherson, S. J. Teat, Y. Cheng, M. D. Frogley, G. Cinque, S. J. Day, C. C. Tang, T. L. Easun, S. Rudić, A. J. Ramirez-Cuesta, S. Yang, M. Schröder, Reversible Coordinative Binding and Separation of Sulfur Dioxide in a Robust Metal-Organic Framework with Open Copper Sites. *Nat. Mater.* **2019**, *18*, 1358–1365.

[82] X.-D. Song, S. Wang, C. Hao, J.-S. Qiu, Investigation of SO_2 Gas Adsorption in Metal–Organic Frameworks by Molecular Simulation. *Inorg. Chem. Commun.* **2014**, *46*, 277–281.

[83] J. H. Carter, X. Han, X.; F. Y. Moreau, I. da Silva, A. Nevin, H. G. W. Godfrey, C. C. Tang, S. Yang, M. Schröder, Exceptional Adsorption and Binding of Sulfur Dioxide in a Robust Zirconium-Based Metal-Organic Framework. *J. Am. Chem. Soc.* **2018**, *140*, 15564–15567.

[84] X. Cui, Q. Yang, L. Yang, R. Krishna, Z. Zhang, Z. Bao, H. Wu, Q. Ren, W. Zhou, B. Chen, H. Xing, Ultrahigh and Selective SO_2 Uptake in Inorganic Anion-Pillared Hybrid Porous Materials. *Adv. Mater.* **2017**, *29*, 1606929, 1–9.

[85] S. Glomb, D. Woschko, G. Makhloufi, C. Janiak, Metal-Organic Frameworks with Internal Urea-Functionalized Dicarboxylate Linkers for SO_2 and NH_3 Adsorption. *ACS Appl. Mater. Interfaces* **2017**, *9*, 37419–37434.

[86] S. Yang, L. Liu, J. Sun, K. M. Thomas, A. J. Davies, M. W. George, A. J. Blake, A. H. Hill, A. N. Fitch, C. C. Tang, M. Schröder, Irreversible Network Transformation in a Dynamic Porous Host Catalyzed by Sulfur Dioxide. *J. Am. Chem. Soc.* **2013**, *135*, 4954–4957.

[87] K. Tan, P. Canepa, Q. Gong, J. Liu, D. H. Johnson, A. Dyevoich, P. K. Thallapally, T. Thonhauser, J. Li, Y. J. Chabal, Mechanism of Preferential Adsorption of SO_2 into Two Microporous Paddle Wheel Frameworks $M(bdc)(ted)_{0.5}$. *Chem. Mater.* **2013**, *25*, 4653–4662.

[88] W. P. Mounfield, C. Han, S. H. Pang, U. Tumuluri, Y. Jiao, S. Bhattacharyya, M. R. Dutzer, S. Nair, Z. Wu, R. P. Lively, D. S. Sholl, K. S. Walton, Synergistic Effects of Water and SO_2 on Degradation of MIL-125 in the Presence of Acid Gases. *J. Phys. Chem. C* **2016**, *120*, 27230–27240.

[89] T. Grant Glover, G. W. Peterson, B. J. Schindler, D. Britt, O. Yaghi, MOF-74 Building Unit has a Direct Impact on Toxic Gas Adsorption. *Chem. Eng. Sci.* **2011**, *66*, 163–170.

[90] M. Savage, Y. Cheng, T. L. Easun, J. E. Eyley, S. P. Argent, M. R. Warren, W. Lewis, C. Murray, C. C. Tang, M. D. Frogley, G. Cinque, J. Sun, S. Rudić, R. T. Murden, M. J. Benham, A. N. Fitch, A. J. Blake, A. J. Ramirez-Cuesta, S. Yang, M. Schröder, Selective Adsorption of Sulfur Dioxide in a Robust Metal-Organic Framework Material. *Adv. Mater.* **2016**, *28*, 8705–8711.

[91] S. Yang, J. Sun, A. J. Ramirez-Cuesta, S. K. Callear, W. I. F. David, D. P. Anderson, R. Newby, A. J. Blake, J. E. Parker, C. C. Tang, M. Schröder, Selectivity and Direct Visualization of Carbon Dioxide and Sulfur Dioxide in a Decorated Porous Host. *Nat. Chem.* **2012**, *4*, 887-894.

[92] X. Han, H. G. W. Godfrey, L. Briggs, A. J. Davies, Y. Cheng, L. L. Daemen, A. M. Sheveleva, F. Tuna, E. J. L. McInnes, J. Sun, C. Drathen, M. W. George, A. J. Ramirez-Cuesta, K. M. Thomas, S. Yang, M. Schröder, Reversible Adsorption of Nitrogen Dioxide within a Robust Porous Metal-Organic Framework. *Nat. Mater.* **2018**, *17*, 691–696.

[93] I. Thomas-Hillman, L. A. Stevens, M. Lange, J. Möllmer, W. Lewis, C. Dodds, S. W. Kingman, A. Laybourn, Developing a Sustainable Route to Environmentally Relevant Metal–Organic Frameworks: Ultra-Rapid Synthesis of MFM-300(Al) using Microwave Heating. *Green Chem.* **2019**, *21*, 5039–5045.

[94] L. Li, I. da Silva, D. I. Kolokolov, X. Han, J. Li, G. Smith, Y. Cheng, L. L. Daemen, C. G. Morris, H. G. W. Godfrey, N. M. Jacques, X. Zhang. P. Manuel. M. D. Frogley. C. A. Murray. A. J. Ramirez-Cuesta, G. Cinque, C. C. Tang, A. G. Stepanov, S. Yang, M. Schröder, Post-Synthetic Modulation of the Charge Distribution in a Metal–Organic Framework for Optimal Binding of Carbon Dioxide and Sulfur Dioxide. *Chem. Sci.* **2019**, *10*, 1472–1482.

[95] J. Hungerford, S. Bhattacharyya, U. Tumuluri, S. Nair, Z. Wu, K. S. Walton, DMOF-1 as a Representative MOF for SO_2 Adsorption in Both Humid and Dry Conditions. *J. Phys. Chem. C* **2018**, *122*, 23493–23500.

[96] R. Domínguez-González, I. Rojas-León, E. Martínez-Ahumada, D. Martínez-Otero, H. A. Lara-García, J. Balmaseda-Era, I. A. Ibarra, E. G. Percástegui, V. Jancik, UNAM-1: A Robust Cu I and Cu II Containing 3D-hydrogen-Bonded Framework with Permanent Porosity and Reversible SO_2 Sorption. *J. Mater. Chem. A* **2019**, *7*, 26812–26817.

[97] M. R. Tchalala, P. M. Bhatt, K. N. Chappanda, S. R. Tavares, K. Adil, Y. Belmabkhout, A. Shkurenko, A. Cadiau, N. Heymans, G. Weireld, G. Maurin. K. N. Salama, M. Eddaoudi. Fluorinated MOF Platform for Selective Removal and Sensing of SO_2 from Flue Gas and Air. *Nat. Commun.* **2019**, *10*, 1328,1–10.

[98] Z. Chen, X. Wang, R. Cao, K. B. Idrees, X. Liu, M. C. Wasson, O. K. Farha, Water-Based Synthesis of a Stable Iron-Based Metal–Organic Framework for Capturing Toxic Gases. *ACS Mater. Lett.* **2020**, *2*, 1129–1134.

[99] Y. Zhang, P. Zhang, W. Yu, J. Zhang, J. Huang, J. Wang, M. Xu, Q. Deng, Z. Zeng, Deng, S. Highly Selective and Reversible Sulfur Dioxide Adsorption on a Microporous Metal-Organic Framework via Polar Sites. *ACS Appl. Mater. Interfaces* **2019**, *11*, 10680–10688.

[100] P. K. Thallapally, R. K. Motkuri, C. A. Fernandez, B. P. McGrail, G. S. Behrooz, Prussian Blue Analogues for CO_2 and SO_2 Capture and Separation Applications. *Inorg. Chem.* **2010**, *49*, 4909–4915.

[101] C. A. Fernandez, P. K. Thallapally, R. K. Motkuri, S. K. Nune, J. C. Sumrak, J. Tian, J. Liu, Gas-Induced Expansion and Contraction of a Fluorinated Metal−Organic Framework. *Cryst. Growth Des.* **2010**, *10*, 1037–1039.

3.3 Metal–Organic Frameworks with Potential Application for SO_2 Separation and Flue Gas Desulfurization

Philipp Brandt, Alexander Nuhnen, Marcus Lange, Jens Möllmer, Oliver Weingart, Christoph Janiak

ACS Appl. Mater. Interfaces, **2019**, *19*, 17350–17358.

DOI: 10.1021/acsami.9b00029, Referenz [154]

Industrielle Prozesse, wie die Verbrennung von fossilen Rohstoffen für die Energiegewinnung führen zu Emissionen von giftigem Schwefeldioxid, welche sowohl der Umwelt als auch dem Menschen schaden. Aus diesem Grund ist es von großem Interesse neue Materialien für die regenerative SO_2-Adsorption zu finden, die eine Alternative zur klassischen Rauchgasreinigung mit irreversiblen Absorptionsprozessen darstellen.

In dieser Arbeit wurden die drei literaturbekannten Metall-organischen Gerüstverbindungen MOF-177, NH_2-MIL-125 und MIL-160 in Bezug auf SO_2-Sorption untersucht. MOF-177 konnte dabei durch seine hohe Porosität Rekordaufnahmewerte für die SO_2-Sorption in MOFs erzielen, stellte sich jedoch in nachfolgenden Stabilitätstests als ungeeignet für eine reversible SO_2-Sorption heraus. Sowohl NH_2-MIL-125(Ti) als auch MIL-160 zeigten gute SO_2-Aufnahmewerte im Niederdruckbereich, was besonders wichtig ist, um kleinste Mengen SO_2 selektiv aus Rauchgasmischungen zu adsorbieren.

MIL-160 zeigte die vielversprechendsten Ergebnisse, welche sich in exzellenten IAST-Selektivitäten, insbesondere unter anwendungsorientierten Bedingungen (79-95 bei 80 °C und 1 bar), und einer hohen Stabilität nach trockener und feuchter SO_2-Exposition widerspiegeln. Eine Erklärung für die hohe Affinität von MIL-160 zu SO_2 konnte durch die Bestimmung der Energien der energetisch günstigsten Bindungsstellen (~40-60 kJ mol^{-1}) mittels Dichtefunktionaltheorie erfolgen und durch experimentelle Ergebnisse zur Bestimmung der Adsorptionswärme bei niedriger SO_2-Beladung (~42 kJ mol^{-1}) weiter gestützt werden.

Abschließend wurden Durchbruchsexperimente für MIL-160 mit typischen Rauchgasmischungen ($N_2/CO_2/SO_2$; v/v/v; 84,9; 15,0; 0,1) simuliert, welche nachfolgend durch dynamische Durchbruchsexperimente verifiziert und weiter verfeinert werden konnten. Die Ergebnisse dieser Untersuchungen zeigten eine herausragende Trennleistung von SO_2 gegenüber CO_2 und N_2 für MIL-160, was dieses poröse Material zu einem interessanten Kandidaten für die regenerative adsorptionsbasierte Rauchgasentschwefelung macht.

Die Beiträge in dieser Veröffentlichung wurden zu gleichwertigen Teilen von Herrn Dr. Alexander Nuhnen und Herrn Philipp Brandt erarbeitet.

Anteile an der Veröffentlichung:

- Idee in Zusammenarbeit mit Herrn Dr. Alexander Nuhnen.
- Konzept, experimentelle Arbeiten und Analytik mit Beteiligung von Herrn Alexander Nuhnen (bis auf unten gelistete Ausnahmen).
- Aufarbeitung der Ergebnisse, Verfassung des Manuskripts mit Ausnahme des theoretischen Teils (von Herrn Dr. Alexander Nuhnen und Herrn Dr. Oliver Weingart) und das Erstellen der Tabellen und Abbildungen mit der SO_2-Bindungsstellen (von Herrn Prof. Dr. Christoph Janiak). Korrektur durch Herrn Prof. Dr. Christoph Janiak.
- Theoretische Berechnungen und deren mathematische Auswertung von Herrn Dr. Alexander Nuhnen.
- Durchbruchsexperimente und deren Auswertung wurden von Herrn Dr. Marcus Lange und Herrn Dr. Jens Möllmer durchgeführt.
- Rechnungen zu Dichtefunktionaltheorie wurden von Herrn Dr. Oliver Weingart durchgeführt.

ACS APPLIED MATERIALS & INTERFACES

Research Article

Cite This: ACS Appl. Mater. Interfaces 2019, 11, 17350−17358

www.acsami.org

Metal−Organic Frameworks with Potential Application for SO_2 Separation and Flue Gas Desulfurization

Philipp Brandt,[†,‡] Alexander Nuhnen,[†,‡] Marcus Lange,[∥] Jens Möllmer,[∥] Oliver Weingart,[§] and Christoph Janiak*[,†,⊥]

[†]Institut für Anorganische Chemie und Strukturchemie and [§]Institut für Theoretische Chemie und Computerchemie, Heinrich-Heine-Universität Düsseldorf, Universitätsstraße 1, Düsseldorf 40225, Germany

[∥]Institut für Nichtklassische Chemie, Permoserstraße 15, Leipzig 04318, Germany

[⊥]Hoffmann Institute of Advanced Materials, Shenzhen Polytechnic, 7098 Liuxian Blvd., Nanshan District, Shenzhen 518055, China

Supporting Information

ABSTRACT: Sulfur dioxide (SO_2) is an acidic and toxic gas and its emission from utilizing energy from fossil fuels or in industrial processes harms human health and environment. Therefore, it is of great interest to find new materials for SO_2 sorption to improve classic flue gas desulfurization. In this work, we present SO_2 sorption studies for the three different metal−organic frameworks MOF-177, NH_2-MIL-125(Ti), and MIL-160. MOF-177 revealed a new record high SO_2 uptake (25.7 mmol·g^{-1} at 293 K and 1 bar). Both NH_2-MIL-125(Ti) and MIL-160 show particular high SO_2 uptakes at low pressures (p < 0.01 bar) and thus are interesting candidates for the removal of remaining SO_2 traces below 500 ppm from flue gas mixtures. The aluminum furandicarboxylate MOF MIL-160 is the most promising material, especially under application-orientated conditions, and features excellent ideal adsorbed solution theory selectivities (124−128 at 293 K, 1 bar; 79−95 at 353 K, 1 bar) and breakthrough performance with high onset time, combined with high stability under both humid and dry SO_2 exposure. The outstanding sorption capability of MIL-160 could be explained by DFT simulation calculations and matching heat of adsorption for the binding sites $O_{furan}\cdots S_{SO2}$ and $OH_{Al\text{-}chain}\cdots O_{SO2}$ (both ∼40 kJ·mol^{-1}) and $O_{furan/carboxylate}\cdots S_{SO2}$ (∼55−60 kJ·mol^{-1}).

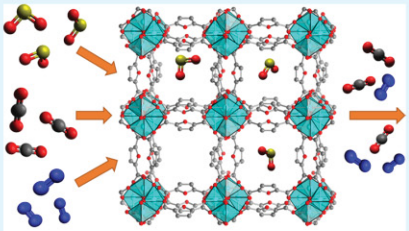

KEYWORDS: *metal−organic framework, sulfur dioxide sorption, gas selectivity, breakthrough, DFT simulation, flue gas desulfurization*

INTRODUCTION

Constant economic growth leads to ever increasing energy consumption and thus to new environmental burdens and hazards for human health.[1] Hence, the development of new methods to capture air pollutants such as CO_2, NO_x, and SO_2 is an important scientific challenge.[2] The majority of anthropogenic SO_2 emission emerges from combustion of coal and heavy oil or is caused by industrial processes.[3,4] The SO_2 content in flue gases is already relatively low, with around 500−3000 ppm, and large parts of it (85−95%) can be scrubbed with classic flue gas desulfurization, using limestone as an absorbent.[5,6] However, this still leaves up to 150−450 ppm of SO_2, which are emitted to the atmosphere, contributing largely to 80 Mt of worldwide anthropogenic SO_2 emissions from energy-related sources in 2015.[3] There are substantial reasons to envision the target of a complete removal of SO_2 from flue gas. On the one hand, SO_2 emissions damage the environment, with effects such as acid rain, and lead to pulmonary diseases and premature deaths of humans caused by declining air quality.[7−9] On the other hand, it is important to note that even traces of SO_2 can significantly reduce other flue gas purification processes by inactivating sorbents for CO_2 removal or catalysts for selective reduction of NO_x.[10−12] This is why the stepwise purification of flue gases, starting with selective and quantitative removal of SO_2, would be highly desirable.[13] Porous materials with high uptake capacity, selectivity, and stability for SO_2 are therefore of major interest to decrease the global emission of anthropogenic pollutants. Metal−organic frameworks (MOFs) are a promising material class to fulfill these specific requirements.[14−17] These organic−inorganic hybrid compounds show remarkable sorption capability including selective capture of a series of toxic and polluting gases.[18−22] However, in comparison to other adsorptives such as N_2, H_2, CO_2, or CH_4, in the past, there are only a few experimental studies dealing with SO_2 adsorption in MOFs.[13,20,23−29] Currently, the research of SO_2 sorption in MOFs is receiving increasing interest for SO_2−CO_2 separation applications.[30−34]

In this study, we examine the three MOFs: MOF-177, NH_2-MIL-125(Ti), and MIL-160 (see Scheme 1 and Section 1 of the Supporting Information for their short structure descrip-

Received: January 8, 2019
Accepted: April 19, 2019
Published: April 19, 2019

Scheme 1. Linker and Metal Ion in MOF-177, NH_2-MIL-125(Ti), and MIL-160

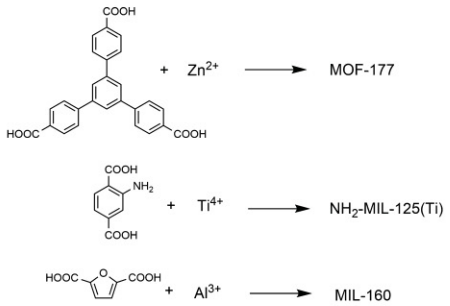

tion).[35−38] Our investigations include single gas sorption, heat of adsorption, IAST selectivity, DFT-calculated binding sites, breakthrough experiments and simulations, and stability tests under dry and humid SO_2 exposure conditions. The selected materials feature a wide range of different properties (BET surface area, total pore volume, pore window size, functionality, etc.).

For the ultrahigh surface framework MOF-177, an unusual SO_2 isotherm shape and incredible high SO_2 uptakes of ∼38 mmol·g^{-1} were theoretically predicted.[15]

Schröder et al. previously examined gas-binding interactions of amine-functionalized materials with the hydroxy-functionalized MFM-300. Here, the amine-functionalized materials showed increased heats of adsorption in comparison to the hydroxy-functionalized MFM-300 aluminum framework.[25]

MIL-160 and NH_2-MIL-125(Ti) had been examined thoroughly for their water sorption properties and showed remarkably high H_2O vapor uptake at low partial pressures and high water stability.[17,36,37] We assume that these H_2O sorption properties should be relevant for the SO_2 sorption properties because SO_2 sequestration applications take place under humid conditions. Therefore, water stability is highly important for any MOF, which is studied for SO_2 adsorption. Further, Walton et al. already performed comprehensive stability tests for MIL-125(Ti) and NH_2-MIL-125(Ti) under aqueous, humid, and dry SO_2 exposure in which the amino-functionalized MOF showed sufficient robustness.[17] An additional aspect, which led to the choice of MIL-160 over other MOFs, is that it can be synthesized in large quantities under green (aqueous) and mild conditions in a single step from readily commercially available compounds.[36] These are especially important factors regarding a possibly larger-scale industrial MOF usage in the future.

■ RESULTS AND DISCUSSION

Detailed information and description about the examined structures and their characterization (BET and PXRD) can be found in the Supporting Information.

SO_2 Sorption. MOF-177 showed by far the highest SO_2 capacity with a maximum uptake of 25.7 mmol·g^{-1} at 0.97 bar and 293 K (20 °C) (Figure 1). To the best of our knowledge, this is the highest reported value, measured from experimental SO_2 isotherms, in the literature so far.[20,27,30] A comparison with SO_2 capturing MOFs from the literature can be found in Table S5 of the Supporting Information. The SO_2 adsorption isotherm of MOF-177 at 293 K shows an "S"-shape or type V isotherm, which can be attributed to relatively weak adsorbent−adsorbate interactions. For such adsorbent−adsorbate pairs, molecular

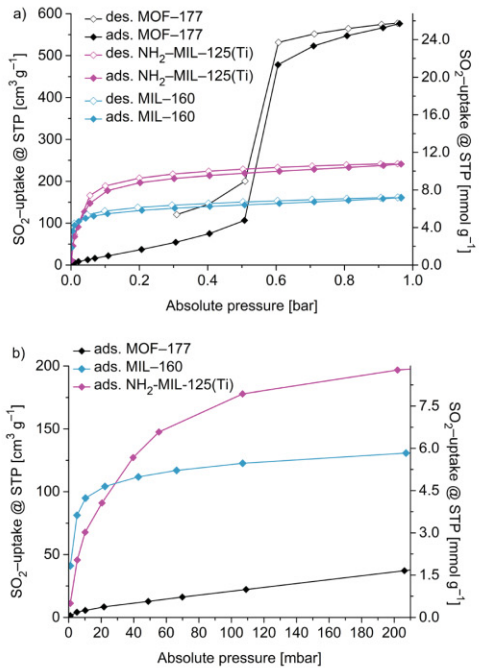

Figure 1. (a) Experimental SO_2 isotherms (0−1 bar) at 293 K; (b) low pressure area (up to 210 mbar) of experimental SO_2 isotherms at 293 K. For the nonclosure of the desorption isotherm for MOF-177 in (a), see the section on SO_2 adsorption in the Supporting Information.

adsorbate clustering only occurs at higher p/p_0, followed by pore filling.[39] Such type V isotherms are typical for water adsorption on hydrophobic microporous and mesoporous (MOF) adsorbents. A similar "S"-shape or type V isotherm behavior for SO_2 sorption has been predicted for a few other materials with non-functionalized linkers, large pore sizes, and high total pore volume (IRMOF-1, IRMOF-8, and IRMOF-15).[15,16] The SO_2 gas uptake in MOF-177 starts slow, with an uptake of 4.8 mmol·g^{-1} at 0.5 bar, rises sharply to 21.3 mmol·g^{-1} at 0.6 bar and reaches a maximum of 25.7 mmol·g^{-1} at 0.97 bar. The desorption isotherm shows a significant hysteresis below 0.5 bar. The SO_2 desorption of MOF-177 had to be aborted at 0.3 bar due to the comparatively slower adsorption and desorption kinetics leading to a long measurement time for this high capacity MOF (see explanation on maximum SO_2 measuring time in Section 2 in the Supporting Information). This sorption performance together with changes in the crystallinity (Figure S22, Supporting Information) and significant decrease of BET surface area (Figure S18, Table S4, Supporting Information) suggests at least partially chemisorption, that is, strong interaction of SO_2 and the MOF-177 framework. The gas uptake at high partial pressures is attributed to the relatively large pore diameter (10.6−11.8 Å).[40] Combined with a high Brunauer−Emmett−Teller (BET) surface area of 4100 m^2·g^{-1} and a total pore volume of 1.51 cm^3·g^{-1}, this leads to the exceptional high maximum uptake. The insignificant adsorption at low partial pressures also suggests that MOF-177 is no effective adsorbent for selective SO_2 capture because in potential applications, adsorbents have to deal with low SO_2 concentrations of 500 ppm and less. These results are in accordance

DOI: 10.1021/acsami.9b00029
ACS Appl. Mater. Interfaces 2019, 11, 17350−17358

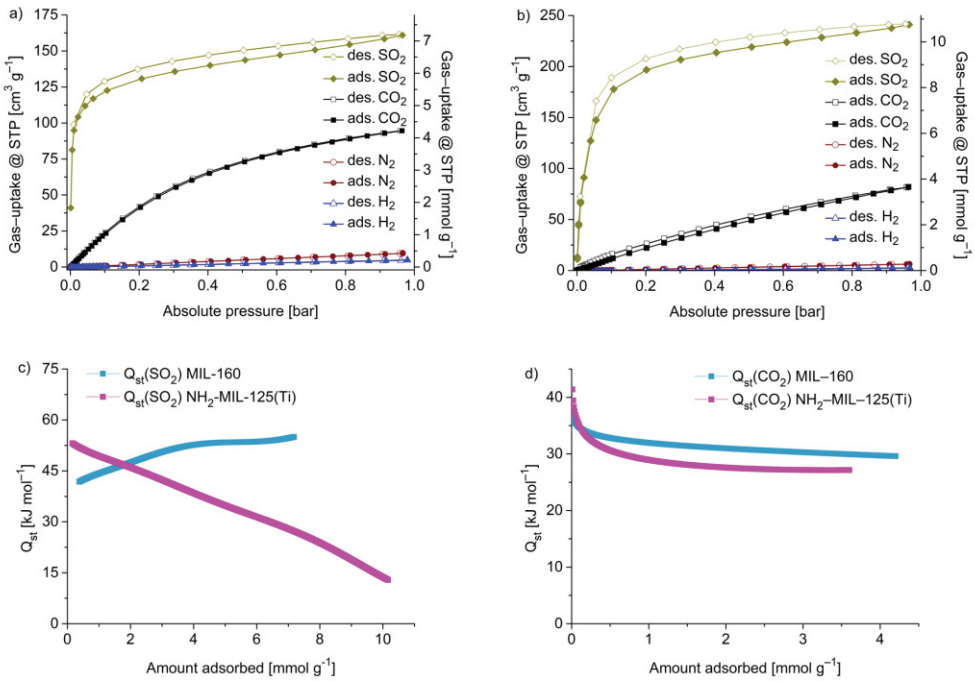

Figure 2. (a) Comparison of single gas sorption isotherms (SO_2, CO_2, N_2, and H_2) for MIL-160 at 293 K. (b) Comparison of single gas sorption isotherms (SO_2, CO_2, N_2, and H_2) for NH_2-MIL-125(Ti) at 293 K. (c) Isosteric heat of adsorption of SO_2 for MIL-160 and NH_2-MIL-125(Ti). (d) Isosteric heat of adsorption of CO_2 for MIL-160 and NH_2-MIL-125(Ti).

with breakthrough experiments performed previously by Yaghi and Brit in which MOF-177 showed no significant retention of 1.0% SO_2 in N_2.[18] Therefore, and also because of the low stability of MOF-177 (see below), no further SO_2 sorption investigations for MOF-177 were considered. In comparison to the simulated SO_2 adsorption isotherms of MOF-177, published by Song et al.[15] and Sun et al.[16] at 298 K and 313 K, respectively, it has to be noted that the high maximum SO_2 uptake of MOF-177 from experimental measurements of 25.7 mmol g^{-1} at 0.97 bar stays below the predictions of ~34 mmol·g^{-1} (298 K) or of ~28 mmol·g^{-1} (313 K) from the simulated isotherms. The adsorption isotherm with "S" or type V shape of MOF-177 at 293 K is in good agreement with the simulations done by Song et al. at 298 K, where a steep SO_2 uptake is predicted at around 0.5 bar,[15] whereas in the simulation of Sun et al. (at 313 K), the steep SO_2 uptake is shifted to higher pressures starting at 0.9 bar.[16]

NH_2-MIL-125(Ti) exhibits a compromising performance in both reasonable SO_2 capacity and good SO_2 uptake at low pressures. The SO_2 adsorption of NH_2-MIL-125(Ti) at 293 K showed a steep rise up to 0.1 bar (7.9 mmol·g^{-1}) while the further uptake proceeds with a lower rise up to the end of the adsorption at 0.95 bar (10.8 mmol·g^{-1}). The uptake agrees with the one reported by Walton et al. at 298 K.[17] The isotherm can be assigned as type Ib.

MIL-160 showed specific high SO_2 uptake at low pressures. The SO_2 adsorption isotherm at 293 K is of type I, shows a steep rise up to 0.01 bar (4.2 mmol·g^{-1}), and quickly approaches the limiting value. Already at 0.1 bar (5.5 mmol·g^{-1}), 76% of the maximum measured uptake at 0.97 bar (7.2 mmol·g^{-1}) is reached. For microporous MIL-160 and NH_2-MIL-125(Ti) with the functionalized and more hydrophilic furan and amino benzene moiety, respectively, in the linker, the interaction with polar adsorbents is increased, and physisorption and micropore filling occurs at lower pressures.[39]

Selectivity of MIL-160 and NH_2-MIL-125(Ti). To further compare the selective sorption capabilities of MIL-160 and NH_2-MIL-125(Ti), we performed sorption experiments, with SO_2, CO_2, N_2, and H_2 as adsorptives at 293 K in a pressure range of 1×10^{-3}–1 bar (Figure 2a,b). Both MOFs have similar adsorption properties, with insignificant adsorption of N_2 and H_2 and a slow rise of CO_2 adsorption across the entire pressure range (1×10^{-3}–1 bar), whereas the majority of the SO_2 adsorption occurs at low pressures of ≤0.1 bar. This encourages that MIL-160 and NH_2-MIL-125(Ti) should be able to separate SO_2 selectively from CO_2, N_2, and H_2 at low partial pressures.

We measured adsorption isotherms at two additional temperatures (313 and 373 K for SO_2 and 273 and 373 K for CO_2) for MIL-160 and NH_2-MIL-125(Ti) and applied several commonly used models on our isotherm data. The best fits for our isotherms were given for the Sips and DSLAI fitting models, which we compare in Figures S4–S7 in the Supporting Information. This enabled us to simulate adsorption isotherms for any given temperature within the interval of the measurement temperatures for this specific gas (Figures S4–S7, Supporting Information). For all fitting and simulation calculations, the "3P sim" software was used.[41] Detailed sets of fitting parameters for Sips and DSLAI models are given in Tables S1 and S2 of the Supporting Information.

Adsorption isotherms measured at 273 and 293 K were used to calculate isosteric heats of adsorption (Q_{st}) of SO_2 and CO_2 for MIL-160 and NH_2-MIL-125(Ti), respectively (Figure 2c,d).

DOI: 10.1021/acsami.9b00029
ACS Appl. Mater. Interfaces 2019, 11, 17350−17358

In case of SO_2, we used virial analysis, whereas for CO_2, the Sips analysis combined with Clausius–Clapeyron calculations (Figures S8–S11, Supporting Information) was applied on isotherm data. For a detailed explanation including equations, fits, and parameters, see the Heat of Adsorption section of the Supporting Information.

The heat of adsorption for SO_2 near zero coverage (Q_{st}^0) in MIL-160 is ~42 kJ·mol^{-1}, whereas the amino-functionalized MOF NH_2-MIL-125(Ti) exhibits Q_{st}^0 values of ~53 kJ·mol^{-1}. For CO_2, both MIL-160 and NH_2-MIL-125(Ti) show similar Q_{st}^0 values with ~37 kJ·mol^{-1} and ~41 kJ·mol^{-1}, respectively. The higher heat of adsorption for the amine-functionalized MOF is in agreement with previous work by Schröder et al.[25]

Normally, a decrease in the heat of adsorption is observed with increased loading as the higher energy binding sites are occupied first. For MIL-160, we see here an unexpected increase in Q_{st} with SO_2 loading. At the same time, we note an agreement in the measured Q_{st} value near a zero loading of ~42 kJ·mol^{-1} with the calculated binding energies for the $O_{furan}\cdots S_{SO2}$ and $OH_{Al\text{-}chain}\cdots O_{SO2}$ sites (~40 kJ·mol^{-1}) and in the measured Q_{st} values for the maximum loading (~55 kJ·mol^{-1}) with the calculated energy for the $O_{furan/carboxylate}\cdots S_{SO2}$ site (60 kJ·mol^{-1}) (see below). Although the close match of experimental and calculated values may be somewhat coincidental, we would rationalize the trend by a phase transition in MIL-160 from an activated empty phase I, where the $O_{furan/carboxylate}\cdots S_{SO2}$ site is not accessible, to a guest-loaded phase II with the accessible $O_{furan/carboxylate}\cdots S_{SO2}$ site. Thus, in the initial phase I, only the lower energy binding sites can be occupied. In this aspect, we point to studies on the water sorption in MIL-160 where a phase transition upon water loading was concluded.[42]

Next, we applied ideal adsorbed solution theory (IAST) calculations on dual-site Langmuir (DSLAI)-fitted isotherms to determine selectivities for mixed gas adsorption in binary SO_2/CO_2 mixtures (10:90–50:50 v/v) (Figure 2c). Note that for meaningful IAST calculations, adsorption capacities of the adsorbates should not differ substantially.[43] Here, we applied IAST calculations on the mixed gas adsorption process of SO_2 versus CO_2, two polar molecules, up to only 1 bar pressure. Known limitations for IAST simulations, that is, high pressure and different polarity, are not present in our case. Therefore, we expect IAST calculations to give a first and sufficiently reliable estimation of the selectivity, and indeed, IAST calculations, albeit with different concentrations, are in good agreement to the experimental breakthrough experiments (see below).

The results from the IAST calculations show that MIL-160, compared to NH_2-MIL-125(Ti), has increased selectivity toward SO_2. The SO_2/CO_2 IAST selectivities at 293 K and 1 bar are between 124–128 and 42–55 for MIL-160 and NH_2-MIL-125(Ti), respectively (Figure 3a). In comparison to the leading MOF materials with regard to SO_2/CO_2 separation, IAST selectivities between 32 and 100 at ambient temperatures are reported.[13,26,27,33] MIL-160 surpasses these values. Using the same method on SO_2/N_2 gas mixtures leads to no quantifiable values because of low N_2 affinities for both frameworks.

As most of the potential SO_2 adsorption applications (e.g., flue gas desulfurization) take place at elevated temperatures, it is important to characterize material properties at these temperatures. A common temperature for flue gas desulfurization is at around 353 K (80 °C) to condense the water vapor before the desulfurization.[44,45] For both MIL-160 and NH_2-MIL-125(Ti), the gas uptake for SO_2 and CO_2 decreases with increasing temperatures. Note that for MIL-160, the SO_2 adsorption curve

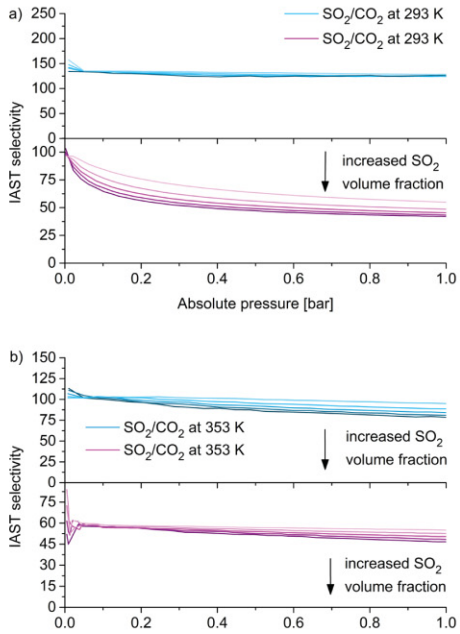

Figure 3. (a) IAST selectivities of MIL-160 (top) and NH_2-MIL-125(Ti) (bottom) with SO_2/CO_2, 10:90 (light)–50:50 (dark) (v/v) at 293 K. (b) IAST selectivities of MIL-160 (top) and NH_2-MIL-125(Ti) (bottom) with SO_2/CO_2, 10:90 (light)–50:50 (dark) (v/v) at 353 K.

in the simulation (353 K) and measurement (373 K) remains type Ib (Figure S4, Supporting Information). At the same time, the CO_2 adsorption isotherm for both materials converts to an almost linear uptake curve with low gas uptakes at these elevated temperatures (Figures S5 and S7, Supporting Information). Even though the SO_2/CO_2 IAST selectivities at 353 K and 1 bar, in comparison to 293 K, are decreasing for MIL-160 and NH_2-MIL-125(Ti) to values between 79–95 and 47–55, respectively, for both materials, a significant selectivity remains (Figure 3b).

Breakthrough Performance for Potential FGD Application. For the most promising material MIL-160, experimental breakthrough experiments were performed to ensure its separation capability not only under equilibrated but also under dynamic conditions. For MOF-177, previous breakthrough experiments with 1.0% SO_2 in N_2 showed no significant retention of SO_2 vapor.[18]

For MIL-160, we measured breakthrough curves of the ternary gas mixture $N_2/CO_2/SO_2$ (84.9:15.0:0.1 v/v/v) at 293 and 353 K and a ternary gas mixture with increased SO_2 concentration with $N_2/CO_2/SO_2$ (84.0:15.0;1.0 v/v/v) at 293 K (Figure 4a,b and Figure S13, Supporting Information). The 0.1% SO_2 ternary gas mixture was also employed in the simulations. The sample was pretreated at 373 K under continuous nitrogen flow (16.6 mL·min^{-1}) until no other gas than nitrogen was detected. The composition of the ternary gas mixture was chosen according to the typical flue gas composition from the air-fired coal combustion.[46] The breakthrough plot in Figure 4a shows an immediate rise of the N_2 and CO_2 concentrations in the outlet. Under the chosen experimental conditions, this immediate rise indicates almost no N_2 adsorption and a rapid saturation for CO_2 inside the MOF, which can be assigned to a spontaneous breakthrough for CO_2.

DOI: 10.1021/acsami.9b00029
ACS Appl. Mater. Interfaces 2019, 11, 17350–17358

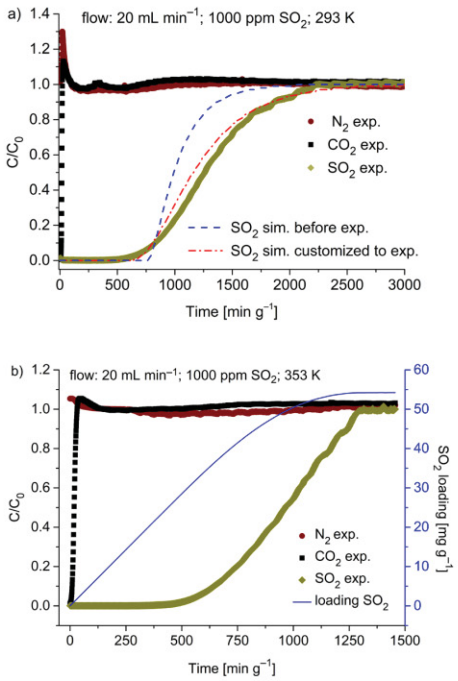

Figure 4. (a) Experimental and simulated breakthrough curves for MIL-160 at 293 K. (b) Experimental breakthrough curve for MIL-160 at 353 K.

In contrast, SO_2 could be retained for about ~600 min·g^{-1} and shows no significant loss in retention time in the second run after identical activation of the MIL-160 material (Figure S12, Supporting Information). Subsequently, to the second run, we investigated regenerability of MIL-160 in purging the column under N_2 flow (16.6 mL·min^{-1}) at 293 K for 12 h. This experiment shows that the MIL-160 material is a fully reversible SO_2 adsorber, which recovers easily at low temperatures and without the need of vacuum (Figure S14, Supporting Information).

At an elevated temperature of 353 K (Figure 4b) or with a 10-fold higher SO_2 concentration of 10,000 ppm SO_2 (Figure S13, Supporting Information), MIL-160 still shows remarkable capability to retain SO_2, with retention times of ~350 and ~500 min·g^{-1}. As expected, the total SO_2 loadings at dynamic conditions (breakthrough experiment, 293 K, 0.1% SO_2, 1.17 mmol·g^{-1}) are lower than SO_2 loadings under equilibrium conditions (sorption isotherm, 293 K, 0.001 bar, 1.8 mmol·g^{-1}). However, the maximal loading of SO_2 increases with rising SO_2 concentration in our breakthrough experiment (293 K, 1% SO_2, 3.65 mmol·g^{-1}).

Note that at 353 K, the dynamic loading of SO_2 for MIL-160 is still 0.85 mmol·g^{-1}. This comparatively high SO_2 loading can be explained by the SO_2 adsorption isotherm at 373 K (Figure S4, Supporting Information), which shifts from type Ia (293 K) to type Ib (373 K), and does not flatten completely, compared to the CO_2 adsorption under the same conditions. For a comparison of maximum loadings under equilibrium or dynamic conditions at selected partial pressures, see Table S3 of the Supporting Information.

Breakthrough Simulations. In addition, we simulated breakthrough curves with an identical gas mixture to our breakthrough experiments with a gas mixture of $N_2/CO_2/SO_2$ (84.9:15.0:0.1 v/v/v) at 293 K (Figure 4a) and further simulated CO_2/carrier gas/SO_2 (90/9.75/0.25) gas mixtures in a style of oxyfuel combustion[46] at 293 and 353 K for MIL-160 and NH_2-MIL-125(Ti), respectively (Figures S15–S17, Supporting Information). The simulated breakthrough curves were calculated from Sips-fitted isotherm data of MIL-160 and NH_2-MIL-125(Ti) (Figures S4–S7 and Tables S4 and S5, Supporting Information).

We would like to point out that breakthrough simulations (Figure 4a, blue dashed line), which were performed ahead of breakthrough experiments, gave already a good estimate for the breakthrough onset time of SO_2 in MIL-160 under identical conditions. These simulations could be further refined by taking into account experimental breakthrough data and slight deviations in the experiment from which we obtained optimized parameters for the mass transfer coefficient and axial flow (Figure 4a, red dashed line). Slight deviations in the experimental and simulated curvature slope are caused by the small particle size of MIL-160 combined with a marginal pressure drop (inlet to outlet) and the low flow rate for the gas mixture.

The simulations based on oxyfuel combustion with strongly increased CO_2 concentration as well show solid separation capability of SO_2 versus CO_2 at 293 K for MIL-160 and NH_2-MIL-125(Ti) with retention times of about 200 min·g^{-1} (Figures S15 and S16, Supporting Information). Even though the retention times are decreased at higher temperatures (353 K) for both materials, it is still worth mentioning that a separation of CO_2 and SO_2 is predicted for both materials (Figures S15 and S16, Supporting Information).

DFT Calculations. To better understand the exceptional good adsorption performance of MIL-160, we used DFT simulation calculations to investigate the possible binding sites for SO_2 in the framework. Geometry optimization of SO_2 within MIL-160 yielded at least three different possibilities for SO_2 binding: First, in one structure (Figure 5a), SO_2 is oriented with sulfur toward the ether oxygen of a furan linker ($O_{furan}\cdots S_{SO2}$ distance 3.27 Å, distances to other nearby oxygens from 3.91 to 4.48 Å). A second binding site is provided by the O–H bridge, where SO_2 associates with one oxygen toward hydrogen (Figure 5b, $OH_{Al\text{-}chain}\cdots O_{SO2}$ distance 2.10 Å). These two binding sites, $O_{furan}\cdots S_{SO2}$ and $OH_{Al\text{-}chain}\cdots O_{SO2}$, exhibit similar binding energies of 39.3 and 40.6 kJ·mol^{-1}, respectively. In a third configuration, SO_2 sits above the plane spanned by two furan units (Figure 5c), with $O_{furan/carboxylate}\cdots S_{SO2}$ distances of 3.15 and 3.36 Å toward the ether oxygens and between 3.22 and 3.68 Å to the carboxylate oxygens. This latter configuration has the largest binding energy of 60.4 kJ·mol^{-1} and may provide a model for low-concentration SO_2 binding. In this geometry, however, SO_2 has much closer proximity to ether and carboxylate oxygens as in the structure Figure 5a, suggesting that at higher loadings, the binding site in Figure 5a is displaced to the binding site in Figure 5c when more SO_2 molecules enter the channel to occupy binding sites. For MFM-300, Schröder et al. located preferred binding sites of SO_2 at the Al–OH groups from the $AlO_4(OH)_2$ chain by in situ inelastic neutron scattering (INS) and DFT calculations.[25]

MIL-160 was also studied profoundly by Maurin et al.,[47] where the preferred binding sites for various guest molecules (H_2O, CO_2, CH_4, CO, N_2, and H_2) to the MIL-160 framework

DOI: 10.1021/acsami.9b00029
ACS Appl. Mater. Interfaces 2019, 11, 17350−17358

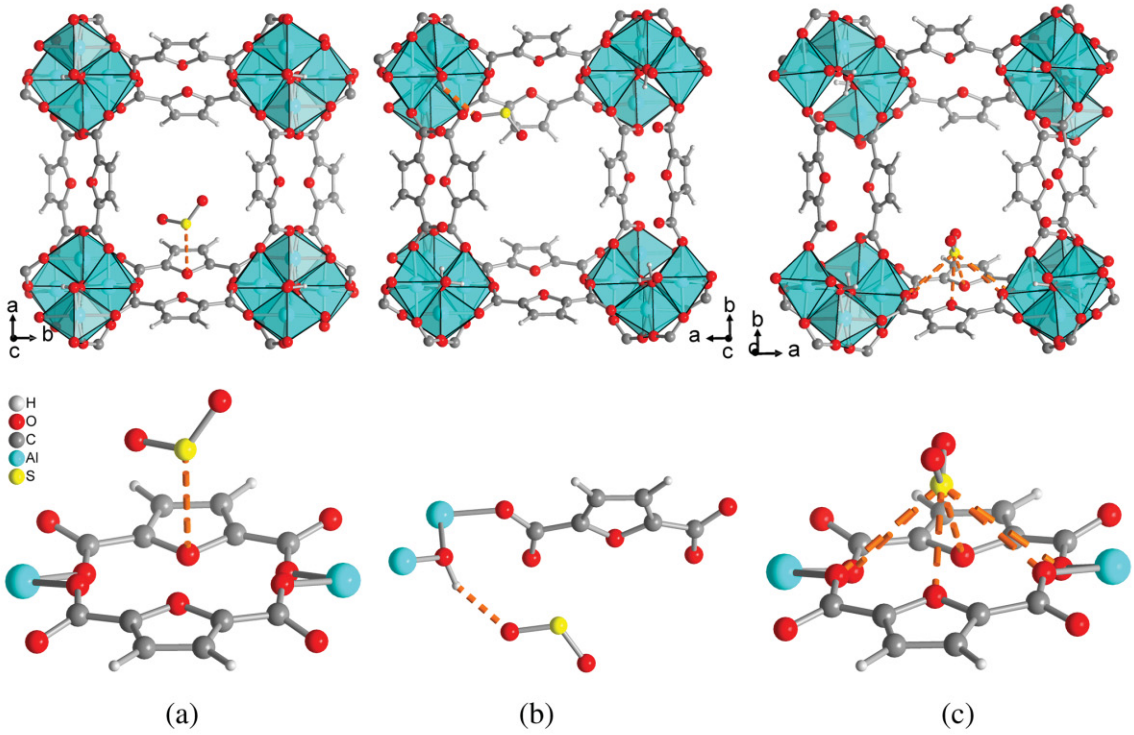

Figure 5. DFT-simulated binding sites of SO_2 in MIL-160. (a) $O_{furan}\cdots S_{SO2}$ interaction, (b) $OH_{Al\text{-}chain}\cdots O_{SO2}$ interaction, and (c) $O_{furan/carboxylate}\cdots S_{SO2}$ interaction. The closest contacts (as given in the text) from the SO_2 molecule to nearby framework atoms are depicted by orange dashed lines. The upper row shows the full channel cross section; the lower row gives an enlarged view of the SO_2 binding site.

were predicted by applying density functional theory (DFT), force field-based grand canonical Monte Carlo (GCMC) simulations, and radial distribution function (RDF). In these studies, CO_2 showed preferred binding to the heteroatom of the furan ligand with a distance of 3.1 Å and a binding energy of 32.5 $kJ\cdot mol^{-1}$ for the $O_{furan}\cdots O_{CO2}$ interaction. Thus, we rationalize the selectivity toward SO_2 by its higher binding energies. We also note that the exceptional selectivity and breakthrough performance of MIL-160 correlate with its small pore size of 5 Å diameter,[36] which is close to the kinetic diameter of SO_2 (4.11 Å)[48] and thus suitable for a selective adsorption of SO_2 under kinetic control.

Stability under Dry and Humid SO_2 Exposure. The stability of MOF materials was tested by SO_2 exposure experiments under dry (SO_2 sorption measurement) and humid conditions (SO_2 humidity chamber). For the experiment under humid conditions, we used a similar setup to Walton et al. (see the Supporting Information for details).[17] To assess the (in)stability, BET surface area and PXRD before and after exposure were measured to see whether porosity and crystallinity were preserved (Figures S18−S20 and S22−S24 and Table S4, Supporting Information).

For MOF-177, the BET surface significantly decreased from 4100 to 2270 $m^2\cdot g^{-1}$ (55%) under dry SO_2 conditions. Changes in the powder diffractogram (Figure S22, Supporting Information) also support the conclusion that MOF-177 undergoes a partial destruction under SO_2 exposure. Regardless of the low stability of MOF-177, we note again that this MOF is not practical for SO_2 adsorption applications at low concentrations where MOF-177 exhibits no uptake due to its "S"-shaped isotherm.

For NH_2-MIL-125(Ti), the BET surface decreased from 1560 to 1270 $m^2\cdot g^{-1}$ (81%) and 1250 $m^2\cdot g^{-1}$ (80%) under dry and humid conditions. Contrarily, MIL-160 showed no significant degradation in the BET surface under the same conditions (1170 $m^2\cdot g^{-1}$ a.s., 1120 $m^2\cdot g^{-1}$ after dry SO_2 exposure, 1130 $m^2\cdot g^{-1}$ after 175 ppm·h SO_2, and 75% relative humidity). PXRD patterns for NH_2-MIL-125(Ti) and MIL-160 remained unchanged.

Both MIL-160 and NH_2-MIL-125(Ti) were further investigated by measuring multiple individual SO_2 sorption runs of the same sample to evaluate SO_2 stabilities (Figure S21, Supporting Information). MIL-160 showed excellent stability with insignificant reduction of the gas uptake over five runs. In contrast, NH_2-MIL-125(Ti) displayed a reduced SO_2 uptake in the second run and then stabilized its adsorption capacity at the third run. This supports the assumption of a partial irreversible adsorption of SO_2 in the pores of NH_2-MIL-125(Ti).

The dry and humid stability tests show MOF-177 is unsuitable, and NH_2-MIL-125(Ti) is only of limited suitability for applications in flue gas desulfurization, where only a highly humid SO_2 stable adsorbent will be feasible. In contrast, MIL-160 showed remarkable stability under both dry and humid SO_2 conditions. These results expand previous studies in which Al-MOFs have shown extraordinary hydrothermal stability[49−51] and thus indicate that Al-MOFs (e.g., MIL-160 and MFM-300[24]) can be considered among the most promising MOF

DOI: 10.1021/acsami.9b00029
ACS Appl. Mater. Interfaces 2019, 11, 17350−17358

materials with regard to application under chemical aggressive conditions.

CONCLUSIONS

MOF-177 showed a record maximum SO_2 uptake of 25.7 mmol·g^{-1} at 293 K and 1 bar but turned out to be unsuitable for flue gas desulfurization (FGD) applications due to its chemical instability and low adsorption at low partial pressures of SO_2. NH_2-MIL-125(Ti) showed promising properties in IAST selectivity and breakthrough simulations for SO_2 but not as good as MIL-160, which exhibited outstanding performances in terms of SO_2/CO_2 selectivity, onset breakthrough time, and stability toward SO_2 under dry and humid conditions. In breakthrough experiments, MIL-160 could retain SO_2 for at least 500 min·g^{-1} from a typical flue gas composition of air-fired coal combustion, even at elevated temperatures. Further, MIL-160 could be easily regenerated at low temperatures (293 K) after breakthrough experiments. We would like to emphasize that for practical separation applications, it is essential for the material to feature an early gas uptake at very low partial pressure rather than a high total uptake at higher pressures. Especially so, if the gas, which ought to be separated, is present in a low volume fraction, such as SO_2 with less than 500 ppm remaining after limestone scrubbing in flue gas. The IAST-based SO_2 selectivity of MIL-160 over other gases (CO_2 and N_2) is on the level of leading benchmark MOFs. Further, MIL-160 features extraordinary stability under both dry and humid SO_2 exposure conditions, which together with the established low cost, green, and easily up scalable synthesis routes make MIL-160 a promising material for FGD applications.

EXPERIMENTAL SECTION

Materials. All reagents were commercially purchased and used without any further purification.

MOF-177. MOF-177 was synthesized by a solvothermal reaction according to the literature.[35] $Zn(NO_3)_2{\cdot}6H_2O$ (0.124 g, 0.41 mmol) and H_3BTB (0.031 g, 0.07 mmol) were dissolved in DEF (3 mL) and transferred into a glass vial. The mixture was then heated to 90 °C, kept at 90 °C for 24 h, and cooled down to 30 °C in 10 h. The resulting crystals were washed with DEF (three times, 3 mL each) and CH_2Cl_2 (three times, 3 mL each). Afterward, the sample was dried under vacuum (1×10^{-3} mbar) for 24 h at room temperature.

MIL-160. The synthesis of MIL-160 was performed according to the literature.[36] $Al(OH)(CH_3COO)_2$ (1.037 g, 6.40 mmol) and 2,5-furandicarbocylic acid (0.999 g, 6.40 mmol) were added to a round-bottom flask (100 mL) and dispersed in ultrapure water (40 mL). The mixture was then stirred and refluxed for 24 h, giving a white precipitate. The solid was washed with water (three times, 50 mL each) and then dried under vacuum at 60 °C for 24 h.

NH_2-MIL-125(Ti). The synthesis of NH_2-MIL-125(Ti) was performed according to the literature.[37] NH_2-benzenedicarboxylic acid (1.086 g, 6.00 mmol) was dissolved in a 50:50 v/v mixture of DMF (3.5 mL) and MeOH (3.5 mL) under sonication. $Ti(iPrO)_4$ (0.44 mL, 1.5 mmol) was added to the solution, which was then transferred in a stainless steel autoclave with a Teflon inlay and was heated in an oven at 150 °C for 16 h. After cooling down to room temperature, the yellow precipitate was at first washed with DMF (7 mL) and secondly washed two times with MeOH (7 mL). The solid was dried under vacuum at 60 °C for 24 h.

Material Characterization. BET and PXRD characterizations were performed on a Quantachrome Autosorb 6 and a Bruker D2 phaser, respectively. SO_2 isotherms were measured with a Quantachrome Autosorb iQ MP (for detailed description see the Supporting Information). Breakthrough curves were determined on an inhouse apparatus. Experimental details for humid SO_2 exposure are also given in the Supporting Information.

ASSOCIATED CONTENT

Supporting Information

The Supporting Information is available free of charge on the ACS Publications website at DOI: 10.1021/acsami.9b00029.

Brief MOF structure description, additional gas sorption isotherms and measurement details, isotherm fitting and simulation parameters, virial analysis, additional breakthrough experiments and simulations, powder X-ray diffractograms, and comparison of SO_2 sorption literature data (PDF)

AUTHOR INFORMATION

Corresponding Author

*E-mail: janiak@uni-duesseldorf.de.

ORCID

Christoph Janiak: 0000-0002-6288-9605

Author Contributions

‡P.B. and A.N. contributed equally to this work. The manuscript was written through contributions of all authors. All authors have given approval to the final version of the manuscript.

Notes

The authors declare no competing financial interest.

ACKNOWLEDGMENTS

We thank Dr. Andreas Möller from 3P Instruments, Germany and Mr. Simon Millan for helpful discussion. We are indebted to the Deutsche Forschungsgemeinschaft for support through grant Ja466/29-1.

ABBREVIATIONS

BET, Brunauer–Emmett–Teller
DFT, density functional theory
FGD, flue gas desulfurization
IAST, ideal adsorbed solution theory
IRMOF, isoreticular MOF
MFM, Manchester framework material
MIL, Matériaux de l'Institut Lavoisier
MOF, metal–organic framework
PXRD, powder X-ray diffraction

REFERENCES

(1) Laurent, A.; Espinosa, N. Environmental Impacts of Electricity Generation at Global, Regional and National Scales in 1980–2011: What can we Learn for Future Energy Planning? *Energy Environ. Sci.* **2015**, *8*, 689–701.

(2) Rezaei, F.; Rownaghi, A. A.; Monjezi, S.; Lively, R. P.; Jones, C. W. SO_x/NO_x Removal from Flue Gas Streams by Solid Adsorbents: A Review of Current Challenges and Future Directions. *Energy Fuels* **2015**, *29*, 5467–5486.

(3) International Energy Agency *World Energy Outlook 2016*; Iea Publications: Paris, 2016.

(4) Fioletov, V. E.; McLinden, C. A.; Krotkov, N.; Li, C.; Joiner, J.; Theys, N.; Carn, S.; Moran, M. D. A Global Catalogue of large SO_2 Sources and Emissions Derived from the Ozone Monitoring Instrument. *Atmos. Chem. Phys.* **2016**, *16*, 11497–11519.

(5) Lee, J.-Y.; Keener, T. C.; Yang, Y. J. Potential Flue Gas Impurities in Carbon Dioxide Streams Separated from Coal-Fired Power Plants. *J. Air Waste Manage. Assoc.* **2012**, *59*, 725–732.

(6) Srivastava, R. K.; Jozewicz, W. Flue Gas Desulfurization: The State of the Art. *J. Air Waste Manage. Assoc.* **2011**, *51*, 1676–1688.

(7) Likens, G. E.; Driscoll, C. T.; Buso, D. C. Long-Term Effects of Acid Rain: Response and Recovery of a Forest Ecosystem. *Science* **1996**, *272*, 244–246.

(8) Gregory, K.; Webster, C.; Durk, S. Estimates of Damage to Forests in Europe due to Emissions of Acidifying Pollutants. *Energy Policy* **1996**, *24*, 655−664.
(9) Rall, D. P. Review of the Health Effects of Sulfur Oxides. *Environ. Health Perspect.* **1974**, *8*, 97−121.
(10) Rao, A. B.; Rubin, E. S. A Technical, Economic, and Environmental Assessment of Amine-Based CO2 Capture Technology for Power Plant Greenhouse Gas Control. *Environ. Sci. Technol.* **2002**, *36*, 4467−4475.
(11) Ding, S.; Liu, F.; Shi, X.; Liu, K.; Lian, Z.; Xie, L.; He, H. Significant Promotion Effect of Mo Additive on a Novel Ce−Zr Mixed Oxide Catalyst for the Selective Catalytic Reduction of NO_x with NH_3. *ACS Appl. Mater. Interfaces* **2015**, *7*, 9497−9506.
(12) Goo, J. H.; Irfan, M. F.; Kim, S. D.; Hong, S. C. Effects of NO_2 and SO_2 on Selective Catalytic Reduction of Nitrogen Oxides by Ammonia. *Chemosphere* **2007**, *67*, 718−723.
(13) Savage, M.; Cheng, Y.; Easun, T. L.; Eyley, J. E.; Argent, S. P.; Warren, M. R.; Lewis, W.; Murray, C.; Tang, C. C.; Frogley, M. D.; Cinque, G.; Sun, J.; Rudić, S.; Murden, R. T.; Benham, M. J.; Fitch, A. N.; Blake, A. J.; Ramirez-Cuesta, A. J.; Yang, S.; Schröder, M. Selective Adsorption of Sulfur Dioxide in a Robust Metal-Organic Framework Material. *Adv. Mater.* **2016**, *28*, 8705−8711.
(14) Han, S.; Huang, Y.; Watanabe, T.; Nair, S.; Walton, K. S.; Sholl, D. S.; Carson Meredith, J. MOF Stability and Gas Adsorption as a Function of Exposure to Water, Humid Air, SO_2, and NO_2. *Microporous Mesoporous Mater.* **2013**, *173*, 86−91.
(15) Song, X.-D.; Wang, S.; Hao, C.; Qiu, J.-S. Investigation of SO_2 Gas Adsorption in Metal−Organic Frameworks by Molecular Simulation. *Inorg. Chem. Commun.* **2014**, *46*, 277−281.
(16) Sun, W.; Lin, L.-C.; Peng, X.; Smit, B. Computational Screening of Porous Metal-Organic Frameworks and Zeolites for the Removal of SO_2 and NO_x from Flue Gases. *AIChE J.* **2014**, *60*, 2314−2323.
(17) Mounfield, W. P., III; Han, C.; Pang, S. H.; Tumuluri, U.; Jiao, Y.; Bhattacharyya, S.; Dutzer, M. R.; Nair, S.; Wu, Z.; Lively, R. P.; Sholl, D. S.; Walton, K. S. Synergistic Effects of Water and SO_2 on Degradation of MIL-125 in the Presence of Acid Gases. *J. Phys. Chem. C* **2016**, *120*, 27230−27240.
(18) Britt, D.; Tranchemontagne, D.; Yaghi, O. M. Metal-Organic Frameworks with High Capacity and Selectivity for Harmful Gases. *Proc. Natl. Acad. Sci. U. S. A.* **2008**, *105*, 11623−11627.
(19) Bobbitt, N. S.; Mendonca, M. L.; Howarth, A. J.; Islamoglu, T.; Hupp, J. T.; Farha, O. K.; Snurr, R. Q. Metal-Organic Frameworks for the Removal of Toxic Industrial Chemicals and Chemical Warfare Agents. *Chem. Soc. Rev.* **2017**, *46*, 3357−3385.
(20) Wang, H.; Lustig, W. P.; Li, J. Sensing and Capture of Toxic and Hazardous Gases and Vapors by Metal-Organic Frameworks. *Chem. Soc. Rev.* **2018**, *47*, 4729−4756.
(21) Han, X.; Yang, S.; Schröder, M. Porous Metal-Organic Frameworks as Emerging Sorbents for Clean Air. *Nat. Rev. Chem.* **2019**, *3*, 108−118.
(22) Glomb, S.; Woschko, D.; Makhloufi, G.; Janiak, C. Metal-Organic Frameworks with Internal Urea-Functionalized Dicarboxylate Linkers for SO_2 and NH_3 Adsorption. *ACS Appl. Mater. Interfaces* **2017**, *9*, 37419−37434.
(23) Fernandez, C. A.; Thallapally, P. K.; Motkuri, R. K.; Nune, S. K.; Sumrak, J. C.; Tian, J.; Liu, J. Gas-Induced Expansion and Contraction of a Fluorinated Metal−Organic Framework. *Cryst. Growth Des.* **2010**, *10*, 1037−1039.
(24) Grant Glover, T.; Peterson, G. W.; Schindler, B. J.; Britt, D.; Yaghi, O. MOF-74 Building Unit has a direct Impact on Toxic Gas Adsorption. *Chem. Eng. Sci.* **2011**, *66*, 163−170.
(25) Yang, S.; Sun, J.; Ramirez-Cuesta, A. J.; Callear, S. K.; David, W. I. F.; Anderson, D. P.; Newby, R.; Blake, A. J.; Parker, J. E.; Tang, C. C.; Schröder, M. Selectivity and Direct Visualization of Carbon Dioxide and Sulfur Dioxide in a Decorated Porous Host. *Nat. Chem.* **2012**, *4*, 887−894.
(26) Yang, S.; Liu, L.; Sun, J.; Thomas, K. M.; Davies, A. J.; George, M. W.; Blake, A. J.; Hill, A. H.; Fitch, A. N.; Tang, C. C.; Schröder, M. Irreversible Network Transformation in a Dynamic Porous Host Catalyzed by Sulfur Dioxide. *J. Am. Chem. Soc.* **2013**, *135*, 4954−4957.
(27) Cui, X.; Yang, Q.; Yang, L.; Krishna, R.; Zhang, Z.; Bao, Z.; Wu, H.; Ren, Q.; Zhou, W.; Chen, B.; Xing, H. Ultrahigh and Selective SO_2 Uptake in Inorganic Anion-Pillared Hybrid Porous Materials. *Adv. Mater.* **2017**, *29*, 1606929.
(28) Tan, K.; Canepa, P.; Gong, Q.; Liu, J.; Johnson, D. H.; Dyevoich, A.; Thallapally, P. K.; Thonhauser, T.; Li, J.; Chabal, Y. J. Mechanism of Preferential Adsorption of SO_2 into Two Microporous Paddle Wheel Frameworks $M(bdc)(ted)_{0.5}$. *Chem. Mater.* **2013**, *25*, 4653−4662.
(29) Thallapally, P. K.; Motkuri, R. K.; Fernandez, C. A.; McGrail, B. P.; Behrooz, G. S. Prussian Blue Analogues for CO_2 and SO_2 Capture and Separation Applications. *Inorg. Chem.* **2010**, *49*, 4909−4915.
(30) Carter, J. H.; Han, X.; Moreau, F. Y.; da Silva, I.; Nevin, A.; Godfrey, H. G. W.; Tang, C. C.; Yang, S.; Schröder, M. Exceptional Adsorption and Binding of Sulfur Dioxide in a Robust Zirconium-Based Metal-Organic Framework. *J. Am. Chem. Soc.* **2018**, *140*, 15564−15567.
(31) Hungerford, J.; Bhattacharyya, S.; Tumuluri, U.; Nair, S.; Wu, Z.; Walton, K. S. DMOF-1 as a Representative MOF for SO_2 Adsorption in Both Humid and Dry Conditions. *J. Phys. Chem. C* **2018**, *122*, 23493−23500.
(32) Han, X.; Godfrey, H. G. W.; Briggs, L.; Davies, A. J.; Cheng, Y.; Daemen, L. L.; Sheveleva, A. M.; Tuna, F.; McInnes, E. J. L.; Sun, J.; Drathen, C.; George, M. W.; Ramirez-Cuesta, A. J.; Thomas, K. M.; Yang, S.; Schröder, M. Reversible Adsorption of Nitrogen Dioxide within a Robust Porous Metal-Organic Framework. *Nat. Mater.* **2018**, *17*, 691−696.
(33) Mon, M.; Tiburcio, E.; Ferrando-Soria, J.; Gil San Millán, R.; Navarro, J. A. R.; Armentano, D.; Pardo, E. A Post-Synthetic Approach Triggers Selective and Reversible Sulphur Dioxide Adsorption on a Metal-Organic Framework. *Chem. Commun.* **2018**, *54*, 9063−9066.
(34) Zhang, Y.; Zhang, P.; Yu, W.; Zhang, J.; Huang, J.; Wang, J.; Xu, M.; Deng, Q.; Zeng, Z.; Deng, S. Highly Selective and Reversible Sulfur Dioxide Adsorption on a Microporous Metal-Organic Framework via Polar Sites. *ACS Appl. Mater. Interfaces* **2019**, 10680−10688.
(35) Li, X.; Cheng, F.; Zhang, S.; Chen, J. Shape-Controlled Synthesis and Lithium-Storage Study of Metal-Organic Frameworks $Zn_4O(1,3,5\text{-benzenetribenzoate})_2$. *J. Power Sources* **2006**, *160*, 542−547.
(36) Permyakova, A.; Skrylnyk, O.; Courbon, E.; Affram, M.; Wang, S.; Lee, U.-H.; Valekar, A. H.; Nouar, F.; Mouchaham, G.; Devic, T.; De Weireld, G.; Chang, J.-S.; Steunou, N.; Frère, M.; Serre, C. Synthesis Optimization, Shaping, and Heat Reallocation Evaluation of the Hydrophilic Metal-Organic Framework MIL-160(Al). *ChemSusChem* **2017**, *10*, 1419−1426.
(37) Sohail, M.; Yun, Y.-N.; Lee, E.; Kim, S. K.; Cho, K.; Kim, J.-N.; Kim, T. W.; Moon, J.-H.; Kim, H. Synthesis of Highly Crystalline NH_2-MIL-125(Ti) with S-Shaped Water Isotherms for Adsorption Heat Transformation. *Cryst. Growth Des.* **2017**, *17*, 1208−1213.
(38) Jeremias, F.; Lozan, V.; Henninger, S. K.; Janiak, C. Programming MOFs for Water Sorption: Amino-Functionalized MIL-125 and UiO-66 for Heat Transformation and Heat Storage Applications. *Dalton Trans.* **2013**, *42*, 15967−15973.
(39) Thommes, M.; Kaneko, K.; Neimark, A. V.; Olivier, J. P.; Rodriguez-Reinoso, F.; Rouquerol, J.; Sing, K. S. W. Physisorption of Gases, with Special Reference to the Evaluation of Surface Area and Pore Size Distribution (IUPAC Technical Report). *Pure Appl. Chem.* **2015**, *87*, 1051−1069.
(40) Saha, D.; Deng, S. Hydrogen Adsorption on Metal-Organic Framework MOF-177. *Tsinghua Sci. Technol.* **2010**, *15*, 363−376.
(41) 3P INSTRUMENTS, 3P sim, Version 1.1.0.7, *Simulation and Evaluation Tool for mixSorb*, 3P INSTRUMENTS 2018.
(42) Wahiduzzaman, M.; Lenzen, D.; Maurin, G.; Stock, N.; Wharmby, M. T. Rietveld Refinement of MIL-160 and Its Structural Flexibility Upon H_2O and N2Adsorption. *Eur. J. Inorg.Chem.* **2018**, *2018*, 3626−3632.
(43) Cessford, N. F.; Seaton, N. A.; Düren, T. Evaluation of Ideal Adsorbed Solution Theory as a Tool for the Design of Metal-Organic Framework Materials. *Ind. Eng. Chem. Res.* **2012**, *51*, 4911−4921.

DOI: 10.1021/acsami.9b00029
ACS Appl. Mater. Interfaces 2019, 11, 17350−17358

(44) Liu, C.-F.; Shih, S.-M.; Lin, R.-B. Kinetics of the Reaction of $Ca(OH)_2$/fly Ash Sorbent with SO_2 at low Temperatures. *Chem. Eng. Sci.* **2002**, *57*, 93−104.
(45) Chu, P.; Rochelle, G. T. Removal of SO_2 and NO_X from Stack Gas by Reaction with Calcium Hydroxide Solids. *JAPCA* **1989**, *39*, 175−179.
(46) Jia, L.; Tan, Y.; Anthony, E. J. Emissions of SO_2 and NO_x during Oxy−Fuel CFB Combustion Tests in a Mini-Circulating Fluidized Bed Combustion Reactor. *Energy Fuels* **2010**, *24*, 910−915.
(47) Damasceno Borges, D.; Normand, P.; Permiakova, A.; Babarao, R.; Heymans, N.; Galvao, D. S.; Serre, C.; de Weireld, G.; Maurin, G. Gas Adsorption and Separation by the Al-Based Metal−Organic Framework MIL-160. *J. Phys. Chem. C* **2017**, *121*, 26822−26832.
(48) Li, J.-R.; Kuppler, R. J.; Zhou, H.-C. Selective Gas Adsorption and Separation in Metal-Organic Frameworks. *Chem. Soc. Rev.* **2009**, *38*, 1477−1504.
(49) Lenzen, D.; Bendix, P.; Reinsch, H.; Fröhlich, D.; Kummer, H.; Möllers, M.; Hügenell, P. P. C.; Gläser, R.; Henninger, S.; Stock, N. Scalable Green Synthesis and Full-Scale Test of the Metal−Organic Framework CAU-10-H for Use in Adsorption-Driven Chillers. *Adv. Mater.* **2018**, *30*, 1705869.
(50) Jeremias, F.; Fröhlich, D.; Janiak, C.; Henninger, S. K. Advancement of Sorption-Based Heat Transformation by a Metal Coating of Highly-Stable, Hydrophilic Aluminium Fumarate MOF. *RSC Adv.* **2014**, *4*, 24073−24082.
(51) Fröhlich, D.; Pantatosaki, E.; Kolokathis, P. D.; Markey, K.; Reinsch, H.; Baumgartner, M.; van der Veen, M. A.; de Vos, D. E.; Stock, N.; Papadopoulos, G. K.; Henninger, S. K.; Janiak, C. Water Adsorption Behaviour of CAU-10-H: a Thorough Investigation of its Structure−Property Relationships. *J. Mater. Chem. A* **2016**, *4*, 11859−11869.

DOI: 10.1021/acsami.9b00029
ACS Appl. Mater. Interfaces 2019, 11, 17350−17358

Supporting Information

Metal-Organic Frameworks with Potential Application for SO_2-Separation and Flue Gas Desulfurization

Philipp Brandt [a,‡], *Alexander Nuhnen* [a,‡], *Marcus Lange* [b], *Jens Möllmer* [b], *Oliver Weingart* [c], *Christoph Janiak* [a,d]*

[a] Institut für Anorganische Chemie und Strukturchemie, Heinrich-Heine-Universität Düsseldorf, Universitätsstraße 1, 40225 Düsseldorf, Germany

[b] Institut für Nichtklassische Chemie, Permoserstr. 15, 04318 Leipzig, Germany

[c] Institut für Theoretische Chemie und Computerchemie, Heinrich-Heine-Universität Düsseldorf, Universitätsstraße 1, 40225 Düsseldorf, Germany

[d] Hoffmann Institute of Advanced Materials, Shenzhen Polytechnic, 7098 Liuxian Blvd, Nanshan District, Shenzhen, China

[‡] These authors contributed equally.

Email addresses: p.brandt@hhu.de; alexander.nuhnen@hhu.de; lange@inc.uni-leipzig.de; moellmer@inc.uni-leipzig.de; oliver.weingart@hhu.de; janiak@hhu.de

Table of contents

1 Synthesis

All reagents were commercially purchased and were used without further purification. MOF-177, MIL-160 and NH_2-MIL-125(Ti) were synthesized according to the literature.[1,2,3]

1.1 MOF-177

The Zn-based MOF-177 contains the tetranuclear and tetrahedral $\{Zn_4(\mu_4\text{-}O)\}$ secondary building unit, SBU as in MOF-5. The linker is benzene-1,3,5-trisbenzoic acid, $btbH_3$ {5'-(4-carboxyphenyl)-[1,1':3',1"-terphenyl]-4,4"-dicarboxylic acid}. The compound is synthesized from $Zn(NO_3)_2{\cdot}(H_2O)_6$ and $btbH_3$ in DEF under solvothermal conditions, to yield the MOF formula $[Zn_4(\mu_4\text{-}O)(btb)_3]$.[1] The linker and SBU connectivity are depicted in Figure S1. The material exhibits a surface area of 4050 $m^2\ g^{-1}$ and a pore volume of 1.51 $cm^3\ g^{-1}$.

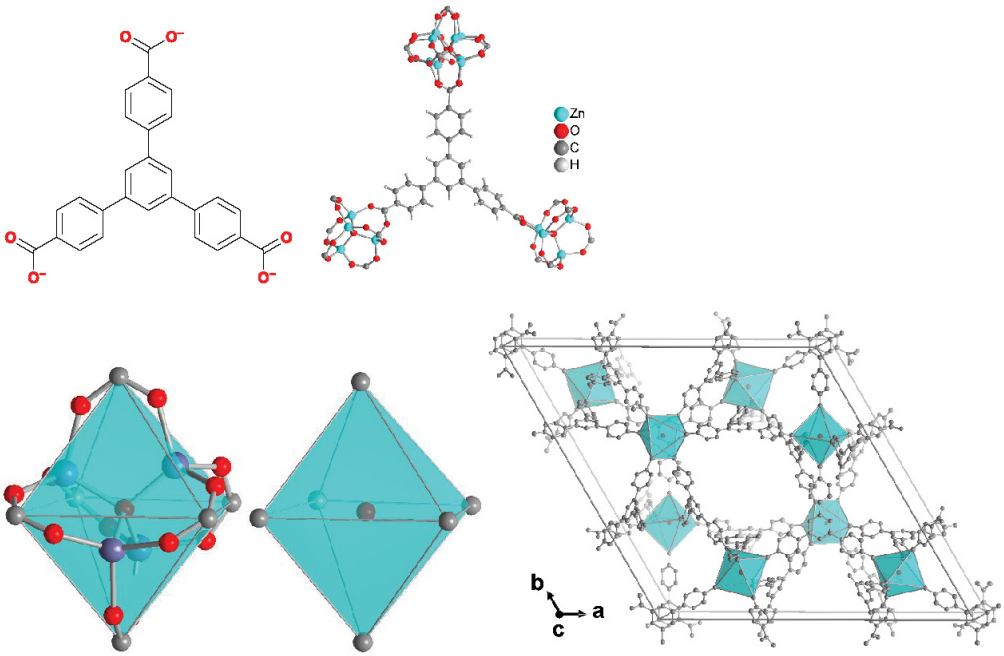

Figure S1. Structural elements in the framework of MOF-177. Top row: Linker and linker connectivity. There are two crystallographically independent SBUs which are both disordered, with one of them disordered about a special position. Bottom row: Due to this disorder, the SBUs were depicted as octahedra, with the carboxylate carbon atoms as vertices, to illustrate a view the trigonal unit cell of the framework in space group *P*–31*c*. Graphic produced by software Diamond[4] from cif-file for MOF-177 (CSD-Refcode BABRII).[5]

1.2 MIL-160

The Al-MOF MIL-160 (*Matériaux Institut Lavoisier*), was described by Cadiau *et al.* in 2015.[6] They obtained the MOF by applying reflux conditions for aqueous solutions of 2,5-furan-dicarboxylic acid, sodium hydroxide and aluminum chloride. MIL-160 is constructed identical to CAU-10-H [7,8] by cis-μ-OH-connected, vertex-sharing $\{AlO_6\}$ octahedra, that form helical chains, which are then joined by the linker 2,5-furandicarboxylate (Fig. S2).

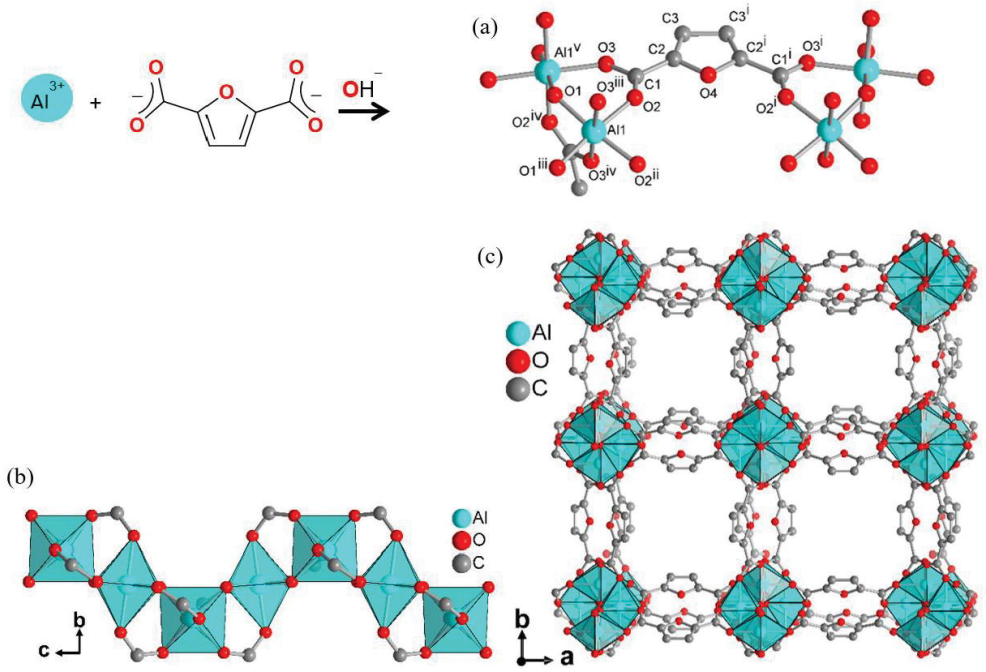

Figure S2. Structural elements in the framework of MIL-160: (a) Extended asymmetric unit with full Al coordination spheres and full ligand bridging mode. Symmetry transformations i = 1–x, y, z; ii = x, –y, –z; iii = 0.25+y, 0.25–x, –0.25+z; iv = 0.25+y, –0.25+x, 0.25–z; v = 0.25–y, –0.25+x, 0.25+z. (b) Helical chains of cis vertex-bridged {AlO_6}-polyhedra and (c) surrounded by the carboxylates ligands, to yield square-shaped one dimensional channels. Graphic produced by software Diamond[4] from cif-file for MIL-160 (CSD-Refcode PIBZOS).[9]

MIL-160 is reported to be isostructural to CAU-10-H, having chains of {AlO_6}-polyhedra that are surrounded by linker molecules.[6] This results in a chemical formula of [$Al(OH)(O_2C\text{-}C_4H_2O\text{-}CO_2) \cdot n\ H_2O]_m$ and microporous square-shaped channels of 5 Å edge length.[6,10] The material exhibits a surface area of 1070 $m^2\ g^{-1}$ and a pore volume of 0.40 $cm^3\ g^{-1}$ from $AlCl_3$ and NaOH (theoretically: 1250 $m^2\ g^{-1}$, 0.48 $cm^3\ g^{-1}$),[6] respectively 1150 $m^2\ g^{-1}$ and 0.46 $cm^3\ g^{-1}$, from $Al(OH)(CH_3COO)_2$,[10] although very recent theoretical calculations suggested a surface area of 776 $m^2\ g^{-1}$ and a pore volume of 0.45 $cm^3\ g^{-1}$.[11]

1.3 NH_2-MIL-125(Ti)

The structure of 3D-[$Ti_8O_8(OH)_4(NH_2\text{-}bdc)_6$] is based on the structure of titanium terephthalate MIL-125.[12] The SBU is an eight-membered ring of edge- and vertex-sharing TiO_6 octahedra, which is connected to 12 neighboring SBUs in a body-centered cubic (bcc) packing arrangement (Fig. S3).

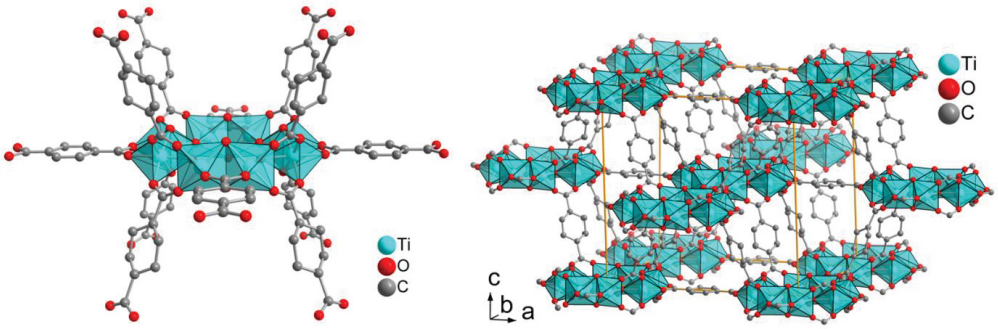

Figure S3. Structural elements in the framework of NH_2-MIL-125(Ti) aka MIL-125: Left the secondary building unit of eight edge- and vertex-sharing TiO_6 octahedra with the twelve surrouding terephthalate ligands. Right the unit cell with the body-centered cubic arrangement of the SBUs. The structure is drawn from the deposited cif-file under CCDC 751157 (MIL-125).[12]

2 Gas sorption experiments

Before each experiment samples were activated for at least 3 hours and at a minimum of 373 K under vacuum < $5 \cdot 10^{-3}$ mbar. All used gases (He, SO_2, CO_2, N_2, H_2) were of ultra-high purity (UHP grade 5.0, 99.999%) and the STP volumes at 293.15 K and 101.325 kPa are given according to the NIST standards. If not described differently, Sorption experiments were performed on an *Autosorb iQ MP* (QUANTACHROME, Odelzhausen, Germany) instrument within a pressure range of $1 \cdot 10^{-3}$-1 bar. For safety precautions of toxic SO_2 a *Dräger Pac 6000* SO_2-detector (0-100 ppm in 0.1 ppm steps) was used in close range to the sorption-device.

SO_2-sorption experiments with our setup involve some limitations emerging from the corrosive nature of the SO_2 adsorptive. Each SO_2 sorption run had to be completed within a maximal time of 10 h. This time limit was specified by the company Quantachrome to prevent damage to the gaskets. After this time the system had to be regenerated by flushing with nitrogen. Irreversible swilling of the SO_2 adsorbing gaskets in the measurement device, which could cause leaks in the system, had to be prevented by setting the measurement time to this maximum (10 h) to meet safety precautions and to protect the device. Then, after each measurement the gas line was flushed with N_2 several times and remained under N_2 atmosphere for at least 12 h to regenerate the gaskets. In the case of long equilibration times upon adsorption and desorption we decided to collect the adsorption data points as complete as possible with long-enough equilibration times at the expense that for desorption, fewer data points could be measured. This compromise then led to incomplete, i.e. not-closed desorption branches, which however are solely due to the experimental boundary conditions and cannot be interpreted in terms of decomposition or chemisorption.

2.1 Isotherm-fitting

Fitting-simulations were calculated using 3P sim software.[13] We applied several commonly used models on our isotherm data. The best fits for our isotherms were given for the Sips and DSLAI fitting models, which we compare in Figure S4-S7.

The Sips model is a combination of Langmuir and Freundlich isotherms with the following equation:

$$q_{eq} = \frac{q_{max} \cdot K \cdot p^t}{1 + K \cdot p^t} \quad (1)$$

Where q_{eq} is the amount adsorbed (mg/g), q_{max} is the maximum adsorption capacity (mg/g), K is the affinity constant for adsorption (L/mg), p is the equilibrium concentration of the adsorbate (mg/L) and t is the index of the heterogeneity.[14]

If K or p approaches 0 the fitting of the model is reduced to a Freundlich equation (eq. 2), whereas for homogeneous materials with $t = 1$ concentrations it is reduced to the Langmuir equation (eq. 3).[15]

$$q_{eq} = K \cdot p^t \quad (2)$$

$$q_{eq} = \frac{q_{max} \cdot K \cdot p}{1 + K \cdot p} \quad (3)$$

The dual-site Langmuir model is based on the following equation:

$$q_{eq} = q_{max1} \cdot \frac{K_1 \cdot p}{1 + K_1 \cdot p} + q_{max2} \cdot \frac{K_2 \cdot p}{1 + K_2 \cdot p} \quad (4)$$

By fitting isotherms of the same adsorptive at three different temperatures the software is able to calculate any given temperature for this specific gas (here 353 K, red line).

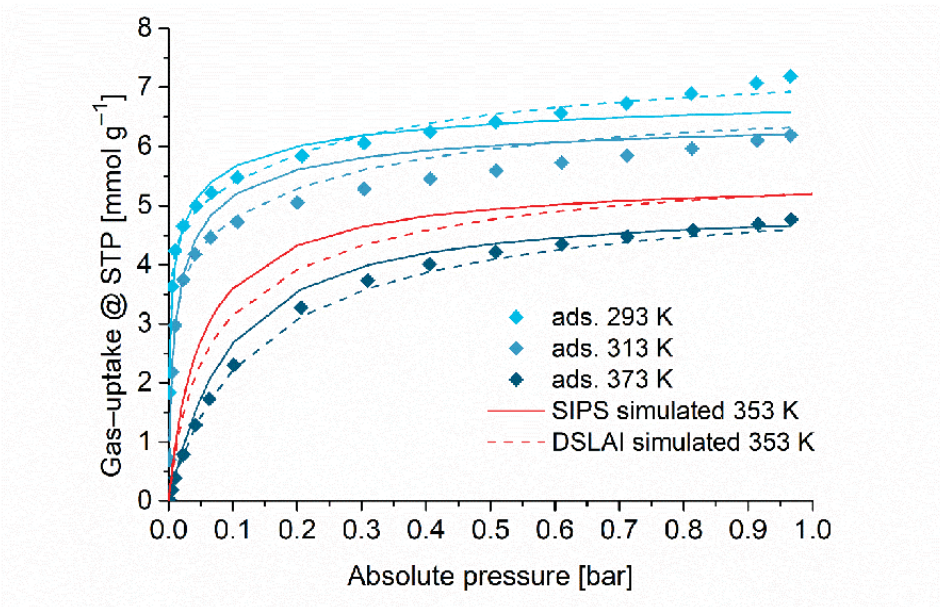

Figure S4. Experimental SO_2-adsorption isotherms (squares) and simulated adsorption isotherms with different models (lines and dashed lines) of MIL-160 at 293 K, 313 K and 373 K. The simulations at 353 K (red) are shown here as this is a common temperature for flue gas desulfurization processes.

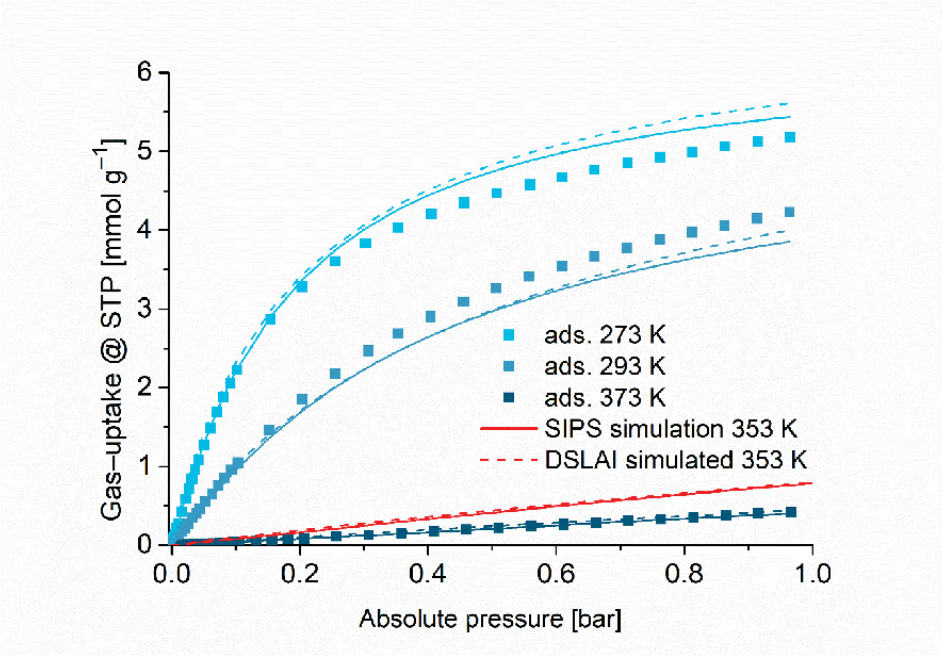

Figure S5. Experimental CO_2-adsorption isotherms (squares) and simulated adsorption isotherms with different models (lines and dashed lines) of MIL-160 at 273 K, 293 K and 373 K. The simulations at 353 K (red) are shown here as this is a common temperature for flue gas desulfurization processes.

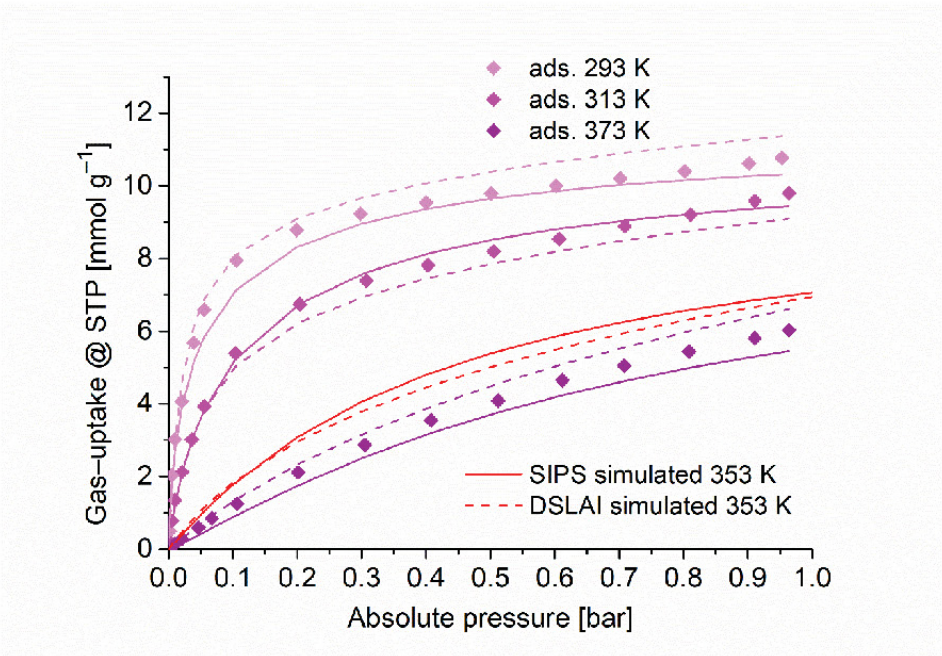

Figure S6. Experimental SO_2-adsorption isotherms (squares) and simulated adsorption isotherms with different models (lines and dashed lines) of NH_2-MIL-125(Ti) at 293 K, 313 K and 373 K. The simulations at 353 K (red) are shown here as this is a common temperature for flue gas desulfurization processes.

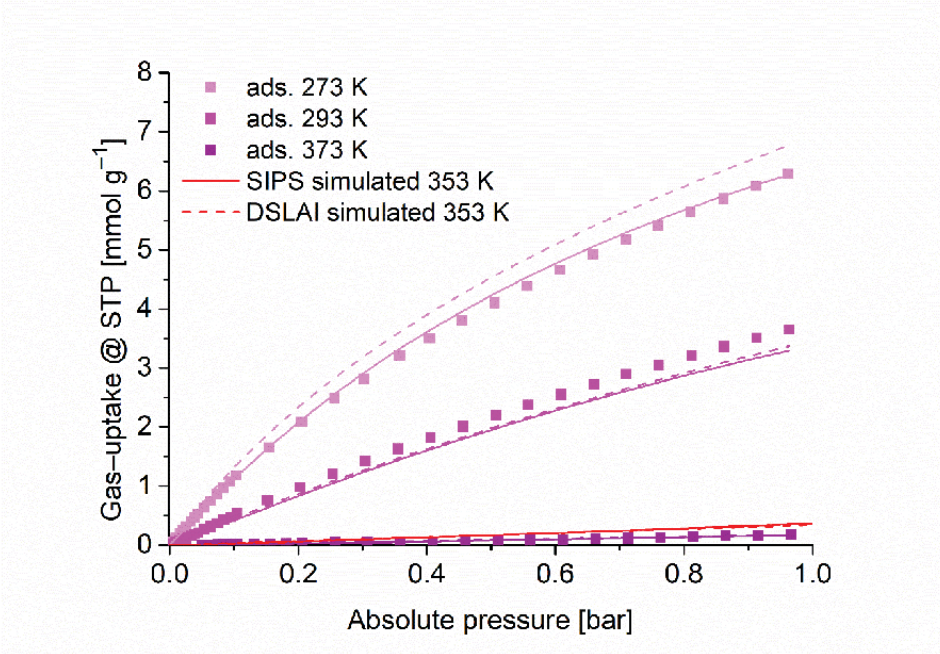

Figure S7. Experimental CO_2-adsorption isotherms (squares) and simulated adsorption isotherms with different models (lines and dashed lines) of NH_2-MIL-125(Ti) at 273 K, 293 K and 373 K. The simulations at 353 K (red) are shown here as this is a common temperature for flue gas desulfurization processes.

Heat of adsorption

2.2 Virial analysis for SO_2

To calculate the isosteric heat of adsorption (Q_{st}) for SO_2 isotherm data virial method was used. Equation (eq. 5) was used to fit the adsorption data simultaneously at 273 K and 293 K in Origin.[16]

$$\ln(P) = \ln(n) + \frac{1}{T}\sum_{i=0}^{n} a_i n^i + \sum_{j=0}^{m} b_j m^j \qquad (5)$$

In equation (4), P is the pressure in kPa, n is the total amount adsorbed in mmol/g, T is the temperature in K (here 273K, 293K), a_i and b_i are virial coefficients, and n, m represent the number of coefficients required to adequately fit the isotherms.

Then Q_{st} can be calculated from equation (eq. 6), where R is the universal gas constant.

$$Q_{st} = -\mathrm{R}\sum_{i=0}^{n} a_i n^i \qquad (6)$$

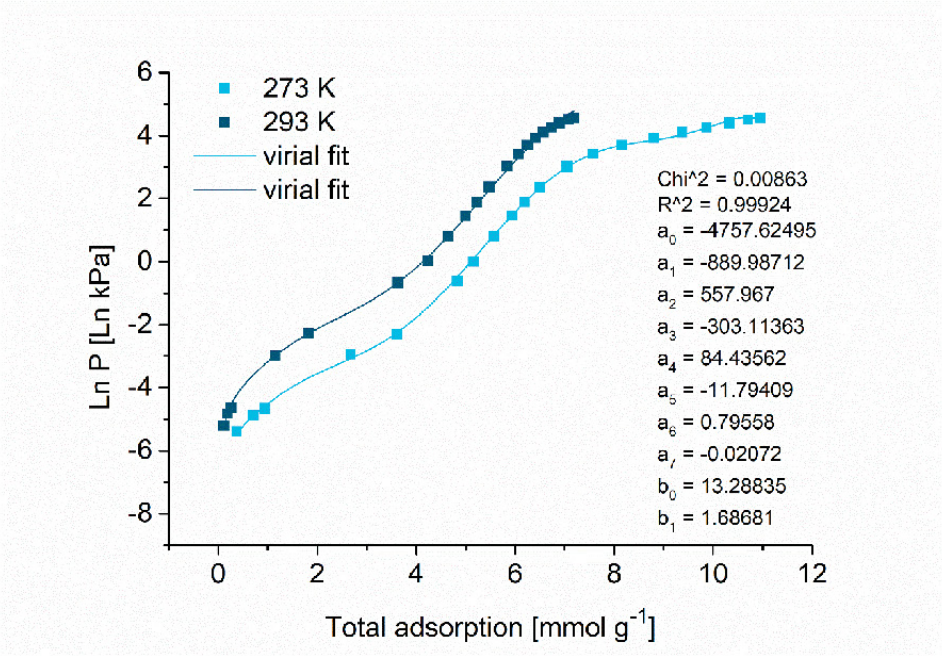

Figure S8. Virial analysis for heat of adsorption of SO_2 and MIL-160 at 273 K and 293 K.

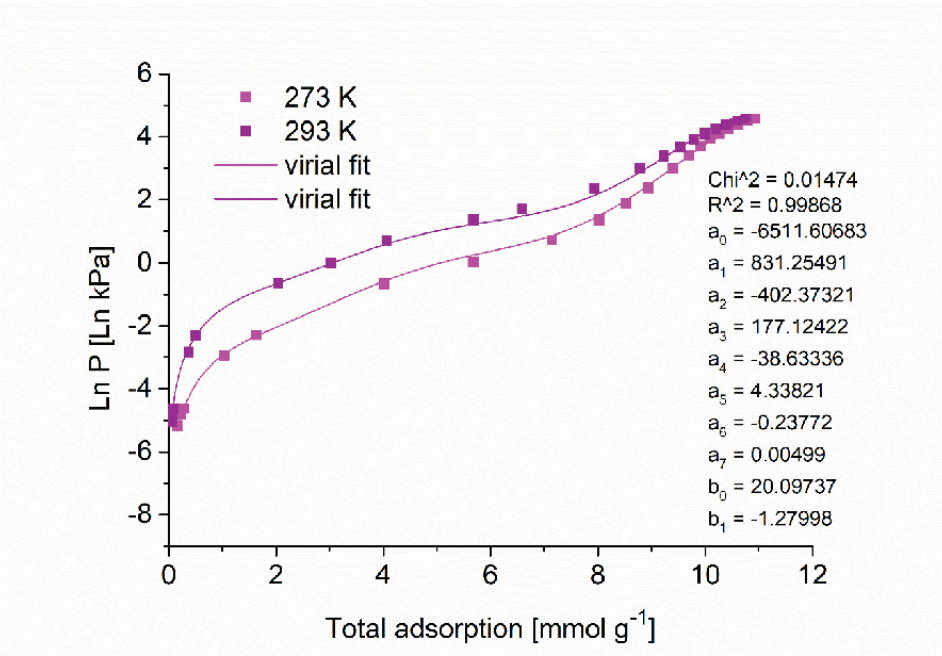

Figure S9. Virial analysis for heat of adsorption of SO_2 and NH_2-MIL-125(Ti) at 273 K and 293 K.

2.3 Sips analysis for CO_2

To calculate the isosteric heat of adsorption (Q_{st}) for CO_2 both isotherms at 273 K and 293 K were fitted according to the Sips equation (eq. 1), to be able to calculate CO_2 loadings for both temperatures at the same pressure.

By applying the Clausius-Clapeyron equation one can now calculate the isosteric heat of adsorption at any loading (eq. 7)

$$Q_{st} = -R \ln\left(\frac{p_2}{p_1}\right) \frac{T_1 T_2}{(T_2 - T_1)} \quad (7)$$

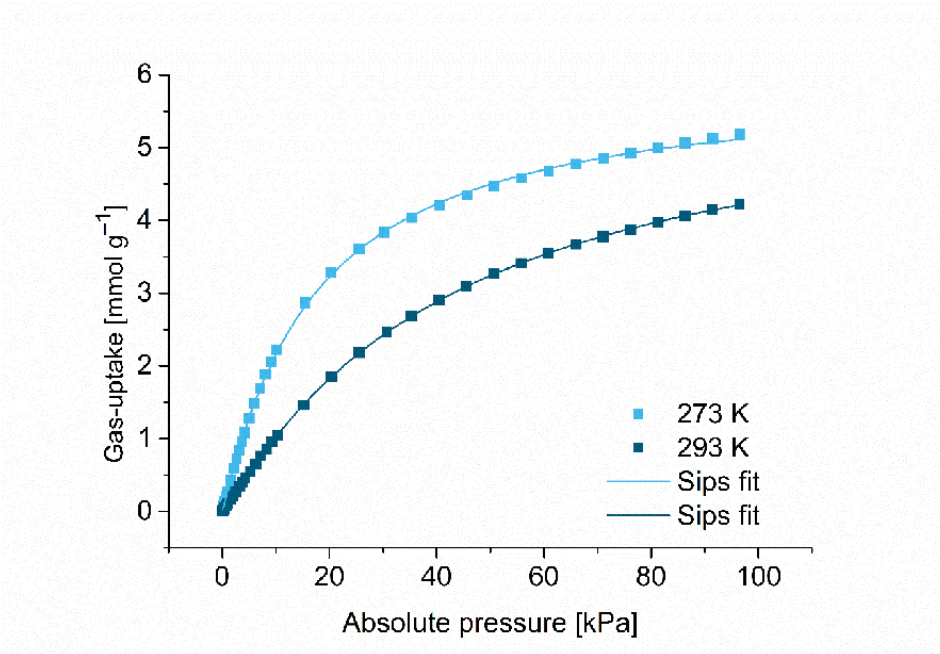

Figure S10. Sips fit of CO_2 for MIL-160 at 273 K and 293 K.

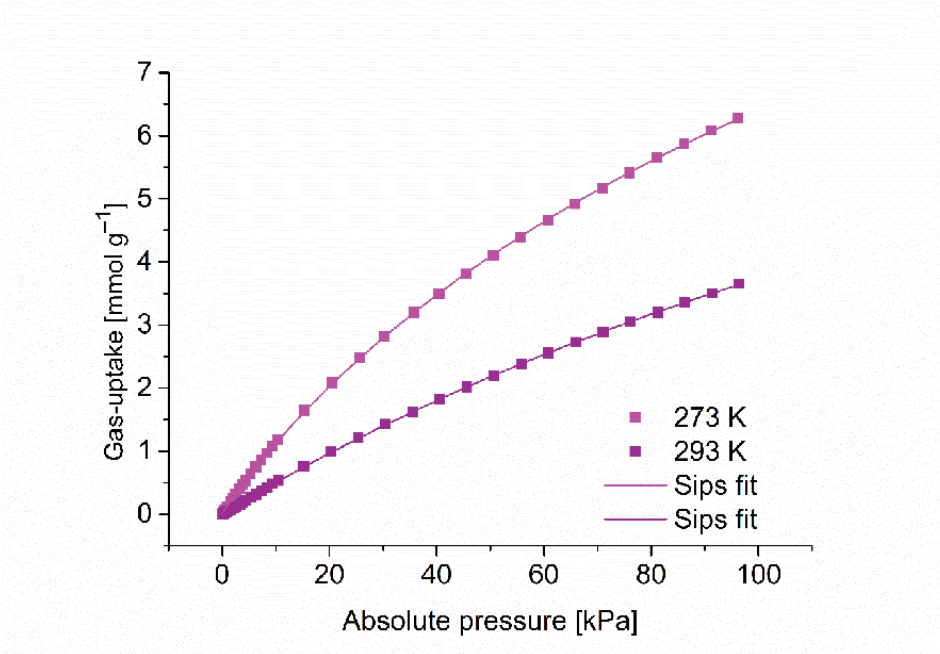

Figure S11. Sips fit of CO_2 for NH_2-MIL-125(Ti) at 273 K and 293 K.

IAST calculations

Selectivities of SO_2 over CO_2 and N_2 of MIL-160 and NH_2-MIL-125(Ti) were calculated from the dual-site Langmuir (DSLAI) (eq. 4) fitted isotherm data.

The 3P sim software (3P Instruments, Germany, version 1.1.0.7) calculates the maximal loadings of each gas depending on the given mole fraction.

IAST selectivities S of binary gas mixtures were calculated using equation 8, where x_i represents the absorbed gas amount and y_i the mole fraction of each adsorptive.

$$S = \frac{x_1/x_2}{y_1/y_2} \quad (8)$$

Table S1: Parameters for SIPS modeling and following simulation calculations.

				fit of isotherm				from fits simulated isotherm			
MOF	**Gas**	**Temp. [K]**	**Model**	**R^2**	**affinity const. [1/bar]**	**max. loading [mmol/g]**	**heterogenity exponent**	**R^2**	**affinity const. [1/bar]**	**max. loading [mmol/g]**	**heterogenity exponent**
MIL-160	SO_2	293	SIPS	0.972	108.281	7.623	0.443	0.954	157.829	7.242	0.458
	SO_2	313	SIPS	0.985	72.091	6.164	0.669	0.954	72.091	6.600	0.648
	SO_2	373	SIPS	0.999	8.532	5.084	1.090	0.988	11.372	4.998	1.096
	SO_2	353	SIPS	–	–	–	–	–	19.629	5.484	0.964
	CO_2	273	SIPS	0.999	5.892	5.931	1.056	0.985	5.515	6.353	1.066
	CO_2	293	SIPS	0.999	2.399	5.893	1.095	0.977	2.399	5.408	1.015
	CO_2	373	SIPS	0.999	0.220	2.792	1.125	0.956	0.210	2.841	1.128
	CO_2	353	SIPS	–	–	–	–	–	0.348	3.337	1.118
NH_2-MIL-125	SO_2	293	SIPS	0.997	22.359	11.775	0.706	0.985	17.855	11.760	0.693
	SO_2	313	SIPS	0.997	8.284	11.122	0.807	0.997	8.284	11.141	0.826
	SO_2	373	SIPS	0.998	1.610	9.478	1.143	0.973	1.356	9.474	1.138
	SO_2	353	SIPS	–	–	–	–	–	2.315	10.000	1.045
	CO_2	273	SIPS	0.999	1.086	12.013	1.040	0.999	0.997	12.812	1.018
	CO_2	293	SIPS	0.999	0.502	11.301	1.033	0.977	0.502	10.427	1.063
	CO_2	373	SIPS	0.992	0.072	4.501	1.204	0.989	0.067	4.574	1.196
	CO_2	353	SIPS	–	–	–	–	–	0.102	5.620	1.168

Table S2: Parameters for DSLAI modeling and following simulation calculations.

				fit of isotherm					from fits simulated isotherm				
MOF	**Gas**	**Temp. [K]**	**Model**	**R^2**	**affinity const. 1 [1/bar]**	**max. loading 1 [mmol/g]**	**affinity const. 2 [1/bar]**	**max. loading 2 [mmol/g]**	**R^2**	**affinity const. 1 [1/bar]**	**max. loading 1 [mmol/g]**	**affinity const. 2 [1/bar]**	**max. loading 2 [mmol/g]**
MIL-160	SO_2	293	DSLAI	0.994	691.984	4.622	3.363	3.123	0.934	787.437	4.638	3.834	2.914
	SO_2	313	DSLAI	0.997	217.734	4.222	3.016	2.481	0.910	217.734	4.203	3.834	2.722
	SO_2	373	DSLAI	0.999	9.535	3.123	5.123	2.272	0.999	10.523	3.127	3.834	2.220
	SO_2	353	DSLAI	–	–	–	–	–	–	25.766	3.451	3.834	2.376
	CO_2	273	DSLAI	0.999	3.155	4.696	13.949	1.792	0.986	3.889	5.017	9.939	1.823
	CO_2	293	DSLAI	0.999	1.306	5.866	4.859	1.226	0.989	1.306	5.400	4.859	1.200
	CO_2	373	DSLAI	0.994	0.046	7.128	0.763	0.225	0.982	0.053	7.246	0.598	0.226
	CO_2	353	DSLAI	–	–	–	–	–	–	0.104	6.733	0.923	0.343
NH_2-MIL-125	SO_2	293	DSLAI	0.998	45.054	9.069	0.560	5.210	0.969	184.670	9.258	4.629	2.055
	SO_2	313	DSLAI	0.999	20.598	7.002	0.648	7.717	0.981	48.410	7.938	3.587	2.563
	SO_2	373	DSLAI	0.999	3.098	2.500	0.484	13.017	0.993	0.960	4.291	1.700	6.207
	SO_2	353	DSLAI	–	–	–	–	–	–	2.166	5.004	1.985	4.976
	CO_2	273	DSLAI	0.999	1.924	5.063	0.176	20.151	0.984	2.082	5.471	0.177	21.385
	CO_2	293	DSLAI	0.999	0.536	6.732	0.063	24.221	0.984	0.536	6.110	0.063	22.487
	CO_2	373	DSLAI	0.999	0.010	9.318	0.003	27.086	0.975	0.010	9.501	0.003	27.491
	CO_2	353	DSLAI	–	–	–	–	–	–	0.023	8.508	0.006	26.144

3 Breakthrough experiments

Breakthrough curves were determined on an inhouse apparatus. The adsorbing unit consists of a stainless-steel column, which holds the adsorbent sample. The column is a ¼" Swagelok®-type tube with a length of max. 10 cm. The dosing unit consist of three different mass flow controllers (Bronkhorst High-Tech B.V., Netherlands, EL-Flow Prestige Series, max. flow 5 $ml_N\ min^{-1}$), each for the carrier gas (Nitrogen, Air Products, Purity 5.2, 99.9992%), CO_2 (Air Products, Purity 4.5, 99.995%) and a testing gas mixture of SO_2 in N_2 (Linde, 5 Vol.-% SO_2). An additional H_2O-bubbling system can be added to the carrier gas dosing unit. The adsorbing unit can be temperated by a thermostat (Julabo GmbH, Germany, Series F25) or by an electrical heating system. The gas phase could be analyzed in a bypass unit after the exit of the adsorber by an on-line mass selective detector (Pfeiffer Vacuum GmbH, Germany, Prisma QMS 200).

Around 110 mg of the sample were filled into the adsorber tube equipped with a stainless-steel seal and embedded in glass wool. The adsorbent material was regenerated at ~ 400 K until no other gas than nitrogen was detected. The sample was purged with 16.6 $ml_N\ min^{-1}$ of carrier gas nitrogen during the regeneration time for the removal of preadsorbed fluids. After the regeneration step, the adsorber column was cooled down to the measurement temperature.

After regeneration, the adsorber was purged with the carrier gas nitrogen and the desired gas mixture was dosed into the system and the gas composition at the outlet of the adsorber was recorded. The measurements were finished after reaching steady state conditions with no significant change in gas composition and temperature. Between each breakthrough experiment the samples were regenerated again to ensure well defined starting conditions for the next experiment. All samples were weighted after the last regeneration step to get the amount of activated samples for further evaluations.

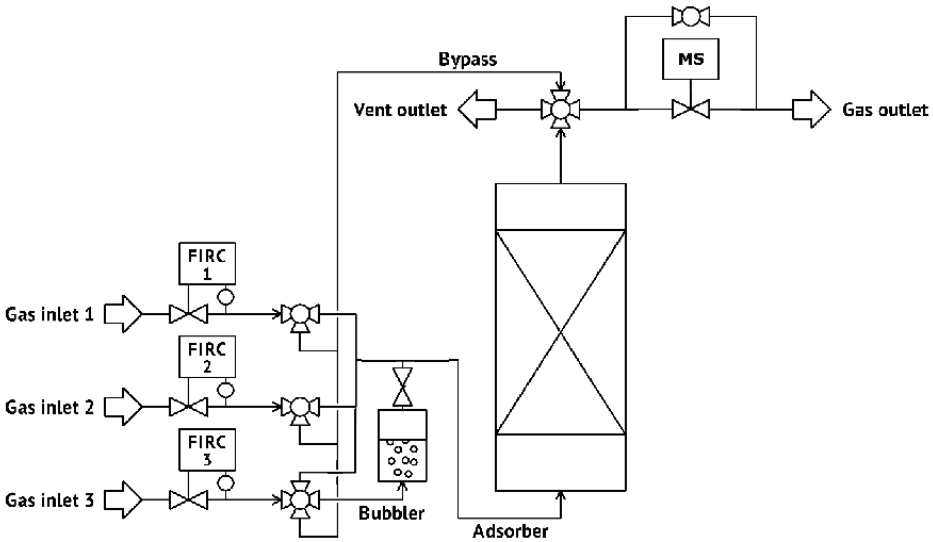

Scheme S1. Schematic of the apparatus used for breakthorguh curve measurements. The dosing unit consist of three mass flow controllers for three independent gas inlets. The carrier gas (gas inlet 3) could also be used for dosing different humidities to the adsorbing unit.

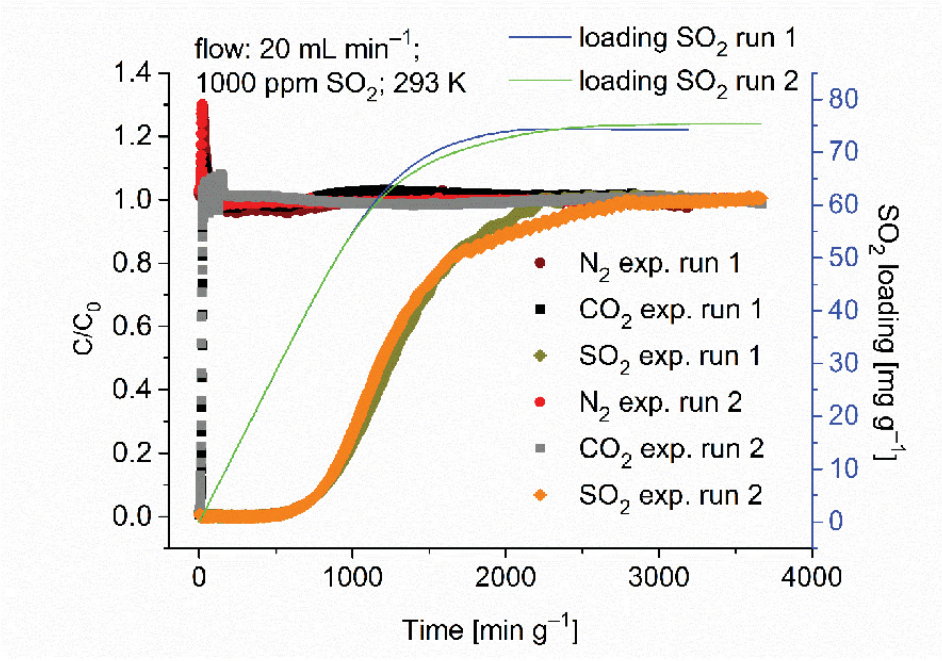

Figure S12. Experimental breakthrough curves of MIL-160 at 293 K with a gas mixture of $N_2/CO_2/SO_2$; 84.0/15.0/0.1; v:v:v (run 1 and 2).

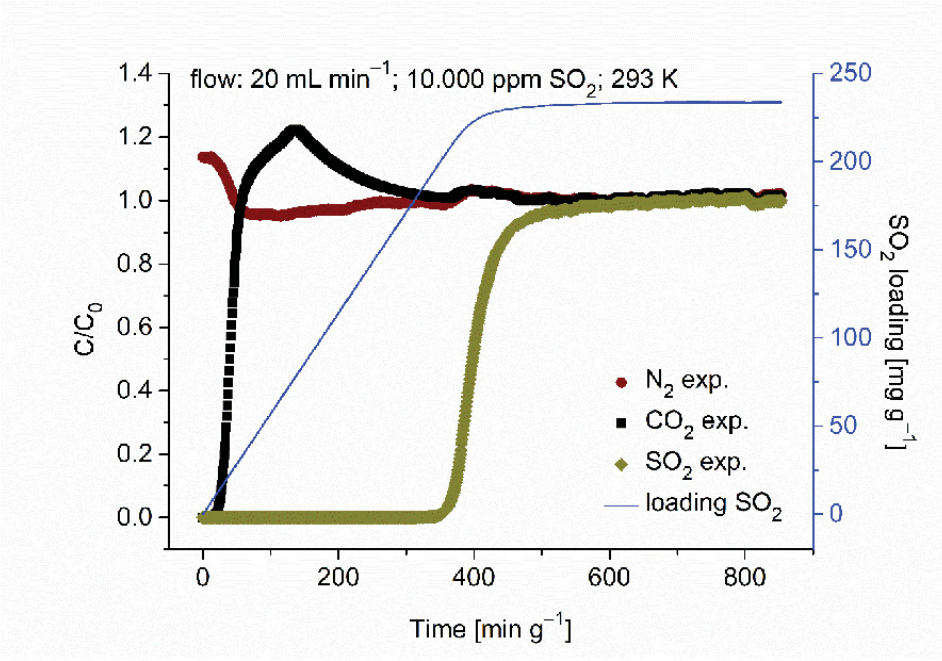

Figure S13. Experimental breakthrough curves of MIL-160 at 293 K with a gas mixture of $N_2/CO_2/SO_2$; 84.0/15.0/1.0; v:v:v.

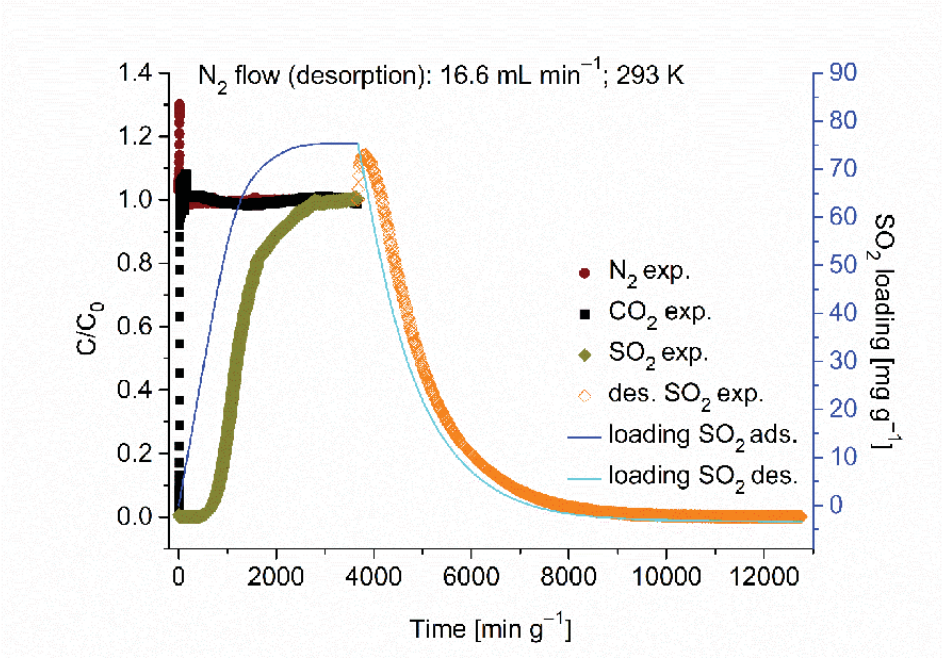

Figure S14. Reversible regeneration of MIL-160 under N_2 flow at 293 K.

Table S3. Comparison of maximal loadings under equilibrium or dynamic conditions with a partial pressure of 0.1% and 1% SO_2.

Material	SO_2-uptake [mmol g^{-1}]				
	Sorption exp. 0.001 bar, 293 K	Sorption exp. 0.01 bar, 293 K	Breakthrough exp. 0.1% SO_2, 293 K	Breakthrough exp. 0.1% SO_2, 353 K	Breakthrough exp. 1.0% SO_2 293 K
MOF-177	0.07	0.25	-	-	-
NH_2-MIL-125(Ti)	0.50	3.0	-	-	-
MIL-160	1.8	4.2	1.17	0.85	3.65

4 Breakthrough simulations

Breakthrough simulations were calculated using 3P sim software calculations are based on a 30 cm high column with an inner diameter of 3 cm, axial dispersion of 50 cm^2 min^{-1} and a continuous gas flow of 20 mL min^{-1}.

Generally mass transfer coefficients in our dispersion model were set to 10 min^{-1} for all gases.

Due to our additional experimental breakthrough measurements for MIL-160 at 293 K and 353 K with flowrates of 20 ml min^{-1} for the ternary gas mixture ($N_2/CO_2/SO_2$ (84.9/15.0/0.1 v:v:v) we were able to optimize the mass transfer coefficient for SO_2 in our simulation for this specific experiments to 0.005 min^{-1} and the axial dispersion to 20 cm^2 min^{-1}.

4.1 DISPERSED PLUG MODEL

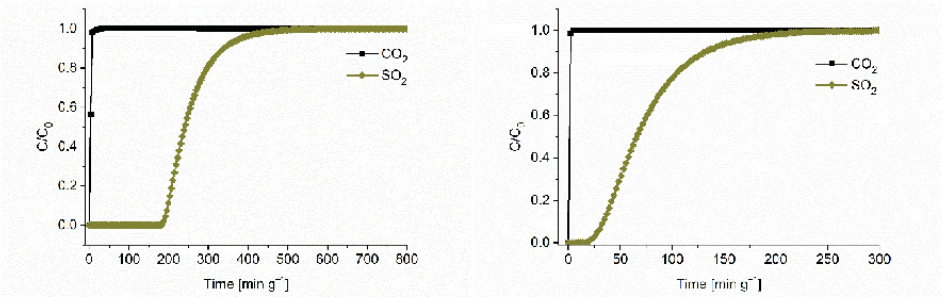

Figure S15. Breakthrough simulations of MIL-160 with CO_2/carrier gas/SO_2; 90/9.75/0.25; v:v:v at 293 (left) and 353 K (right).

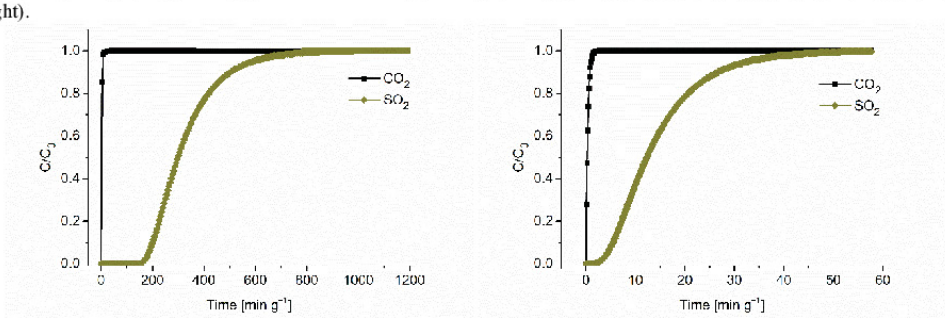

Figure S16. Breakthrough simulations of NH_2-MIL-125(Ti) with CO_2/carrier gas/SO_2; 90/9.75/0.25; v:v:v at 293 (left) and 353 K (right).

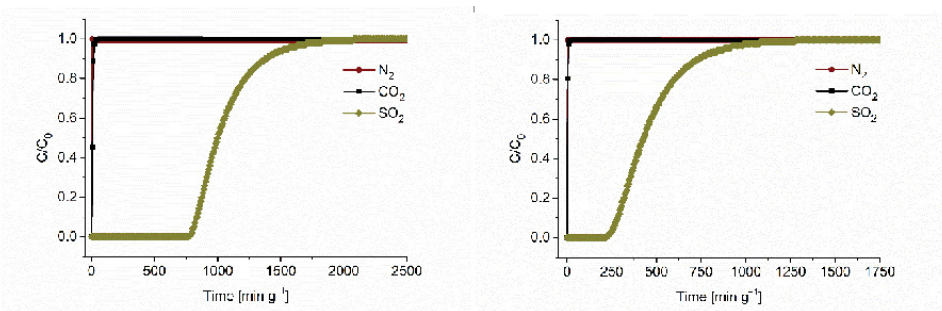

Figure S17. Breakthrough simulations of MIL-160 (left) and NH_2-MIL-125(Ti) (right) with $SO_2/CO_2/N_2$; 0.1/15.0/84.9; v:v:v at 293 K.

5 DFT calculations

Quantum mechanical calculations for MIL-160 alone and MIL-160 with adsorbed SO_2 were performed using density functional theory (DFT) and the Quantum-Espresso software.[17] The crystal structure of MIL-160 served as starting geometry. Oxygen atoms belonging to water were removed, and hydrogen atoms were added to saturate the furan linker and oxygen atoms forming OH-bridges. The structure was geometry-optimized using the Broyden-Fletcher-Goldfarb-Shanno (BFGS) scheme, ultrasoft Vanderbilt –type pseudoptentials and the generalized gradient approximation (GGA) with Perdew-Burke-Enzerhof (PBE) exchange correlation. To account for dispersion effects, the semi-empirical Grimme D2-correction scheme was applied.[18] Calculations were performed using the Monkhorst pack scheme with a 2 x 2 x 2 k-point mesh, an energy cutoff of 40 Rydberg and a charge cutoff of 400 Rydberg. After geometry optimization of the MIL-160 structure, SO_2 was placed at various locations and the geometries were allowed to fully relax. To compute the binding energy of SO_2, we optimized a single SO_2 molecule in an empty cell of the same size as the MIL-160 structure and under the same conditions stated before. The binding energy was then obtained as the difference between the sum of energies of MIL-160 and SO_2 and the energy of MIL-160 including the adsorbed SO_2 molecule.

6 Stability investigations

Experimental details: Before and after stability tests for dry and humid SO_2 exposure all MOFs were activated as described. For the dry exposure, a SO_2 isotherm was measured. For humid SO_2 exposure a controlled air flow of 2 L min^{-1} was bubbled through a sodium hydrogen sulfite solution (0.4 g $Na_2S_2O_5$ in 100 mL water) in a Schlenk round bottom flask to transport gaseous SO_2 into a humidity chamber (desiccator vessel). The desiccator was equipped with a crystallizing dish filled with saturated sodium chloride solution (80 mL, relative humidity (RH) 75%) and the sample (50 mg). The RH and the amount of SO_2 in the desiccator was monitored with a hygrometer (VWR TH300 hygrometer) and an SO_2-sensor (Dräger Pac 6000 electrochemical sensor), respectively. MIL-160 and NH_2-MIL-125(Ti) were exposed to a humid SO_2 environment at room temperature with 75 ± 6% RH and 35 ± 5 ppm SO_2 for 1 h and 5 h. The unit for humid SO_2 exposure is given by multiplying the concentration by the exposure time.

6.1 N_2-sorption isotherms before and after exposure to dry and humid SO_2

N_2-sorption isotherms were measured on an *Autosorb 6* (QUANTACHROME, Odelzhausen, Germany) instrument at 77 K within a pressure range of $1 \cdot 10^{-2}$-1 bar. Before each experiment samples were activated for at least 3 hours and at a minimum of 373 K under vacuum $<-5 \cdot 10^{-3}$ mbar.

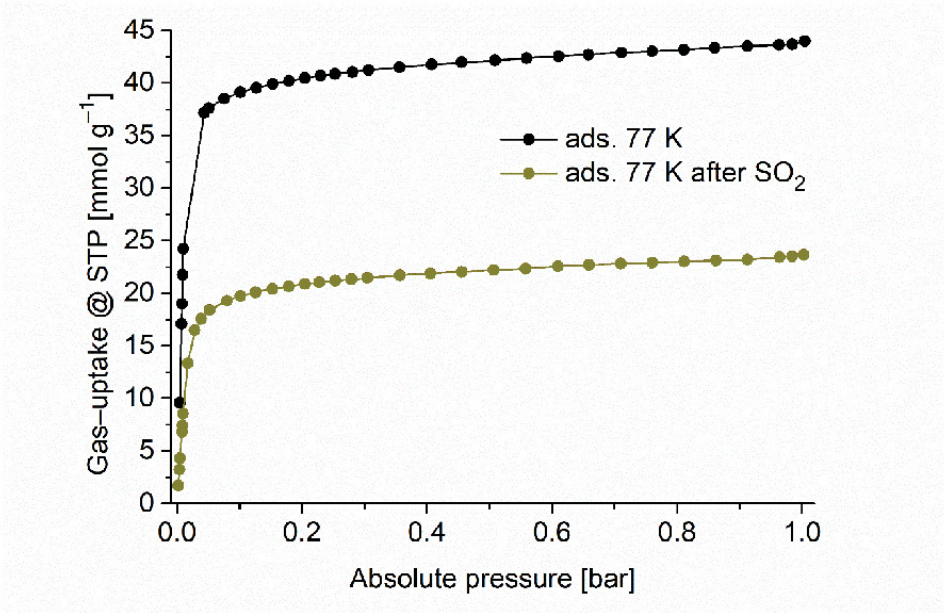

Figure S18. N_2-adsorption isotherms (77 K) of MOF-177 before and after exposure to dry or humid SO_2.

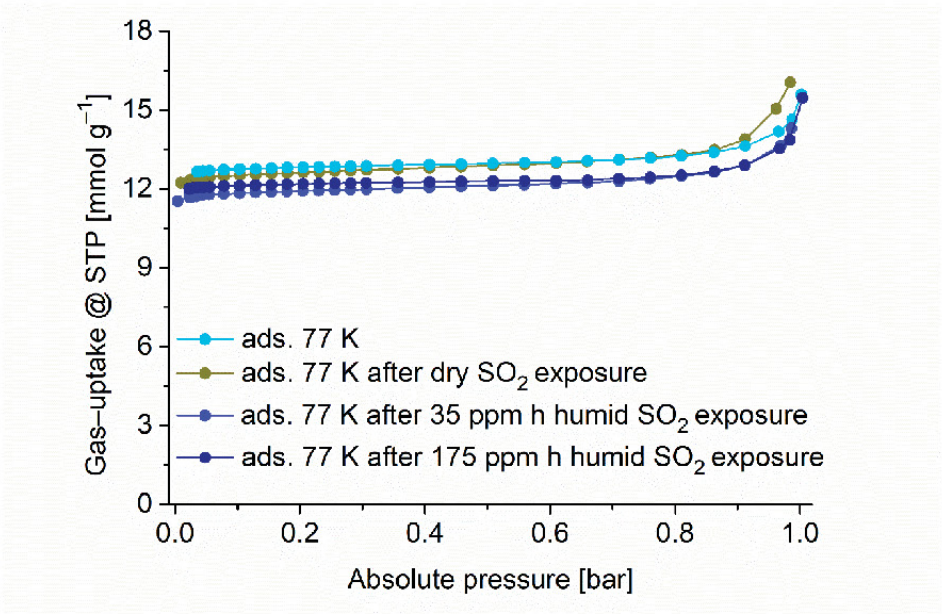

Figure S19. N_2-adsorption isotherms (77 K) of MIL-160 before and after exposure to dry or humid SO_2.

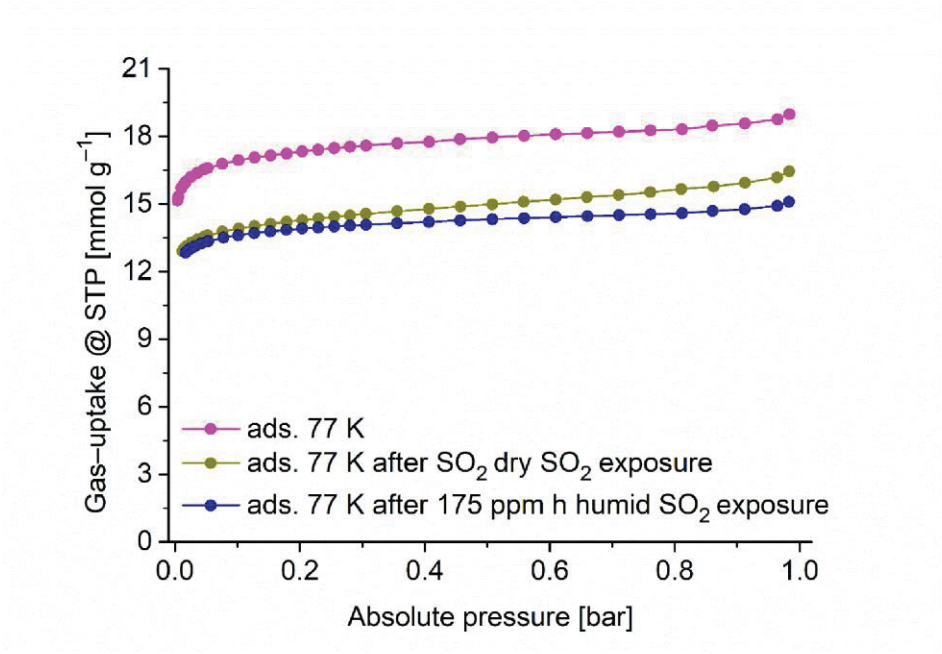

Figure S20. N_2-adsorption isotherms (77 K) of NH_2-MIL-125(Ti) before and after exposure to dry or humid SO_2.

6.2 SO_2-sorption cycling

Between each individual sorption experiment the samples were activated under same conditions.

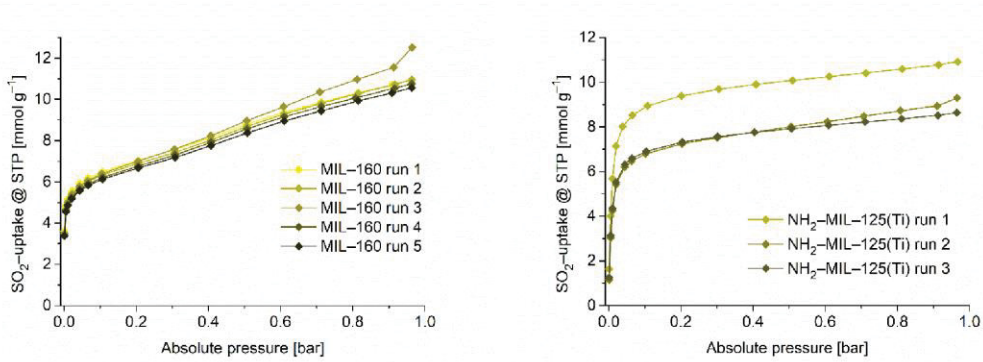

Figure S21. SO_2-sorption recycling of MIL-160 (left) and NH_2-MIL-125(Ti) (right) at 273 K.

Beginning at the third measurement of five cycles for MIL-160 a slightly higher SO_2-uptake was observed due to measurement inaccuracies. The more so as the samples had to be regenerated by heating to 373 K under vacuum and not by pressure-swing desorption due to the noted instrument time-limitations for SO_2 sorption (see Section 2 in Supporting Information).

6.3 PXRD

Powder X-ray diffraction (PXRD) measurements were performed on a Bruker *D2 Phaser* (300 W, 30 kV, 10 mA) at ambient temperatures. As radiation source a Cu-Kα-cathode (λ = 1.54182 Å) between 5° < 2Θ < 50° was used. Diffraction patterns were obtained using a silicon "low background" sample holder.

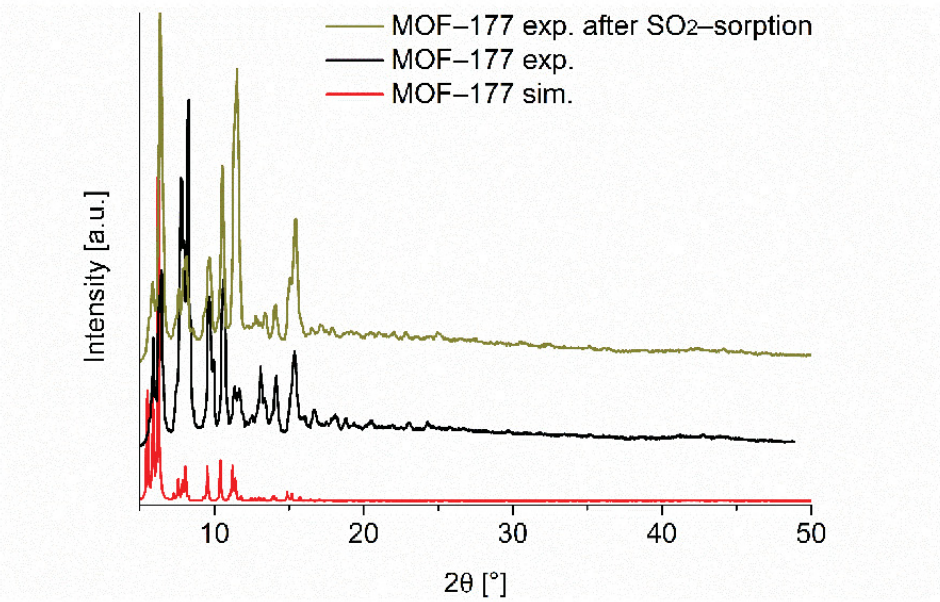

Figure S22. Comparison of PXRD patterns of MOF-177 (sim., based on crystal structure data, CCDC 230642, Reference 19).

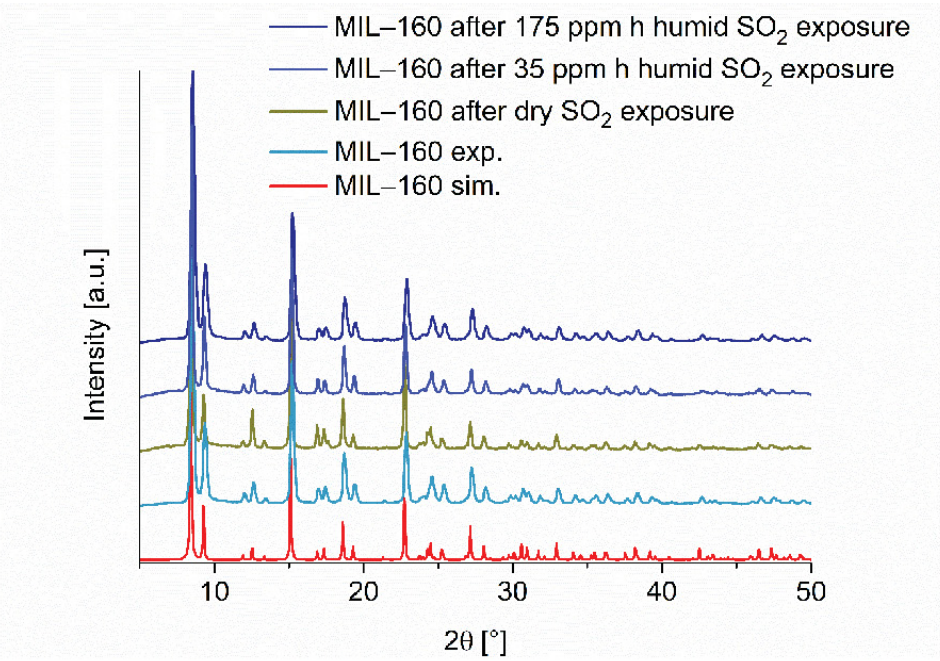

Figure S23. Comparison of PXRD patterns of MIL-160 (sim., based on x-ray data refinement, CCDC 1828694, Reference 9).

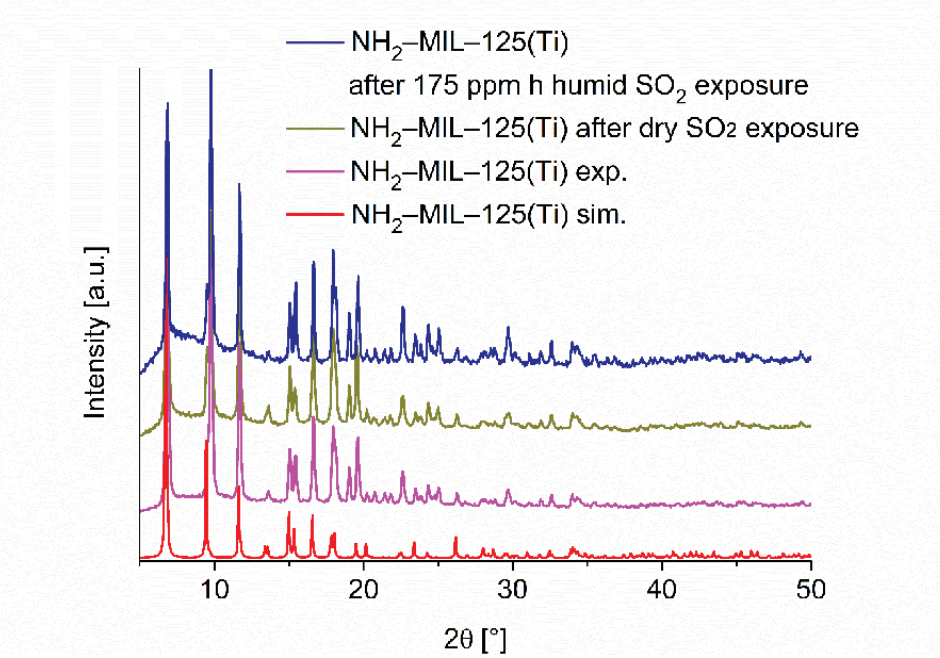

Figure S24. Comparison of PXRD patterns of NH_2-MIL-125(Ti) (sim., based on x-ray data refinement, CCDC 948966, Reference 20).

Table S4. Summary of stability tests for MOF-177, NH_2-MIL-125(Ti) and MIL-160.

Material	BET [m^2 g^{-1}]	BET after dry SO_2 [m^2 g^{-1}]	BET after humid SO_2 (35 ppm h at 75% RH) [m^2 g^{-1}]	BET after humid SO_2 (175 ppm h at 75% RH) [m^2 g^{-1}]	max. relative SO_2-uptake of multiple runs at 0.2 bar, with first run set to 100%	PXRD after SO_2-exposure
MOF-177	4100	2270	-	-	no multiple runs	changed
NH_2-MIL-125(Ti)	1560	1270	-	1250	100%, 77.7%, 77.9%	unchanged
MIL-160	1170	1170	1120	1130	100%, 98.0%, 99.4%, 96.2%, 94.9%	unchanged

7 Comparison of SO_2 sorption materials with literature

Table S5. Comparison of SO_2-uptake and characteristics of different MOFs.

Material	SO_2-uptake [mmol g^{-1}]			Temp. [K]	BET [m^2 g^{-1}]	Total pore-volume [cm^3 g^{-1}]	Pore width [Å]	Lit.
	0.01 bar	0.1 bar	1 bar					
MOF-177	0.3	1.0	25.7	293	4100	1.51	10.6-11.8[21,22]	this work
NH_2-MIL-125(Ti)	3.0	7.9	10.8	293	1560	0.651	5-8[23]	this work
MIL-160	4.2	5.5	7.2	293	1170	0.460	5[2]	this work
MIL-125(Ti)	-	3[a]	9.8[a]	298	1527	-	-	24
NH_2-MIL-125(Ti)	-	5[a]	9.7[a]	298	1861	-	-	24
MFM-600	-	~3[a]	5.0	298	2281	-	-	25
MFM-601	-	~8[a]	12.3	298	3644	-	-	25
SIFSIX-1-Cu	3.43	8.74	11.01	298	-	-	-	26
SIFSIX-2-Cu-i	4.16	6.01	6.90	298	630	-	-	26
MFM-300(Al)	-	-	8.1, ~5[a]	273, 298	1370	0.375	-	27, 28
MFM-300(In)	-	-	8.28	298	1071	0.419	-	29
MFM-202a	-	3.0	10.2	298	2220	-	-	30
ELM-12	-	1.95	2.73	298	706	0.26	4.3-6.1	31
$[Zn_2(oxo\text{-}dihbac)_2(bipy)]$	-	-	10.9	293	47 / 275[c]	0.059/ 0.098[c]	4.5-6.5, 8	32
$Ni(bdc)(ted)_{0.5}$	-	4.54	9.97	298	1783	0.74	7.8	33
$Zn(bdc)(ted)_{0.5}$	-	-	4.41	298	1888	0.84	7.8	33
Mg-MOF-74	-	6.44	8.60	298	1206	-	-	33, 34
FMOF-2	-	-	2.2	298	378	-	-	35
$Co_3[Co(CN)_6]_2$	-	-	2.5	298	712	-	-	36
$Zn_3[Co(CN)_6]_2$	-	-	1.8	298	700	-	-	36
MOF-505	-	-	12.9[a]	298	2216	0.73	8.3, 10.1	37
Ni-DMOF-TM	-	-	4.8[a]	298	940	0.459	-	38

[a] taken from isotherm, [b] at 1.11 bar, [c] emerged from CO_2 isotherm data.

8 References

(1) Li, X.; Cheng, F.; Zhang, S.; Chen, J. Shape-Controlled Synthesis and Lithium-Storage Study of Metal-Organic Frameworks Zn_4O(1,3,5-benzenetribenzoate)$_2$. *J. Power Sources* **2006**, *160*, 542–547.

(2) Permyakova, A.; Skrylnyk, O.; Courbon, E.; Affram, M.; Wang, S.; Lee, U.-H.; Valekar, A. H.; Nouar, F.; Mouchaham, G.; Devic, T.; De Weireld, G.; Chang, J.-S.; Steunou, N.; Frère, M.; Serre, C. Synthesis Optimization, Shaping, and Heat Reallocation Evaluation of the Hydrophilic Metal-Organic Framework MIL-160(Al). *ChemSusChem* **2017**, *10*, 1419–1426.

(3) Sohail, M.; Yun, Y.-N.; Lee, E.; Kim, S. K.; Cho, K.; Kim, J.-N.; Kim, T. W.; Moon, J.-H.; Kim, H. Synthesis of Highly Crystalline NH_2-MIL-125 (Ti) with S-Shaped Water Isotherms for Adsorption Heat Transformation. *Cryst. Growth Des.* **2017**, *17*, 1208–1213.

(4) Brandenburg, K.; *Diamond 4.3.1, Crystal and Molecular Structure Visualization*, Crystal Impact - K. Brandenburg & H. Putz GbR: Bonn, 2009.

(5) Feng, Y.; Wang, T.; Li, Y.; Li, J.; Wu, J.; Wu, B.; Jiang, L.; Wang, C. Steering Metallofullerene Electron Spin in Porous Metal-Organic Framework. *J. Am. Chem. Soc.* **2015**, *137*, 15055-15060.

(6) Cadiau, A.; Lee, J. S.; Borges, D. D.; Fabry, P.; Devic, T.; Wharmby, M. T.; Martineau, C.; Foucher, D.; Taulelle, F.; Jun, C.-H.; Hwang, Y. K.; Stock, N.; De Lange, M. F.; Kapteijn, F.; Gascon, J.; Maurin, G.; Chang, J.-S.; Serre, C. Design of Hydrophilic Metal Organic Framework Water Adsorbents for Heat Reallocation. *Adv. Mater.* **2015**, *27*, 4775-4780.

(7) Reinsch, H.; van der Veen, M. A.; Gil, B.; Marszalek, B.; Verbiest, T.; de Vos, D.; Stock, N. Structures, Sorption Characteristics, and Nonlinear Optical Properties of a New Series of Highly Stable Aluminum MOFs. *Chem. Mater.* **2012**, *25*, 17-26.

(8) Fröhlich, D.; Pantatosaki, E.; Kolokathis, P. D.; Markey, K.; Reinsch, H.; Baumgartner, M.; van der Veen, M. A.; de Vos, D. E.; Stock, N.; Papadopoulos, G. K.; Henninger, S. K.; Janiak, C. Water Adsorption Behaviour of CAU-10-H: a Thorough Investigation of its Structure–Property Relationships. *J. Mater. Chem. A* **2016**, *4*, 11859-11869.

(9) Wahiduzzaman, M; Lenzen, D.; Maurin, G.; Stock, N.; Wharmby, M. T. Rietveld Refinement of MIL-160 and its Structural Flexibility Upon H_2O and N_2 Adsorption. *Eur. J. Inorg. Chem.* **2018**, 3626-3632.

(10) Permyakova, A.; Skrylnyk, O.; Courbon, E.; Affram, M.; Wang, S.; Lee, U.-H.; Valekar, A. H.; Nouar, F.; Mouchaham, G.; Devic, T.; De Weireld, G.; Chang, J.-S.; Steunou, N.;

Frère, M.; Serre, C. Synthesis Optimization, Shaping, and Heat Reallocation Evaluation of the Hydrophilic Metal-Organic Framework MIL-160(Al). *ChemSusChem* **2017**, *10*, 1419–1426.

(11) Borges, D. D.; Maurin, G.; Galvao, D. S. Design of Porous Metal-Organic Frameworks for Adsorption Driven Thermal Batteries. *MRS Adv.* **2017**, *2*, 519-524.

(12) Dan-Hardi, D.; Serre, C.; Frot, T.; Rozes, L.; Maurin, Sanchez, C.; Férey, G. A New Photoactive Crystalline Highly Porous Titanium(IV) Dicarboxylate. *J. Am. Chem. Soc.* **2009**, *131*, 10857-10859.

(13) 3P INSTRUMENTS, 3P sim, Version 1.1.0.7, *Simulation and Evaluation Tool for mixSorb*, 3P INSTRUMENTS 2018.

(14) Jeppu, G. P.; Clement, T. P.; A Modified Langmuir-Freundlich Isotherm Model for Simulating pH-Dependent Adsorption Effects. *J. Contam. Hydrol.* **2012**, *129-130*, 46-53.

(15) Turiel, E.; Perez-Conde, C.; Martin-Esteban, A. Assessment of the Cross-Reactivity and Binding Sites Characterisation of a Propazine-Imprinted Polymer Using the Langmuir-Freundlich Isotherm. *Analyst* **2003**, *128*, 137-141.

(16) OriginLab Corporation, OriginPro, Version 9.0.0G., OriginLab Corporation 1991-2012.

(17) Giannozzi, P.; Baroni, S.; Bonini, N.; Calandra, M.; Car, R.;Cavazzoni, C.; Ceresoli, D.; Chiarotti, G. L.; Cococcioni, M.; Dabo, I.; Dal Corso, A.; de Gironcoli, S.; Fabris, S.; Fratesi, G.; Gebauer, R.; Gerstmann, U.; Gougoussis, C.; Kokalj, A.; Lazzeri, M.; Martin-Samos, L.; Marzari, N.; Mauri, F.; Mazzarello, R.; Paolini, S.; Pasquarello, A.; Paulatto, L.; Sbraccia, C.; Scandolo, S.; Sclauzero, G.; Seitsonen, A. P.; Smogunov, A.; Umari, P.; Wentzcovitch, R. M. QUANTUM ESPRESSO: A Modular and Open-Source Software Project for Quantum Simulations of Materials. *J. Phys.: Condens. Matter* **2009**, *21*, 395502, 1-19.

(18) Grimme, S. Semiempirical GGA-Type Density Functional Constructed with a Long-Range Dispersion Correction. *J. Comput. Chem.* **2006**, *27*, 1787–1799.

(19) Chae, H. K.; Siberio-Pérez, D. Y.; Kim, J.; Go, Y.; Eddaoudi, M.; Matzger, A. J.; O´Keeffe, M. Yaghi, O. M. A Route to High Surface Area, Porosity and Inclusion of Large Molecules in Crystals. *Nature* **2004**, *427*, 521–523.

(20) Smalley, A. P.; Reid, D. G.; Tan, J. C.; Lloyd, G. O. Alternative Synthetic Methodology for Amide Formation in the Post-Synthetic Modification of Ti-MIL125-NH_2. *CrystEngComm* **2013**, *15*, 9368-9371.

(21) Saha, D.; Deng, S. Hydrogen Adsorption on Metal-Organic Framework MOF-177. *Tsinghua Sci. Technol.* **2010**, *15*, 363–376.

(22) Peterson, G. W.; Mahle, J.; Balboa, A.; Wagner, G.; Sewell, T.; Karwacki, C. J. Defense Technical Information Center: Fort Belvoir, VA, 2008.

(23) Fan, Y.-H.; Zhang, S.-W.; Qin, S.-B.; Li, X.-S.; Qi, S.-H. An Enhanced Adsorption of Organic Dyes onto NH_2 Functionalization Titanium-Based Metal-Organic Frameworks and the Mechanism Investigation. *Microporous Mesoporous Mater.* **2018**, *263*, 120–127.

(24) Mounfield, W. P.; Han, C.; Pang, S. H.; Tumuluri, U.; Jiao, Y.; Bhattacharyya, S.; Dutzer, M. R.; Nair, S.; Wu, Z.; Lively, R. P.; Sholl, D. S.; Walton, K. S. Synergistic Effects of Water and SO_2 on Degradation of MIL-125 in the Presence of Acid Gases. *J. Phys. Chem. C* **2016**, *120*, 27230–27240.

(25) Carter, J. H.; Han, X.; Moreau, F. Y.; da Silva, I.; Nevin, A.; Godfrey, H. G. W.; Tang, C. C.; Yang, S.; Schröder, M. Exceptional Adsorption and Binding of Sulfur Dioxide in a Robust Zirconium-Based Metal-Organic Framework. *J. Am. Chem. Soc.* **2018**, *140*, 15564-15567.

(26) Cui, X.; Yang, Q.; Yang, L.; Krishna, R.; Zhang, Z.; Bao, Z.; Wu, H.; Ren, Q.; Zhou, W.; Chen, B.; Xing, H. Ultrahigh and Selective SO_2 Uptake in Inorganic Anion-Pillared Hybrid Porous Materials. *Adv. Mater.* **2017**, *29*, 1606929.

(27) Yang, S.; Sun, J.; Ramirez-Cuesta, A. J.; Callear, S. K.; David, W. I. F.; Anderson, D. P.; Newby, R.; Blake, A. J.; Parker, J. E.; Tang, C. C.; Schröder, M. Selectivity and Direct Visualization of Carbon Dioxide and Sulfur Dioxide in a Decorated Porous Host. *Nat. Chem.* **2012**, *4*, 887–894.

(28) Han, X.; Godfrey, H. G. W.; Briggs, L.; Davies, A. J.; Cheng, Y.; Daemen, L. L.; Sheveleva, A. M.; Tuna, F.; McInnes, E. J. L.; Sun, J.;Drathen, C.; George, M. W.; Ramirez-Cuesta, A. J.; Thomas, K. M.; Yang, S.; Schröder, M. Reversible Adsorption of Nitrogen Dioxide Within a Robust Porous Metal-Organic Framework. *Nat. Mater.* **2018**, *17*, 691–696.

(29) Savage, M.; Cheng, Y.; Easun, T. L.; Eyley, J. E.; Argent, S. P.; Warren, M. R.; Lewis, W.; Murray, C.; Tang, C. C.; Frogley, M. D.; Cinque, G.; Sun, J.; Rudić, S.; Murden, R. T.; Benham, M. J.; Fitch, A. N.; Blake, A. J.; Ramirez-Cuesta, A. J.; Yang, S.; Schröder, M. Selective Adsorption of Sulfur Dioxide in a Robust Metal-Organic Framework Material. *Adv. Mater.* **2016**, *28*, 8705–8711.

(30) Yang, S.; Liu, L.; Sun, J.; Thomas, K. M.; Davies, A. J.; George, M. W.; Blake, A. J.; Hill, A. H.; Fitch, A. N.; Tang, C. C.; Schröder, M. Irreversible Network Transformation in a Dynamic Porous Host Catalyzed by Sulfur Dioxide. *J. Am. Chem. Soc.* **2013**, *135*, 4954–4957.

(31) Zhang, Y.; Zhang, P.; Yu, W.; Zhang, J.; Huang, J.; Wang, J.; Xu, M.; Deng, Q.; Zeng, Z.; Deng, S. Highly Selective and Reversible Sulfur Dioxide Adsorption on a Microporous Metal-Organic Framework via Polar Sites. *ACS Appl. Mater. Interfaces* **2019**, DOI: 10.1021/acsami.9b01423.

(32) Glomb, S.; Woschko, D.; Makhloufi, G.; Janiak, C. Metal-Organic Frameworks with Internal Urea-Functionalized Dicarboxylate Linkers for SO_2 and NH_3 Adsorption. *ACS Appl. Mater. Interfaces* **2017**, *9*, 37419–37434.

(33) Tan, K.; Canepa, P.; Gong, Q.; Liu, J.; Johnson, D. H.; Dyevoich, A.; Thallapally, P. K.; Thonhauser, T.; Li, J.; Chabal, Y. J. Mechanism of Preferential Adsorption of SO_2 into Two Microporous Paddle Wheel Frameworks M(bdc)(ted)$_{0.5}$. *Chem. Mater.* **2013**, *25*, 4653–4662.

(34) Grant Glover, T.; Peterson, G. W.; Schindler, B. J.; Britt, D.; Yaghi, O. M. MOF-74 Building Unit has a Direct Impact on Toxic Gas Adsorption. *Chem. Eng. Sci.* **2011**, *66*, 163–170.

(35) Fernandez, C. A.; Thallapally, P. K.; Motkuri, R. K.; Nune, S. K.; Sumrak, J. C.; Tian, J.; Liu, J. Gas-Induced Expansion and Contraction of a Fluorinated Metal−Organic Framework. *Cryst. Growth Des.* **2010**, *10*, 1037–1039.

(36) Thallapally, P. K.; Motkuri, R. K.; Fernandez, C. A.; McGrail, B. P.; Behrooz, G. S. Prussian Blue Analogues for CO_2 and SO_2 Capture and Separation Applications. *Inorg. Chem.* **2010**, *49*, 4909–4915.

(37) Song, X.-D.; Wang, S.; Hao, C.; Qiu, J.-S. Investigation of SO_2 Gas Adsorption in Metal–Organic Frameworks by Molecular Simulation. *Inorg. Chem. Commun.* **2014**, *46*, 277–281.

(38) Hungerford, J.; Bhattacharyya, S.; Tumuluri, U.; Nair, S.; Wu, Z.; Walton, K. S. DMOF-1 as a Representative MOF for SO_2 Adsorption in Both Humid and Dry Conditions. *J. Phys. Chem. C* **2018**, *122*, 23493-23500.

3.4 A chemically stable cucurbit[6]uril-based hydrogen-bonded organic framework for potential SO_2/CO_2 separation

Jun Liang, Shang Hua Xing, Philipp Brandt, Alexander Nuhnen, Carsten Schlüsener, Yangyang Sun, Christoph Janiak

J. Mater. Chem. A **2020**, *38*, 19799–19804.

DOI: 10.1039/d0ta07457h, Referenz [155]

In dieser Publikation wird die käfigbasierte wasserstoffbrückengebundene organische Gerüstverbindung (engl. *hydrogen-bonded organic framework*, HOF) Cucurbit[6]uril (CB6), bezogen auf dessen selektive SO_2-Adsorption für die potenzielle Anwendung als Adsorbens in der Rauchgasentschwefelung, untersucht.

CB6 weist mit seiner fassartigen Form zwei Typen von Porenfenstern (5,8 und 3,9 Å) auf und kann der neuen Materialklasse der porösen organischen Käfige (engl. *porous organic cages* POCs) zugeordnet werden. POCs weisen intrinsische Poren innerhalb der Käfige auf. Neben diesen intrinsischen Poren entsteht durch Wasserstoffbrückenbindungen zwischen 6 benachbarter Käfige eine extrinsische wabenförmige Pore mit einem Durchmesser von 6 Å. Hierbei sind beide Porentypen für die Gasaufnahme von SO_2 zugänglich. Die intrinsische Pore bietet dabei Platz für zwei SO_2 Moleküle. Nanopartikuläres Cucurbit[6]uril (nanoCB6) zeigte mit einer Gasaufnahme von 4,98 mmol g^{-1} bei 293 K und einer SO_2/CO_2-IAST-Selektivitäten von 120 bei einer SO_2-Molfraktion von 0,1 einem Druck von 1 bar und ist damit ein vielversprechender Kandidat für eine potenzielle Anwendung der selektiven SO_2-Adsorption. Darüber hinaus konnte durch verschiedene Expositionsexperimente die strukturelle Stabilität sowie die Zyklierbarkeit von nanoCB6 verifiziert werden.

Anteile an der Veröffentlichung:

- Hilfestellung bei der der Aufnahme der Sorptionsisothermen und Berechnung der IAST-Selektivitäten.
- Die Entwicklung des Konzepts der Stabilitätsexperimente und Hilfestellung bei deren Durchführung.
- Durchsicht und Korrektur des Manuskripts als Co-Autor.
- Die Entwicklung des Konzepts und die maßgebliche Laborarbeit wurden von Herrn Dr. Jun Liang durchgeführt.

- Das Manuskript wurde von Herrn Dr. Jun Liang erstellt. Korrekturen erfolgten durch Prof. Dr. Christoph Janiak.
- Theoretische Berechnungen wurden von Frau Dr. Shang Hua Xing durchgeführt.
- Hilfestellung bei der Berechnung der Adsorptionsenthalpien durch Herrn Dr. Alexander Nuhnen.
- Aufnahme von Bildern mittels Rasterelektronenmikroskopie (REM) durch Herrn Dr. Carsten Schlüsener.
- Die Charakterisierung mittels Stickstoffsorption wurde von Frau Yangyang Sun durchgeführt.

3.5 Capture and Separation of SO_2 Traces in Metal-Organic Frameworks via Pre-synthetic Pore Environment Tailoring by Methyl Groups

Shang-Hua Xing, Jun Liang, Philipp Brandt, Felix Schäfer, Alexander Nuhnen, Tobias Heinen, István Boldog, Jens Möllmer, Marcus Lange, Oliver Weingart, Christoph Janiak

Angew. Chem. Int. Ed., **2021**, *60*, 2–10.

DOI: 10.1002/anie.202105229, Referenz [156]

In dieser Publikation wurde der Effekt des pre-syntetischen Zuschneidens der Porenumgebung (engl. *pre-synthetic pore environment tailor*, PPET) am Beispiel von 1,4-Diazabicyclo[2.2.2]octan-basierten DMOF-Derivaten in Bezug auf deren SO_2-Adsorptionseigenschaften untersucht.

Hierzu wurde der Benzoldicarboxylatligand des DMOFs durch den mono-, di- bzw. tetra-methylierten Liganden substituiert. Die Substitution von Wasserstoffmolekülen durch sterisch anspruchsvollere Methylgruppen führt zu einer graduellen Verkleinerung der Porendurchmesser von quadratischen (7,5 Å) und rechteckigen (6,9 × 5,3 Å) Kanälen zu schmaleren rechteckigen Kanälen (4,9 und 6.7 × 4,5 Å). Die damit verbundene Annäherung der Porengröße an den kinetischen Durchmesser von SO_2 (4,1 Å) führte auf der einen Seite zwar zu einer Abnahme der maximalen SO_2-Kapazität bei einem Druck von 1 bar, auf der anderen Seite konnte jedoch die Niedrigdruck-SO_2-Adsorption deutlich verbessert werden, was für die angestrebte Anwendung der Entfernung von SO_2 im ppm Bereich relevant ist. Zusätzlich konnte in Expositionsexperimenten gegenüber trockenem und feuchtem SO_2 gezeigt werden, dass die Methylierung des Benzoldicarboxylatliganden zu einer Steigerung der chemischen Stabilität des Netzwerkes führt.

Anteile an der Veröffentlichung:

- Hilfestellung bei der Aufnahme der Sorptionsisothermen.
- Die Entwicklung des Konzepts der Stabilitätsexperimente und Hilfestellung bei deren Durchführung.
- Beladung der Probenkristalle mit flüssigem SO_2 in dickwandigen Kapillaren für die Lokalisierung von SO_2 innerhalb der Poren mittels Pulverdiffraktometrie.
- Durchsicht und Korrektur des Manuskripts als Co-Autor.
- Die Entwicklung des Konzepts und die maßgebliche Laborarbeit wurden von Frau Dr. Shang-Hua Xing durchgeführt.

- Hilfestellungen bei der Bestimmung der Adsorptionsenthalpien, IAST-Selektivitäten und Auswertung der IR-Spektren durch Herrn Dr. Jun Liang.
- Rechnungen zu Dichtefunktionaltheorie wurden von Herrn Felix Schäfer und Herrn Dr. Oliver Weingart durchgeführt.
- Simulationen zu Durchbruchskurven wurden von Herrn Dr. Alexander Nuhnen durchgeführt.
- Durchbruchsexperimente und deren Auswertung wurden von Herrn Dr. Marcus Lange und Herrn Dr. Jens Möllmer durchgeführt.
- Die Kristallographischen Messungen wurden von Herrn Tobias Heinen durchgeführt.
- Rietveld-Verfeinerung und Hilfestellung bei den Strukturexperimenten durch Herrn Dr. István Boldog.

4 Zusammenfassung

Im Rahmen dieser Arbeit wurden Metall-organische Gerüstverbindungen (MOFs) und andere poröse Materialien in Bezug auf deren SO_2-Adsorptionseigenschaften hinsichtlich ihrer potenziellen Anwendung in der Rauchgasentschwefelung (engl. *flue gas desulfurization*, FGD) untersucht.

Nach Synthese und Charakterisierung der zu untersuchenden porösen Materialien wurden SO_2-Adsorptionsisothermen bei 293 K im Druckbereich zwischen 0,001 und 1 bar gemessen, um Aussagen über das Sorptionsverhalten der Materialien treffen zu können (Abb. 15).

Durch den Vergleich der individuellen Sorptionsverläufe konnten Isothermen-Charakteristika in Zusammenhang mit spezifischen Eigenschaften der porösen Materialien gebracht werden. Anschließend wurden etwaige Veränderungen von Materialeigenschaften der Proben wie Kristallinität und Porosität nach Exposition der Proben gegenüber trockenem und feuchtem SO_2 untersucht. Hierdurch konnten Rückschlüsse auf die Stabilität bzw. die potenzielle Zyklierbarkeit der Materialien gezogen werden, welche in der angestrebten Anwendung als regenerierbarer Adsorber für die FGD-Prozesse vorausgesetzt wird.

Weiter wurden SO_2/CO_2-IAST-Selektivitäten der Materialien aus entsprechenden Einzelgasisothermen bestimmt, um eine erste quantitative Einordnung des potenziellen Trennvermögens der Adsorber vornehmen zu können. Abschließend wurden für ausgewählte Netzwerke Adsorptionsenthalpien für SO_2 experimentell bestimmt und in Zusammenhang mit theoretischen Rechnungen der Dichtefunktionaltheorie (DFT) für präferierte Bindungsstellen und Bindungsenergien von SO_2 innerhalb der Gerüste diskutiert.

Durch die Analyse der SO_2-Sorptionsisothermen einer Vielzahl von diversen porösen Materialien, war es möglich, Rückschlüsse auf Einflussfaktoren für die SO_2-Sorption zu ziehen. Darunter fallen unteranderem die Porenstruktur, sowie das Vorkommen von Funktionellen Gruppen innerhalb der *secondary building unit* (SBU) oder des Liganden. Die hieraus abgeleiteten Einflussfaktoren können in Zukunft die Auswahl und das Design neuer Materialien erheblich vereinfachen.

Mehrstufige SO_2-Adsorptionsisothermen deuteten beispielsweise auf eine ausgeprägte bimodale Porenverteilung (MOF-808 und DUT-67(Zr), einen „Atmungseffekt“ in hoch-flexiblen MOFs (NH_2-MIL-53(Al) und MIL-53(Al)) oder einem „*gate-opening*“-Effekt bei rotierenden Liganden (ZIF-8 und ZIF-67) hin.

Weiter zeigt die Auftragung der SO_2-Gasaufnahme bei 293 K und 1 bar gegen die zugängliche Oberfläche der untersuchten Materialien einen annähernd linearen Verlauf (Abb. 16). Diese Beobachtung deutet darauf hin, dass die SO_2-Kapazität von vorwiegend mikroporösen Materialien, nahe den Standardbedingungen, maßgeblich von der Oberfläche der Materialien abhängig ist. Weitergehende Materialcharakteristika wie Struktur und etwaige Porenmodifikationen spielen bei diesen Bedingungen hingegen nur eine untergeordnete Rolle. Aufgrund des niedrigen Anteils an SO_2 in Rauchgasen ist die SO_2-Aufnahmekapazität bei Normaldruck für eine potenzielle Anwendung in FGD-Prozessen jedoch von niedriger Relevanz. Die SO_2-Gasadsorption im Niederdruckbereich ($\leq$ 0,1 bar) beeinflusst maßgeblich die Selektivität eines Adsorbers und ist daher für die Abtrennung von kleinen Molekülfraktionen SO_2 aus Rauchgasmischungen von großer Bedeutung.

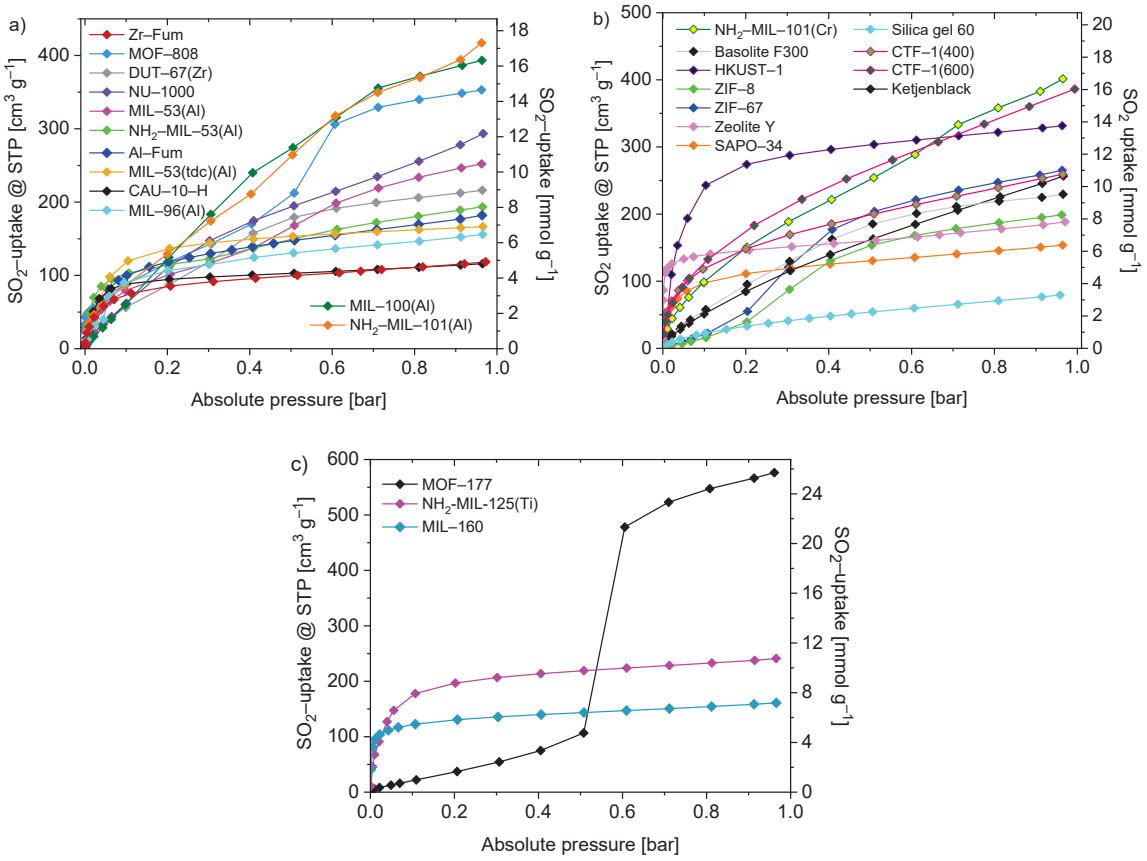

Abb. 15: SO_2-Adsorptionsisothermen (293 K) der untersuchten Materialien. SO_2-Desorptionsisothermen wurden aus Gründen der Übersichtlichkeit nicht dargestellt. a) MOFs publiziert in 3.1, b) MOFs und weiter poröse Materialien publiziert in 3.2, c) MOFs publiziert in 3.3.

In Abb. 17 wird ersichtlich, dass die Korrelation zwischen SO_2-Aufnahme und Oberfläche bei niedrigeren Druckpunkten nicht mehr beobachtet wird. Stattdessen kann ein Zusammenhang

zwischen dem kleinsten Porendurchmesser und der Niedrickdruck-SO_2-Adsorption (0,1 und 0,01 bar) beobachtet werden (Abb. 20). Hierbei zeigten untersuchte Materialien mit kleinem Porendurchmesser im Bereich zwischen 4 – 8 Å ein lokales Maximum der Oberflächennormierten-SO_2-Adsorption. Diese Beobachtung ist durch den kinetischen Durchmesser von SO_2 (4,1 Å) zu erklären, bei dem die an das Gastmolekül angepasste Porengröße zu erhöhten Adsorbat-Adsorbens-Wechselwirkungen führen.

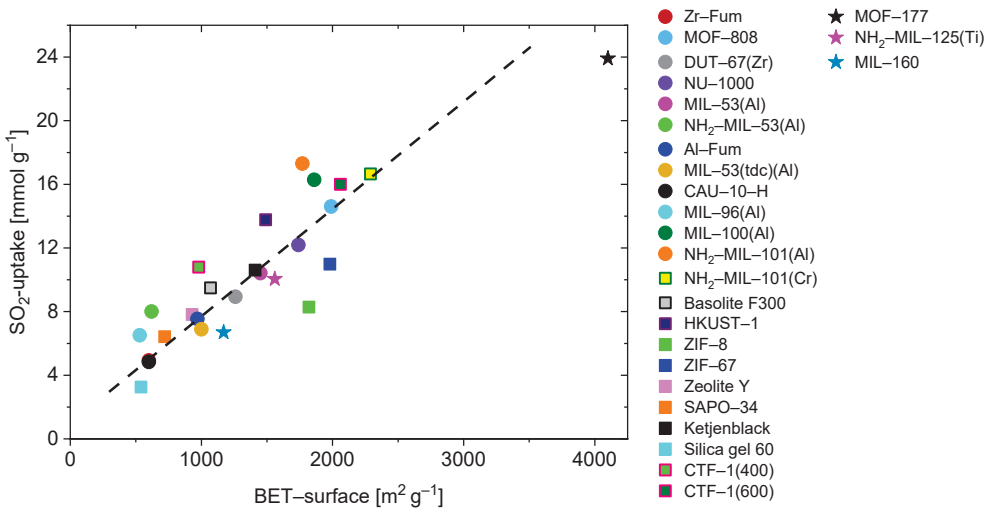

Abb. 16: SO_2-Aufnahme (293 K und 1 bar) versus BET-Oberfläche (bestimmt mittels N_2-Sorption bei 77 K). Die gestrichelte Linie dient als Orientierungshilfe für das Auge. MOFs publiziert in 3.1 (Kreise), MOFs und weiter poröse Materialien publiziert in 3.2 (Quadrate) und MOFs publiziert in 3.3. (Sterne).

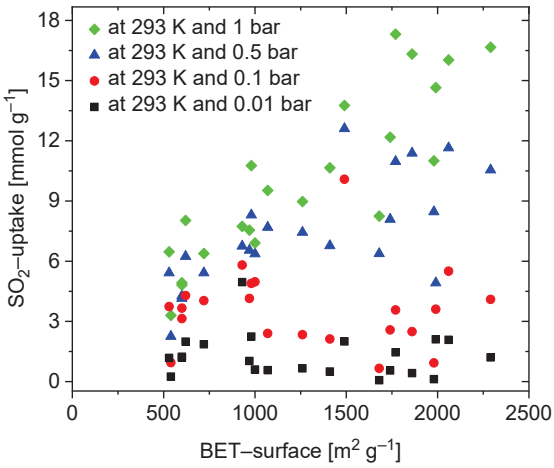

Abb. 17: SO_2-Aufnahme (293 K) bei einem Druck von 1 bar (grüne Rauten); 0,5 bar (blaue Dreiecke); 0,1 bar (rote Kreise) und 0,01 bar (schwarze Quadrate) versus BET-Oberfläche (bestimmt mittels N_2-Sorption bei 77 K).

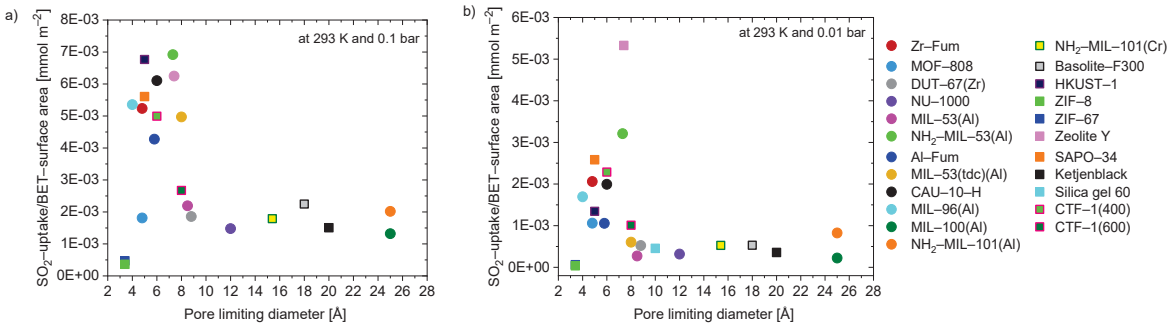

Abb. 18: Oberflächen-spezifische SO_2-Aufnahme (i. e., die Gasaufnahme normiert auf die BET-Oberfläche) bei a) 0,1 bar und b) bei 0,01 bar aufgetragen gegen den porenlimitierenden Durchmesser. MOFs publiziert in 3.1 (Kreise), MOFs und weiter poröse Materialien publiziert in 3.2 (Quadrate).

Die Auswertung der Stabilitätstests zeigte, dass die Kristallinität der Netzwerke weitestgehend erhalten bleibt (Abb. 19), wohingegen teilweise deutliche Verringerungen in den bestimmten BET-Oberflächen beobachtet wurden (Abb. 20). Insbesondere unter feuchten Bedingungen konnte bei vielen der untersuchten Materialien eine signifikante Abnahme ihrer Porosität festgestellt werden. Die verringerte Porosität nach den Expositionsexperimenten kann verschiedene Erklärungen haben. Einerseits ist es möglich, dass im Falle von besonders starken Wechselwirkungen SO_2 irreversibel in den Poren gebunden wird (Chemisorption). Andererseits kann beispielsweise die Bildung von schwefliger Säure (H_2SO_3) oder Hydrogensulfit (HSO_3^-) zu einer Verstopfung der Porenöffnungen führen oder, durch Bruch der Metall-Ligand Bindung, unter Formung von Metall-sulfit und dem protonierten Liganden eine partielle Degradierung der Netzwerkstruktur bewirken. Auch konnte beobachtet werden, dass MOFs mit aminofunktionalisiertem Liganden im Vergleich zu ähnlichen unfunktionalisierten MOFs schlechtere Ergebnisse bei der Auswertung der Stabilitätstests erzielten.

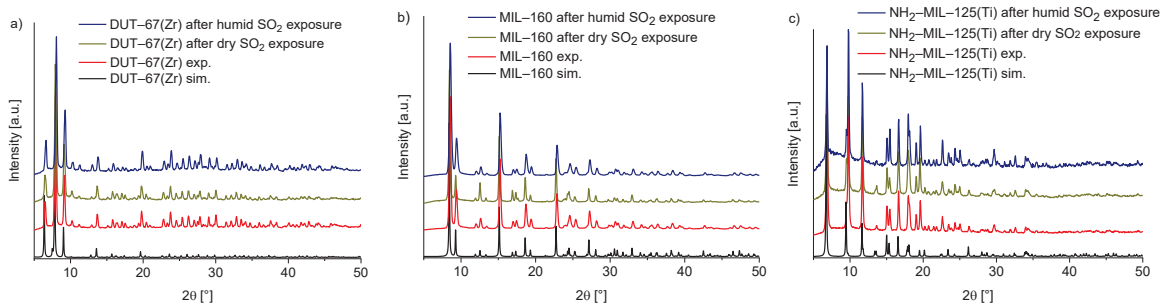

Abb. 19: Pulverdiffraktogramme der untersuchten MOFs: a) DUT-67(Zr), b) MIL-160 und c) NH_2-MIL-125(Ti); simuliert (schwarz), experimentell (rot), nach trockener SO_2-Exposition (gelb) und nach feuchter SO_2-Exposition (blau).

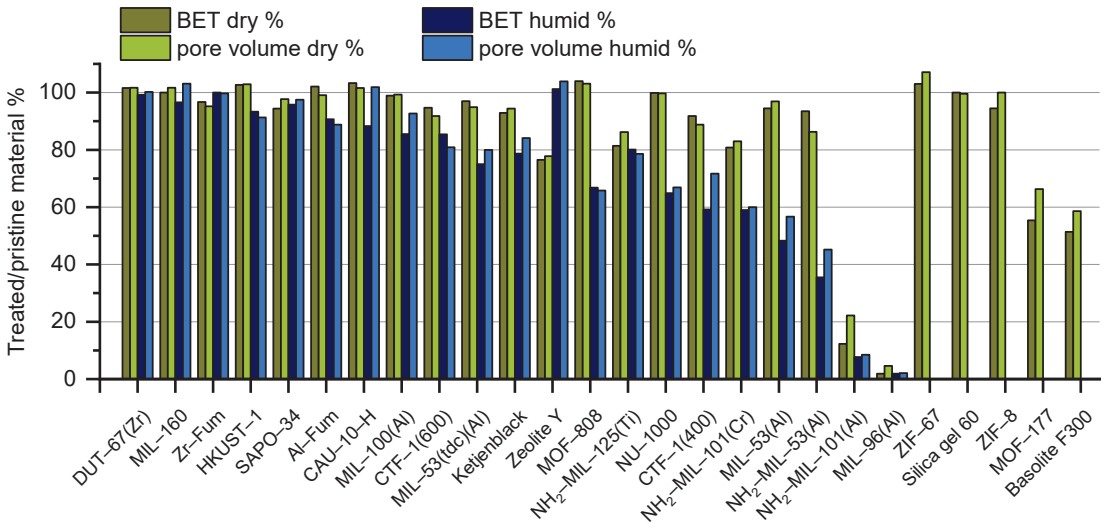

Abb. 20: Relative (behandelte/ursprüngliche) BET-Oberfläche und totales Porenvolumen der untersuchten porösen Materialien nach trockener und feuchter SO_2-Exposition.

Die Ergebnisse der berechneten SO_2/CO_2-Selektivitäten entsprechend der *ideal adsorbed solution theory* (IAST) (Abb. 21) zeigen, dass viele der untersuchten MOFs potenziell dazu fähig sein sollten, SO_2 aus Gasmischungen mit einem vielfach höheren CO_2-Anteil unter Standardbedingungen selektiv zu adsorbieren. Die besten Ergebnisse bei niedrigen Molfraktionen (0,1 SO_2 bzw. einem Verhältnis von 10/90; v:v; SO_2/CO_2) zeigten Zeolith Y (180) und das Al-MOF MIL-160 (127), was im bzw. über dem Bereich von Benchmark-Materialien wie MFM-305 (135), SIFSIX-1-Cu-i (87) und MFM-300(In) (70) liegt.

Es zeigte sich, dass stickstoffhaltige Netzwerke wie CTFs und aminofunktionalisierte MOFs bei 10/90 SO_2/CO_2-Gasmischungen ebenfalls gute Ergebnisse mit SO_2/CO_2-IAST-Selektivitäten zwischen 30 und 58 erzielten, während vorwiegend mesoporöse Materialien wie Ketjenblack und Silicagel mit Werten von 10 und 7 die niedrigsten SO_2/CO_2-IAST-Selektivitäten zeigten.

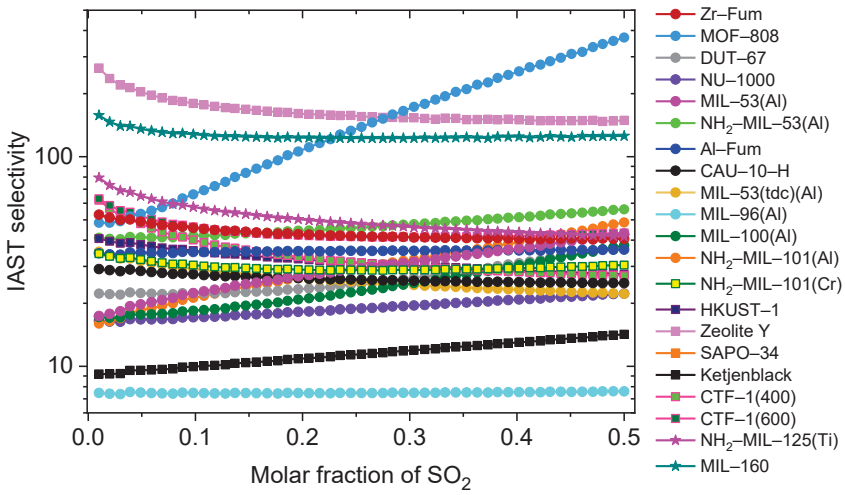

Abb. 21: SO_2/CO_2-IAST-Selektivität in Abhängigkeit zur Molfraktion SO_2 im Bereich zwischen 0,01 – 0,5 (293 K und 1 bar). MOFs publiziert in 3.1 (Kreise), MOFs und weiter poröse Materialien publiziert in 3.2 (Quadrate) und MOFs publiziert in 3.3 (Sterne).

Weiter wurden für ausgewählte MOFs isosterische Adsorptionsenthalpien (ΔH_{ads}) für SO_2 aus Datensätzen zweier Adsorptionsisothermen mit $\Delta T \leq 20$ K mittels Virial-Analyse bestimmt (Abb. 22). Die isosterische Adsorptionsenthalpie nahe einer Beladung von Null (ΔH^0_{ads}) beschreibt die stärksten Wechselwirkungen des Gastmoleküls in einem Netzwerk und lag nahe den theoretisch berechneten Bindungsenergien. Durch diese Übereinstimmung konnten die, mit DFT-Methoden ermittelten, präferierte Bindungsstellen weiter verifiziert werden und lieferten damit einen Beitrag zur Aufklärung des Adsorptionsgeschehens in den untersuchten Netzwerken. Die beiden MOFs, NH_2-MIL-53(Al) und NH_2-MIL-125(Ti) zeigten mit ΔH^0_{ads}-Werten von –67 und –53 kJ·mol^{-1} die stärksten Wechselwirkungen, welche durch die Polarisierbarkeit der Aminofunktionen erklärt werden können. Die beiden Al-basierten MOFs Al-Fum und MIL-160 zeigten ΔH^0_{ads}-Werte von jeweils –42 kJ·mol^{-1}. Die schwächere Physisorption der Al-MOFs kann dabei vorteilhaft für eine energieeffiziente und vollständige Regeneration der Adsorptionsmaterialien sein.

Weiter wurden in allen MOFs, für welche Bindungsstellen mittels DFT berechnet wurden, Wechselwirkungen zwischen den μ/μ_3-OH-Gruppen der Al/Zr-MOFs und SO_2 (MOF-OH$^{\delta+}$...$^{\delta-}$O=S=O) gefunden, was auf eine zentrale Rolle von Wasserstoffbrückenbindungen bei der SO_2-Sorption in MOFs hindeutet.

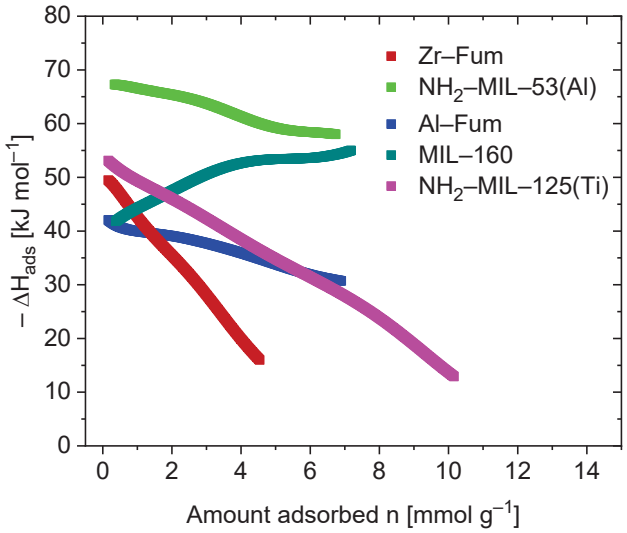

Abb. 22: Isosterische Adsorptionsenthalpie von SO_2 zu untersuchten MOFs, bestimmt mittels Virial-Analyse, angewandt auf Datenpunkte von SO_2-Adsorptionsisothermen, gemessen bei zwei unterschiedlichen Temperaturen zwischen 273 und 303 K ($\Delta T \leq 20$ K).

Ein weiteres hervorzuhebendes Ergebnis dieser Arbeit war die Rekord SO_2-Aufnahme (25,7 mmol g^{-1}, bei 293 K und 1 bar) für das hoch poröse Netzwerk MOF-177, welches jedoch wegen der geringen Gasaufnahme bei Drücken ≤ 0,5 bar und einer unzureichenden Stabilität als ungeeignet für die FGD bewertet wurde. Das Al-MOF MIL-160 zeigte hingegen trotz seiner geringeren SO_2-Kapazität (7,2 mmol g^{-1}, bei 293 K und 1 bar) ein hohes Potenzial für die Entfernung von SO_2 aus Rauchgasmischungen, da es sowohl in Selektivität, Stabilität, als auch unter anwendungsorientierten Bedingungen (T=353 K) in Durchbruchsexperimenten gute Ergebnisse erzielen konnte.

Diese Eigenschaften, in Zusammenhang mit einer kostengünstigen, umweltfreundlichen und skalierbaren Synthese, machen MIL-160 zu einem vielversprechenden Kandidaten für den potenziellen Einsatz in der adsorptionsbasierten Rauchgasentschwefelung.

5 Literaturverzeichnis

[1] H.-C. J. Zhou and S. Kitagawa, Metal-organic frameworks (MOFs). *Chem. Soc. Rev.* **2014**, *43*, 5415–5418.

[2] O. M. Yaghi, M. J Kalmutzki, C. S. Diercks, *Introduction to reticular chemistry. Metal-organic frameworks and covalent organic frameworks.* Wiley-VCH, Weinheim **2019**.

[3] S. Kaskel, *The chemistry of metal-organic frameworks: Synthesis, characterization, and applications*, Wiley-VCH, Weinheim **2016**.

[4] B. F. Hoskins, R. Robson, Infinite polymeric frameworks consisting of three dimensionally linked rod-like segments. *J. Am. Chem. Soc.* **1989**, *111*, 5962–5964.

[5] B. F. Hoskins, R. Robson, Design and construction of a new class of scaffolding-like materials comprising infinite polymeric frameworks of 3D-linked molecular rods. A reappraisal of the zinc cyanide and cadmium cyanide structures and the synthesis and structure of the diamond-related frameworks $[N(CH_3)_4][Cu^{I}Zn^{II}(CN)_4]$ and Cu^{I}[4,4',4",4'"-tetracyanotetraphenylmethane]$BF_4.xC_6H_5NO_2$. *J. Am. Chem. Soc.* **1990**, *112*, 1546–1554.

[6] M. Eddaoudi, D. B. Moler, H. Li, B. Chen, T. M. Reineke, M. O'Keeffe, O. M. Yaghi, Modular chemistry: secondary building units as a basis for the design of highly porous and robust metal-organic carboxylate frameworks. *Acc. Chem. Res.* **2001**, *34*, 319–330.

[7] S. Wuttke, Introduction to Reticular Chemistry, *Metal–Organic Frameworks and Covalent Organic Frameworks.* Wiley-VCH, Weinheim **2019**.

[8] S. R. Batten, N. R. Champness, X.-M. Chen, J. Garcia-Martinez, S. Kitagawa, L. Öhrström, M. O'Keeffe, M. Paik Suh, J. Reedijk, Terminology of metal–organic frameworks and coordination polymers (IUPAC Recommendations 2013). *Pure Appl. Chem.* **2013**, *85*, 1715–1724.

[9] A. J. Howarth, Y. Liu, P. Li, Z. Li, T. C. Wang, J. T. Hupp, O. K. Farha, Chemical, thermal and mechanical stabilities of metal–organic frameworks. *Nat. Rev. Mater.* **2016**, *1*, 1–15.

[10] C. N. R. Rao, S. Natarajan, R. Vaidhyanathan, Metal carboxylates with open architectures. *Angew. Chem. Int. Ed.*, **2004**, *43*, 1466–1496.

[11] A. V. Desai, S. Sharma, S. Let, S. K. Ghosh, N-donor linker based metal-organic frameworks (MOFs): Advancement and prospects as functional materials. *Coord. Chem. Rev.* **2019**, *395*, 146–192.

[12] C. J. Rhodes, Properties and applications of zeolites. *Sci. Prog.* **2010**, *93*, 223–284.

[13] Y. Li, L. Li, J. Yu, Applications of Zeolites in Sustainable Chemistry. *Chem* **2017**, *3*, 928–949.

[14] L. F. Giraldo, B. L. López, L. Pérez, S. Urrego, L. Sierra, M. Mesa, Mesoporous Silica Applications. *Macromol. Symp.* **2007**, *258*, 129–141.

[15] S. M. Moosavi, A. Nandy, K. M. Jablonka, D. Ongari, J. P. Janet, P. G. Boyd, Y. Lee, B. Smit, H. J. Kulik, Understanding the diversity of the metal-organic framework ecosystem. *Nat. Commun.* **2020** *11*, 4068.

[16] P. Z. Moghadam, A. Li, S. B. Wiggin, A. Tao, A. G. P. Maloney, P. A. Wood, S. C. Ward, D. Fairen-Jimenez, Development of a Cambridge Structural Database Subset: A Collection of Metal–Organic Frameworks for Past, Present, and Future. *Chem. Mater.* **2017**, *29*, 2618–2625.

[17] M. Zhang, M. Bosch, T. Gentle III, H.-C. Zhou, Rational design of metal–organic frameworks with anticipated porosities and functionalities. *CrystEngComm* **2014**, *16*, 4069–4083.

[18] O. M. Yaghi, M. O'Keeffe, N. W. Ockwig, H. K. Chae, M. Eddaoudi, J. Kim, Reticular synthesis and the design of new materials. *Nature* **2003**, *423*, 705–714.

[19] L. Feng, S. Yuan, J.-S. Qin, Y. Wang, A. Kirchon, Di Qiu, L. Cheng, S. T. Madrahimov, H.-C. Zhou, Lattice Expansion and Contraction in Metal-Organic Frameworks by Sequential Linker Reinstallation. *Matter* **2019**, *1*, 156–167.

[20] M. Eddaoudi, J. Kim, N. Rosi, D. Vodak, J. Wachter, M. O´Keeffe, O. M. Yaghi, Systematic Design of Pore Size and Functionality in Isoreticular MOFs and Their Application in Methane Storage. *Science* **2002**, 295, 469–472.

[21] J. H. Cavka, S. Jakobsen, U. Olsbye, N. Guillou, C. Lamberti, S. Bordiga, K. P. Lillerud, A new zirconium inorganic building brick forming metal organic frameworks with exceptional stability. *J. Am. Chem. Soc.* **2008**, *130*, 13850–13851.

[22] K. P. Lillerud, U. Olsbye, M. Tilset, Designing Heterogeneous Catalysts by Incorporating Enzyme-Like Functionalities into MOFs. *Top. Catal.* **2010**, *53*, 859–868.

[23] E. Biemmi, S. Christian, N. Stock, T. Bein, High-throughput screening of synthesis parameters in the formation of the metal-organic frameworks MOF-5 and HKUST-1. *Microporous Mesoporous Mater.* **2009**, *117*, 111–117.

[24] R. S. Forgan, Modulated self-assembly of metal–organic frameworks. *Chem. Sci.* **2020**, *11*, 4546–4562.

[25] N. Stock and S. Biswas, Synthesis of metal-organic frameworks (MOFs): routes to various MOF topologies, morphologies, and composites. *Chem. Rev.* **2012**, *112*, 933–969.

[26] A. Rabenau, The Role of Hydrothermal Synthesis in Preparative Chemistry. *Angew. Chem. Int. Ed.* **1985**, *24*, 1026-1040.

[27] D. Fröhlich, E. Pantatosaki, P. D. Kolokathis, K. Markey, H. Reinsch, M. Baumgartner, M. A. van der Veen, D. E. de Vos, N. Stock, G. K. Papadopoulos, S. K. Henninger, C. Janiak, Water adsorption behaviour of CAU-10-H. *J. Mater. Chem. A*, **2016**, *4*, 11859–11869.

[28] S. H. Jhung, T. Jin, Y. K. Hwang, J.-S. Chang, Microwave effect in the fast synthesis of microporous materials: which stage between nucleation and crystal growth is accelerated by microwave irradiation? *Chem. Eur. J.* **2007**, *13*, 4410–4417.

[29] D. Chen, J. Zhao, P. Zhang, S. Dai, Mechanochemical synthesis of metal–organic frameworks. *Polyhedron* **2019**, 162, 59–64.

[30] A. P. Nelson, O. K. Farha, K. L. Mulfort, J. T. Hupp, Supercritical processing as a route to high internal surface areas and permanent microporosity in metal-organic framework materials. *J. Am. Chem. Soc.* **2009**, *132*, 458–460.

[31] W.-J. Son, J. Kim, J. Kim, W.-S. Ahn, Sonochemical synthesis of MOF-5. *Chem. Commun.* **2008**, *47*, 6336–6338.

[32] Z. Zhang and M. J. Zaworotko, Template-directed synthesis of metal-organic materials. *Chem. Soc. Rev.*, **2014**, *43*, 5444–5455.

[33] R. Seetharaj, P. V. Vandana, P. Arya, S. Mathew, Dependence of solvents, pH, molar ratio and temperature in tuning metal organic framework architecture. *Arabian J. Chem.* **2019**, *12*, 295–315.

[34] M. Guo and Z.-M. Sun, Solvents control over the degree of interpenetration in metal-organic frameworks and their high sensitivities for detecting nitrobenzene at ppm level. *J. Mater. Chem.* **2012**, *22*, 15939.

[35] R. Haldar, N. Sikdar, T. K. Maji, Interpenetration in coordination polymers: structural diversities toward porous functional materials. *Mater. Today*, **2015**, *18*, 97–116.

[36] Z. Fang, B. Bueken, D. E. de Vos, R. A. Fischer, Defect-Engineered Metal-Organic Frameworks. *Angew. Chem. Int. Ed.* **2015**, *54*, 7234–7254.

[37] C. A. Trickett, K. J. Gagnon, S. Lee, F. Gándara, H.-B. Bürgi, O. M. Yaghi, Definitive molecular level characterization of defects in UiO-66 crystals. *Angew. Chem. Int. Ed.* **2015**, *54*, 11162–11167.

[38] G. C. Shearer, S. Chavan, S. Bordiga, S. Svelle, U. Olsbye, K. P. Lillerud, Defect Engineering: Tuning the Porosity and Composition of the Metal–Organic Framework UiO-66 via Modulated Synthesis. *Chem. Mater.* **2016**, *28*, 3749–3761.

[39] F. Gándara, T. D. Bennett, Crystallography of metal-organic frameworks. *IUCrJ* **2014**, *1*, 563–570.

[40] S. M. Cohen, Postsynthetic methods for the functionalization of metal-organic frameworks. *Chem. Rev.* **2012**, *112*, 970–1000.

[41] F.-G. Xi, W. Sun, Z.-Y. Dong, N.-N. Yang, T. Gong, E.-Q. Gao, An in situ approach to functionalize metal-organic frameworks with tertiary aliphatic amino groups. *Chem. Commun.* **2020**, *56*, 13177–13180.

[42] S. Ali Akbar Razavi and A. Morsali, Linker functionalized metal-organic frameworks. *Coord. Chem. Rev.* **2019**, *399*, 213023.

[43] V. Bon, N. Kavoosi, I. Senkovska, P. Müller, J. Schaber, D. Wallacher, D. M. Többens, U. Mueller, S. Kaskel, Tuning the flexibility in MOFs by SBU functionalization. *Dalton Trans.* **2016**, *45*, 4407–4415.

[44] G. E. Cmarik, M. Kim, S. M. Cohen, K. S. Walton, Tuning the adsorption properties of UiO-66 via ligand functionalization. *Langmuir* **2012**, *28*, 15606–15613.

[45] A. U. Czaja, N. Trukhan, U. Müller, Industrial applications of metal-organic frameworks. *Chem. Soc. Rev.* **2009**, *38*, 1284–1293.

[46] A. J. Rieth, A. M. Wright, M. Dincă, Kinetic stability of metal–organic frameworks for corrosive and coordinating gas capture. *Nat. Rev. Mater.* **2019**, *4*, 708–725.

[47] M. Bosch, M. Zhang, H.-C. Zhou, Increasing the Stability of Metal-Organic Frameworks. *Adv. Chem.* **2014**, *2014*, 1–8.

[48] G. Mouchaham, S. Wang, C. Serre, The Stability of Metal-Organic Frameworks, *Metal-Organic Frameworks: Applications in Separations and Catalysis*; H. García, S. Navalon, Hrsg.; Wiley-VCH, Weinheim **2018**.

[49] J. T. Hughes, T. D. Bennett, A. K. Cheetham, A. Navrotsky, Thermochemistry of zeolitic imidazolate frameworks of varying porosity. *J. Am. Chem. Soc.* **2013**, *135*, 598–601.

[50] S. Han, Y. Huang, T. Watanabe, S. Nair, K. S. Walton, D. S. Sholl, J. Carson Meredith, MOF stability and gas adsorption as a function of exposure to water, humid air, SO_2, and NO_2. *Microporous Mesoporous Mater.* **2013**, *173*, 86–91.

[51] M. Ding, X. Cai, H.-L. Jiang, Improving MOF stability. *Chem. Sci.* **2019**, *10*, 10209–10230.

[52] N. Li, J. Xu, R. Feng, T.-L. Hu, X.-H. Bu, Governing metal-organic frameworks towards high stability. *Chem. Commun.* **2016**, *52*, 8501–8513.

[53] M. Eigen, Fast elementary steps in chemical reaction mechanisms. *Pure Appl. Chem.* **1963**, *6*, 97–116.

[54] D. T. Richens, Ligand substitution reactions at inorganic centers. *Chem. Rev.* **2005**, *105*, 1961–2002.

[55] L. Helm and A. E. Merbach, Inorganic and bioinorganic solvent exchange mechanisms. *Chem. Rev.* **2005**, *105*, 1923–1959.

[56] J. E. Mondloch, O. Karagiaridi, O. K. Farha, J. T. Hupp, Activation of metal–organic framework materials. *CrystEngComm* **2013**, *15*, 9258.

[57] A. P. Nelson, O. K. Farha, K. L. Mulfort, J. T. Hupp, Supercritical processing as a route to high internal surface areas and permanent microporosity in metal-organic framework materials. *J. Am. Chem. Soc.* **2009**, *131*, 458–460.

[58] H. Fan, C. Hartshorn, T. Buchheit, D. Tallant, R. Assink, R. Simpson, D. J. Kissel, D. J. Lacks, S. Torquato, C. J. Brinker, Modulus-density scaling behaviour and framework architecture of nanoporous self-assembled silicas. *Nat. Mater.* **2007**, *6*, 418–423.

[59] S. M. Moosavi, P. G. Boyd, L. Sarkisov, B. Smit, Improving the Mechanical Stability of Metal-Organic Frameworks Using Chemical Caryatids. *ACS Cent. Sci.* **2018**, *4*, 832–839.

[60] J. Lee, O. K. Farha, J. Roberts, K. A. Scheidt, S. T. Nguyen, J. T. Hupp, Metal-organic framework materials as catalysts. *Chem. Soc. Rev.* **2009**, *38*, 1450–1459.

[61] A. Dhakshinamoorthy, M. Alvaro, H. Garcia, Commercial metal-organic frameworks as heterogeneous catalysts. *Chem. Commun.* **2012**, *48*, 11275–11288.

[62] J. Liu, L. Chen, H. Cui, J. Zhang, L. Zhang, C.-Y. Su, Applications of metal-organic frameworks in heterogeneous supramolecular catalysis. *Chem. Soc. Rev.* **2014**, *43*, 6011–6061.

[63] L. E. Kreno, K. Leong, O. K. Farha, M. Allendorf, R. P. van Duyne, J. T. Hupp, Metal-organic framework materials as chemical sensors. *Chem. Rev.* **2012**, *112*, 1105–1125.

[64] H.-Y. Li, S.-N. Zhao, S.-Q. Zang, J. Li, Functional metal-organic frameworks as effective sensors of gases and volatile compounds. *Chem. Soc. Rev.* **2020** *49*, 6364–6401.

[65] Y. Cui, Y. Yue, G. Qian, B. Chen, Luminescent functional metal-organic frameworks. *Chem. Rev.* **2012**, *112*, 1126–1162.

[66] H. D. Lawson, S. P. Walton, C. Chan, Metal-Organic Frameworks for Drug Delivery: A Design Perspective. *ACS Appl. Mater. Interfaces* **2021**, *13*, 7004–7020.

[67] D.-W. Lim and H. Kitagawa, Proton Transport in Metal-Organic Frameworks. *Chem. Rev.* **2020**, *120*, 8416–8467.

[68] L. R. Mingabudinova, V. V. Vinogradov, V. A. Milichko, E. Hey-Hawkins, A. V. Vinogradov, Metal-organic frameworks as competitive materials for non-linear optics. *Chem. Soc. Rev.* **2016**, *45*, 5408–5431.

[69] J.-R. Li, R. J. Kuppler, H.-C. Zhou, Selective gas adsorption and separation in metal-organic frameworks. *Chem. Soc. Rev.* **2009**, *38*, 1477–1504.

[70] C. A. Trickett, A. Helal, B. A. Al-Maythalony, Z. H. Yamani, K. E. Cordova, O. M. Yaghi, The chemistry of metal–organic frameworks for CO_2 capture, regeneration and conversion. *Nat. Rev. Mater.* **2017**, *2*, 17045.

[71] M. P. Suh, H. J. Park; T. K. Prasad, D.-W. Lim, Hydrogen storage in metal-organic frameworks. *Chem. Rev.* **2012**, *112*, 782–835.

[72] Y. Peng, V. Krungleviciute, I. Eryazici, J. T. Hupp, O. K. Farha, T. Yildirim Methane storage in metal-organic frameworks: current records, surprise findings, and challenges. *J. Am. Chem. Soc.* **2013**, *135*, 11887–11894.

[73] He, Y.; Zhou, W.; Qian, G.; Chen, B. Methane storage in metal-organic frameworks. *Chem. Soc. Rev.* **2014**, *43*, 5657–5678.

[74] Li, J.-R.; Sculley, J.; Zhou, H.-C. Metal-organic frameworks for separations. *Chem. Rev.* **2012**, *112*, 869–932.

[75] R.-B. Lin, S. Xiang, W. Zhou, B. Chen, Microporous Metal-Organic Framework Materials for Gas Separation. *Chem* **2020**, *6*, 337–363.

[76] S. Chaemchuen, N. A. Kabir, K. Zhou, F. Verpoort, Metal-organic frameworks for upgrading biogas via CO_2 adsorption to biogas green energy. *Chem. Soc. Rev.* **2013**, *42*, 9304–9332.

[77] M. Wutz, H. Adam, W. Walcher, Sorption und Desorption, *Handbuch Vakuumtechnik: Theorie und Praxis*, Vieweg+Teubner Verlag, Wiesbaden **1997**.

[78] P. W. Atkins, J. de Paula, J. Keeler, in *Atkins' physical chemistry: Molecular thermodynamics and kinetics*, Oxford University Press, Oxford 2019.

[79] R. W. Baker, *Membrane technology and applications*, Wiley, Chichester **2012**.

[80] K. S. W. Sing, Reporting physisorption data for gas/solid systems with special reference to the determination of surface area and porosity (Recommendations 1984). *Pure Appl. Chem.* **1985**, *57*, 603–619.

[81] M. Thommes, K. Kaneko, A. V. Neimark, J. P. Olivier, F. Rodriguez-Reinoso, J. Rouquerol, K. S.W. Sing, Physisorption of gases, with special reference to the evaluation of surface area and pore size distribution (IUPAC Technical Report). *Pure Appl. Chem.* **2015**, *87*, 1051–1069.

[82] I. Langmuir, The Adsorption of Gases on Plane Surfaces of Glass, Mica and Platinum. *J. Am. Chem. Soc.* **1918**, *40*, 1361–1403.

[83] S. Brunauer, P. H. Emmett, E. Teller, Adsorption of Gases in Multimolecular Layers. *J. Am. Chem. Soc.* **1938**, *60*, 309–319.

[84] J. Rouquerol; P. Llewellyn, F. Rouquerol, Is the BET equation applicable to microporous adsorbents? *Stud. Surf. Sci. Catal.* **2007**, *160*, 49-56.

[85] G. Y. Gor, P. Huber, J. Weissmüller, Elastocapillarity in nanopores: Sorption strain from the actions of surface tension and surface stress. *Phys. Rev. Materials* **2018**,*2*, 86002.

[86] M. Thommes and K. A. Cychosz, Physical adsorption characterization of nanoporous materials: progress and challenges. *Adsorption* **2014**, *20*, 233–250.

[87] F. Rouquerol, J. Rouquerol, K. S. W. Sing, P. L. Llewellyn, G. Maurin, in *Adsorption by powders and porous solids: Principles, methodology and applications*, 2nd edn, Elsevier/Academic Press, Amsterdam 2014.

[88] S. Lowell, J. Shields, M. A. Thomas, M. Thommes, Characterization of Porous Solids and Powders: Surface Area, Pore Size and Density, Springer International Publishing, Cham 2004.

[89] J. Deboer, Studies on pore systems in catalysts VI. The universal t curve. *J. Catal.* **1965**, *4*, 643–648.

[90] A. Galarneau, F. Villemot, J. Rodriguez, F. Fajula, B. Coasne, Validity of the t-plot method to assess microporosity in hierarchical micro/mesoporous materials. *Langmuir*, **2014**, *30*, 13266–13274.

[91] D. S. Sholl and R. P. Lively, Seven chemical separations to change the world. *Nature* **2016**, *532*, 435–437.

[92] B. Wang, L.-H. Xie, X. Wang, X.-M. Liu, J. Li, J.-R. Li, Applications of metal–organic frameworks for green energy and environment: New advances in adsorptive gas separation, storage and removal. *Green Energy Environ.* **2018**, *3*, 191–228.

[93]S. Mokhatab, W.A. Poe, J.G. Speight, Natural gas dehydration. In *Handbook of natural gas transmission and processing.*, Gulf Professional Publ, Burlington, MA 2006, S. 323–364.

[94] A. Nuhnen and C. Janiak, A practical guide to calculate the isosteric heat/enthalpy of adsorption via adsorption isotherms in metal-organic frameworks, MOFs. *Dalton Trans.* **2020**, *49*, 10295–10307.

[95] S. Yang, J. Sun, A. J. Ramirez-Cuesta, S. K. Callear, W. I. F. David, D. P. Anderson, R. Newby, A. J. Blake, J. E. Parker, C. C. Tang, M. Schröder, Selectivity and direct visualization of carbon dioxide and sulfur dioxide in a decorated porous host. *Nat. Chem.* **2012**, *4*, 887–894.

[96] J. H. Carter, X. Han, F. Y. Moreau, I. da Silva, A. Nevin, H. G. W. Godfrey, C. C. Tang, S. Yang, M. Schröder, Exceptional Adsorption and Binding of Sulfur Dioxide in a Robust Zirconium-Based Metal-Organic Framework. *J. Am. Chem. Soc.* **2018**, *140*, 15564-15567.

[97] N. Bimbo, J. E. Sharpe, V. P. Ting, A. Noguera-Díaz, T. J. Mays, Isosteric enthalpies for hydrogen adsorbed on nanoporous materials at high pressures. *Adsorption* **2014**, *20*, 373–384.

[98] N. F. Cessford, N. A. Seaton, T. Düren, Evaluation of Ideal Adsorbed Solution Theory as a Tool for the Design of Metal–Organic Framework Materials. *Ind. Eng. Chem. Res.* **2012**, *51*, 4911–4921.

[99] A. L. Myers and J. M. Prausnitz, Thermodynamics of mixed-gas adsorption. *AIChE J.* **1965**, *11*, 121–127.

[100] K. S. Walton and D. S. Sholl, Predicting multicomponent adsorption: 50 years of the ideal adsorbed solution theory. *AIChE J.* **2015**, *61*, 2757–2762.

[101] K. Gregory, C. Webster, S. Durk, Estimates of Damage to Forests in Europe due to Emissions of Acidifying Pollutants. *Energy Policy* **1996**, *24*, 655–664.

[102] R. Reiss, E. L. Anderson, C. E. Cross, G. Hidy, D. Hoel, R. McClellan, S. Moolgavkar, Evidence of health impacts of sulfate- and nitrate-containing particles in ambient air. *Inhalation Toxicol.* **2007**, *19*, 419–449.

[103] M. A. Hanif, N. Ibrahim, A. Abdul Jalil, Sulfur dioxide removal: An overview of regenerative flue gas desulfurization and factors affecting desulfurization capacity and sorbent regeneration. *Environ. Sci. Pollut. Res.* **2020**, *27*, 27515–27540.

[104] European Environment Agency. *EEA: Air Quality in Europe-2017 report. Report no. 13/2017.* Luxemburg 2017.

[105] G. E. Likens, C. T. Driscoll, D. C. Buso, Long-Term Effects of Acid Rain: Response and Recovery of a Forest Ecosystem. *Science* **1996**, *272*, 244–246.

[106] C.-L. Horng and M.-T. Cheng, Characterization of PM 2.5 and conversion rate of sulfur dioxide to sulfate in inland areas of Taiwan. *J. Environ.l Eng. Sci.* **2008**, *7*, 175–182.

[107] J.-Y. Lee, T. C. Keener, Y. J. Yang, Potential Flue Gas Impurities in Carbon Dioxide Streams Separated from Coal-Fired Power Plants. *J. Air Waste Manage. Assoc.* **2012**,*59*, 725–732.

[108] F. Birol, L. Cozzi, T. Gould, S. Bouckaert, T.-Y. Kim, K. McNamara, B. Wanner, C. McGlade, P. Olejarnik, Z. Adam, L. Arboleya Sarazola, Y. Arsalane, B. Baruah, S. Bennett, M. Cappannelli, O. Chen, A. Contejean, H. Cisse Coulibaly, D. Crow, D. D'Ambrosio, A. Dasgupta, J. C. Donovan, M. Dos Santos, L. Gallarati, T. Goodson, L. Y. Lee, J. Liu, W. Matsumura, Y. Nobuoka, S. Papapanagiotou, C. Pavarini, D. Perugia, A. Petropoulos, A. Rouget, M. Ruiz de Chavez Velez, A. Schröder, G. Sondak, L. Staas, A. Toril, M. Waldron, M. A. Walton, W. Yu, P. Zeniewski, *International Energy Agency, World Energy Outlook 2019*, OECD Publishing, Paris **2019**.

[109] W. W. Kellogg, R. D. Cadle, E. R. Allen, A. L. Lazrus, E. A. Martell, The sulfur cycle. *Science* **1972**, *175*, 587–596.

[110] I. Manisalidis, E. Stavropoulou, A. Stavropoulos, E. Bezirtzoglou, Environmental and Health Impacts of Air Pollution: A Review. *Front. Public Health* **2020**, *8*, 14.

[111] International Maritime Organization, in *MARPOL Annex VI and NTC 2008: With guidelines for implementation*, 2017th edn, IMO International Maritime Organization, London **2017**.

[112] S. Åström, G. Kiesewetter, W. Schöpp, R. Sander, S. Andersson, Investment perspectives on costs for air pollution control affect the optimal use of emission control measures. *Clean Techn. Environ. Policy* **2019**, *21*, 695–705.

[113] A. B. Rao and E. S. Rubin, A Technical, Economic, and Environmental Assessment of Amine-Based CO_2 Capture Technology for Power Plant Greenhouse Gas Control. *Environ. Sci. Technol.* **2002**, *36*, 4467–4475.

[114] S. Ding, F. Liu, X. Shi, K. Liu, Z. Lian, L. Xie, H. He, Significant Promotion Effect of Mo Additive on a Novel Ce-Zr Mixed Oxide Catalyst for the Selective Catalytic Reduction of NO(x) with NH_3. *ACS Appl. Mater. Interfaces* **2015**, *7*, 9497–9506.

[115] J. H. Goo, M. F. Irfan, S. D. Kim, S. C. Hong, Effects of NO_2 and SO_2 on selective catalytic reduction of nitrogen oxides by ammonia. *Chemosphere* **2007**, *67*, 718–723.

[116] G. H. Luttrell and R. Q. Honaker, Coal coal Preparation coal preparation, *Encyclopedia of sustainability science and technology*, Springer, New York **2012**.

[117] R. A. Pandey, R. Biswas, T. Chakrabarti, S. Devotta, Flue Gas Desulfurization: Physicochemical and Biotechnological Approaches. *Crit. Rev. Env. Sci. Technol.* **2005**, *35*, 571–622.

[118] R. K. Srivastava, W. Jozewicz, C. Singer, SC_2 scrubbing technologies: A review. *Environ. Prog.* **2001**, *20*, 219–228.

[119] S. de Gisi, A. Molino, M. Notarnicola, Enhancing the recovery of gypsum in limestone-based wet flue gas desulfurization with high energy ball milling process: A feasibility study. *Process Saf. Environ. Prot.* **2017**, *109*, 117–129.

[120] R. K. Srivastava, W. Jozewicz, Flue Gas Desulfurization. *J. Air Waste Manage. Assoc.* **2011**, *51*, 1676–1688.

[121] X. Han, S. Yang, M. Schröder, Porous metal–organic frameworks as emerging sorbents for clean air. *Nat. Rev. Chem.* **2019**, *3*, 108–118.

[122] B. Schreiner, Der Claus-Prozess. Reich an Jahren und bedeutender denn je. *Chem. unserer Zeit* **2008**, *42*, 378–392.

[123] W. Moeller and K. Winkler, The Double Contact Process for Sulfuric Acid Production. *J. Air Pollut. Control Assoc.* **1968**, *18*, 324–325.

[124] C. E. Hudak, J. M. Burke, *Summary Report Sulfur Oxides Control Technology Series: Flue Gas Desulfurization Wellman-Lord Process. Summary report*, EPA, Michigan **1979**.

[125] H. Becker, Varianten der Rauchgas-Entschwefelung nach dem Linde-SOLINOX-Verfahren. *Chem. Ing. Tech.* **1987**, *59*, 346–347.

[126] J. Sporer, The Linde Solinox process: Gypsum-free flue-gas desulphurization. *Gas Sep. Purif.* **1992**, *6*, 133–140.

[127] H. Bai, P. Biswas, T. C. Keener, SO_2 Removal by NH_3 Gas Injection: Effects of Temperature and Moisture Content. *Ind. Eng. Chem. Res.* **1994**, *33*, 1231–1236.

[128] D. Bathen, M. Breitbach, *Adsorptionstechnik*, Springer, Heidelberg, **2001**.

[129] L. Jia, Y. Tan, E. J. Anthony, Emissions of SO_2 and NO_x during Oxy–Fuel CFB Combustion Tests in a Mini-Circulating Fluidized Bed Combustion Reactor. *Energy Fuels* **2010**, *24*, 910–915.

[130] L. Riboldi, O. Bolland, Overview on Pressure Swing Adsorption (PSA) as CO_2 Capture Technology: State-of-the-Art, Limits and Potentials. *Energy Procedia* **2017**, *114*, 2390–2400.

[131] D. Britt, D. Tranchemontagne, O. M. Yaghi, Metal-organic frameworks with high capacity and selectivity for harmful gases. *Proc. Natl. Acad. Sci. U. S. A.* **2008**, *105*, 11623–11627.

[132] N.S. Bobbitt, M. L. Mendonca, A. J. Howarth, T. Islamoglu, J. T. Hupp, O. K. Farha, R. Q. Snurr, Metal-organic frameworks for the removal of toxic industrial chemicals and chemical warfare agents. *Chem. Soc. Rev.* **2017**, *46*, 3357–3385.

[133] H. Wang, W. P. Lustig, J. Li, Sensing and capture of toxic and hazardous gases and vapors by metal-organic frameworks. *Chem. Soc. Rev.* **2018**, *47*, 4729–4756.

[134] E. Martínez-Ahumada, A. López-Olvera, V. Jancik, J. E. Sánchez-Bautista, E. González-Zamora, V. Martis, D. R. Williams, I. A. Ibarra, MOF Materials for the Capture of Highly Toxic H_2S and SO_2. *Organometallics* **2020**, *39*, 883–915.

[135] M. Savage, Y. Cheng, T. L. Easun, J. E. Eyley, S. P. Argent, M. R. Warren, W. Lewis, C. Murray, C. C. Tang, M. D. Frogley, G. Cinque, J. Sun, S. Rudić, R. T. Murden, M. J. Benham, A. N. Fitch, A. J. Blake, A. J. Ramirez-Cuesta, S. Yang, M. Schröder, Selective Adsorption of Sulfur Dioxide in a Robust Metal-Organic Framework Material. *Adv. Mater.* **2016**, *28*, 8705–8711.

[136] N. C. Burtch, H. Jasuja, K. S. Walton, Water stability and adsorption in metal-organic frameworks. *Chem. Rev.* **2014**, *114*, 10575–10612.

[137] J.-X. Liu, J. Li, W.-Q. Tao, Z. Li, 3.Al-Based Metal-Organic Framework MFM-300 and MIL-160 for SO_2 Capture: A Molecular Simulation Study. *Fluid Phase Equilibria* **2021**, *536*, 112963.

[138] A. S. Ruhl and A. Kranzmann, Investigation of corrosive effects of sulphur dioxide, oxygen and water vapour on pipeline steels. *Int. J. Greenh. Gas Con.* **2013**, *13*, 9–16.

[139] A. C. Elder, S. Bhattacharyya, S. Nair, T. M. Orlando, Reactive Adsorption of Humid SO_2 on Metal–Organic Framework Nanosheets. *J. Phys. Chem. C* **2018**, *122*, 10413–10422.

[140] C. A. Fernandez, P. K. Thallapally, R. K. Motkuri, S. K. Nune, J. C. Sumrak, J. Tian, J. Liu, Gas-Induced Expansion and Contraction of a Fluorinated Metal–Organic Framework. *Cryst. Growth Des.* **2010**, *10*, 1037–1039.

[141] P. K. Thallapally, R. K. Motkuri, C. A. Fernandez, B. P. McGrail, G. S. Behrooz, Prussian blue analogues for CO_2 and SO_2 capture and separation applications. *Inorg. Chem.* **2010** *49*, 4909–4915.

[142] X. Han, H. G. W. Godfrey, L. Briggs, A. J. Davies, Y. Cheng, L. L. Daemen, A. M. Sheveleva, F. Tuna, E. J. L. McInnes, J. Sun, C. Drathen, M. W. George, A. J. Ramirez-Cuesta, K. M. Thomas, S. Yang, M. Schröder, Reversible adsorption of nitrogen dioxide within a robust porous metal-organic framework. *Nat. Mater.* **2018**, *17*, 691–696.

[143] S. Yang, L. Liu, J. Sun, K. M. Thomas, A. J. Davies, M. W. George, A. J. Blake, A. H. Hill, A. N. Fitch, C. C. Tang, M. Schröder, Irreversible network transformation in a dynamic porous host catalyzed by sulfur dioxide. *J. Am. Chem. Soc.* **2013**, *135*, 4954–4957.

[144] G. L. Smith, J. E. Eyley, X. Han, X. Zhang, J. Li, N. M. Jacques, H. G. W. Godfrey, S. P. Argent, L. J. McCormick McPherson, S. J. Teat, Y. Cheng, M. D. Frogley, G. Cinque, S. J. Day, C. C. Tang, T. L. Easun, S. Rudić, A. J. Ramirez-Cuesta, S. Yang, M. Schröder, Reversible coordinative binding and separation of sulfur dioxide in a robust metal-organic framework with open copper sites. *Nat. Mater.* **2019**, *18*, 1358–1365.

[145] W. Sun, L.-C. Lin, X. Peng, B. Smit, Computational screening of porous metal-organic frameworks and zeolites for the removal of SO_2 and NO_x from flue gases. *AIChE J.* **2014**, *60*, 2314–2323.

[146] X.-D. Song, S. Wang, C. Hao, J.-S. Qiu, Investigation of SO_2 gas adsorption in metal–organic frameworks by molecular simulation. *Inorg. Chem. Commun.* **2014**, *46*, 277–281.

[147] X. Cui, Q. Yang, L. Yang, R. Krishna, Z. Zhang, Z. Bao, H. Wu, Q. Ren, W. Zhou, B. Chen, H. Xing, Ultrahigh and Selective SO_2 Uptake in Inorganic Anion-Pillared Hybrid Porous Materials. *Adv. Mater.* **2017**, *29*, 1606959.

[148] M. R. Tchalala, P. M. Bhatt, K. N. Chappanda, S. R. Tavares, K. Adil, Y. Belmabkhout, A. Shkurenko, A. Cadiau, N. Heymans, G. de Weireld, G. Maurin, K. N. Salama, M. Eddaoudi, Fluorinated MOF platform for selective removal and sensing of SO_2 from flue gas and air. *Nat. Commun.* **2019**, *10*, 1328.

[149] J. A. Zárate, E. Sánchez-González, D. R. Williams, E. González-Zamora, V. Martis, A. Martínez, J. Balmaseda, G. Maurin, I. A. Ibarra, High and energy-efficient reversible SO_2 uptake by a robust Sc(iii)-based MOF. *J. Mater. Chem. A* **2019**, *7*, 15580–15584.

[150] M. Rivera-Almazo, M. L. Díaz-Ramírez, R. Hernández-Esparza, R. Vargas, A. Martínez, V. Martis, P. A. Sáenz-Cavazos, D. Williams, E. Lima, I. A. Ibarra, J. Garza, Identification of the preferential CO and SO_2 adsorption sites within NOTT-401. *Phys. Chem. Chem. Phys.* **2021**, *23*, 1454–1463.

[151] E. Martínez-Ahumada, M. L. Díaz-Ramírez, H. A. Lara-García, D. R. Williams, V. Martis, V. Jancik, E. Lima, I. A. Ibarra, High and reversible SO_2 capture by a chemically stable Cr(iii)-based MOF. *J. Mater. Chem. A* **2020**, *8*, 11515–11520.

[152] P. Brandt, S.-H. Xing, J. Liang, G. Kurt, A. Nuhnen, O. Weingart, C. Janiak, Zirconium and Aluminum MOFs for Low-Pressure SO_2 Adsorption and Potential Separation: Elucidating the Effect of Small Pores and NH_2 Groups. *ACS Appl. Mater. Interfaces* **2021**, *13*, 29137–29149.

[153] P. Brandt, A. Nuhnen, S. Öztürk, G. Kurt, J. Liang, C. Janiak, Comparative Evaluation of Different MOF and Non-MOF Porous Materials for SO_2 Adsorption and Separation Showing the Importance of Small Pore Diameters for Low-Pressure Uptake. *Adv. Sustainable Syst.* **2021**, *5*, 2000285.

[154] P. Brandt, A. Nuhnen, M. Lange, J. Möllmer, O. Weingart, C. Janiak, Metal–Organic Frameworks with Potential Application for SO_2 Separation and Flue Gas Desulfurization. *ACS Appl. Mater. Interfaces* **2019**, *11*, 17350–17358.

[155] J. Liang, S. Xing, P. Brandt, A. Nuhnen, C. Schlüsener, Y. Sun, C. Janiak, A chemically stable cucurbit[6]uril-based hydrogen-bonded organic framework for potential SO_2/CO_2 separation. *J. Mater. Chem. A* **2020**, *8*, 19799–19804.

[156] S. Xing, J. Liang, P. Brandt, F. Schäfer, A. Nuhnen, T. Heinen, I. Boldog, J. Möllmer, M. Lange, O. Weingart, C. Janiak, Capture and Separation of SO_2 Traces in Metal-Organic Frameworks via Pre-synthetic Pore Environment Tailoring by Methyl Groups. *Angew. Chem. Int. Ed.* **2021**, *60*, 2–10.